UNIVERSITY OF GENOA
POLYTECHNIC SCHOOL

DIME – Department of Mechanical, Energy, Management and Transportation Engineering

DIME/MEC

PhD Course in Mechanical, Energy and Management Engineering (PhD IMEG)

Curriculum Mechanics, Measurements and Materials (MMM)

PhD Thesis

XXXIV Course

"Analysis of dynamic responses and instabilities in rotating machinery"

PhD Coordinator:
Prof. Giovanni Berselli

Tutor supervisors:
Prof. Paolo Silvestri
Prof. Aristide Fausto Massardo

PhD Candidate:
Carlo Alberto Niccolini Marmont Du Haut Champ

March 2022

Contents

Abstract

The first task of the present research is to characterize both experimentally and numerically journal bearings with low radial clearances for rotors in small-scale applications (e.g., micro Gas Turbines); their diameter is in the order of ten millimetres, leading to very small dimensional clearances when the typical relative ones (order of 1/1000) are employed; investigating this particular class of journal bearings under static and dynamic loading conditions represents something unexplored. To this goal, a suitable test rig was designed, and the performance of its bearings were investigated under steady load. For the sake of comparison, numerical simulations of the lubrication were also performed by means of a simplified model. The original test rig adopted is a commercial Rotor Kit (RK), but substantial modifications were carried out in order to allow significant measurements. Indeed, the relative radial clearance of RK4 RK bearings is about 2/100, while it is around 1/1000 in industrial bearings. Therefore, the same original RK bearings are employed in this new test rig, but a new shaft was designed to reduce their original clearance. The new custom shaft allows to study bearing behaviour for different clearances, since it is equipped with interchangeable journals. Experimental data obtained by this test rig are then compared with further results of more sophisticated simulations. They were carried out by means of an in-house developed finite element (FEM) code, suitable for ThermoElasto-HydroDynamic (TEHD) analysis of journal bearings both in static and dynamic conditions. In this work, bearing static performances are studied to assess the reliability of the experimental journal location predictions by comparing them with the ones coming from already validated numerical codes. Such comparisons are presented both for large and small clearance bearings of original and modified RK, respectively. Good agreement is found only for the modified RK equipped with small clearance bearings (relative radial clearance 8/1000), as expected. In comparison with two-dimensional lubrication analysis, three-dimensional simulation improves prediction of journal location and correlation with experimental results.

The second main task of the present work is the development and the implementation of a suitable analytical model to correctly capture rolling bearing radial stiffness, particularly nearby the critical speeds of the investigated rotor-bearings system. In this work, such bearing non-linear stiffness lumped parameter model is firstly validated on the commercial RK and then it is applied to both air bladeless turbines (or Tesla turbines) and to an innovative microturbine, in order to assess their global rotodynamic behavior when they are mounted on ball bearings. In order to properly investigate all the issues related to critical speeds and stiffness, an adequate number of experimental tests was performed by exploiting an experimental air Tesla turbine prototype located at TPG experimental facility of the University of Genoa. The correlation between measured flexural critical speeds and their numerical predictions is markedly conditioned by the correct identification of ball bearings

dynamic characteristics; in particular, bearings stiffness effect may play a significant role in terms of rotor-bearings system natural frequencies and therefore it must be properly assessed. Indeed, Tesla turbine rotor FE model previously employed for numerical modal analysis relies on rigid bearings assumption and therefore it does not account for bearings stiffness overall contribution, which may become crucial in case of "hard mounting" of rotor-bearings systems. Subsequently, high-speed air Tesla rotor is investigated by means of an enhanced FE model for numerical modal analysis within Ansys® environment, where ball bearings are modelled as non-linear springs whose stiffness is expressed according to the analytic model implemented in Matlab®. Two different numerical FE models are devised for microturbine rotor modelling which respectively rely on beam elements and on three-dimensional solid elements for mechanical system spatial discretization. The obtained results in terms of rotor-bearings system modal analysis exhibit an improvement in experimental-numerical results correlation by relying on such ball bearing stiffness model; moreover, beam-based FE model critical speeds predictions are coherent with experimental evidence and with respect to solid elements model it is characterized by lower computational time and it is more easily interpretable. Thus, such experimentally validated numerical model represents a reliable and easily adaptable tool for high-speed rotating machinery critical speeds prediction in practical industrial application cases.

Finally In this work, several signal processing techniques performed on vibro-acoustic signals acquired from a T100 Turbec microturbine (which is furnished with a centrifugal compressor) are illustrated. Research activity goal focuses on the investigation different kinds of system response starting from non-intrusive probes signals like accelerometers and microphones; this is made by means of techniques such as HOSA and Wavelet Transform, developed in Matlab® environment, for early detection of the onset of unstable phenomena in centrifugal compressors. These new and different methods have been applied to the same set of data to get sufficiently independent information useful to synergistically improve knowledge in the diagnostic system. Data were acquired by means of an experimental facility based on a T100 turbine developed by the Thermochemical Power Group (TPG) at the University of Genoa. Sampling rate and sensor placement were carefully taken into account, basing both on the physical phenomena to be observed and on the sensor dynamic characteristics. In this context, it is meant to study microphones and accelerometers signals not from an isolated centrifugal turbomachine installed in a dedicated line, but from a whole compressor placed in a mGT system for energy generation. Indeed, the investigated machine is not operating in stand-alone mode, but its working point and angular velocity depend on the coupling with several elements. In particular, compressor working point and then its vibro-acoustic signals are expected to convey vibration and sound contributions coming from all the plant components; thus, they are more representative of machine realistic behavior in the energy system.

1 Introduction

In the last two decades the attention for the environmental protection has been spread widely, especially in developed countries [1]. In particular, great efforts have been made to limit the global warming, in order to avoid serious consequences for mankind. In this context, the Kyoto Protocol represents an important milestone, that entered into force on 16 February 2005. For the first time in history, most countries set the common goal of reducing carbon dioxide (CO2) emissions, in order to limit global warming. In particular, the recent ratification of "Paris agreement" fixed the limitation of the global warming below 1.5 °C, imposing specific targets for each signatory state.

The challenging targets for the reduction greenhouse gas emissions, set by European Union and other international institutions [2][3] led the EU power generation mix to change considerably in favour of renewable sources, which have become the fastest growing source of electricity among the member countries [4][5].

Considering this scenario, distributed generation [6][7]based on the installation of small size generators close to users is expected to decrease energy losses and to improve fuel energy exploitation through cogeneration and trigeneration plants. Non-dispatchable Renewable Energy Sources, e.g., wind and solar, are characterized by an extreme hour by hour production variability, due to their stochastic and non-programmable nature. A good approach is based on using renewable generation plants and dispatching the remaining loads to fossil fuel plants, favouring the highest efficiency (or lower marginal cost) devices. Land-based simple-cycle gas turbines are well-known for their compactness, flexibility and rapidity of installation, despite the fact that they are affected by relatively poor efficiencies due to the high exhaust temperatures. On the other hand, the waste heat can be reutilized (cogeneration) while promising micro gas turbines (MGT) cycle innovations [8]are in development. They will increase efficiency and open up new fields of application as for the distributed generation. For example, mixed gas-steam cycles are able to show good performance and competitive costs [9]while hybrid MGT/Solid Oxide Fuel Cell (SOFC) power plants have the potential to reach electrical efficiency values above 65% [10][11][12][13]This kind of innovative energy systems employ additional components and volume connected to the micro gas turbine, but presents critical issues related to surge risk due to a delayed response in the pressurization/depressurization phases during the transient operations [14].

1.1 Surge

Surge is a fluid dynamic instability phenomenon typical of dynamic compressors [15][16], which affects flow conditions throughout the entire compression system. Pressure and mass flow oscillations as well as the transmitted vibrations, due to surge can lead to severe damage to the system in terms

of its structural integrity. Surge instability can also occur in axial and centrifugal pumps and blowers, but it is less frequent, and the damage is less severe [16]. Another fluid dynamic instability that is likely to occur in dynamic compressors is stall. It is sometimes confused with surge, but the consequences of stall are usually less severe in terms of machine performance decrease, even if they can lead to structural damage due to the induced vibrations, particularly in case of VDRS. As the flow through a compressor is reduced, a point is reached at which the flow pattern becomes unstable. If the flow oscillates in localized regions around the rotor, such instability is referred to as stall; it consists of a boundary layer separation from the compressor blade profile generally due to excessive variations in flow incidence angle with respect to its nominal value. The drop in compressor performance due to stalling will depend on the number of blades affected by the phenomenon and, in general, it will be more contained in centrifugal compressors than in axial ones due to the contribution of the centrifugation term. For axial compressors the region of unstable forward flow can be extended over just a few blades or up to 180 degrees around fluid machine annulus [15]. In rotating stall, the region of unstable forward flow rotates around compressor annulus. Rotating stall characteristic frequency is some fraction of compressor angular speed, but it does not depend on the piping system in which the compressor is installed (i.e., it depends only on machine characteristics), while the average mass flow rate across the compressor annulus, when it stalls, is still positive. Stall can develop into a more global type of instability referred to as surge: In surge the average mass flow rate across the annulus goes through large amplitude oscillations whose frequency depends on both the compressor and piping (so on the whole plant volume) system.

Figure 1.1 shows a compressor map for a variable-speed centrifugal compressor. A compressor map is the single most important piece of information to describe surge from the plant level point of view. A compressor map shows the compressor characteristic curve for different operating conditions. Each curve traces the rise in discharge pressure developed by the compressor as the suction flow is varied according to a given operating condition (such as system angular speed).

The X axis can report the mass or volumetric flow (or the reduced/referred mass flow rate) at the stated suction temperature, pressure, and molecular weight. The Y axis can report either the discharge pressure, the ratio of discharge pressure to suction pressure β, or it can refer to the differential pressure rise from suction to discharge. The compressor characteristic curves cover the negative sloped region and end where the slope approaches zero (A negative slope means the pressure will change in the opposite direction for a change in flow rate, and a zero slope means the pressure will not change at all for a change in flow rate). If a curve is drawn through the point of zero slope for each characteristic curve, the region to the left of this line is where the instabilities related to surge and stall are likely to occur. Indeed, in literature, this line is referred to as either the stall curve or surge line. The

characteristic curve to the left of such instability line is difficult to be experimentally characterized, but its general shape resembles what shown in Figure 1.1. The negative flow rate portion of the curve can be found by supplying pressurized gas to the compressor discharge to force a steady negative flow rate, while its positive sloped portion is obtained by smoothly connecting a third-order polynomial curve between the negative sloped part and the positive flow rate portions of the curve [17]

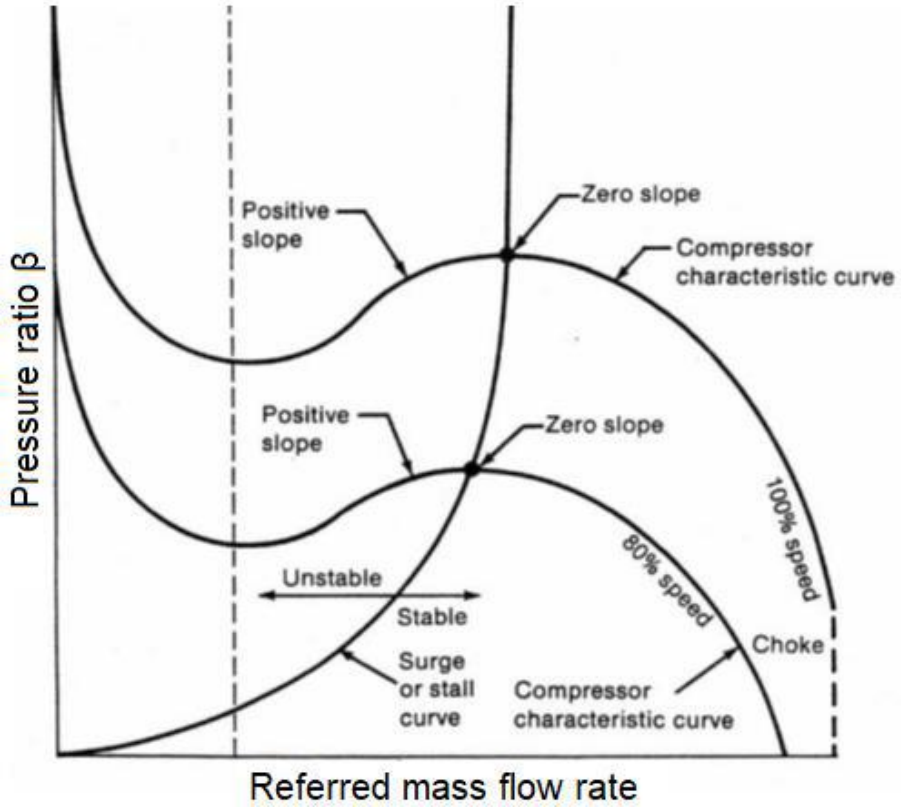

Figure 1.1 – Compressor map for a variable-speed centrifugal compressor [16]

Surge can be better understood by visualizing a block or throttle valve closing downstream of the compressor, which acts as a load for the operating machine (refer to Figure 1.2).

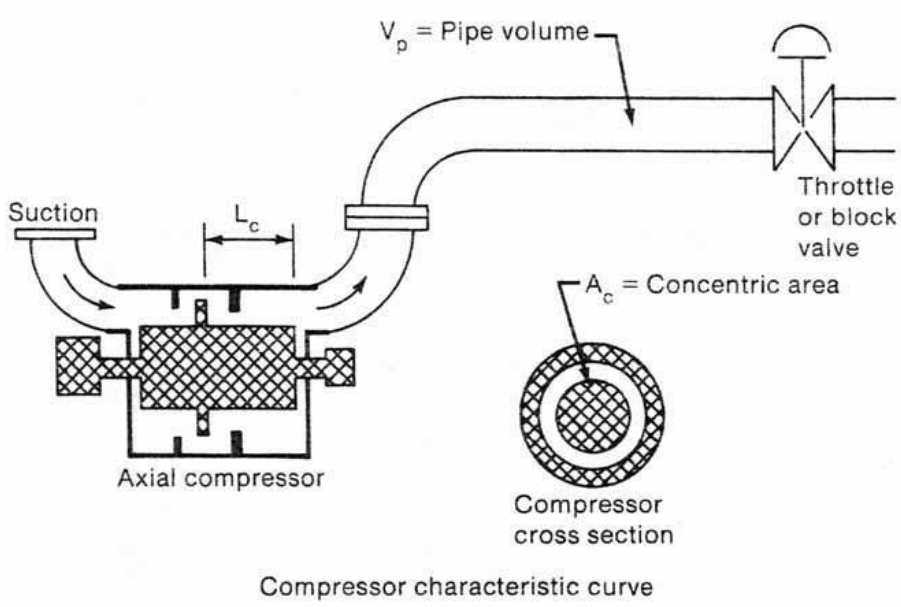

Figure 1.2 – Diagram of a simple plant with a valve closing downstream of the compressor [16]

As this valve closes, the suction flow decreases, and the operating point moves to the left along a characteristic curve. If compressor angular speed or its Inlet Guide Vane (IGV) position does not change, system operating point eventually will pass by the point of zero slope on the characteristic curve. Just to the left of this point, which is the intersection of the surge line with the characteristic curve, the pressure rise developed by the compressor is less than the pressure in the piping between the compressor discharge and the closing valve. For this reason, the forward flow rate through the compressor decreases and eventually it may even reverse its direction, in this way the gas flows from the discharge piping back through the compressor to the suction piping. The returning back of the flow rate makes the pressure in the discharge piping start to drop. When this pressure is below the pressure developed by the compressor, forward flow rate starts again. If the gas in the discharge piping is still trapped by the closing block or throttle valve, the gas pressure builds up and the surge cycle is repeated. Note that the alternating pressure build up and decay cycle does not require the flow to actually reverse direction, but only to alternately decrease below or increase above the flow rate through the block or throttle valve. Only in severe (deep) surge conditions the flow rate through the compressor actually reverses direction. Whether a compressor system is stable or unstable depends on how its operating point reacts to a disturbance. If the deviation of the operating point from its initial value grows or continually oscillates after a disturbance, the system is unstable. A uniform growing deviation is classified as a static instability and an oscillating deviation of growing or constant amplitude is classified as a dynamic instability. Surge is classified as a dynamic instability. Dynamic instability is characterized by growing oscillations and it can occur if either the discharge plenum volume or the compressor impeller speed is large enough to cause a system response

parameter B to exceed a minimum value and the slope of the compressor characteristic curve is positive. The general criterion, for dynamic instability, is reported in (1.1) [16][18] based on the Greitzer's B parameter [19][20]which can be interpreted as the ratio between pressure and inertial forces:

$$B > B_m \; ; \; S_c > 0; \; B = \frac{U\sqrt{V_p/(A_c L_c)}}{2a} \tag{1.1}$$

B = system dynamic response parameter (dimensionless)

S_c = slope of the compressor characteristic curve

B_m = minimum B for dynamic instability (typically 0.1 to 1.0)

a = speed of sound in the gas (m/s)

A_c= cross-sectional area of flow path in compressor (m^2)

L_c= length of flow path in compressor (m)

N = compressor impeller tangential speed (m/s)

V_p = volume of the plenum (m^3)

Considering the system in Figure 1.2 as example, the plenum is any enclosed volume of gas. In a compressor installation, the plenum may be a vessel or distribution header between the compressor and the block or throttle valve (or turbine). If the valve is installed directly at the end of a section of the pipe or the duct connected to the compressor discharge, the volume of this section can be regarded as an equivalent plenum.

The compressor flow path length and area are small enough and the plenum volume is large enough in most industrial installations to satisfy the criterion for dynamic instability when the operating point crosses over from the negative to the positive sloped portion of the compressor characteristic curve. However, the oscillation amplitude stops growing due to the nonidealities and nonlinearities of compression in real-world applications. The resulting constant amplitude oscillation is referred to as a limit cycle. Surge is a dynamic instability that develops into a limit cycle. Stall is not a dynamic instability because oscillations amplitude decreases (i.e. decays) with time. Thus, the minimum B value (typically 0.1 to 1.0) is the boundary line between surge onset and stall inception. Surge occurs when B is above the minimum B, and stall occurs when B is below the minimum B [16]. Also, the severity of surge is proportional to the magnitude of B. Note that this minimum B parameter depends on compressor design, speed, and system dimensions, even if some efforts has been done to normalize the shape of compressor characteristic curve to bring about a universal value of the minimum B [21]. Surge occurs when an unstable operating point reacts to a disturbance. While in centrifugal compressors the rotating stall is weaker and not always stalling behaviour appears to initiate surge [20], in axial ones, it is the collapse of the pressure rise associated with rotating stall onset which

provides the driving force for the flow oscillations associated with surge; in an engine-type compressor, surge is not only preceded by stall but even caused by it [21]. Moore and Greitzer presented a unified theory of stall and surge in multistage axial compressors [19][22]. Based on theoretical work of the 1980s, during the nineties, special efforts have been made in order to obtain a stall (and so surge) active control for automotive and aeroengine gas turbines. In spite of reported successes, work on active control died out in the UK after the Viper engine experiments by Freeman [23]. Indeed, improvements in efficiency achieved by active controls were at the expense of a considerably more complex control system.

Nowadays, an innovative approach to early detect surge onset is being investigated: it is based on vibro-acoustic signals emitted by the compressor. The aim is to diagnose in advance and therefore to prevent instability phenomena of compression systems by directly exploiting information conveyed by vibro-acoustic signals [24]. At the University of Ferrara [25] some accelerometers and microphones were placed on a small compressor with six axial stages and one centrifugal stage to perform vibro-acoustic measurements; suitable post-processing techniques allowed the identification of incoming stall, demonstrating the usefulness of vibration measurements in the detection and analysis of incoming flow instabilities, as also indicated by Bently [26]. One of the most important frequency regions to be investigated in vibro-acoustic signals is the sub-synchronous range of frequencies below the compressor rotational speed. At the University of Athens [27] experimental investigations were performed on turbocharger compressors to find out whether vibration or acoustic measurements can be correlated to an unstable operating condition (stall or surge). An increase in low frequency spectral contents energy (below rotational frequency) was observed as compressor operating point was moving from the stable into the unstable operation regime. The most sensitive sensor to changes of system operational conditions was found to be the microphone facing the compressor from its inlet side. For this reason, the authors suggested as stall and surge precursor collected acoustic signal RMS value, filtered in spectrum sub-synchronous frequency range. In [28] FFT algorithm and cyclostationary analysis technique [29][30] were employed to detect stall and surge by means of vibrational and acoustic signals from the same compressor in [25] equipped with and without a bigger discharge volume. The considered accelerometer signal was that in axial direction, since both surge and stall seem capable of affecting axial vibrations, while the microphone was placed at compressor intake duct. Moreover, FFT revealed a clear amplitude increase in sub-synchronous frequency range but the authors investigated also the higher frequency region around vane passing frequency and blade pass frequency spectral contents. These later appear to decrease their energy due to compressor instability onset, but the blade pass frequency spectral content becomes modulated with rotating stall characteristic frequency and the surge cyclic frequency.

1.2 Theoretical basis about turbine rotor vibrations

Since the research work of this thesis will show the role of vibro-acoustic analysis of surge transients, it is necessary to introduce the concepts of vibration modes and critical speeds of a rotor. They are useful to investigate turbine rotor vibrational behaviour in stable (safe) and unstable operational condition to be able then to better identify surge contributes when assessing machine operating response.

1.2.1 Vibration modes

Every physical object or structure has its own vibration modes or normal modes that depend on the structure itself, its materials and boundary conditions. A mode is a combination of a deformed shape in the space, in which the structure will exchange kinetic-energy and strain-energy continuously, and the natural frequency at which such mode shape occurs. This fixed frequency of a system is referred to as natural frequency or resonant frequency. A structural mode has an associated modal shape, not a displacement: this means that the magnitude of the mode shape is arbitrary. If only one mode is present all parts/points of the structure will move sinusoidally following a pattern with the same frequency and with a fixed phase relation. In a mode shape there are typically some points or lines where the modal amplitude is zero; they are referred to as nodes (in mono-dimensional analysis) or nodal lines (in 2D): Since the vibration of a linear mechanical system is given by the mode shape multiplied by a time function, the displacement of the node points and lines remain zero at all times. While the moving, the structure passes from an un-deformed state to a maximum deformed state: In the un-deformed state, the velocity at every point will be at its maximum. At this time, the kinetic energy is at its peak and the strain energy is zero. At the maximum deformed state, the instantaneous velocity is zero. The kinetic energy at this point is zero while the strain energy is at a maximum. If a structure is deformed into any of its modal shapes and then released, it oscillates continuously from its initial shape to the negative of its initial shape and back again, at the natural frequency of the excited vibration mode. The most general motion of a structure is a superposition of its normal modes: if it is deformed into any linear combination of mode shapes and released, each mode is present in the resulting deformation over time. Furthermore, each mode oscillates at its own natural frequency. For an undamped structure, after the first deformation, no external load is needed to keep the oscillation going on at constant amplitude. Vibration modes are also named normal modes in the sense that they can move independently, i.e., an excitation of one mode will never cause motion of a different one. In mathematical terms, normal modes are orthogonal to each other. A load applied at the natural frequency of any mode would cause additional motion for that mode, increasing the vibrational amplitude of its oscillation. All the energy available from the load is absorbed into the structure. If there is no damping (theoretical case), the oscillation ideally grows to infinity, or rather

until failure. With some damping (real case), the oscillation grows to the point where the damping removes exactly the same amount of energy from the system as the amount of energy being added by the excitation load. This can lead to failure due to the relatively large oscillations that can result from a relatively small excitation force. Such condition is referred to as mechanical resonance.

1.2.2 Rotor vibrational response during operations

All three main modes of rotor-vibrations – lateral, torsional, and axial modes – may be present during rotor operation [31][32]. Among these modes, rotor flexural modes are of the greatest concern.

There is a long list of factors which contribute to the energy transfer from rotation to vibrations. The first and best known among them is rotor unbalance. When the rotor mass centerline does not coincide with its rotational axis, then mass unbalanced inertia-related rotating forces occur. They rotate together with the rotor and are oriented perpendicularly to the rotational axis. The rotor unbalance acts, therefore, in the lateral vibration mode, like an external exciting centrifugal force. As a result, the rotor responds with lateral vibrations with frequency, synchronous to rotational speed. Since rotor unbalance is an almost inevitable element of the rotor system, it is important to ensure that during operating conditions unbalance-related synchronous vibration amplitudes are acceptable, and that during starts-ups and shutdowns a high-speed turbomachine should be able to smoothly pass several lateral balance resonance speeds (‘‘critical speeds’’).

The American Petroleum Institute (API) [33], defines critical speeds and resonances as follows:

Critical Speed – A shaft rotational speed that corresponds to the peak of a noncritically damped (amplification factor > 2.5) rotor-bearings system resonance frequency. The frequency location of the critical speed is defined as the frequency of the peak vibration response as defined by a Bode plot (for unbalance excitation).

Resonance – The way a rotor vibrates when the frequency of a harmonic (periodic) external exciting force coincides with a natural frequency of rotor-bearings system. It is important to consider that, in rotor-dynamics, the natural frequencies of the modes are not constant but a function of the speed the rotor is spinning at (e.g. stress stiffening/softening effects due to centrifugal field, gyroscopic effects). The frequency of the response vibrations to an exciting force corresponds to the frequency of such force (only in case of system linear behaviour): e.g., the frequency of rotor-bearings system lateral vibrations due to unbalance will be equal to revolution frequency. In industry, the frequency of vibrations is usually related as ratios of the rotational speed; thus, the unbalance-related synchronous lateral vibrations are referred to as (1X) vibrations.

In Figure 1.3 a damped natural frequency versus speed plot (Campbell Diagram) is drawn for reference. Note that a line corresponding to 1X synchronous speed has been added to the damped

natural frequency plot for reference (green dashed lines). As in the definition, critical speeds occur at the peak response speed when a system natural pulsation frequency is excited by the shaft unbalance. As with any resonance, very large amplitudes are possible, and are controlled only by system damping. Not all the natural frequencies can be excited by residual mechanical unbalance. In example, backward modes (dashed blue lines) in the system of Figure 1.3 are not excited when there are the intersections shown in the Campbell diagram between the synchronous (1X) line and backward modes natural pulsation frequencies.

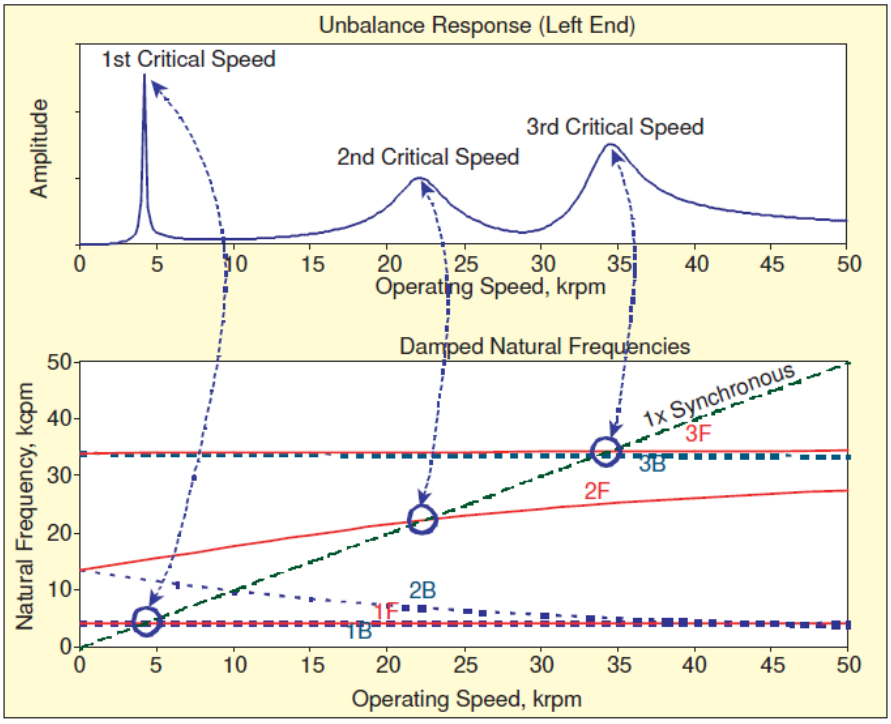

Fig. 1.3 – Campbell diagram and comparison between natural frequencies and critical speeds [32]

Since rotor unbalance is not the only force that would excite rotor vibrations, the other periodic force-excited vibrations of rotors (for example, blade-passing frequency periodic excitations) must be recognized and kept under control. Figure 1.4 shows Input/output relationships for different kind of loads acting on a rotor. The frequency of the response vibrations to an exciting force corresponds to its characteristic frequency only under the hypothesis of system linear behaviour.

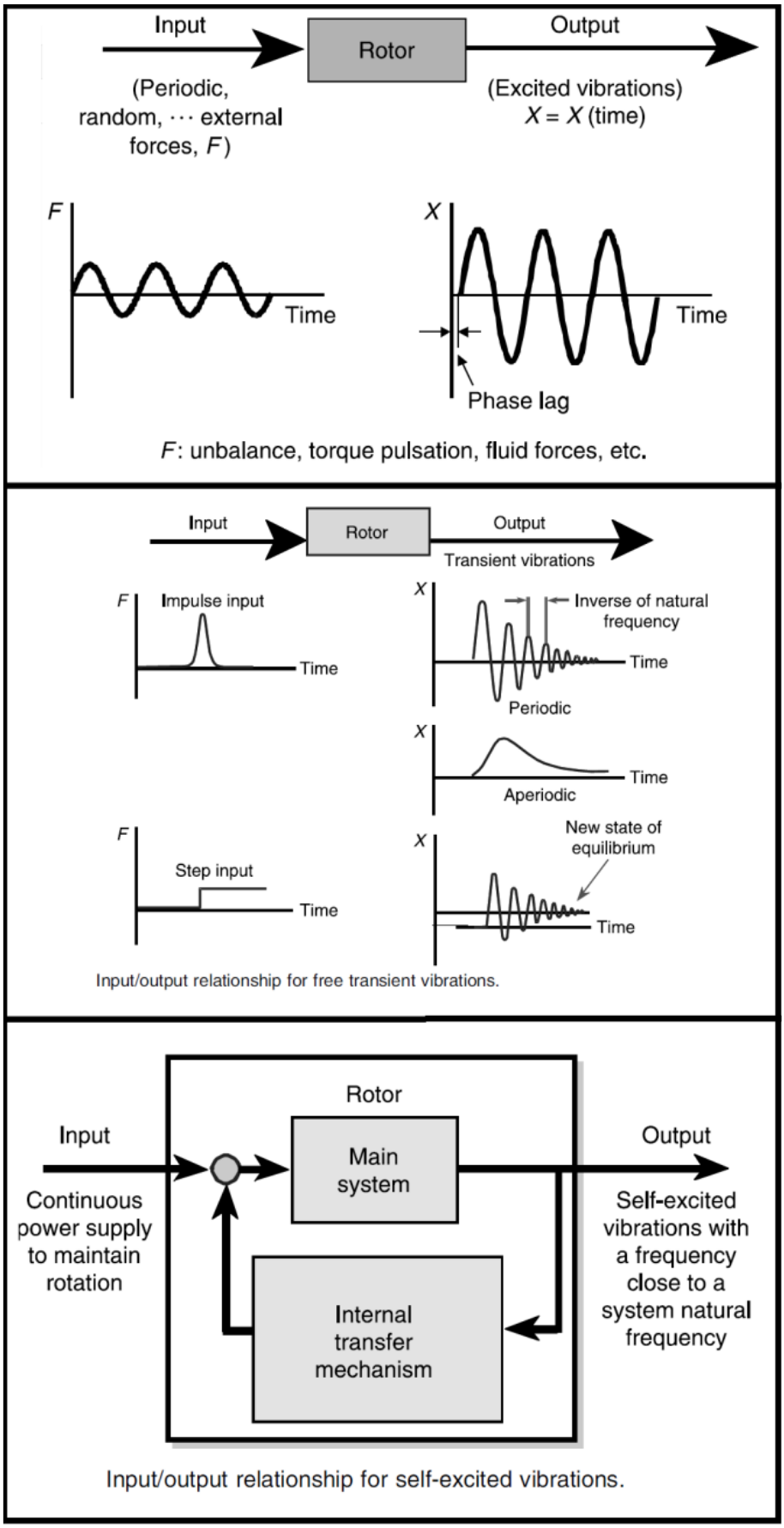

Figure 1.4 – Input/output relationship for different kind of forces on a rotor

If the rotor-bearings system is nonlinear (e.g. due to fluid-structure interactions in hydrodynamic shaft supports), which is usually the case to a certain degree, then, in the system, more frequency components can be generated in response to an exciting force of a single frequency. The corresponding frequencies usually represent multiples of the excitation frequency. A nonlinear rotor-bearings system synchronous (1X) response to unbalance will then be accompanied by higher harmonic components (2X, 3X, …). Additionally, often a single-frequency force can excite rotor responses with fractional frequencies, such as 1/2X, 1/3X, ...Such responses are also accompanied by their corresponding higher harmonic components. Excitations of nonlinear systems by several forces, with different frequencies, usually results in responses with frequency bands of fractional/multiple sums and differences.

Parallel to excited vibrations described above, there is the second category of vibrations in mechanical systems, called ‘‘free vibrations’’ or ‘‘transient vibrations’’, which occurs when the system is excited by a short-lasting impact, causing instantaneous changes in system acceleration, velocity, and/or position. In this case, the system responds to the impact with free vibrations characterized by its ‘‘natural’’ frequencies, which, in case of damped systems, will eventually decay if no exciting forces are applied again.

There exists also a third category of vibrations in physical systems, known as self-excited vibrations. These vibrations are steady, usually with constant amplitude, phase, and frequency. They are maintained by a constant source of energy, which may be external, or is a part of the system. In this type of vibrations, through the feedback mechanism, the constant energy is ‘‘portioned’’ by the oscillatory motion. The frequency of self-excited vibrations is close to one of the system natural frequencies.

In the presented research activity, the influence of bearing static and dynamic characteristics in rotating machinery behavior is assessed by means of analytical, experimental, and numerical investigations. Indeed, hydrodynamic bearings may play a significant role in triggering instability phenomena which involve fluid-structure interaction and may eventually lead to mechanical failures (e.g., oil-whip). Indeed, fluid-structure interactions may be influential even in case of real-size complex shaft lines supported by hydrodynamic supports. Before presenting a practical industrial study case, a basic research activity on hydrodynamic journal bearings is presented to validate an in-house developed experimental model in order to study even on small scale fluid-structure interactions. On the other hand, rolling bearings (e.g., ball bearings) constitute the simplest class of mechanical bearings but in some rotor mounting configurations (e.g., hard mounting) they can significantly affect system flexural critical speeds, thus leading to unexpected dynamic amplifications in system response. Such amplitude peaks in unexpected frequency regions in FRFs can be somehow predicted

by accurately modeling ball bearings stiffness and by adequately combining such contribution with rotor system FE analysis. Finally, only in the case of ball bearings, their behavior in shaft lines mounted on such supports will be investigated in order to find surge precursors by comparing bearing response in unstable conditions induced by fluid-dynamic instabilities (i.e., surge) and the one in nominal system working conditions, when dealing with energy systems system moved by centrifugal compressors.

1.3 Structure of the thesis

The presented thesis is structured according to the following scheme:

- Chapter 2: hydrodynamic journal bearings static performance characterization by means of both experimental test benches and FE simulations. Several test rigs are presented and tested to assess their reliability in correctly detecting journal center locations within the bearings.
- Chapter 3: the influence of ball bearings characteristics in determining critical speeds of rotor system mounted on such supports is deeply investigated by implementing a non-linear stiffness model and applying it to different industrial study cases.
- Chapter 4: hydrodynamic journal bearings dynamic behavior in presence of a complex shaft line configuration is investigated and some unconventional instability triggering mechanisms are described which may lead to fluid-structure interactions different from classical oil-whip.
- Chapter 5: rolling bearings behavior in presence of centrifugal compressors flow instability (i.e. surge and rotating stall) is investigated by means of several signal processing techniques by relying on both time-frequency analysis and Higher Order Spectral Analysis (HOSA).
- Conclusions

Bibliography chapter 1

[1] Curto D., Franzitta V., Trapanese M., Cirrincione M., "A Preliminary Energy Assessment to Improve the Energy Sustainability in the Small Islands of the Mediterranean Sea", Journal of Sustainable Development of Energy, Water and Environment Systems Year 2020, Volume 8, Issue 4, pp 735-753

[2] Vannoni A., Giugno A., Sorce A., "Thermo-economic analysis under electrical market uncertainties of a combined cycle gas turbine integrated with a flue gas-condensing heat pump", Proceedings of ASME Turbo Expo 2020, June 22-26, 2020, London, England.

[3] European Commission, 2014, "A Policy Framework for Climate and Energy in the Period from 2020 to 2030," p. Brussels.

[4] Eurostat, 2018, Energy, Transport and Environment Indicators. 2018 Edition.

[5] European Commission, 2011, "Energy Roadmap 2050."

[6] Ferrari M.L., Traverso A., Massardo A.F., "Smart polygeneration grids: experimental performance curves of different prime movers" Applied Energy 162 (2016) 622–630

[7] Jana K., Ray A., Majoumerd M.M., Assadi M., De S., Polygeneration as a future sustainable energy solution – A comprehensive review. Applied Energy, 202 (2017) 88-111

[8] Henke M., Monz T., Aigner M., Introduction of a New Numerical Simulation Tool to Analyze Micro Gas Turbine Cycle Dynamics. Journal of Engineering for Gas Turbine and Power, 139 (2017) 042601_1-7.

[9] Pedemonte A.A., Traverso A., Massardo A.F., Experimental analysis of pressurized humidification tower for humid air gas turbine cycles. Part A: Experimental campaign. Applied Thermal Engineering, 28 (2008) 1711-1725.

[10] Zaccaria V., Tucker D., Traverso A., Transfer function development for SOFC/GT hybrid systems control using cold air bypass. Applied Energy, 165 (2016) 695-706.

[11] Ferrari M.L., Pascenti M., Magistri L., Massardo A.F., MGT/HTFC hybrid system emulator test rig: Experimental investigation on the anodic recirculation system. Journal of Fuel Cell Science and Technology, 8 (2011) 021012_1-9.

[12] Ferrari M.L., Pascenti M., Magistri L., Massardo A.F., Hybrid system test rig: Start-up and shutdown physical emulation. Journal of Fuel Cell Science and Technology, 7 (2010) 021005_1-7.

[13] McLarty D., Brouwer J., Samuelsen S., Fuel cell-gas turbine hybrid system design part II: Dynamics and control. Journal of Power Sources, 254 (2014) 126-136.

[14] Abrassi, A., Traverso A., Tucker D., Liese E., Impact of different volume sizes on dynamic stability of a gas turbine-fuel cell hybrid system, Journal of Engineering for Gas Turbines and Power Volume 142, Issue 5, May 2020.

[15] Day I. J., "Stall, surge and 75 years of research", Proceedings of ASME Turbo Expo, Montréal, Canada, 3-8 (2015)

[16] McMillan G. K., "Centrifugal and Axial Compressor Control", Momentum Press, 2010

[17] Abrassi, A., Traverso, A., Ferrari, M. L. Turbocharger-based hybrid systems: Modeling and validation of a free spool subject to compressor surge, Proceedings of the ASME Turbo Expo Volume 3, 2018

[18] Abrassi, A., Fuel cell hybrid systems, dynamics and surge analysis, PhD Thesis,

[19] Greitzer E. M., Moore F. K., "Surge and Rotating Stall in Axial Flow Compressors. Part I: Theoretical Compression System Model". Journal of Engineering for Power, 98 (1976) 190-198.

[20] Fink D. A., Cumpsty N. A., Greitzer E. M., 1992, "Surge dynamics in a free spool centrifugal compressor system", Journal of Turbomachinery 114, 321-322.

[21] Day, I., 1994, "Axial Compressor Performance During Surge," J. Propul. Power, 10(3), pp. 329–336.

[22] Greitzer, E. M., Moore, F. K., 1986, "A Theory of Post-Stall Transients in Axial Compression Systems: Part II—Application," ASME J. Eng. Gas Turbines Power, 108(2), pp. 231–239.

[23] Freeman, C., Wilson, A., Day, I., and Swinbanks, M., 1998, "Experiments in Active Control of Stall on an Aeroengine Gas Turbine," ASME J. Turbomach.,120(4), pp. 637–647.

[24] Niccolini Marmont Du Haut Champ, C.A., Massardo, A.F., Ferrari, M.L., Silvestri, P. "Surge prevention in gas turbines: An overview over historical solutions and perspectives about the future" E3S Web of Conferences, 2019, 113, 02003

[25] Morini M., Pinelli M., Venturini M., "Acoustic and Vibrational Analyses on a Multi-Stage Compressor for Unstable Behavior Precursor Identification", ASME Paper GT2007-27040, ASME Turbo Expo 2007, Montreal, Canada.

[26] Bently D. E., Goldman P., "Vibrational Diagnostics of Rotating Stall in Centrifugal Compressors", ORBIT First Quarter 2000

[27] Aretakis N., Mathioudakis K., Kefalakis M., Papailiou K., “Turbocharger unstable operation diagnosis using vibroacoustic measurements”, ASME Journal of Engineering for Gas Turbines and Power,126 (Nov. 2004) pages 840-847

[28] Munari E., D’Elia G., Morini M., Mucchi E., Pinelli M., Spina P.R., “Experimental Investigation of Vibrational and Acoustic Phenomena for Detecting the Stall and Surge of a Multistage Compressor”, ASME Journal of Engineering for Gas Turbines and Power. 2018; 140(9).

[29] Antoni J., “Cyclostationarity by examples”, Mechanical Systems and Signal Processing 23, (2009) 987–1036

[30] Antoni J., “Cyclic spectral analysis in practice”, Mechanical Systems and Signal Processing 21, (2007) 597–630

[31] Muszyńska A., “Rotordynamics” 2005 by Taylor & Francis Group, LLC

[32] Swanson E., Powell C. D., Weissman S., “A Practical Review of Rotating Machinery Critical Speeds and Modes” SOUND AND VIBRATION/MAY 2005

[33] API publication 684 (First Edition, 1996)

2 Hydrodynamic bearings: characterization of static performance

Hydrodynamic journal bearings and more in general fluid film bearings are often employed to support rotors in modern energy plants (e.g., microGT fuel cell hybrid systems) and crankshafts in automotive applications (e.g., connecting rod bearing in Internal Combustion Engines). Their working principle is based on the interposition of a thin self-pressurized lubricant film between the two opposing bearing surfaces that are in relative motion. For instance, assuming that the relative radial clearance is one per thousandth (1/1000), since journal diameters of micro-GT bearings are usually in the range 10-20 mm, then film thickness is about 10 microns. Therefore, very high-quality standards and tolerances are required to produce this class of bearings, which must be manufactured with high precision processes [1].

The comparison between experimental and numerical results has been employed since the first studies on instability of hydrodynamic journal bearings. In example, by considering all of the non-linear terms in the involved equations and using in-house developed test rigs, the effect of both journal and bearing defects on rotor-bearings system stability has been studied [2].

More recently, experimental investigations have focused on journal bearings friction. In [3] an innovative test rig has been employed in order to evaluate friction with high measurement accuracy. The Authors have carried out different tests varying load and sliding velocity both in mixed and full film lubrication regimes. They have obtained results in the form of a Stribeck curve whose trend is in good agreement with literature findings.

The static and dynamic performances of small hydrodynamic journal bearings (i.e., in laboratory applications) have already been investigated in several works by means of both numerical methods and RK-type experimental test rigs. For instance, Tůma and Biloš [4] have studied the stability of rotor vibrations in a journal bearing by means of full spectrum analysis and a RK4 Rotor Kit device; they have concluded that journal motion inside the bearing is ruled by two equations of motion, which can be referred to as linear and non-linear models. Meruane and Pascual [5] have found that non-linear dynamic coefficients can strongly affect hydrodynamic bearings stiffness and its damping properties. They have employed a CFD simulation model in ADINA and a Rotor Kit 2000 experimental

rig. Tůma et al. [6] have carried out both experimental and theoretical investigations to assess the influence of external excitations on rotor-bearings system behaviour and stability; according to the obtained results they have found out that kinematic excitation can affect vibration amplitudes but not system stability limit. They have taken advantage of both a lumped parameter model for the numerical simulations and a RK4 RK together with a suitable test stand (bearing diameter 30 mm) for the rotor active experimental control.

Deepak and Noah [7] have taken advantage of a commercial RK to study the effects of load, speed, and imbalance mass on journal dynamic behaviour; they have experimentally proved that it can undergo instability with supercritical or subcritical bifurcation, according to Hopf bifurcation theory (HBT), by varying shaft stiffness, imbalance mass and the magnitude of external perturbations applied to the system. They made use of sleeve bearings in their investigation. Boedo [8] performed experimental investigations in order to assess the reliability of HBT in predicting cylindrical fluid film bearings unstable behaviour onset by exploiting a commercial RK. Van De Vorst et al. [9] performed numerical investigations on static behaviour of flexible rotordynamic systems supported by one hydrodynamic journal bearing, without comparing them to experimental results; indeed, it is difficult to find publications in literature in which a RK-type test bench has been used to perform static measurements with small clearances, like what it is meant to do in this work. Indeed, all the above-cited publications rely on experimental results obtained by means of large clearance journal bearings when compared to industrial ones, whose relative radial clearance is in the order of one per thousandth (1/1000), as previously mentioned. Indeed, from our measurement relative radial clearance of RK 4 original bearings is 1.7/100 at ambient temperature, as reported in the following, while also for Rotor Kit 2000 a high value of relative radial clearance (1.3/100 at ambient temperature) can be found in [5]. In addition, due to differential thermal dilatation the hot relative radial clearance increases during operating conditions.

In all of the previous cited works about dynamics, the ratio c/R (relative radial clearance) is not similar to the one which is encountered in real bearings, but it is always very high and far from the values employed in industrial field. At this end here we mean to fill this lack starting from static investigations. The aim of the presented research project is then to develop test benches and simulation methods well-suited for the reliable assessment of performance and stability characteristics of small fluid film bearings designed with significant relative clearance values for rotors in different applications, with particular

reference to their vibrational and rotordynamic behaviour. In this perspective, the comparison of numerical prediction and experimental measurement of journal locations inside the bearing is essential. Furthermore, the investigated test rig bearings should work in significant operating conditions, characterized by small values of film thickness, i.e., hot relative clearance in the order of one per a thousandth (1/1000). To this goal, the tested bearings should have much lower relative clearance in comparison with original RK supports and, at the same time, they should still allow the assembly of the modified test bench, together with ensuring a good alignment between the two shaft bushings. Since the original RK is not designed with radial clearances typical of industrial journal bearings, in order to preserve its original dimensions, it is mandatory to reach higher precision and tolerances levels. Enhanced manufacturing of the new test rig is a key aspect in the presented investigation. Indeed, in order to satisfy the above-cited requirements while maintaining negligible rotor assembly errors and acceptable geometrical defects, it is essential to employ high precision mechanical manufacturing processes. At this beginning step of the research activity, the test-rig bearings have been lightly loaded. Indeed, manufacturing problems and structural resonance characteristics have limited the total mass of the tested shaft. Hence, in order to achieve realistic operating loads, springs or other additional loading components would have been required. Since the test rig is aimed to study dynamic phenomena and fluid-structure interactions after the present preliminary setup study, its structure has been kept as simple as possible. Nevertheless, it is already planned to modify the shaft design in order to increase its mass without introducing strong modification of its critical speeds.

The present work is aimed to setup the test rig for future dynamic analyses on small hydrodynamic journal bearings with realistic relative clearance. To this goal, it is essential to study the static behavior of the bearings in study and, particularly, to measure journal locations with the highest possible accuracy. In order to assess the reliability of the performed measurements, they have been compared with numerical results coming from in-house developed FEM codes already validated by comparing their output with previous experimental evidence [10-11].

Numerical simulations have been performed by exploiting a previously validated ([10-11]) in-house developed FEM code for journal bearing TEHD analysis. Since the employed simulation models rely on the classical Reynolds hypothesis which assumes a thin lubricant film, bearing clearance must be enough small in the experiments in order to satisfy simplification of Navier-Stokes general momentum equations.

In conclusion, the presented research project is aimed to develop a test rig and simulation methods suited to study the performance of small fluid film bearings for rotors, i.e., for microGT applications, with particular reference to their vibrational behaviour. In such perspective, the correct prediction and measurement of journal locations within the bearing is essential. In addition, the test rig bearings must have reasonable relative clearance. Indeed, it should be typical one of real bearings and, simultaneously, it should still allow the assembly of the test rig and the alignment of the two rotor bushings. Therefore, in the present work, in order to determine the design and a basic set-up of the test rig, the influence of bearing clearance in the assessment of journal position in hydrodynamic plain bearings is studied by comparing experimental and numerical results.

2.1 Experimental devices

Rotordynamic investigations can be performed on simplified rotor models, arranged in order to reproduce particular working conditions of actual rotating machines. The first experiments were performed on the original RK. Subsequently, a modified version of the RK was designed for further measurements.

The first experimental device used for measurements is the RK4 Rotor Kit [12]. This commercial RK is a modular rotating machine, that can be assembled and operated in several arrangements. In the original configuration that is adopted in the experiments, the shaft is supported by a fluid film bearing on one side and by a self-lubricated bush located at its opposite end. The original RK4 RK is furnished with an electric motor, which allows regulation of rotation speed in modulus and direction in the range 250-10000 rpm, and it is equipped with a frame characterized by a V-shaped design which houses motor, bearings and rotor. The fluid film bearing is expected to work in hydrodynamic lubrication regime under nominal supply pressure (0.007 MPa) and, in order to be able to avoid possible inception of oil-whirl instability, it can add hydrostatic lift if it is fed at higher pressure (up to 0.24 MPa).

The bearing assembly is provided with holes that support proximity sensors. These magnetic probes can detect with high accuracy journal displacements in two directions (X and Y) normal to the rotor axis, which are turned into voltage variations. More in detail, they are eddy current proximity sensors that are capable of measuring displacements of any desired shaft point. They are connected to a special external unit (Proximitor Assembly), which can receive and acquire signals coming from five different channels simultaneously. All of the proximity probes are arranged in pairs at right angles

(Figure 2.1); therefore, both horizontal (X) and vertical (Y) displacement vector components are properly measured, as required by comparisons with FEM numerical results.

An oil tank is required in order to store lubricant fluid circulating during journal rotation. The lubricant oil used during the present experimental campaign is ISO VG 32. In order to avoid measurement disturbances due to vibrations of the model structure, RK4 RK is supported by a massive and large marble basement mounted on four anti-vibrating supports. The acquisition hardware and software used during the experimental campaigns are provided by Siemens and they are respectively LMS Scadas III and LMS Test Lab.

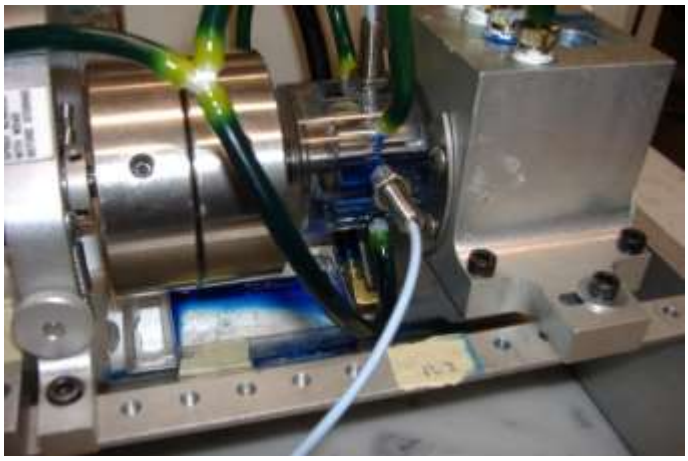

Figure 2.1 – Instrumented hydrodynamic bearing with proximity probes

RK4 original fluid film bearing is characterized by a too high relative radial clearance (around one per hundredth), i.e., one order of magnitude more with respect to hydrodynamic journal bearings for industrial and automotive applications (whose relative radial clearance is indeed about one per thousandth). Therefore, in order to increase the correlation between experiments and real-world applications, a new rotor with increased and variable journal diameter has been designed. Such expedient allows us to reduce the investigated fluid film bearing radial clearance without changing its bush. As a consequence, simulations by means of thin film assumption are expected to provide better agreement with experimental results. The new shaft designed for this modified RK can be equipped with variable diameter journals: this ensures a wide range of possibilities to study the hydrodynamic behaviour of the lubricant film. Indeed, now relative radial clearance becomes a variable parameter of experiments. The journal instrumented with proximity sensors can be easily assembled by means of a splined connection. Figs. 2.2-

2.3 respectively show assembly drawings of the new rotor designed for the modified RK and an actual image of the detail of the interchangeable journal.

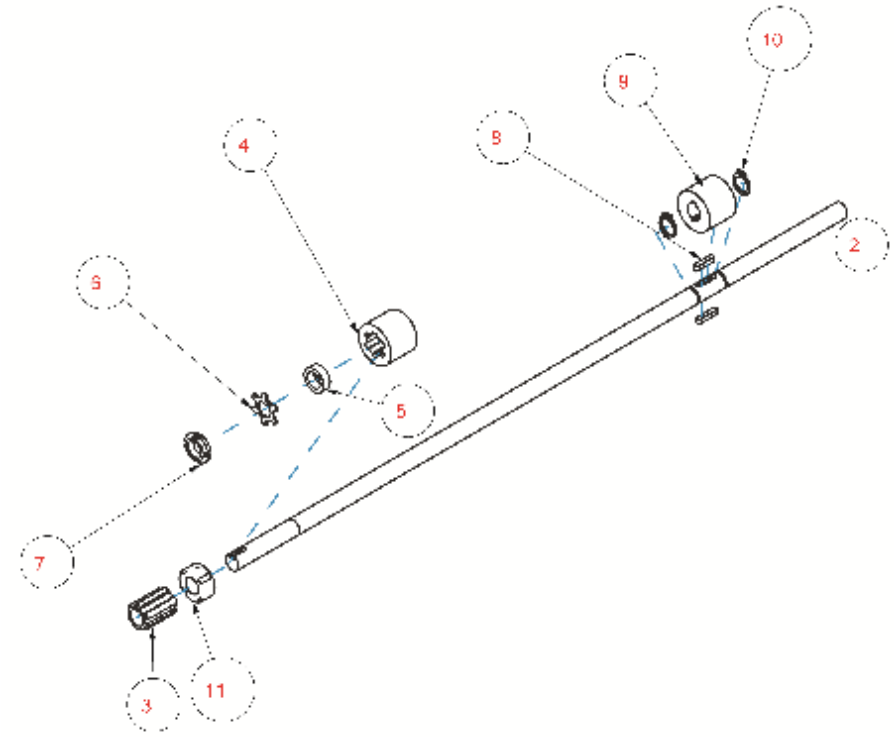

(a)

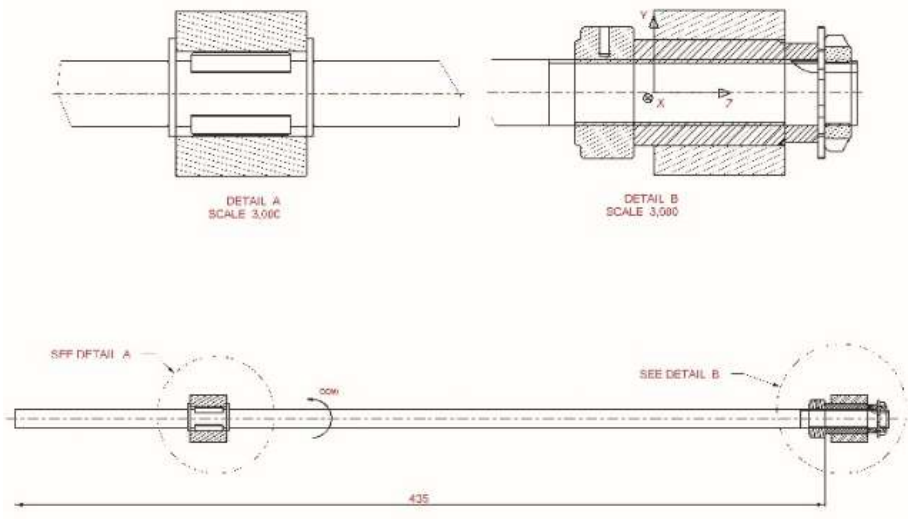

(b)

Figure 2.2 – Shaft designed for the modified RK: a) exploded view, b) section. The following components are shown: 2–shaft; 3–splined connection; 4–splined hub (journal 1); 5–spacer; 6–safety washer; 7–threaded locking nut; 8–key; 9–hub with keyways (journal 2); 10–retaining ring; 11–lock nut with locking screw

Figure 2.3 – Prototype of the custom shaft with interchangeable journals

The design of the new custom shaft has required proper dimensional and geometrical tolerances. Particularly, a total runout tolerance ensures shaft balancing and rectilinearity. In addition, in order to obtain the required radial clearance, suitable dimensional tolerances have been imposed to the journal diameter. For the results presented in this work relevant to a relative hot radial clearance equal to 8/1000, the dimensional tolerances of bearing and journal diameters are listed in Table 2.1, where modified RK geometrical data are reported, together with original RK ones for comparison. Since the journal and the bearing are respectively made of steel and polycarbonate (PC), the strong thermal differential dilatation has been taken into account in the choice of the dimensional tolerances applied to the journal diameter by assuming a working temperature of 40°C and linear radial dilatation of bush and shaft. Their differential variation is shown in Figure 2.4 as a function of temperature. Later the computed hot clearance has been verified experimentally and good agreement has been found. Particularly, the experimental radial hot clearance is 109.5 μm, while the computed radial clearance at 40°C is 108 μm.

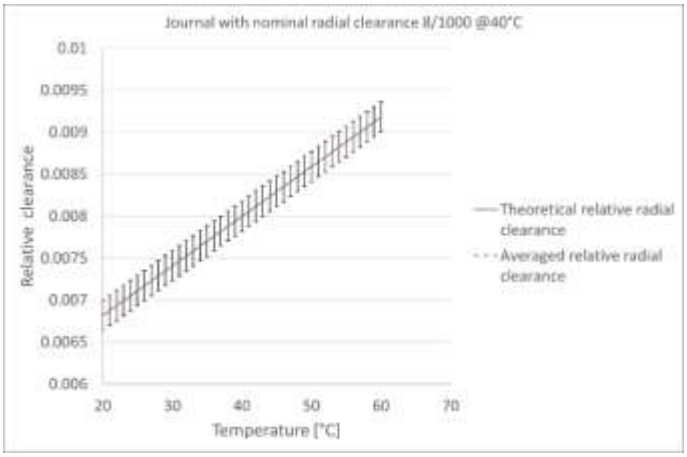

Figure 2.4 – Relative radial clearance as a function of temperature

Parameter [unit]	Symbol	Value (Modified)
Bearing length [mm]	L	20
Journal diameter [mm]	D	25.245-25.254
External diameter of bush [mm]	D_e	51
Inner diameter of bush [mm]	D_i	25.42
Radial clearance (original RK) [micron]	c	210
Hot radial clearance (original RK) [micron]	c_h	260
Relative radial clearance (original RK)	c/R	1.68/100
Radial clearance (modified RK) [micron]	c	90
Hot radial clearance (modified RK) [micron]	c_h	108
Relative (hot) radial clearance (modified RK)	c_h/R	8/1000
Diameter of feed holes [mm]	d_g	3.3

Table 2.1 – Original-Modified RK design data

Experiments have been then carried out by taking advantage of this modified test rig in two different arrangements. The first configuration adopted (configuration 1), somehow inherited from the original RK, places the two shaft supports at opposite ends of the shaft, i.e., the hydrodynamic bearing to be investigated at the free shaft end and a self-lubricated bush at the electric motor side (Figure 2.5). Differently, the second configuration (configuration 2) arranges another identical hydrodynamic bearing at the electric motor side (Figure 2.6); this second arrangement has been adopted in order to limit expected journal lift-off within the self-lubricated bearing. In any case, the oil supply pressure and temperature have been always controlled, respectively in order to avoid hydrostatic lubrication conditions and to maintain temperature as constant as possible during tests. Indeed, the purpose of the present work is to test the bearings in hydrodynamic regime solely. Processing experimental data of configuration 1 has shown that such arrangement causes a certain climbing of the shaft due to the mixed lubrication conditions in the motor-side bearing, as described in [13]. Figure 2.7 respectively reports two examples of time-averaged journal center orbits measured in configuration 1 (Fig. 2.7a) and 2 (Fig. 2.7b). As shown by the comparison of such plots, the orbits in configuration 1 are more likely to display angular points and locations with attitude angle higher than 90 degs.

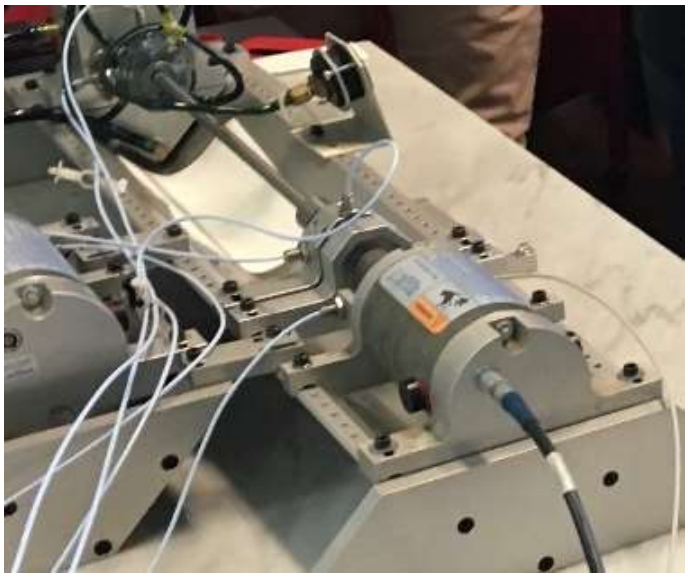

Figure 2.5 – Rotor assembly mounted with custom shaft in configuration 1

Figure 2.6 – Rotor assembly mounted with custom shaft in configuration 2

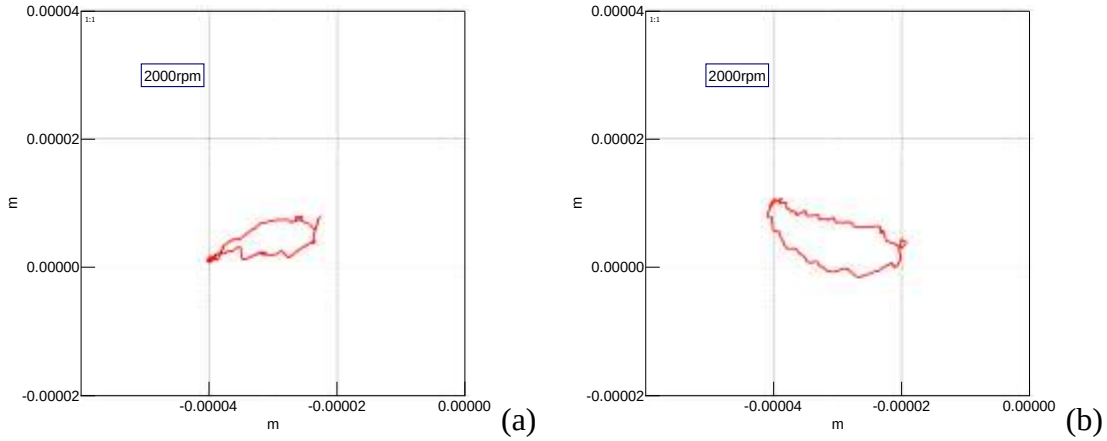

Figure 2.7 – Averaged orbit at 250 rpm: a) configuration 1, b) configuration 2

In order to improve bushings alignment procedure, a totally new RK, shown in Figure 2.8, has been designed with a frame made up by two cylindrical bars put in contact along their generatrixes. The two bearing bushes are placed tangent to the bars. Both bush external surfaces and round bars are manufactured by precision grinding in order to

ensure the required assembly tolerance. Moreover, volanic masses can be added by mounting them on the shaft in order to increase bearing load; in example two of them are mounted in the configuration shown in Fig. 2.8a.

(a)

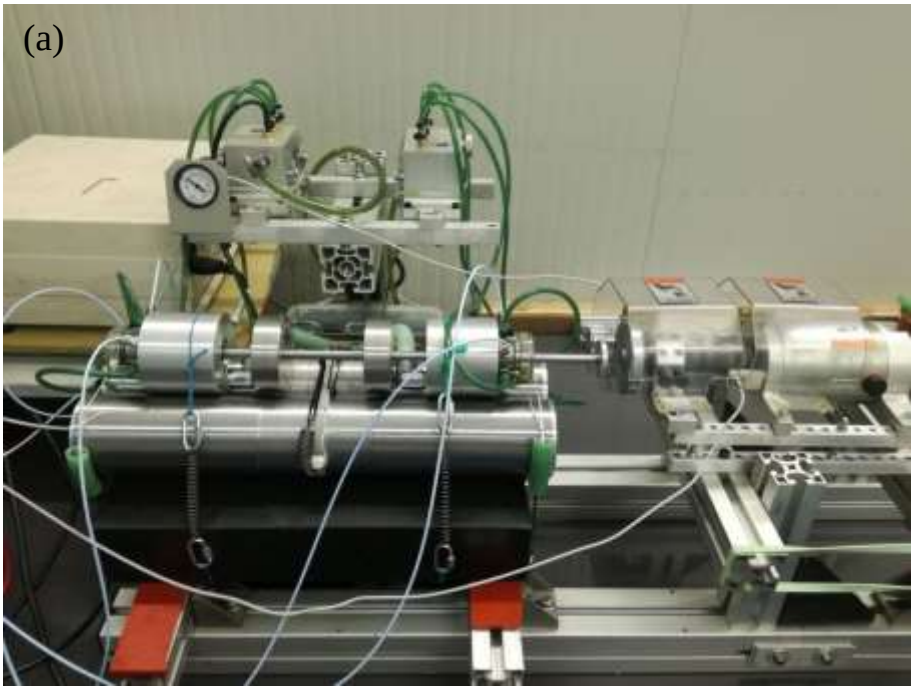

(b)

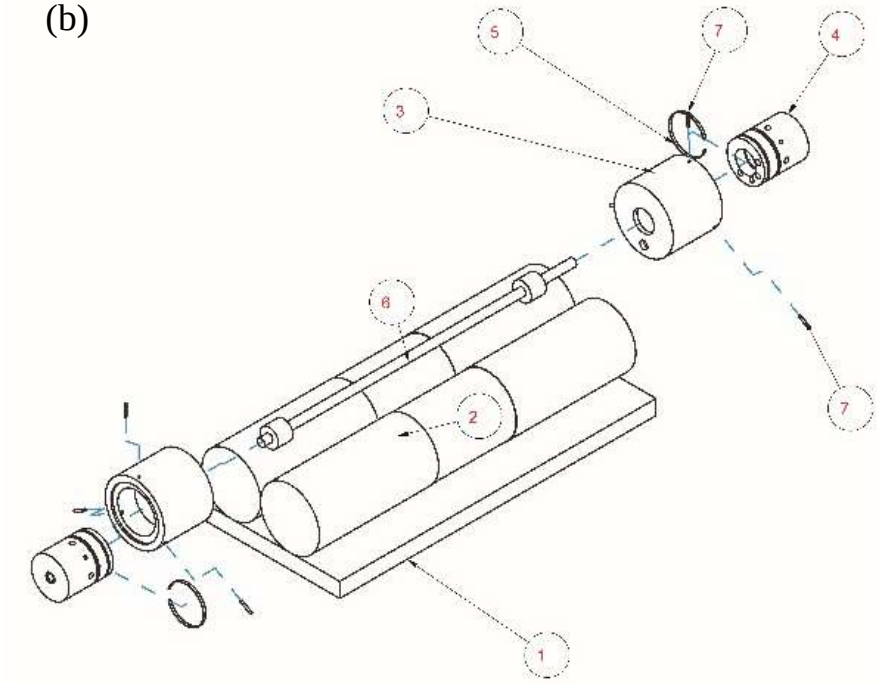

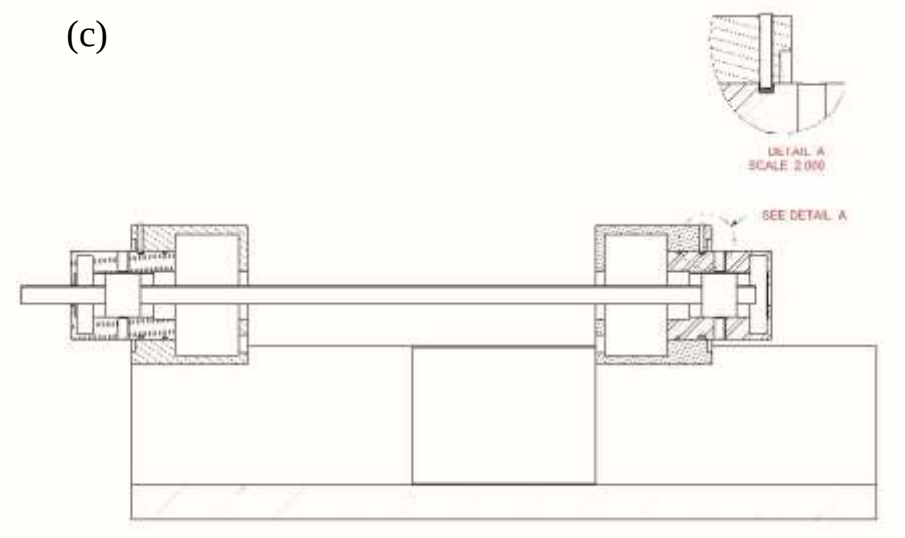

Figure 2.8 – Prototype of the new RK: (a) picture of front view; (b) exploded view; (c) section. The following components are shown: 1-block; 2-ground round bar; 3-external bush; 4-bearing; 5-spacer; 6-shaft; 7-set screw.

Moreover, as it can be seen from Figure 2.9, the electrical motor is mechanically decoupled form such experimental model by means of a suitable elastic joint, whose task is indeed to isolate the bearings under investigation from the vibrations generated by the motor. In such way, a regular motion transmission is achieved. Finally, as for the previously employed test rigs, the two metallic cylinders are put over a massive marble block which acts as a frame with respect to the system to be experimentally characterized.

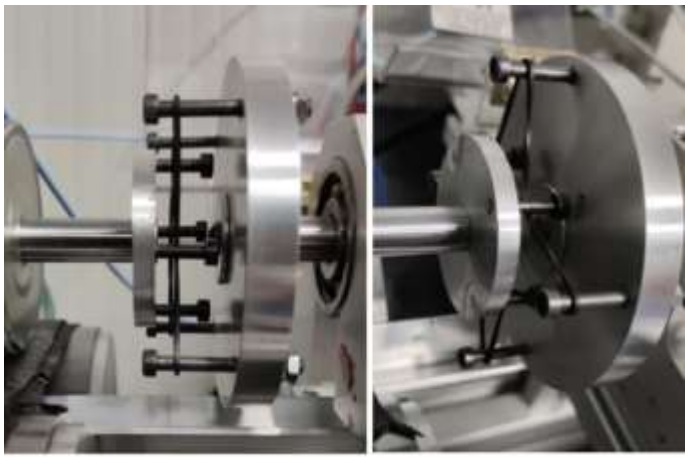

Figure 2.9 – Elastic joint for electric motor-shaft coupling

2.2 Numerical models

The experimental data are compared in the following with numerical results obtained by means of different simulation models, which are listed in Table 2.2, from the simplest to

most complex. All of the models allow the simulation of the fluid flow in the thin oil film (hydrodynamic sub-model) as well as of heat generation and exchange in the lubricant (thermal sub-model). In addition, the global model may include the simulation of heat conduction in the bush and journal (3D thermal sub-model) and of thermo-mechanical deformation of the kinematic pair members (structural sub-model). The three sub-models can be coupled and solved simultaneously by using a suitable solution algorithm [10].
All of the models that require the solution of integro-differential problems rely on the finite element method (FEM) for spatial discretization. Isoparametric 4-node rectangular and 8-node hexahedral elements for two-dimensional (2D) and three-dimensional (3D) problems are used.

Model name	Analysis type	Hydrodynamic sub-model	Thermal sub-model	Structural sub-model	Variants
THD 2D adiabatic	THD	2D mass conserving	2D adiabatic	–	–
THD 2D correlation	THD	2D mass conserving	2D with Luke formula	–	–
THD 3D	THD	3D mass conserving	3D conduction	–	–
TEHD 3D (free expansion)	TEHD	3D mass conserving	3D conduction	3D thermo-mechanical	Free expansion
TEHD 3D (radial constraint)	TEHD	3D mass conserving	3D conduction	3D thermo-mechanical	Partial radial constraint

Table 2.2 – Simulation models and sub-models

All of the simulation models take advantage of mass conserving hydrodynamic sub-models. They are based on the JFO theory [15-16], which is valid for moderately and highly loaded bearings and assumes a cavitated film region with infinite streamers and variable density ρ. According to JFO theory, thin film mechanics equation for journal bearings is:

$$\frac{\rho_L}{R^2}\frac{\partial}{\partial \vartheta}\left(g_L\frac{\partial p}{\partial \vartheta}\right)+\rho_L\frac{\partial}{\partial z}\left(g_L\frac{\partial p}{\partial z}\right)-\omega\frac{\partial}{\partial \vartheta}\left[\rho\left(H-f_L\right)\right]-\frac{\partial}{\partial t}\left(\rho H\right)=0 \tag{2.1}$$

where p is the hydrodynamic pressure, R the journal radius, ρ the fluid film density, ρ_L the liquid phase density, H the film thickness, ϑ the circumferential coordinate, z the axial coordinate, t is the time, while the remaining parameters are given by:

$$\left.\begin{aligned} f_L &= i_{L1} / i_{L0} \\ g_L &= i_{L2} - {i_{L1}}^2 / i_{L0} \end{aligned}\right\} \tag{2.2}$$

$$i_{Ls} = \int_0^H \frac{y^s}{\mu_L}\, dy \tag{2.3}$$

where μ_L is the liquid dynamic viscosity and y the cross-film coordinate. Equation (2.1) rules the lubricant flow in the "3D mass conserving" sub-model. Indeed, although lubrication problem is two-dimensional (in ϑ, z coordinate domain), it considers the cross-film variation of viscosity. Hence, the 3D mass conserving sub-model is used together with 3D thermal models. Differently, the 2D mass conserving sub-model complies with the following form of thin film mechanics equation:

$$\frac{\rho_L}{R^2}\frac{\partial}{\partial\vartheta}\left(\frac{H^3}{12\mu_L}\frac{\partial p}{\partial\vartheta}\right)+\rho_L\frac{\partial}{\partial z}\left(\frac{H^3}{12\mu_L}\frac{\partial p}{\partial z}\right)-\frac{\omega}{2}\frac{\partial}{\partial\vartheta}(\rho H)-\frac{\partial}{\partial t}(\rho H)=0 \tag{2.4}$$

which is a particularization of Eq. (1.1) for constant μ_L and resembles the classic Reynolds equation. Equations (2.1) and (2.4) are solved in weak form in agreement with [10]. As far as the film domain is concerned, the thermal sub-model relies on the cross-film averaged energy equation:

$$\frac{\partial}{R^2\partial\vartheta}\left(kH\frac{\partial T_m}{\partial\vartheta}\right)+\frac{\partial}{\partial z}\left(kH\frac{\partial T_m}{\partial z}\right)-\rho cH\left(u_m\frac{\partial T_m}{R\partial\vartheta}+w_m\frac{\partial T_m}{\partial z}\right)-\rho cH\frac{\partial T_m}{\partial t}+H\Phi_m-q_0-q_1=0 \tag{2.5}$$

Where u and w are the circumferential and axial fluid velocities, respectively, k the conductivity of the film, c the specific heat, T the film temperature, Φ the power dissipation density function and the subscript m denotes a variable averaged in the cross-film direction. In addition, q_0 and q_1 are the heat transfers (per unit area) to bearing and journal surfaces, respectively. If they are both equal to zero, the thermal sub-model is referred to as "2D adiabatic" [17], although heat exchange is allowed in the feed grooves [10]. By using Luke formula [18], q_0 and q_1 can be computed [14] and the heat exchange roughly taken into account ("2D with Luke formula" sub-model). To this goal, in THD 2D correlation model bush and journal temperature are assumed to be constant and equal to the corresponding averaged temperatures, T_B and T_S respectively, reported in Table 2.3. In the "3D conduction" sub-model q_0 and q_1 are calculated by obtaining the temperature gradients at the walls, in the hypothesis that the temperature profile across the film thickness is a fourth-order polynomial [10]. Only this last thermal sub-model requires FEM simulation of heat conduction in both bush and journal, while the same

finite element mesh of the bush, shown in Figure 2.10, is used to simulate structural deformations (“3D thermo-mechanical” sub-model) due to pressure and temperature rise [11]. Two variants of such sub-model are arranged with different boundary conditions. In the first variant (“free expansion"), the thermo-mechanical model of the polycarbonate bearing is left free to expand radially over its entire outer surface. In the second (“partial radial constraint”), the part of the bearing inserted in the frame (delimited by the two O-ring grooves) is radially constrained. In reality, the radial expansion of the bearing in the insertion area will certainly be in an intermediate situation between the two simulated variants due to the differential dilatation. In all cases, in order to compute structural deformations due to pressure, “partial radial constraint” conditions are used. All of the data required for thermo-mechanical computations are included in Table 2.3.

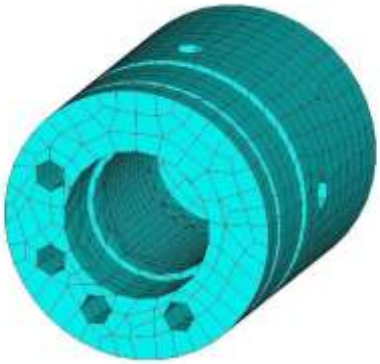

Figure 2.10 – Bush model and mesh

As far as thermal boundary conditions applied to all of the 3D models are concerned, free convection is assumed at the external bushing surfaces. Differently, isothermal conditions are imposed on other surfaces inside the bushing, i.e., the bottom surface of the small reservoir for the leak oil as well as the bottom half of the four ducts that convey such lubricant to the external reservoir tank in the main frame. Table 2.3 lists all of the data relevant to 3D thermal boundary conditions. Particularly, for convection boundaries it reports the overall heat transfer coefficient h and the environmental temperature T_e assumed as bulk temperature. In addition, the oil supply temperature T_s is considered as the constrained temperature of the isothermal surfaces.

In 3D models, thermal simulation of the journal is carried out by means of uniaxial conduction elements, which model only the part of the steel shaft inside the bearing. At both the journal ends (first and last node of the mesh) isothermal conditions are assumed

by imposing the averaged shaft temperature T_S. Its value is listed in Table 2.3, together with the journal thermal conductivity k_j.

Table 2.3 – Lubrication analysis data

Parameter [unit]	**Symbol**	**Value**
Viscosity (at T_0=40°C) [Pa s]	μ_{L0}	0.0251
Viscosity temperature coefficient [1/°C]	β	0.0317
Mass density [kg/m^3]	ρ_L	870
Specific heat [J/Kg °C]	c_L	2000
Thermal conductivity [Wm/K]	k_L	0.14

Lubricant (ISO VG 32) properties

Parameter [unit]	**Symbol**	**Value**
Feed temperature [°C]	T_s	51
Feed pressure [MPa]	p_s	0.069

Supply conditions

Parameter [unit]	**Symbol**	**Value**
Bearing load (half shaft weight) for original RK [N]	W_g	2.8
Bearing load (half shaft weight) for modified RK [N]	W_g	2.14
Environmental temperature [°C]	T_e	20
Rotation speed range [rpm]	ω	250-3000

Working conditions

Parameter [unit]	**Symbol**	**Value**
Averaged bush temperature [°C]	T_B	51
Averaged journal temperature [°C]	T_S	40
Thermal conductivity of the bush [W/(m°C)]	k	0.2
Thermal conductivity of the journal [W/(m°C)]	k_j	50
Heat transfer coefficient [W/(m^2°C)]	h	2
Young modulus [GPa]	E	2
Poisson ratio	ν	0.37
Linear dilatation coefficient [1/°C]	a	7 10^{-5}

Thermo-mechanical data

2.3 Analysis of numerical and experimental results

In this section a comparison between experimental and numerical results is performed for all the adopted test rigs each of one with its different employed experimental setups. Firstly, the results coming from the original RK are shortly presented for the sake of completeness, whereas more detail is devoted to stress the problems in the modified RK. Finally, the new test bench is presented more in detail and a further analysis is performed by comparing experimental results coming from iso speed measurements and slow ramps, in order to assess its reliability.in terms of static and dynamic experimental investigations.

2.3.1 First two test rigs: original RK and modified RK

Static characteristics have been computed by means of all of the global models listed in Table 2.2 for the modified RK, while only 2D models have been used for the original RK, due to the large disagreement with experimental results, which does not mainly depend on thermal model. The same bearing bushes have been employed in both original and modified RK, while journal diameters are different, so that radial relative clearances are 1.68/100 and 8/1000, respectively. Lubricant supply is carried out by means of four holes in the bearing axial midplane oriented at 45 degs with reference to the vertical direction. Bearing data required by all of the lubrication analysis methods employed are listed in Table 2.1 and Table 2.3. Hot clearances c_h are used as input data for THD calculations. Here the temperature-viscosity dependence is described by means of three parameters (reference oil viscosity μ_{L0} at temperature T_0 and coefficient β) according to the exponential law described in [7, 8]. The oil film in half bearing is discretized by means of 80x8 elements in circumferential and axial directions, respectively.

Experimental and numerical journal center locations (components X, Y) are shown in Figs. 10-11-12 for the original and modified RK in configuration 1 and 2, respectively [1]. Journal locations are plotted at different shaft angular speeds (250, 500, 1000, 2000, 3000 rpm) in clockwise (cw) and counterclockwise (ccw) directions. Let ε be the operational relative eccentricity equal to e/c_h, where $e=(X^2+Y^2)^{0.5}$. Black and red circles identify the loci of points located at ε equal to 1 and 0.5, respectively. The curves of different colors reported are useful to attribute the different computed positions to the relative method adopted to evaluate them. Reference system for position components (e_x, e_y) has its origin in the bearing center; consequently, the represented position becomes the journal eccentricity expressed in dimensional terms. To allow a better comparison between experimental and numerical results, Figs. 2.11-12-13 do not show the whole

journal mobility area, which has a diameter of 0.2 mm (e_x, e_y values included between -0.1 and 0.1 mm), but only a restricted area with half the diameter (e_x, e_y values included between -0.05 and 0.05 mm). Numerical data reported in Figs. 2.11-12-13 are the same, the three plots compare them with experimental results of the corresponding configuration adopted.

Experimental "static" journal points are obtained by averaging the measured locations during several shaft rotations. Indeed, If the journal bearing works in steady conditions, the theoretical journal location does not vary with time, while its actual location undergoes small oscillations due to shaft unbalance and dynamics (in physical reality a perfectly steady condition does not exists). Therefore, in actual "steady" conditions the mean of the locations measured during several shaft rotation is required to identify the real journal location.

Both in numerical and experimental cases, the obtained results exhibit a coherent trend of the journal position as the angular speed changes. Indeed, by increasing rotational speed, the journal raises and moves itself towards bearing center in a continuous way (this trend permits an immediate identification of the rotational speed level for each operating condition reported in the plots).

The agreement between experimental analysis and all of the numerical simulations, which are based on thin film assumption, is better in modified RK, both in configuration1 and in configuration 2, than in original RK, due to the clearance reduction. In experimental results relevant to configuration 1 of modified RK the above-cited lift-off of the journal in the self-lubricated bearing may be influential and, together with misalignment, can explain the occurrence of positive *Y* components of journal location. Indeed, the effects of misalignment can be considerable when rotational speed is not high and, particularly, for low external loads, as in the present experimental campaign. Such result has been proved and widely discussed in [19], where many tests are presented on hydrodynamic plain journal bearings submitted to misalignment torque controllable by means of a suitable experimental rig.

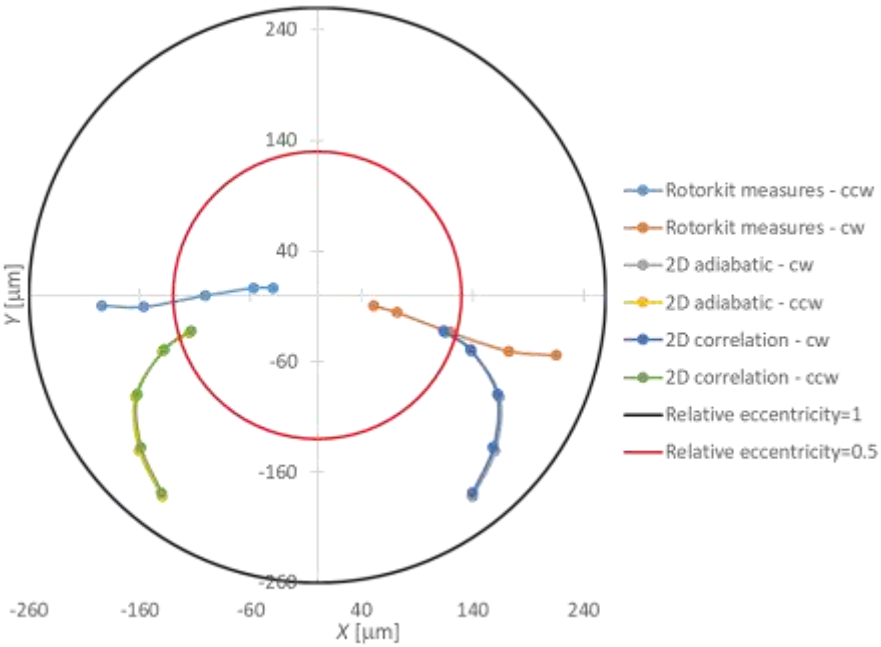

Figure 2.11 – Journal center locations for the original RK

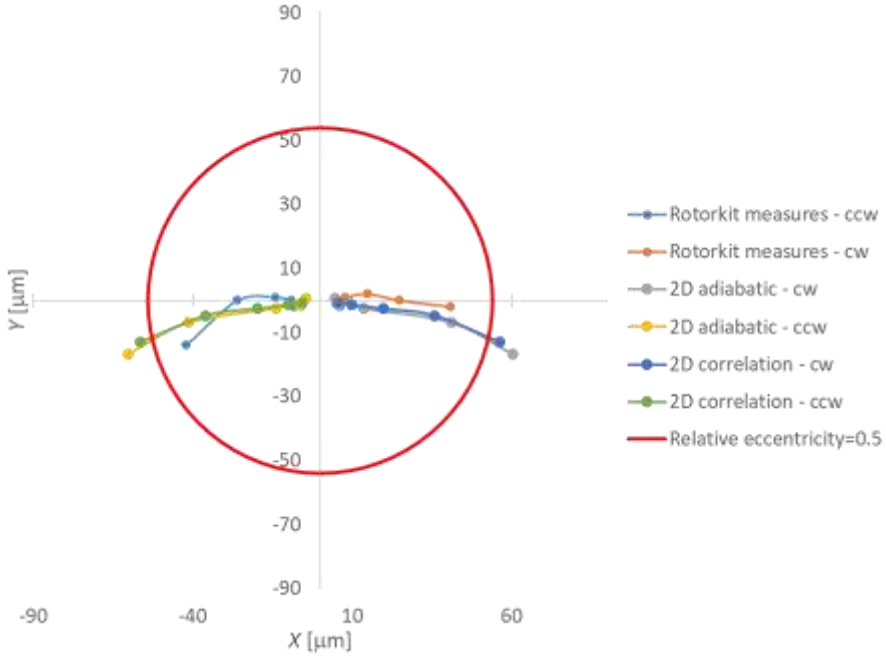

Figure 2.12 – Journal center locations for the modified RK in configuration 1

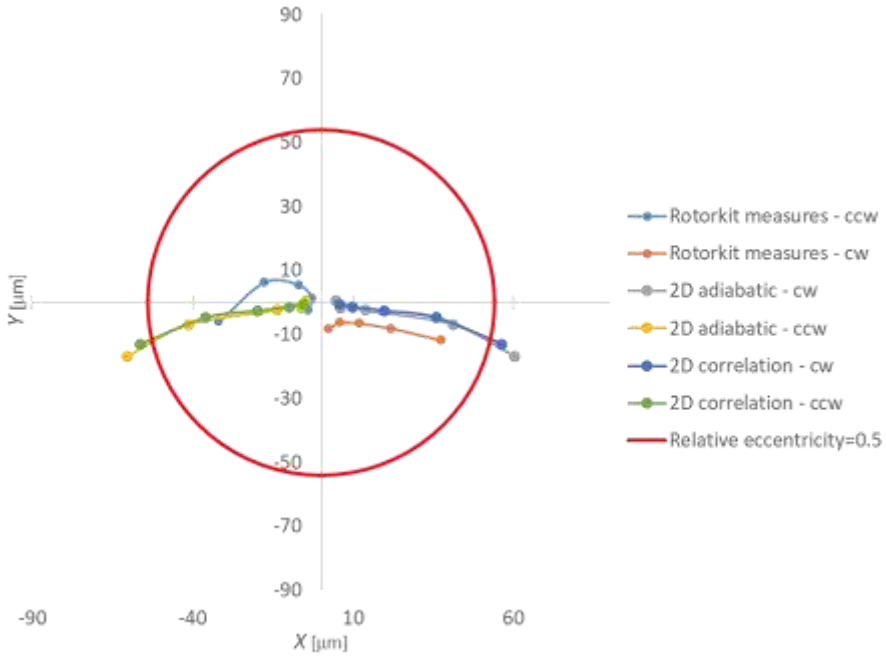

Figure 2.13 – Journal center locations for the modified RK in configuration 2

As already mentioned, the asymmetry between clockwise (cw) and corresponding counterclockwise (ccw) experimental locations is mainly due to misalignments. For configuration 2 due to oil-whirl instability ccw locations are not significant as well as positive Y components of journal location. Signal processing has shown that the asymmetry between experimental cw and ccw journal positions shown in Figure 2.13 is due to the onset of oil-whirl phenomenon. Indeed, in the cascade plot (time-frequency analysis evaluated by means of Short-time Fourier Transform, STFT) recorded at ccw shaft speed (Figure 2.14) a line relevant to engine order 0.5X appears. On the contrary, no corresponding sub-synchronous relevant spectral content is visible in the cascade plot relevant to cw speed results (Figure 2.15) in the same configuration tested [1].

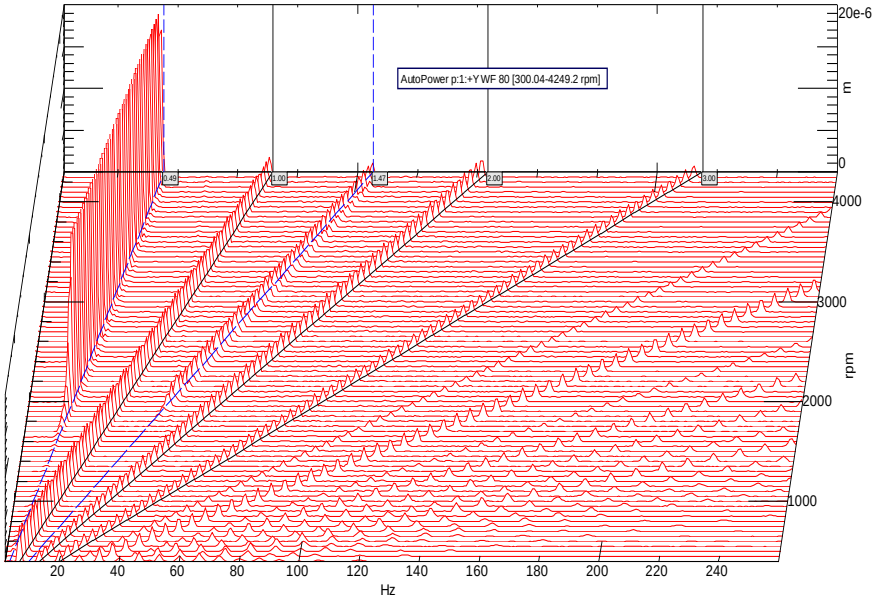

Figure 2.14 – Cascade plot for modified RK in configuration 2, ccw rotation

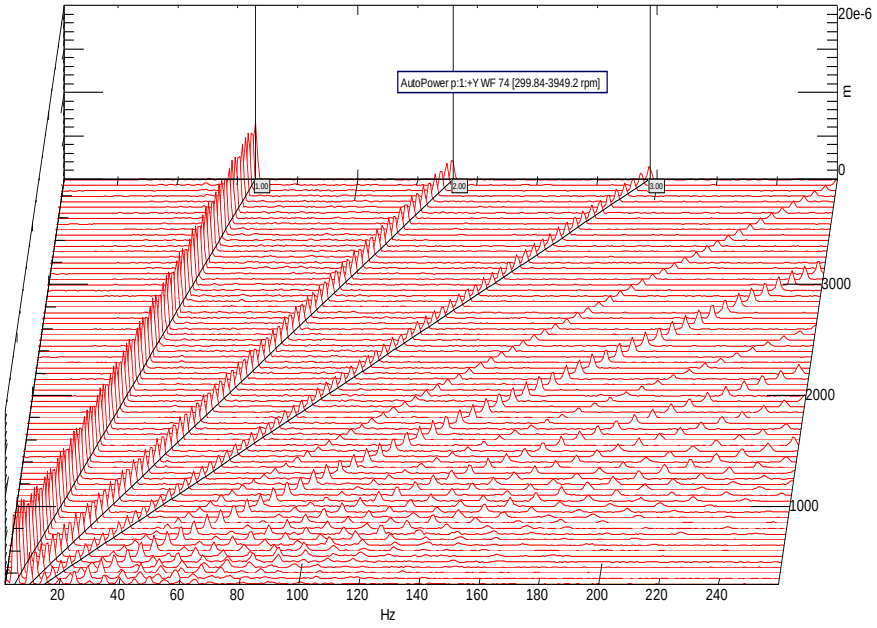

Figure 2.15 – Cascade plot for modified RK in configuration 2, cw rotation

Oil-whirl inception in plain journal bearings depends on two independent non-dimensional parameters, i.e., the Sommerfeld number S and the ratio between bearing axial length and diameter. The inverse of S is the nondimensional bearing load, so that the higher the Sommerfeld number, the lower the load and the threshold speed. Particularly, S is inversely proportional to the square of the clearance and, therefore, oil-whirl inception is very sensitive to this parameter, i.e., the lower the clearance, the lower the threshold speed. Sommerfeld number and clearance are global bearing parameters

that are sensible for accurately aligned bearings. Differently, when the shaft misalignment is considerable, oil-whirl inception should be linked to local parameters, i.e., the local film thickness or the average clearance in the active film region (where the oil film pressure distribution develops). Consequently, if the shaft is not misaligned, oil-whirl threshold does not depend on rotation speed direction. Indeed, for opposite rotation speeds, the corresponding film thickness distributions are symmetric with respect to the vertical bearing mid-plane and the average clearance of the active film is the same. Differently, if the shaft is misaligned, the average thickness of the active film and consequently the threshold speed may depend on the rotation speed direction.

In order to assess the degree of agreement between experiments and simulations, Figs. 2.16-2.17 report in percentage the differences, also referred to as errors, between measured and relative eccentricities (the ratio between journal eccentricity and hot radial clearance) computed by means of two-dimensional (2D) THD models [20]. Errors of "2D adiabatic" and "2D correlation" models are respectively reported in Figs. 2.16-2.17. Modified RK errors both in configuration 1 and in configuration 2 (red and green columns, respectively) are far lower than original RK ones (blue columns). Thus, for further investigations and comparisons with numerical results from more advanced simulations, experimental results coming from modified RK will be regarded as a reference. All the following diagrams rely only on experimental data obtained only in cw direction, in order to always deal with physically meaningful journal equilibrium position within the bearing, in the sense explained above.

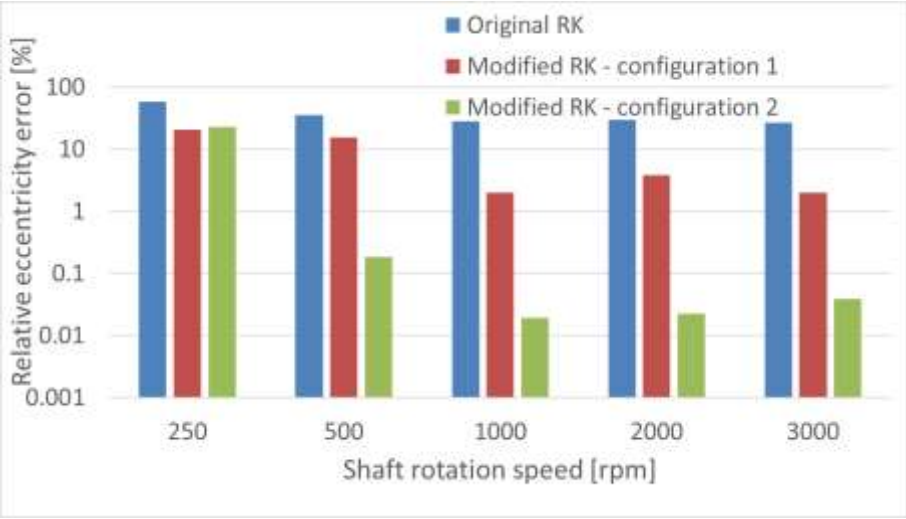

Figure 2.16 – Difference between measured and 2D adiabatic model relative eccentricities for different test rigs (logarithmic scale)

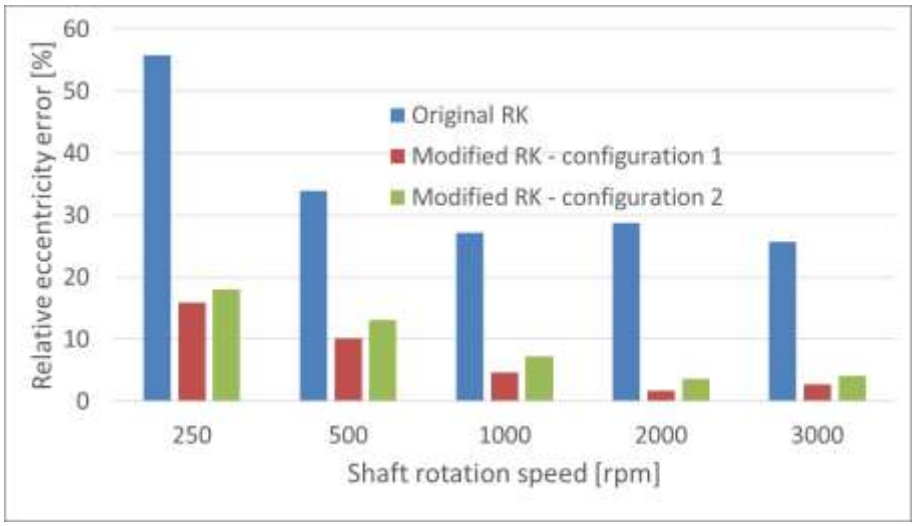

Figure 2.17 – Difference between measured and 2D correlation model relative eccentricities for different test rigs

Afterwards, full 3D simulations with THD and TEHD models have been carried out. The relevant results are then compared with measurements coming from both configurations of modified RK.

Figs. 2.18-2.19 report such comparison in terms of mobility plot for configuration 1 and 2, respectively [20]. The model in best agreement with modified RK experimental data in both configurations is the "TEHD 3D radial constraint".

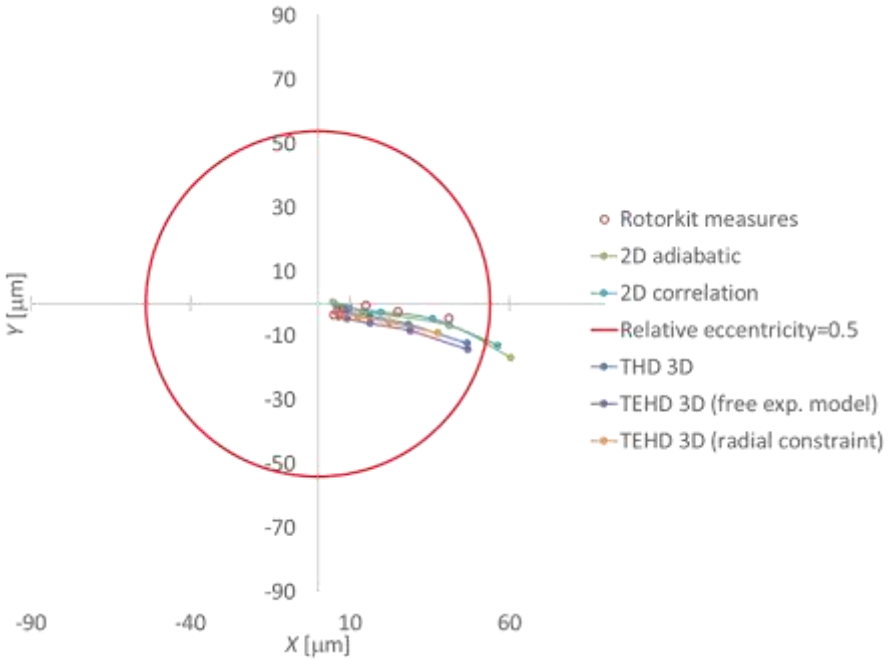

Figure 2.18 – Mobility plot for modified RK with respect to 3D numerical THD and TEHD simulations results in configuration 1

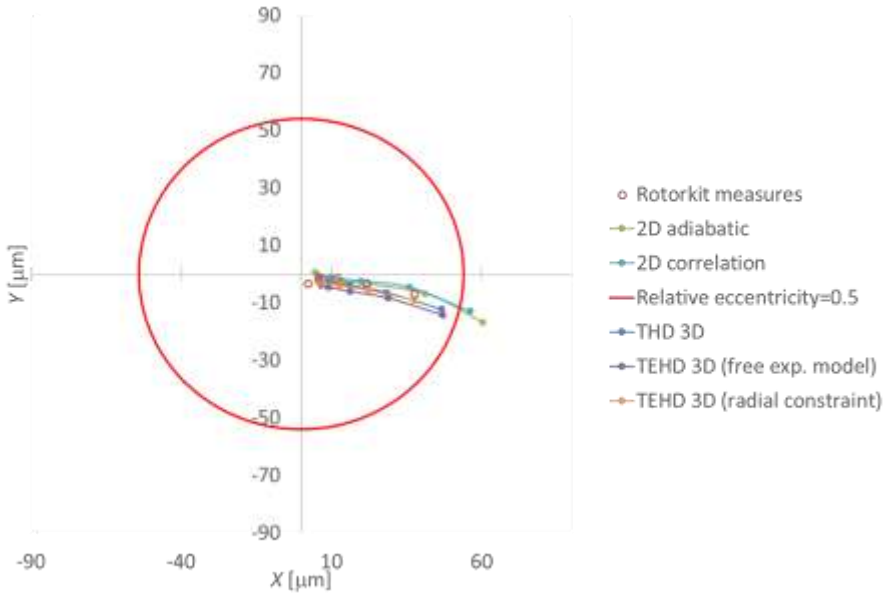

Figure 2.19 – Mobility plot for modified RK with respect to 3D numerical THD and TEHD simulations results in configuration 2

In the following, with the aim of a better visualization of computed and measured journal locations, numerical and experimental results are also compared in terms of polar coordinates, i.e., eccentricity ratio and attitude angle. Figs. 2.20-2.21 depict relative eccentricity as a function of shaft angular speed [20]. For both the two configurations the model in best agreement with experimental results is the "TEHD 3D radial constraint". More generally, all of the 3D models are in better agreement with the experimental reference results. Particularly, TEHD analysis still improves predictions in comparison with THD simulation.

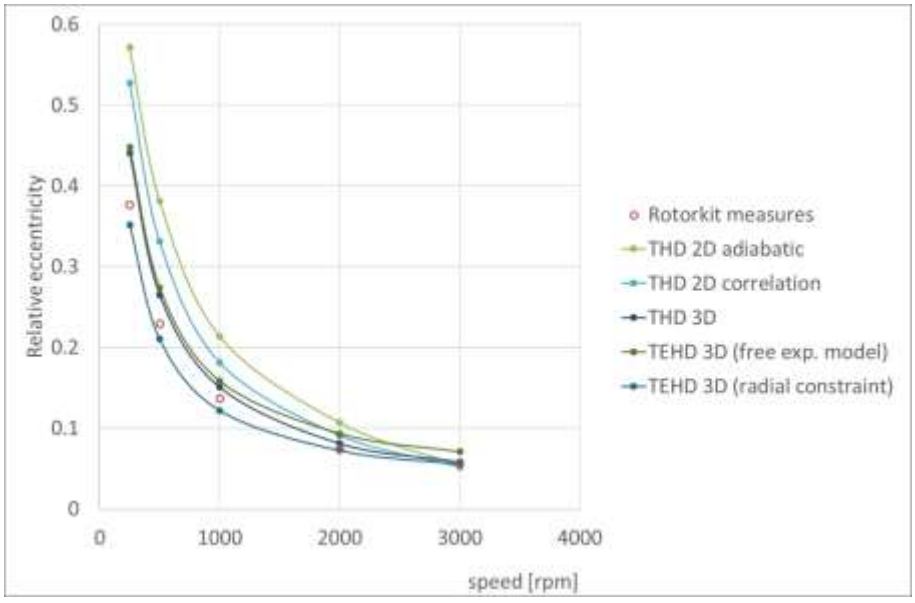

Figure 2.20 – Relative eccentricity plot for modified RK with respect to 3D numerical THD and TEHD simulations results in configuration 1

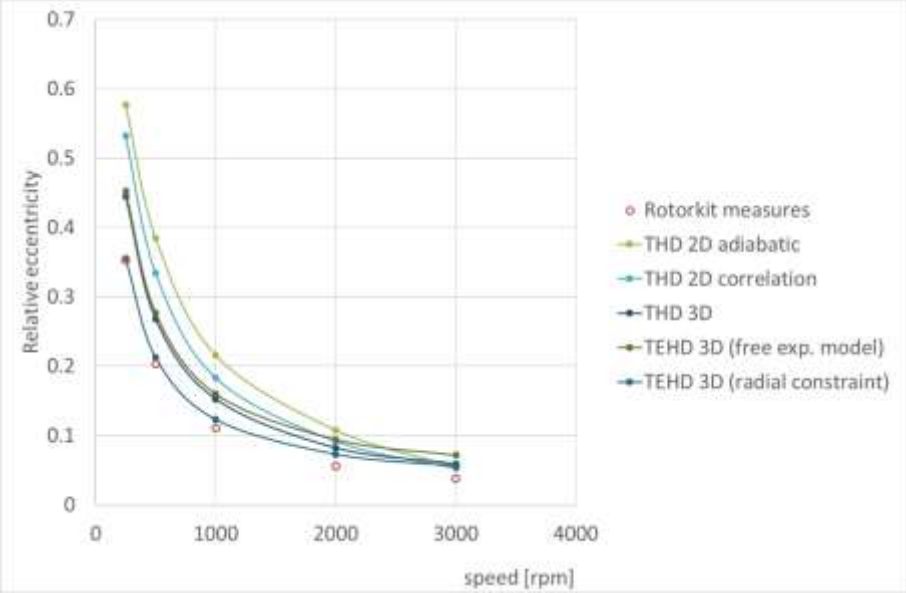

Figure 2.21 – Relative eccentricity plot for modified RK with respect to 3D numerical THD and TEHD simulations results in configuration 2

With the same goal, Figs. 2.22-2.23 compare attitude angle obtained numerically and experimentally in polar coordinates for shaft different rotational speeds [20]. The closest numerical predictions for both the configurations come from the THD models ("THD 2D correlation" and "THD 3D"). Indeed, as far as attitude angles are concerned, they are in better agreement with modified RK measurements than the TEHD models (both "free expansion" and "radial constraint"). For both configurations of the modified RK radial clearance values are very small; therefore, the measurement error in journal position may affect experimental evaluation of attitude angle when the journal moves close to the center of mobility area. The indeterminacy of the attitude angle near to the mobility region center yields high sensitivity of such parameter with respect to journal location.

As a consequence, such effect reduces the correlation between experimental and numerical results at the highest angular speed, when the journal runs almost centered. Indeed, for such operating conditions, the increase in experimental-numerical difference reveals measurement errors more significant than simulation ones. This issue has been encountered regardless of the considered numerical models, and this seems to further indicate a limit in the experimental data set. The last step of the experimental activity will be conducted by means of the in-house designed RK (i.e., the one made up by cylindrical ground bars frame) furnished with new metallic bushings, so that wear effects in the

bearing will be negligible, being equal the usage time, while this does not hold for the tested bushes made up by polycarbonate.

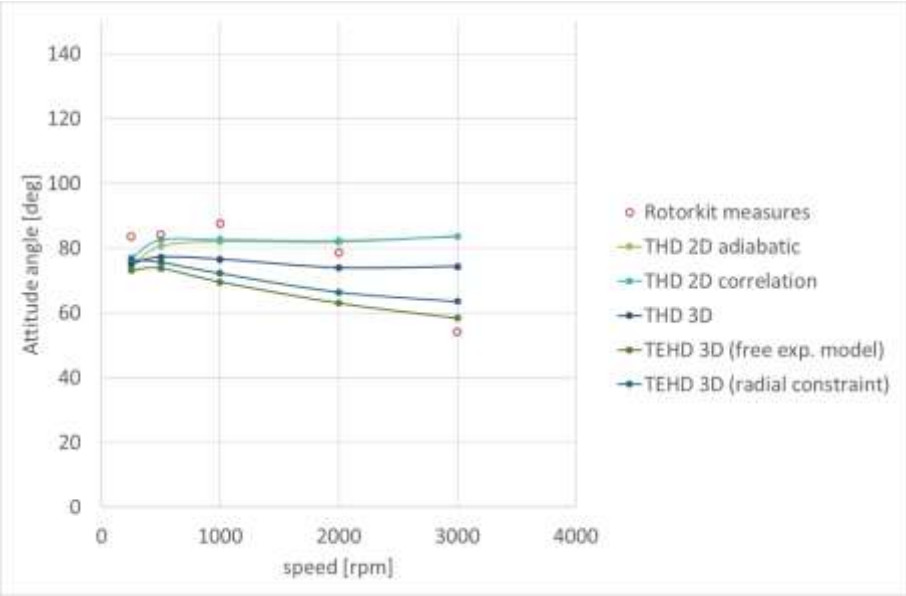

Figure 2.22 – Attitude angle plot for modified RK with respect to 3D numerical THD and TEHD simulations results in configuration 1

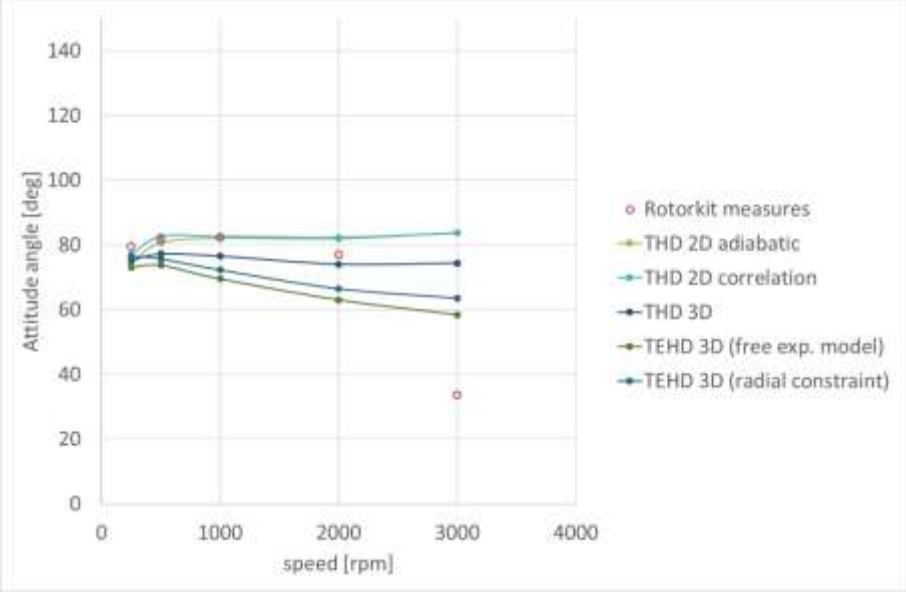

Figure 2.23 – Attitude angle plot for modified RK with respect to 3D numerical THD and TEHD simulations results in configuration 2

The comparison between numerical and experimental curves points out that more sophisticated models are in better agreement with experimental results. Among two-dimensional models, “THD 2D correlation” gives a slightly better agreement than “THD 2D adiabatic”, and this improvement is more perceivable for low rotational speeds. In comparison, 3D models give predictions in better agreement with measurements, by

means of the more accurate heat exchange simulation. Predictive differences among the 3D models are not remarkable. Indeed, although only the “TEHD 3D” model computes structural and thermomechanical deformations, “THD 3D” model does not neglect thermal expansion, since it is included in the hot clearance value (0.1 mm) used as input for this model. Differently, the “TEHD 3D” simulation requires the cold clearance value (0.85 mm) as input so that the thermomechanical deformation is computed during the simulation. Therefore, response differences between “THD 3D” and “TEHD 3D” models are only related to the radial thermal deformation distribution and not to its mean value. While thermal deformations cause significant bearing displacements (in the order of 10 μm), the mechanical ones (due to hydrodynamic pressure) yield negligible displacements (micron fractions even at higher speeds) in comparison with the minimum film thickness (about 85 μm). Indeed, due to the very low bearing load the hydrodynamic pressure (in the order of bar fractions) cannot cause important mechanical deformations. The influence of constraint locations in the thermomechanical sub-model is also not very significant. The “radial constraint” sub-model yields better agreement with experimentation than the “free-expansion” one. The actual structure should be in an intermediate condition between the conditions simulated by the two sub-models, since the region included between the two O-rings is somehow constrained, but it can also expand. Generally, differences on the journal positions predictions provided by simulation and experimentation are not substantial, particularly in the modified RK configuration.

3D models, by using a quasi-3D mass-energy conserving algorithm, have shown an excellent agreement between numerical and experimental results published in literature as far as temperatures are concerned [10]. Therefore, their prediction of journal location is also expected to be sufficiently reliable. Actually, differences on the journal positions predictions provided by simulation and experiments are not substantial in the modified RK configuration.

Comparisons of relative eccentricity errors for both 3D and 2D models are depicted in Figs. 2.24-2.25 and Figs. 2.25-2.26 for configuration 1 and 2, respectively. Figure 2.24 shows that the TEHD simulation almost for all of the speeds can yield errors lower than the “THD 3D” simulation, while between the two TEHD models, the most reliable is the “TEHD 3D radial constraint”, as already mentioned [20].

Figure 2.25 compares in terms of relative eccentricity errors the two TEHD 3D models and the most consistent 2D simulation for configuration 1 [20]. The "2D correlation" model is not far from the results of the two 3D TEHD models for all of the angular speeds.

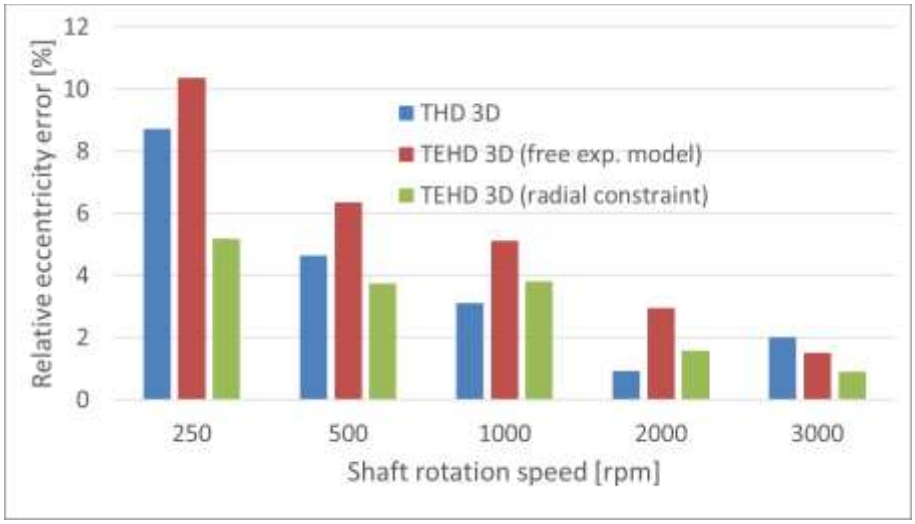

Figure 2.24 – Difference between relative eccentricities measured and computed by means of 3D models for modified RK in configuration 1

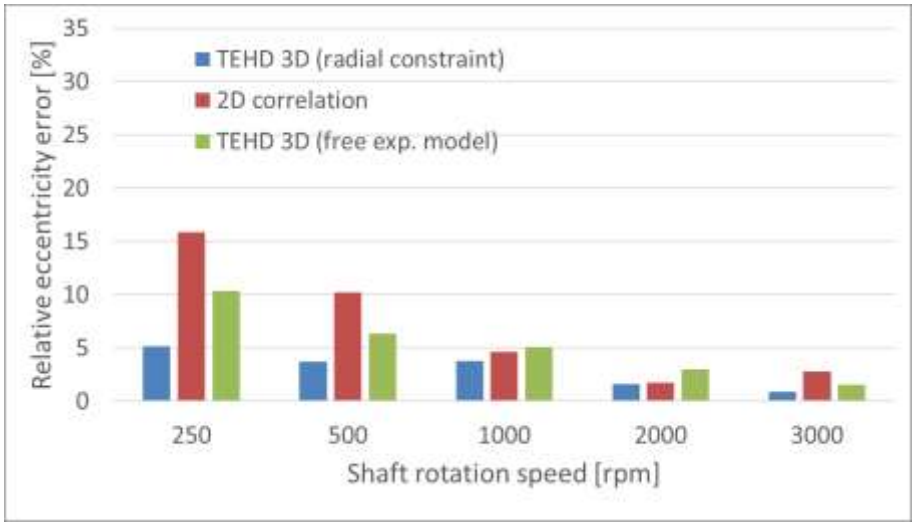

Figure 2.25 – Difference between relative eccentricities measured and computed by means of most consistent 3D and 2D models for modified RK in configuration 1

Figure 2.26 shows that the improvement in journal location prediction obtained by using the "TEHD 3D radial constraint" model instead of THD simulations, already observed for configuration 1 (Figs. 2.24-2.25), is even more evident for configuration 2 [20].

Finally, Figure 2.27 shows for configuration 2 a further improvement in eccentricity prediction of TEHD simulations against 2D models. Indeed, eccentricity errors of the most consistent 2D THD model ("2D correlation") are always bigger and similar in

comparison with errors of “TEHD radial constraint” and “TEHD 3D free expansion” models, respectively [20].

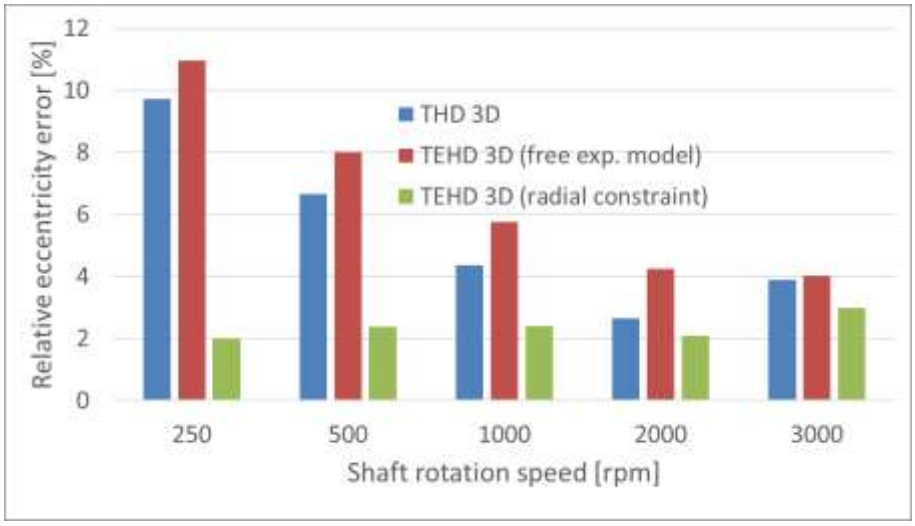

Figure 2.26 – Difference between relative eccentricities measured and computed by means of 3D models for modified RK in configuration 2

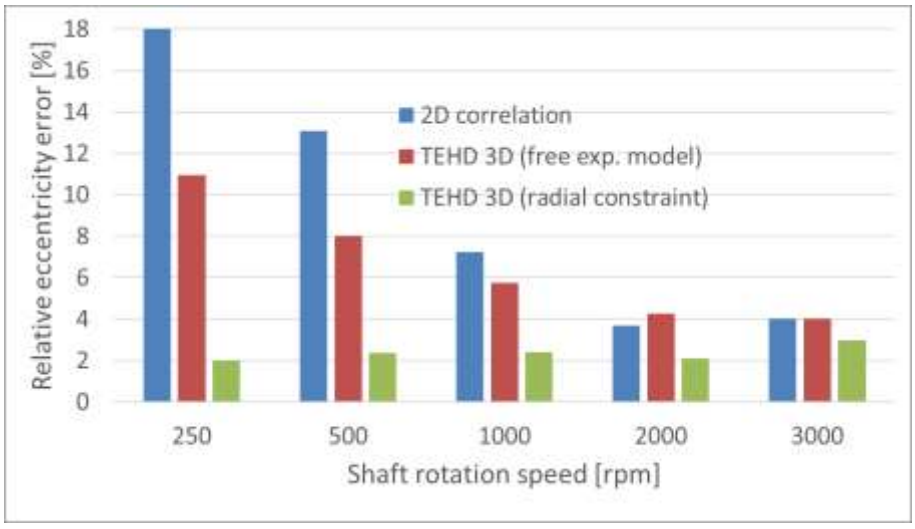

Figure 2.27 – Difference between relative eccentricities measured and computed by means of most consistent 3D and 2D models for modified RK in configuration 2

The comparison between numerical and experimental results presented in this section underlines a consistent behaviour of simulation models even with very small clearances, whose reliability is enhanced by model complexity and accuracy. Furthermore, a good correlation between journal locations predicted by numerical computations and measured in modified RK has been found out. Therefore, a relative radial clearance of 8/1000 fulfils the thin film Reynolds hypothesis on which calculation models are based. Furthermore, since FEM codes had been already validated in the past, this also confirms that the

modified test bench is reliable for further experimental investigations on this type of journal bearings, allowing us to study their dynamic behavior in future research activity.
TEHD analysis results prove that, while displacements due to hydrodynamic pressures are negligible, thermal deformations strongly affect journal position even under low external load (rotor weight is around 0.5 kg) and small temperature rise in the bearing. This is due to the high expansion coefficient of the bearing polycarbonate material and the resulting the high differential thermal dilatation between steel journal and polymeric bush. After a series of experiments and related data processing, reasonable temperature boundary conditions have been determined on the basis of the temperature control at the bearing supply and simulations performed by means of different models.
Discrepancies found in journal center location predictions may also be ascribable to oil temperature variations with rotation speed. Indeed, bearing supply oil temperature control has shown that such variations are not substantial so that they have not been simulated numerically. This can explain part of the obtained differences between experimental and numerical results.
From the relevant results the most accurate simulation model for the bearing in analysis has been identified. It includes three-dimensional simulation of heat exchange phenomena. Indeed, at the rotational speeds investigated (250-3000 rpm), the thermal model is crucial in the assessment of bearing static characteristics.
The reduction of relative radial clearance from original to modified RK values has improved the correlation between experiments and real-world applications as well as their agreement with numerical results from in-house developed FEM codes implemented for lubrication analysis. This result is the starting point of future studies about dynamic behavior of journal bearings and, particularly, about fluid-structure interactions in this class of fluid film bearings. Nevertheless, industrial bearing casings are still different from our test rig ones in that they are usually manufactured in metallic materials. Therefore, thermo-mechanical behaviour in real-world bearings differs from our experimental models and numerical simulations, so that temperature and thermal displacements distribution within the bearing pair cannot be fairly compared. Obviously, in the present work we have assumed as main simulation parameter an average hot clearance and we have subsequently run the bearings in order to achieve that corresponding operating condition. Therefore, our numerical and experimental assessments of journal center location are reasonable and consistent. In order to appropriately deal with industrial bearings considering thermo-mechanical effects, only

the experimental device should be enhanced, simply by manufacturing a metallic bushing. On the contrary, our numerical model would not require any correction. We expect that employing a metal bush would simplify experimental procedure by both improving repeatability and ensuring quicker stationarity of experimental conditions, thus allowing to study even lower relative clearance ratios. We have not yet adopted this expedient as we are gradually updating the existing in-house designed new test rig. Indeed, in order to achieve the clearance adjustments required for the present investigation, only the journal has been modified accordingly. The high differential thermal dilatation between PC and steel makes it practically impossible to study clearance ratios lower than 3/1000 by assuming an average running temperature of 40°C.

In the next section, the completely new and original test rig set up, already presented in section 1.2, is going to be characterized with the same approach previously adopted for the former test benches; in future research activity it will be employed both for static and even for dynamic analysis of hydrodynamic journal bearing-rotor systems with smaller relative clearances, realistic loads, and metallic bushings.

2.3.2 Analysis of results collected on the new test rig final setup

In this last step of the conducted research activity, the measurements collected from the in-house designed test bench presented in section 1.2 (i.e., the new RK made up by cylindrical bars ground frame) are presented and deeply discussed, as they represent the current evolution of the adopted experimental model. At first, the obtained static characteristics for the same relative clearance (8/1000) are presented and compared with numerical results. The new RK is tested in a final setup with four volanic masses mounted with respect to its previous configuration shown in Figure 2.8a. This is done with the aim of furtherly increasing bearings load and thus to suppress oil-whirl inception in all their experimentally investigated operating conditions. Indeed, even in the arrangement with two volanic masses oil-whirl onset has been detected at the highest angular speeds. Such final experimental setup is presented in Figure 2.28.

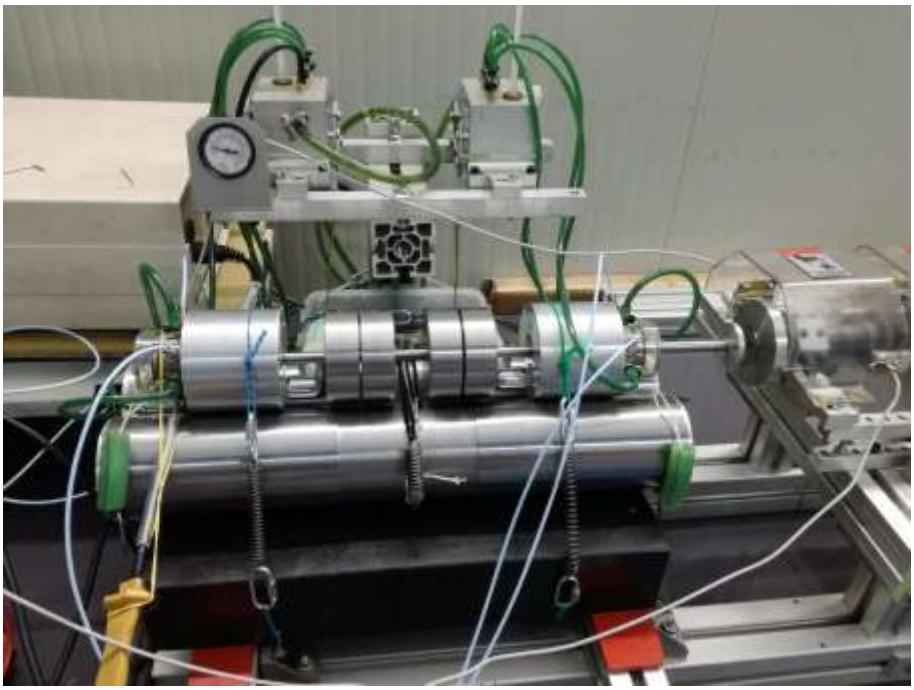

Figure 2.28 – New RK final setup with four volanic masses mounted

In the last part of the experimental activity conducted on the new RK, the employed proximity probes arrangement is different, in order to ensure a better and more uniform oil supply to the bearing. To achieve this, proximity sensors are placed at a 45 degs with respect to bearing previous absolute coordinate system, which is reported in Figure 2.29a. Moreover, a thermistor is placed tangent to the external bushing to monitor its temperature during the whole experimental campaigns. Such proximity sensors arrangement in the final setup of the new RK is shown in Figure 2.29b.

Figure 2.29 – Proximity probes arrangement: (a) in previous setups, (b) in the new RK final setup

In the following, the obtained experimental results are presented and compared with FE simulations in terms of static journal center locations, as already did for the former test benches. In this case, only the numerical results coming from the most accurate models, that is TEHD ones, according to the error analyses previously conducted, are plotted versus measurements, since this is an intermediate step of the activity; indeed, a complete error analysis will be performed only on the new RK with metallic bushings.

In the presented results, the maximum experimental angular speed is set at 1500 rpm, so that also numerical simulations are performed only up to 2000 rpm. In the following Figure 2.30 the relative eccentricity plot versus shaft angular speed is shown for the new RK in its final configuration in both cw and ccw directions since oil-whirl never occurs in such test bench setup, differently from what happened in former test rigs (refer to Figs. 2.20-2.21).

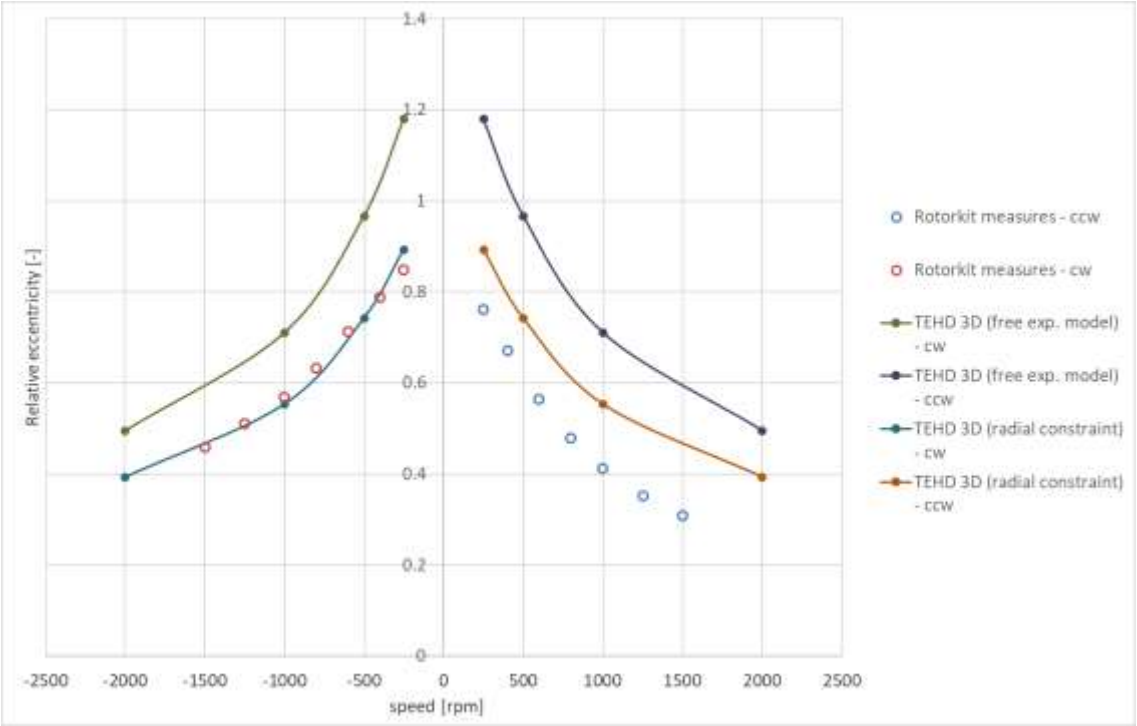

Figure 2.30 – Relative eccentricity plot for new RK with respect to 3D numerical TEHD simulations results in its final setup

From the reported eccentricity plot it can be noticed how there is still discrepancies between experimental and numerical results and that a certain asymmetry in measurements between cw and ccw is still present; this may be ascribable to an asymmetric wear in the polymeric bushings; for this reason, such experimental results are not still reliable, and a more accurate experimental data set will be collected with the new metallic bushings. In the following Figure 2.31 the attitude angle plot is reported for completeness. Even in this case the experimental data set shows an asymmetry between cw and ccw directions, while the agreement with numerical results is poor at the highest angular speeds. This mismatch is to be attributable to the experimental indetermination in assessing the measured attitude angle, as already stated for the former test benches. It is thought that the final improvement of the final RK with the metallic bushings in place of polymeric ones should mitigate the experimental errors in determining the attitude angle.

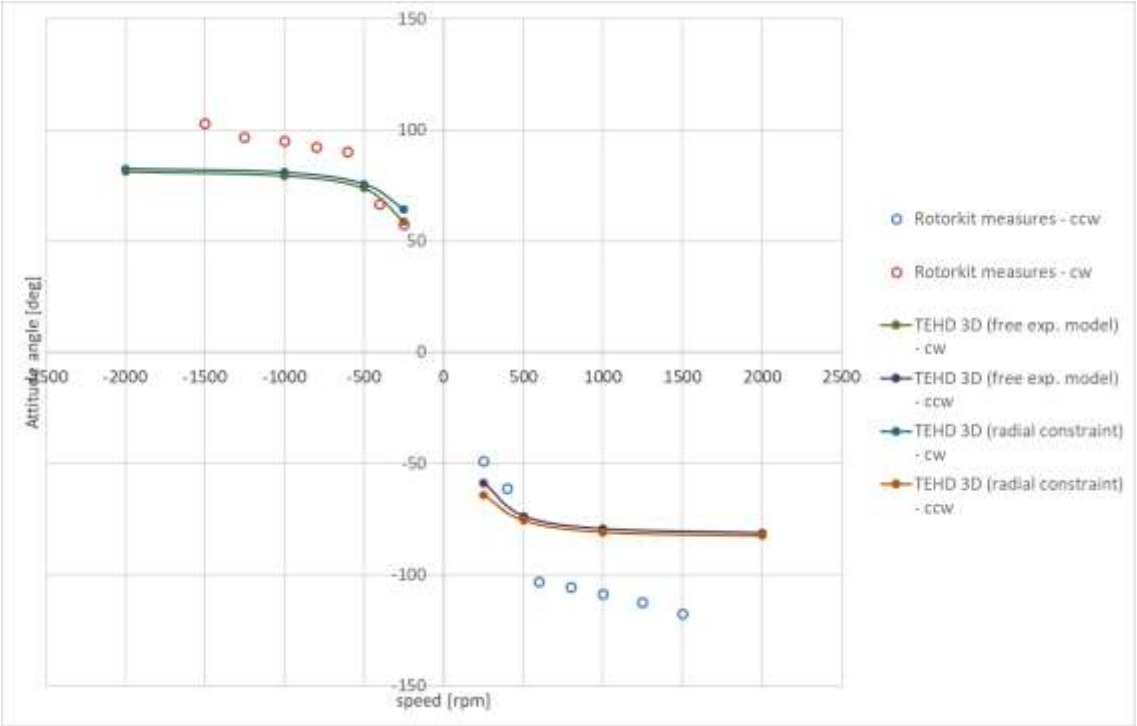

Figure 2.31 – Attitude angle plot for new RK with respect to 3D numerical TEHD simulations results in its final setup

A further analysis is performed on experimental data by comparing slow run-up transients with iso speed measurements to assess if large discrepancies are met between them. The results confirm that for the final setup of the new RK, iso speed measurements are in family with slow run-up transients both in cw and ccw directions, thus showing a good agreement between faster and slower measurements. This is very important since it allows us to affirm that the issues related to differential thermal dilatations are not so influential; indeed, each iso speed measurement is performed after the thermal transient is completed for each angular speed to be characterized; therefore, with respect to ramp measurements it would lead to a strong difference if thermal effects were dominant. Such experimental comparisons are still performed on the current setup with the polycarbonate bushing, and this is encouraging since it is expected that with metallic bushings such undesired effects will be even more negligible; moreover, also bushing wear will be null, thus leading to more accurate measurements in static and dynamic conditions in both cw and ccw directions. In Figure 2.32 such experimental comparison is reported for clockwise direction: it can be observed how there is a good agreement between the points relative to iso speed measurements and the continuous run-up in terms of journal absolute Y location.

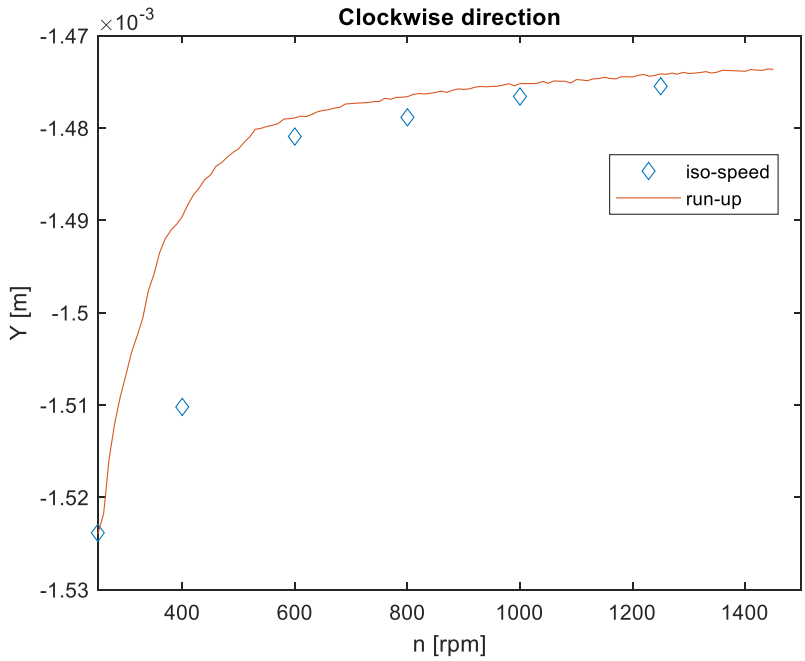

Figure 2.32 – Comparison between slow run-up and iso-speed measurements in cw

The same comparison is reported in Figure 2.33 for counterclockwise direction: even in this case there is a good match between the iso speed measurements and the slow run-up in terms of absolute Y journal locations. Nonetheless, a certain asymmetry persists between cw and ccw directions but this last issue is expected to be solved by adopting metallic bushings.

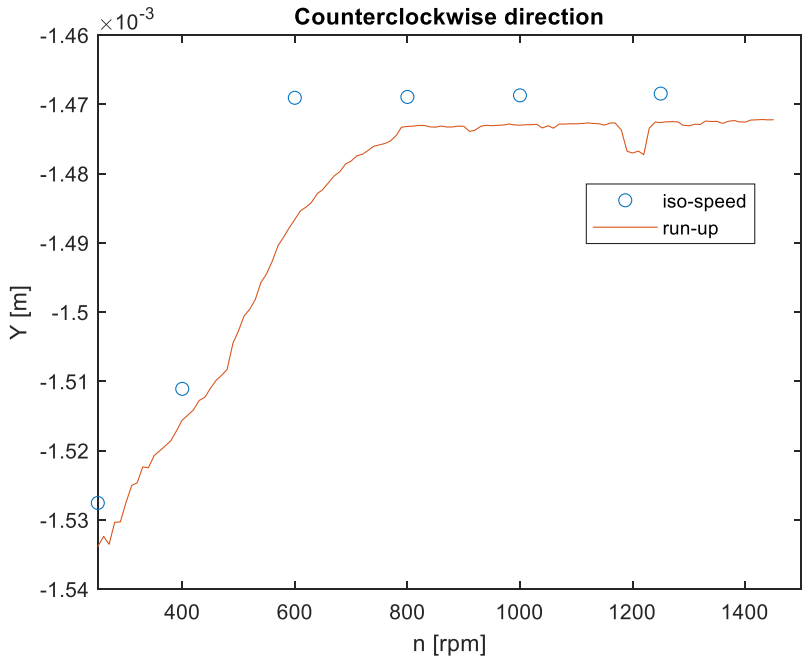

Figure 2.32 – Comparison between slow run-up and iso-speed measurements in ccw

Bibliography chapter 2

[1] Niccolini Marmont Du Haut Champ C.A., Stefani F., Silvestri P., Development of a new test rig for the analysis of hydrodynamic bearings for rotors of microGT (2019) E3S Web of Conferences, 113, art. no. 03002

[2] Huggins N. J., Hydrodynamic instability in plain journal bearings, PhD thesis, Imperial College, London-UK (1961)

[3] Sandvik K., Lehtovaara A., Makkonen E., Kallio M., Kuvaja K., Kuokkala V-T., Development of a test device for the evaluation of journal bearings, Tampere University of Technology, Tampere-Finland (2012)

[4] Tůma J., Biloš J., Fluid Induced Instability of Rotor Systems with Journal Bearings, Journal of Engineering Mechanics, **14**, 1-2, 69-80 (2007)

[5] Meruane V., Pascual R., Identification of nonlinear dynamic coefficients in plain journal bearings, Tribology International, **41**, 8, 743-754 (2008)

[6] Tůma J., Bilošová, A. Šimek, J., Svoboda R., A Simulation Study of the Rotor Vibration in a Journal Bearing, Journal of Engineering Mechanics, **15**, 6, 461-470 (2008)

[7] Deepak J. C., Noah, S. T., Experimental Verification of Subcritical Whirl Bifurcation of a Rotor Supported on a Fluid Film Bearing, ASME Journal of Tribology, **120,** 605-609 (1998)

[8] Boedo S., Experimental Verification of Subcritical Whirl Bifurcation of a Rotor Supported on a Fluid Film Bearing" (Deepak J. C., Noah, S. T., 1998, ASME Journal of Tribology, 120, pp. 605–609), **121** (2): 421–422 (1999)

[9] Van De Vorst E. L. B., Fey R. H. B., De Kraker A., and Van Campen D. H., Steady State Behavior of Rotordynamic Systems with Oil Journal Bearings, ASME Nonlinear and Stochastic Dynamics, **78**, 107-114 (1994).

[10] Stefani F., Rebora A., steadily loaded journal bearings: Quasi-3D mass–energy-conserving analysis, Tribology International, **42**, 3, 448-460 (2009)

[11] Stefani F., FEM Applied to Hydrodynamic Bearing Design, New Tribological Ways, 451-476 (2011)

[12] Bently, D.E., Grant, J.W., Hanifan, P.C., Active controlled hydrostatic bearings for a new generation of machines, Proceedings of the ASME Turbo Expo, Munich, Germany, May 8-11, 2000

[13] Trachsel M., Pittiti R., Dual J., Friction and 2D position measurements in small journal bearings, Tribology International, **6** (2016)

[14] Stefani F., Design and fast verification of pocket elliptical journal bearings, Industrial Lubrication and Tribology, **66**, 393-401 (2014)

[15] Jacobsson B., Floberg L., The Finite Journal Bearing Considering Vaporization, Transactions of Chalmers University of Technology, **190** (1957)

[16] Olsson K., Cavitation in Dynamically Loaded Bearings, Transactions of Chalmers University of Technology, **308** (1965)

[17] Kumar A., Booker J.F., A Mass and Energy Conserving Finite Element Lubrication Algorithm, ASME Journal of Tribology, **116**, 4, 667-671 (1994)

[18] Gazley C., Heat-transfer characteristics of the rotational axial flow between concentric cylinders, Transactions of the ASME, **80**, 79-90 (1958)

[19] Bouyer J., Fillon M., An Experimental Analysis of Misalignment Effects on Hydrodynamic Plain Journal Bearing Performances, ASME Journal of Tribology, **124**, 313-319 (2002)

[20] Niccolini Marmont Du Haut Champ, C.A., Stefani, F., Silvestri, P. (2020), "Experimental and numerical investigation about small clearance journal bearings under static load conditions", Advances in Tribology, 2020, art. no. 8844879.

3 Rolling bearings: influence on rotor systems flexural critical speeds

In technical literature there are many rotor-bearings system available analytical models which have been formulated in order to assess real systems rotordynamic behavior. Indeed, such models are characterized by an increasing inherent complexity according to the number of considered DOFs; in example, when passing from one DOF model (e.g., classical Jeffcott rotor) to four DOFs one, the more accurate modelling is at expenses of easiness of usage and immediate physical interpretation of the obtained results. By generalizing such approach, when dealing with numerical rotor-bearings system models, that is, when the number of the considered DOFs is too big to allow an analytical solution, many advantages typical of simplest approaches are lost. To this aim, in this section, an analytical non-linear bearing stiffness model is proposed, and it will be firstly applied to rotor system simplest models, in order to be able to carry out a sensitivity analysis, easily achievable in such case. After classical rotor systems analytical models which rely on flexible bearings are presented and investigated, such bearing stiffness model will be applied even to rotor system FE models in order to assess its reliability in real industrial study cases, typically solved by means of structural simulations. In the following, the main employed analytical models will be shortly revised, and then it will be stressed how the difference in rotor mounting conditions is crucial in determining bearing stiffness contribution to overall system bending stiffness and consequently on its flexural critical speeds.

3.1 Rotor-bearings system analytical models for rotordynamic analysis

As already mentioned, there are many well-known analytical models whose complexity is dependent on the considered number of DOFs. Moreover, other simplifying hypotheses can be formulated in correspondence of the considered DOFs, such as to deal with isotropic supports, on the chance of neglecting cross-coupled stiffness, on the importance of gyroscopic effects influence, and finally on the relevance of damping contributions. A brief description of the models employed for the investigations of the considered study cases is presented hereinafter.

3.1.1 One degree of freedom rotor-bearings system model

The simplest shaft model to assess rotor-bearings system behavior is Jeffcott's one, which is characterized by one DOF, without neither internal or external damping, whose only excitation is due to static unbalance; indeed, dynamic unbalance is not modeled as inertias moments are neglected, and then gyroscopic effects cannot be taken into account in such first level of system approximation. Nonetheless, Jeffcott's classical rotor model, which is idealized as with only distributed elasticity and no distributed mass, in this context is supported by two nonlinear springs, representative of actual

ball bearings, whose stiffness is taken into account together with rotor's one. On the other hand, as well-known, all the inertia effects are reduced in the eccentric lumped mass, which is located at shaft centerline, representative of static unbalance. Such model is represented in Figure 3.1 for reference. Since in the present research activity both the bearings and the shaft are always thought as flexible, the well-known analytical solution for the classical Jeffcott model (that is, rigid bearings and flexible shaft) is not presented; whereas only the results obtained from the implementation of such rotor-bearings system model with stiffness contributions ascribable to both bearings and shaft, referred to as "fully flexible" model , performed in Matlab® environment will be reported in the following.

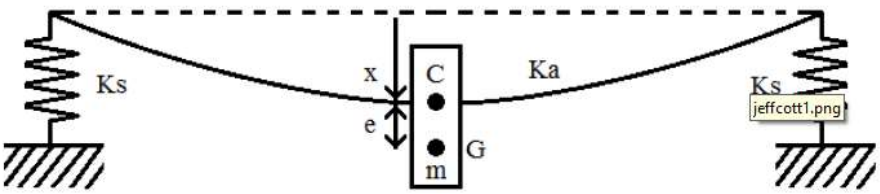

Figure 3.1 – One degree of freedom "fully flexible" rotor-bearings system model

3.1.2 Four degrees of freedom rotor-bearings system model

A brief description of the four DOFs model is reported to underline its characteristics and capabilities with respect to the already presented one DOF model. The main differences are that in this case four displacements are considered for the mass M, of which two of translations in x and y directions and two of rotations θ and φ respectively around the same axes (which are orthogonal to shaft rotational axis z). In this way, the effect of dynamic unbalance can be taken into account, since the mass M is thought as a disk with its inertia tensor (and then, for a defined reference system its inertia matrix can be obtained). Moreover, ball bearings are modelled as two translational non-linear springs, which have in general different stiffness in x and y directions. In this context, the springs are assumed to be isotropic, that is to have the same stiffness in both directions (since in a polar system reference, both of them are equal to bearing radial stiffness according to the adopted bearing non-linear stiffness model), and damping is neglected. Indeed, the main goal is to look for undamped system critical speeds and to assess the influence of bearings stiffness in determining it even in this model, as already said for the one DOF case. Therefore, even in this model, shaft stiffness is also taken into account, according to Jeffcott rotor model, in the form of a matrix (analogous to the one DOF case) and combined with bearing non-linear stiffness as stiffness in series. In this model this is not trivial as in one DOF case, since the two stiffness matrixes (and not two scalar values) need to be properly combined. The same operation has been performed by adequately combining element per element of

each matrix and then a global stiffness system matrix is obtained. Even in this case, the model is referred to "fully flexible", since, differently from the classical Jeffcott model, both shaft and bearing stiffness contributions are taken into account in assessing system global stiffness, this time in the form of matrixes. Hence, the well-known analytical solution is not presented, as it is not of research interest, but the same model is implemented in Matlab® environment, by considering all the inertia properties and generalizing stiffness ones as remarked. Indeed, the aim is to assess and validate bearing stiffness model, which is the main novelty of the proposed research activity.

The classical four DOFs model is reported in Figure 3.2 for reference. It is stressed once again that in the proposed implementation, damping is neglected and bearing stiffness properties are isotropic.

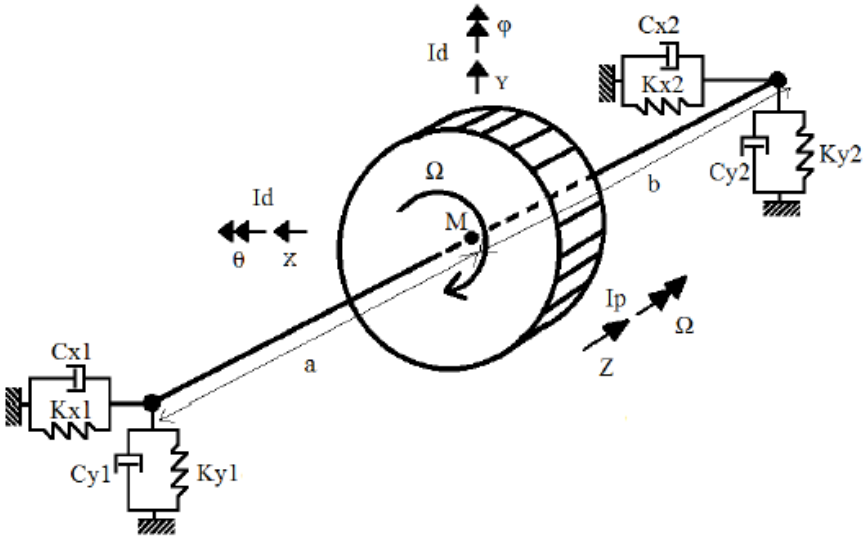

Figure 3.2 – Four degree of freedom "fully flexible" rotor-bearings system model

The equations of a four DOFs undamped model, referred to a statically and dynamically unbalanced rotor are presented hereinafter for the sake of completeness; in general, cross-coupled stiffness terms are present. With the hypothesis of isotropic spring stiffness and equal distance between bearing location and shaft centerline (where inertia matrix effects are concentrated) such terms become null. The general form of motion equations in fixed frame is reported in (3.1) for an undamped system:

$$\begin{cases} m\ddot{x} + K_{11}x + K_{12}\varphi_y = m\varepsilon\Omega^2\cos(\Omega t + \alpha) \\ m\ddot{y} + K_{11}y + K_{12}\varphi_x = m\varepsilon\Omega^2\sin(\Omega t + \alpha) \\ J_t\ddot{\varphi}_x + J_p\Omega\dot{\varphi}_y - K_{12}y + K_{22}\varphi_x = -\chi\Omega^2(J_t - J_p)\sin(\Omega t) \\ J_t\ddot{\varphi}_y + J_p\Omega\dot{\varphi}_x - K_{12}x + K_{22}\varphi_y = -\chi\Omega^2(J_t - J_p)\cos(\Omega t) \end{cases} \quad (3.1)$$

Where J_t is the transverse inertia moment, J_p is the polar inertia moment, Ω is shaft angular speed, whereas ε and α are representative of static and dynamic unbalance, respectively. Such equations system in general yields to four natural pulsation frequencies, of which two are referred to translations

and two to rotations, always in couples of Forward (FW) and Backward (BW) precession (Forward Whirling and Backward Whirling). Indeed, written in this way, such system yields four natural pulsation frequencies which are all function of angular speed. This because the cross-coupled terms of stiffness characteristics among the various DOFs cause that even the first two natural pulsation frequencies are function of angular speed even if they are not directly subjected to gyroscopic effects which are included only in the third and fourth equations.

Finally, it is to remark that if gyroscopic effects are neglected, being null the cross-coupled stiffness terms as in the proposed implementation, and if also shaft stiffness parameters are regarded as isotropic, the previous equations system becomes decoupled, which is analogous to have one DOF model for both the transverse and rotational direction. This gives rise to only two (and no more four) natural pulsation frequencies, each of the two correlated to typical one DOF systems lateral critical and torsional speeds, according to the classical formulae which are only mentioned for completeness. The classical formula which is obtained for bending natural pulsation frequency is analogous to one DOF Jeffcott laterally flexible shaft model, that is reported in equation (3.2).

$$\Omega_{n1} = \Omega_{n2} = \sqrt{\frac{k_T}{m}} \tag{3.2}$$

where k_T is system bending stiffness considered in the previous 1DOF model. Finally, the classical formula obtained for torsional natural pulsation frequency is reported in equation (3.3).

$$\Omega_{n3} = \Omega_{n4} = \sqrt{\frac{k_R}{m}} \tag{3.3}$$

In which k_R stands for system torsional stiffness.

3.2 Differences between rotor-bearings system mounting configurations

The importance of rotor-bearings system characteristics and mounting configurations gives rise to a wide range of possible different behavior of the involved rotating machinery. For what concerns shaft characteristics, in general there can exist substantial differences between the behavior of stubby rotors with respect to slender ones. Indeed, they can be characterized by significantly different vibration modes. When dealing with rotor vibration modes, it is natural to immediately think about bending modes of an unconstrained elastic beam, free in the air, which are reported in Figure 3.3.

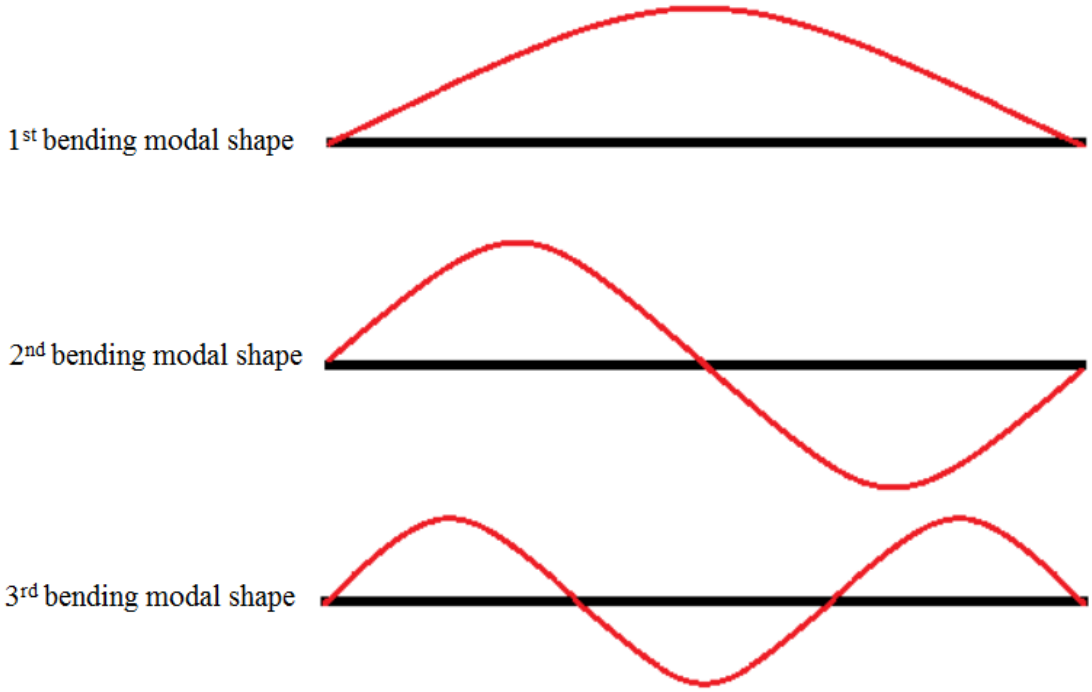

Figure 3.3 – First three bending modes of an elastic beam

In real rotor-bearing systems the situation is much more complex, since the rotating shaft is not fixed to the frame by means of an infinitely stiff support (i.e. rigid constraints typically used in elastic beam theory), but by means of bearings, which may significantly affect system dynamic behavior; indeed, depending on the kind of support on which the rotor is mounted (only rolling bearings and hydrodynamic ones are investigated in this work, respectively in terms of assessing system critical speeds for the firsts and system instability regions for the seconds), they can be more or less stiff, thus directly affecting system natural pulsation frequencies; moreover, they can introduce more or less damping, in this way influencing mainly system stability properties, and indirectly slightly changing its critical speeds. Such kind of constraint characterized by a finite stiffness with damping (in example ball bearings, whose stiffness model is presented hereinafter) generally yields a substantial difference in rotor-bearings system vibrational behavior with respect to the case of rigid supports. Furthermore, if a shaft were ideally suspended in the air, it would be characterized by rigid body motions like the cylindrical and the conical ones, which are reported in Figure 3.4 for the sake of completeness.

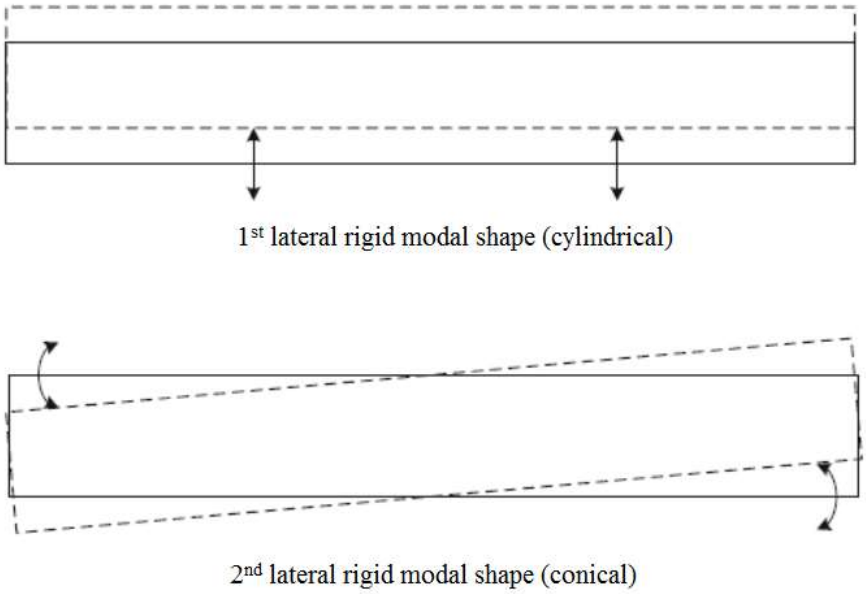

Figure 3.4 – Rigid body motions of a rotor suspended in the air

Usually such rigid body modes are investigated separately with respect to deformative ones (that is, flexural in case of lateral system response which is the only one investigated in this context) because in general, it is easy to affirm that rotors with bending stiffness much lower than bearings' one (e.g. slender shafts) are characterized by the first modes which are purely flexural ones and only at higher frequencies rigid body ones occur. On the contrary, rotors with bending stiffness much higher than bearings' one (e.g. stubby shafts) exhibit the first modes which are characterized by rigid body motions whereas flexural modes are found only at higher frequencies. Such second behavior is the typical of slender rotors mounted on rigid constraints, which is generally a common hypothesis when dealing with system rotordynamics. Therefore, normally rigid body modes are likely to occur at lower rotor angular speed whereas flexural ones are found at higher shaft revolution frequency.

A rigid body motion, as already mentioned, does not cause any deformation within the shaft, thus in general when investigating its dynamics, it is less dangerous than the other modes which deserve more attention. By defining a non-dimensional stiffness k_N as the ratio between bearing stiffness k_B and bending stiffness of beam constrained on two hinges k_F, according to following equation (3.4):

$$k_N = \frac{k_B}{k_F} \tag{3.4}$$

In the case of $k_N<1$ the first two vibration modes are likely to be related to rigid body motions, whereas if $k_N >>1$ only flexural modes are likely to occur at the lowest angular speed range, ideally. In real

world there are intermediate conditions where bearing stiffness may significantly affect system flexural modes, and thus their related modal shapes, as it can be intuitively observed in Figure 3.5.

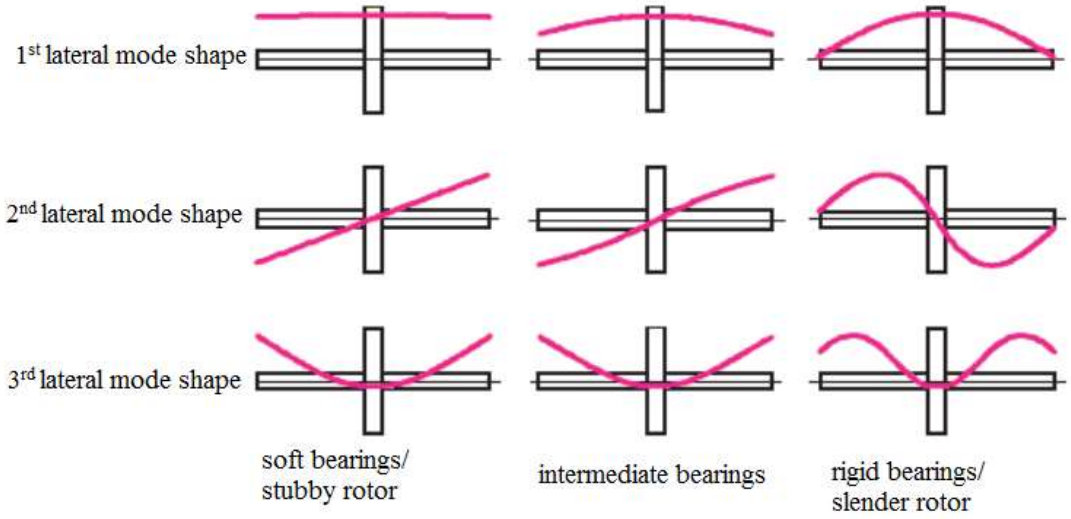

Figure 3.5 – Influence on lateral modal shapes due to shaft and bearing stiffness combinations

Practically it happens that when bearing stiffness is small if compared with rotor's one, it mainly affects rigid body motions whereas the vibration modes at higher frequencies like bending ones are mainly influenced by the slenderness of the shaft.

3.3 Rolling bearings stiffness modelling

In this section the core of the chapter is presented, that is, non-linear ball bearings stiffness model which will be applied firstly on the RK by means of analytical rotor models (1 DOF and 4 DOFs) and afterwards to an industrial study case by means of numerical models in Ansys® environment.

3.3.1 Introduction

Rolling bearings stiffness typically changes nonlinearly with bearing deflection in a significant way. Therefore, an accurate rotordynamic analysis requires that bearing non-linear forces corresponding to the current bearing deformation are employed, in order to adequately capture its actual stiffness. Indeed, as already mentioned, in general rotordynamic response of not too flexible rotors (i.e. not too slender ones) is strongly dependent on bearing stiffness and on its damping properties. When rolling bearings are investigated as nonlinear elements, accurate rotor response calculations require the use of variable bearing properties which reflect better the actual experimental conditions occurring, with respect to the average characteristics which are typically found in constructors manuals. While fluid film bearings are often reasonably linear for small deflections, although there is usually a strong speed dependence [1], rolling element bearings have a much less linear force-displacement relationship, and therefore an intrinsically non-linear stiffness.

Load-stress correlations for rolling element bearings were firstly discovered by Lundberg and Palmgren [2] in the 40's. Such relationships have not been easily implemented until the analytical additions of Jones [3] led to the marketing of a suitable computer code. Nowadays, Jones' code still represents one of the most widely employed rolling element bearing analysis tool despite its age. Poplawski et al. [4] have recently developed a suitable computational "Code for Optimized Ball and Roller bearing Analysis - Advanced High-Speed" (COBRA-AHS) under a NASA "Small Business Innovative Research" (SBIR) contract. Fleming and Poplawski [5], employed COBRA-AHS in combination with a transient rotordynamics code to predict system response to a suddenly applied large mechanical unbalance emulating a blade loss. The results found employing nonlinear bearings characteristics could not be obtained with any other averaged bearing stiffness value. Furthermore, steady state rotordynamic codes have been employed for several years to evaluate permanent system response. One of such early and still usable codes was devised by Lund [6]. It relies on the transfer-matrix method to predict unbalance response for a flexible rotor mounted on asymmetric bearings. Such code has been simplified for the case of symmetric bearings (i.e. same stiffness and damping properties in different directions) by Kirk [7]. Fleming and Poplawski [8] have further tuned Kirk's code to allow the exploitation of nonlinear bearings properties by iterating on rotor response amplitude. In detail, unbalance response data are presented for a rotor mounted on ball bearings with accurate bearing stiffness computed as a function of angular speed and actual load. Rolling bearing stiffness is found to be a strong function of bearing deformation, with higher deflections yielding markedly higher stiffness. Rotordynamic analyses indicated that unbalance response changed nonlinearly with residual mechanical rotor imbalance amount. Furthermore, the rise in bearing stiffness as critical speeds are approached produces a large increase in rotor-bearings system vibrations over part of its operating speed range with respect to the case of constant stiffness bearings. Moreover, it is proven how regions of bistable operation are possible, in which vibration amplitude at a specified angular speed was much larger during system run-up than during run-down. A moderate amount of damping can suppress such bistable region, but this kind of damping is not characteristic of ball bearings.

Ball bearings stiffness can be also markedly influenced by internal clearance and bearing ring mounting compliance, in addition to bearing center deformation and applied loads, between whom the ones correlated to rotor-bearings system angular speed (due to residual mechanical unbalance). As ball bearings stiffness plays a key role in determining rotor-bearings system critical speeds, it is necessary to accurately estimate their radial stiffness in a preliminary design phase. Indeed, an exact estimate of rolling bearing stiffness is crucial to avoid that unexpected structural resonances occur within rotating machinery operational angular speed ranges. To this aim, Beatty, and Rowan [9]

conducted an extensive experimental campaign in order to directly evaluate bearing stiffness employed for rotordynamic investigations compare it with classical analytical predictions, as well as to assess the effects of system actual working conditions. Butner et al. [10] performed an experimental activity aimed to assess the effect on ball bearing stiffness due to angular speed, dynamic radial load, internal clearance, axial preload, and mounting compliance variations with respect to analytical predictions. In detail, an experimental validation of the rolling element bearing code developed by Jones [3] was carried out by examining the influence of several parameters on ball bearing radial stiffness. Indeed, the estimates predicted by such analytical code agree with the obtained experimental results only when system actual operating conditions, comprising mounting compliance, are properly taken into account. Overall, analytical predictions of ball bearing stiffness obtained by Jones' code [3] slightly overestimated on average the measured radial stiffness.

In the present work, an experimental validation of an analytical code for ball bearings non-linear stiffness prediction is firstly carried out on the commercial RK and afterwards it is applied both on a Tesla air turbine, which is an unconventional fluid machine, and to a micro-gas turbine. To this goal, a beam-based FE model of Tesla turbine rotor is devised in Ansys® environment and a numerical modal analysis is performed basing on bearing stiffness obtained by exploiting the analytical model proposed by Tiwari [11]. Indeed, the previously employed ball bearings radial stiffness suggested by constructors led to a relevant mismatch between critical speeds numerical predictions and the ones experimentally detected during machine operating conditions. Moreover, the previous FE Tesla model based on three-dimensional solid elements is characterized by higher computational times and a major inherent complexity. The aim of the work is indeed to obtain a simpler numerical model of such rotor-bearings system, with lower computational costs, more effective in predicting structural resonances and which requires easily available input data (e.g., ball bearing external geometric dimensions, materials constituting balls and raceways in case of hybrid bearings, mounted contact angle in case of spindle bearings). In such way, it may become a useful tool for industrial applications involving both conventional fluid machinery (e.g., micro-gas turbines) and unconventional one (e.g., Tesla turbines).

3.3.2 Analytical model to predict ball bearings non-linear stiffness

The methodology proposed in this work relies on an analytical model suited for predicting ball bearings non-linear radial stiffness as a function of its geometrical parameters as proposed by Harris [13]. Following such approach, Tiwari [11] showed this procedure only for the case of both raceways and balls made of steel. As it relies on Hertz contact theory [14], when investigating conventional ball bearings characteristics, the steel ball and steel raceway contact yields a function of solely geometrical quantities for bearing stiffness. In the present work such bearing stiffness model is

applied even to hybrid bearings, and thus the influence of materials constituting rolling elements and raceways must also be taken into account. Moreover, such employed ball bearings can be mounted even in a spindle configuration, that is, they can face both radial and axial loads, thus resulting in both radial and axial stiffness other than zero. Initially, a non-linear expression of radial stiffness in function of bearing center deformation is obtained for purely radial ball bearings. Afterwards, after an equilibrium position for bearing center resulting from external operating loads (rotor weight plus its residual mechanical unbalance) and bearing non-linear restoring force is found, the actual stiffness is assessed by means of the so obtained bearing center position and then it is projected into radial and axial components. In the following, a detailed explanation of such procedure, implemented in Matlab® environment, is given and all the input parameters (simply deducible from any commercial bearings catalogue) are described to underline its ease of application and therefore its advantages for industrial application study cases.

Model first part requires a very limited set of effortlessly obtainable input data, that is, bearing outer (D) and bore (d) diameters, and optionally its width as well as number (z) and diameter of balls (D_b); if these two last parameters are not known from bearing data sheet, they can be respectively estimated according to (3.5) and (3.6), as reported in [11], according to bearing general proportion formulae.

$$z = 2.9(D + d)/(D - d) \tag{3.5}$$

$$D_b = 0.3(D - d) \tag{3.6}$$

After all these input parameters are set, bearing internal geometrical quantities can be computed according to general proportion formulas based only on its boundary dimensions; firstly, bearing pitch diameter D_m is assessed according to (3.7), in which d_i and d_o respectively stand for the inner and outer ring raceway contact diameter. Then the radial thickness of rings is assessed according to (3.8); afterwards, the curvature radii r_i and r_o of internal and external rings groove are estimated according to (3.9); moreover, in the hypothesis of zero radial clearance (i.e. mounting interference neglectable with respect to other bearing internal dimensions) the diameters of external and internal rings in correspondence with the raceway grooves are respectively evaluated according to equation (3.10).

$$D_m = 0.5(d_i + d_o) \approx 0.5(D + d) \tag{3.7}$$

$$t = 0.15(D - d) \tag{3.8}$$

$$r_i = 0.515D = r_o \tag{3.9}$$

$$d_i = D_m - 6 \quad d_o = D_m + 6 \tag{3.10}$$

Based on the previous bearing internal dimensions, it is possible to quantify all the parameters necessary to assess ball bearing stiffness. By defining γ according to (3.11), being α the mounted contact angle, such geometrical parameter can be interpreted as the ratio between ball diameter and bearing pitch diameter, in the case of purely radial bearings (that is, $\alpha=0$).

$$\gamma = (D_b \cos\alpha)/D_m \tag{3.11}$$

Afterwards, another intermediate parameter can be computed both for the inner and for the outer raceway, which represents the ratio between the inner and outer raceway groove radii and ball diameter. In this case, according to (3.12) a unique value for f is found as r_o equals r_i.

$$f_i = \frac{r_i}{D_b} = f_o = \frac{r_o}{D_b} = f \tag{3.12}$$

After γ and f have been computed, the curvature sum $\Sigma\rho$ can be assessed both for the inner and for the outer raceway, respectively according to (3.13) and (3.14).

$$\sum \rho_i = 1/D_b \times (4 - \frac{1}{f} + \frac{2\gamma}{1-\gamma}) \tag{3.13}$$

$$\sum \rho_o = 1/D_b \times (4 - \frac{1}{f} - \frac{2\gamma}{1+\gamma}) \tag{3.14}$$

Once these parameters have been assessed, then it is possible to estimate the curvature difference F(ρ) both for the inner and the outer raceway, according to (3.15) and (3.16), as they are defined in [11].

$$\mathrm{F}(\rho_i) = \frac{\frac{1}{f} + \frac{2\gamma}{1-\gamma}}{4 - \frac{1}{f} + \frac{2\gamma}{1-\gamma}} \tag{3.15}$$

$$\mathrm{F}(\rho_o) = \frac{\frac{1}{f} + \frac{2\gamma}{1+\gamma}}{4 - \frac{1}{f} - \frac{2\gamma}{1+\gamma}} \tag{3.16}$$

Once $F(\rho)_i$ and $F(\rho)_o$ have been computed, the dimensionless contact deformation δ^* can be obtained as a function of $F(\rho)$ as proposed by Harris [13]. It represents the non-dimensional relative displacement due to a ball-plane elastic contact which results in an elliptical contact area for a not

ideal point contact between ball and raceway. More details about this application of Hertz contact theory can be found in [11], where the trend of δ^* versus F(ρ) is reported both in graphical and tabular form for a generic raceway. By means of such correlation, δ^* can be quantified both for the inner and the outer raceway. Once δ^* is known for both raceways, the constants of load deflection to the internal and external raceway contacts, respectively denoted by K_{pi} and K_{po}, can be estimated according to (3.17) and (3.18) as proposed in [16].

$$K_{pi} = 2.15 \times 10^5 (\sum \rho_i)^{-1/2} (\delta_i^*)^{-3/2} \tag{3.17}$$

$$K_{po} = 2.15 \times 10^5 (\sum \rho_o)^{-1/2} (\delta_o^*)^{-3/2} \tag{3.18}$$

The previous formulas are valid only for the case of elastic contact between steel ball and steel raceway since they implicitly consider steel Young's modulus as well as its Poisson's ratio. Subsequently, the total load deflection factor for a single ball K_{pio}, can be computed, which is a proportionality coefficient dependent on bearing geometric as well as material properties, expressed according to (3.19), as proposed in [16].

$$K_{pio} = \left\{ \frac{1}{\left(\frac{1}{K_{pi}}\right)^{\frac{2}{3}} + \left(\frac{1}{K_{po}}\right)^{\frac{2}{3}}} \right\}^{\frac{3}{2}} \tag{3.19}$$

By denoting with ψ_i the angle between the radial load action line (that is, the moving ring displacement direction) and the radius passing through the considered ball, a line diagram of a radially loaded ball bearing is reported in Figure 3.6.

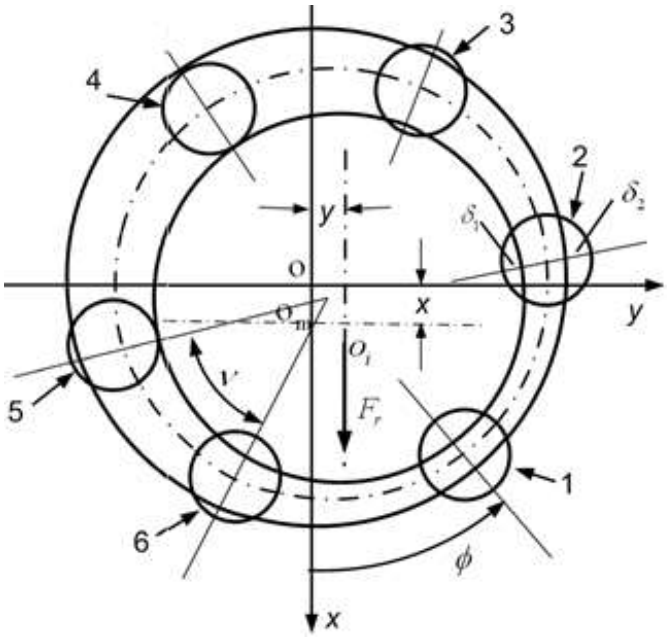

Figure 3.6 – Line diagram of a radially loaded ball bearing **[18]**

The value of ψ_i can be estimated by means of equation (3.20), where v stands for the angular step between the balls, defined as in (3.21), and Φ is the angle between x axis and the closest ball in counterclockwise direction [15].

$$v = 2\pi/z \tag{3.20}$$

$$\psi_i = \phi + (i-1)v \tag{3.21}$$

In (2.17) i depends on the number of balls z ($i=1...z$). When a given external purely radial load F_r is applied to a bearing (Figure 3.6), the resultant elastic reaction force due to the contacts of a generic ball with both raceways f_i can be expressed according to (3.22), as proposed in [15].

$$f_i = \mathrm{K}_{pio}(g + x\cos\psi_i + y\sin\psi_i)^{3/2} \tag{3.22}$$

In (3.22) g stands for the radial preloading between balls and raceways, while x and y represent the displacements of the moving ring in direction of the applied external load and in the direction perpendicular to radial one, respectively. The contribution of f_i in the direction of the applied load is then obtained by projecting it onto the action line of the external load, according to equation (3.23).

$$F_i = \mathrm{K}_{pio}(g + x\cos\psi_i + y\sin\psi_i)^{3/2}\cos\psi_i \tag{3.23}$$

The total elastic reaction force in the direction of the external load F_r is then obtained as in (3.24):

$$F_r = \sum_{i=1}^{z} F_i \tag{3.24}$$

Indeed, equation (3.24) is the summation of F_i extended to the total number of balls within the bearing. By exploiting the condition of zero elastic reaction in direction perpendicular to the elastic force, the displacement *y*, in the direction perpendicular to external load action line can be expressed as reported in (3.25):

$$y = \sum_{i=1}^{z}(g + x\cos\psi_i)^{3/2}\sin\psi_i \,/\, \sum_{i=1}^{z}(g + x\cos\psi_i)^{1/2}\sin\psi_i{}^2 \tag{3.25}$$

By substituting equation (3.25) into (3.24) and then the so obtained expression of (3.23) into (3.24), the most general formulation for ball bearing stiffness can be obtained as a function of the radial displacement *x* by deriving the so obtained expression with respect to x direction, according to (3.26):

$$k_r(x) = \partial F_r/\partial x \tag{3.26}$$

This leads to the most general bearing stiffness law expressed as a function of solely its radial deformation as reported in equation (3.27):

$$k(x) = K_{pio}\sum_{i=1}^{z}\left\{g + \cos\psi_i - \left(\frac{A}{1.5B}\right)\sin\psi_i\right\}^{0.5}\{\cos\psi_i - [(BCz - 0.5AD)/1.5B^2]\sin\psi_i\}\cos\psi_i \tag{3.27}$$

Where the expressions of variables *A* and *D*, are respectively reported in (3.28) and (3.29). whereas *B* and *C* will be mad explicit in the following since they will be the only ones relevant for the final expression of bearing radial stiffness. All of them depend only on bearing geometry as well as on its radial deformation.

$$A = \sum_{i=1}^{z}(g + \cos\psi_i)^{1.5}\sin\psi_i \tag{3.28}$$

$$D = \sum_{i=1}^{z}(g + \cos\psi_i)^{-0.5}\sin\psi_i{}^2\cos\psi_i \tag{3.29}$$

In rolling bearings the coupling effect can be commonly neglected, that is the displacement in direction perpendicular to external load is assumed null (*y=0*); moreover, a further hypothesis is introduced which leads to a simplified expression for k(x); indeed, a particular case is considered in which *Φ=γ/2*, that is, the radial load action line is aligned with the bisector of the two neighbouring balls. By imposing *y=0* in equation (2.21) the formula reported in (3.30) is obtained, which is valid only in the hypothesis of neglecting coupling stiffness effect. In this case it follows that *A* is null.

$$\sum_{i=1}^{z}(g + x\cos\psi_i)^{3/2}\ \sin\psi_i = 0 \equiv A \tag{3.30}$$

In such case the stiffness expression is strongly simplified and leads to the formula reported in (3.31).

$$k(x) = \mathrm{K}_{pio} \sum_{i=1}^{z} (g - \mathrm{x}\cos\psi_i)^{\frac{1}{2}} (\cos\psi_i - C/(1.5B)\sin\psi_i)\cos\psi_i \qquad (3.31)$$

Where the expressions of variables *B* and *C* are reported respectively in (3.32) and (3.33), while (2.21) is modified by exploiting the geometric relation $\Phi = v/2$; then, by substituting the definition of angular step reported in (2.16), the simplified relationship reported in (2.34) is obtained.

$$B = \sum_{i=1}^{z} (g + x\cos\psi_i)^{1/2} \ \sin\psi_i{}^2 \qquad (3.32)$$

$$C = \sum_{i=1}^{z} (g + x\cos\psi_i)^{1/2} \sin\psi_i \cos\psi_i \qquad (3.33)$$

$$\psi_i = \pi/z(2i - 1) \qquad (3.34)$$

Radial preloading g is defined according to (3.35). A reasonable value of this parameter needs to be assumed, since it cannot be directly found on commercial ball bearings catalogues (e.g. SKF). In the presented study case, a nominal level of 0.002mm is assumed, as it is reasonable for such class of ball bearings. In (3.35) P_d and c_r respectively stand for diametral and radial clearance. With such an assumption, a positive preloading condition is obtained, that is, g is positive and therefore the clearance is negative. This means that balls and raceways are mounted with mutual interference. Such definition of pre-loading deals only with internal preloading, while the effect of external loads is crucial in determining the equilibrium position of bearing centre and hence its current stiffness level.

$$g = -0.5P_d = -0.5(2c_r) = -c_r \qquad (3.35)$$

Basing on the previous definition, in such preloading condition, bearing non-linear stiffness can be expressed as a decreasing function when the absolute value of bearing centre deformation is less than g and as an increasing one when it is bigger than g, as proposed by Tiwari [11], according respectively to (3.36) and (3.37).

$$k(x) = a - bx^2 \ \ when\ |x| \leq g \qquad (3.36)$$

$$k(x) = \ b_1 x^{\frac{2}{3}} \ when\ |x| \geq g \qquad (3.37)$$

Initially, bearing stiffness for a radial displacement equal to zero is computed (referred to as k_0); in such case, from equation (3.37) we get $a = k_0$; k_0 is then obtained from equation (3.31) by imposing $x = 0$, thus leading to equation (3.38).

$$k_0 = \mathrm{K}_{pio} g^{0.5} \sum_{i=1}^{z} (\cos\psi_i - C/(1.5B)\sin\psi_i)\cos\psi_i \qquad (3.38)$$

In such case, the expressions of *B* and *C* reported in (3.38) are obtained by respectively replacing *x=0* in their previous definitions in (3.32) and (3.33), thus leading to the simplified constant expressions reported in the following formulae (3.39).

$$B = g^{0.5} \sum_{i=1}^{z} \sin\psi_i{}^2 \qquad C = g^{0.5} \sum_{i=1}^{z} \sin\psi_i \cos\psi_i \tag{3.39}$$

Afterwards, following the same approach described above, bearing stiffness for x=*g* can be evaluated in order to find *b* and b_1 constants respectively necessary to quantify stiffness expressions (3.36) and (3.37). Indeed, by imposing *x=g*, k_g can be computed in analogous way to k_0. Once k_g is known, *b* and b_1 can be evaluated according to the formulae reported in (3.40).

$$b = -(k_g - k_0)/g^2 \qquad b_1 = -k_g g^{-2/3} \tag{3.40}$$

It can be observed how bearing radial stiffness strongly depends on rolling elements radial preloading *g* by means of all polynomial coefficients in the two different curve sectors. Even if the constructor might sometimes provide a preload range, it is very hard to determine the accurate value of rolling elements bearing preloading in the shaft-casing assembly, particularly after wearing due to long-life operations [18].

A plot of an equivalent steel bearing radial stiffness (with the same geometric dimensions of the hybrid bearing employed to support Tesla turbine rotor, but with both raceways and balls made of stainless steel) versus its centre displacement is reported in Figure 3.7, for the maximum nominal radial preloading level, that is obtained with the maximum interference of 13μm [11].

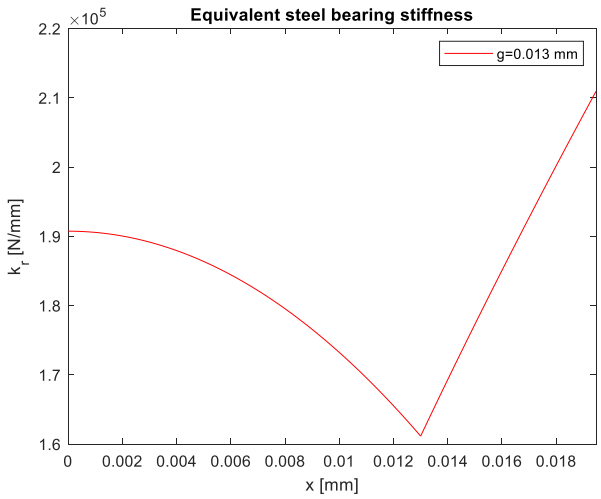

Figure 3.7 – Equivalent steel ball bearing radial stiffness as a function of its centre deflection

In such plot ball bearing radial stiffness shows a first monotonic decreasing tract until bearing centre deflection reaches radial preloading level, as expected from (3.36). Once the radial internal preload in terms of interference is overcame, then bearing stiffness shows a monotonic increasing law, as predicted by (3.37). Afterwards, the same procedure is repeated considering both the minimum allowable pre-load and a medium one (respectively set as 0.2μm and as 2μm, as suggested in [11]) to further underline the influence of g in determining bearing dynamic properties as well as to test the effectiveness of the stiffness law adopted hereinafter. The resulting plots for an equivalent steel bearing are shown in Figure 3.8.

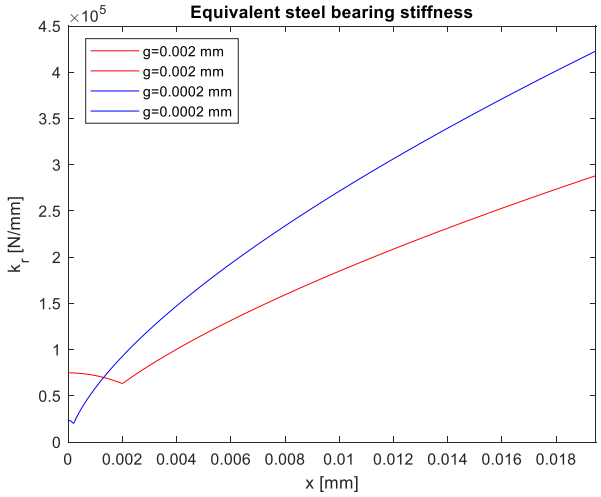

Figure 3.8 – Equivalent steel ball bearing radial stiffness for different radial pre-loadings

For the minimum radial pre-load level, bearing stiffness exhibits a trend closer to the one of theoretical case of no radial clearance; indeed, with such negligible preload, stiffness is nearly always monotonic increasing, with respect to nominal radial pre-loading condition.

In the case two surfaces in contact made up of different constituting materials (i.e. steel raceways and ceramic carbides balls), the force contact must be assessed according to Hertz contact theory in its most general way. To this aim, mechanical characteristics of both the materials must be properly set. In the employed hybrid bearings, raceways are made of steel, and hence their young modulus E_1 and Poisson's ratio v_1 are respectively set as 206GPa and 0.31, as implicitly done in [16] for steel bearings. Indeed, in equations (3.17) and (3.18) both raceways and balls are assumed to be made in steel, which justifies the value of the constant (equal to $2.15 \cdot 10^5$) in the expressions of K_{pi} and K_{po} in case of steel bearing. The most generic approach for two bodies in contact, which comes from theory of elasticity [14], gives the following expression for the contact force (3.41), where (E_1,v_1) and (E_2,v_2) are referred respectively to mechanical properties of the first and second contacting bodies. In this context, for hybrid bearings E_1 and v_1 refer to raceways (steel), whereas E_2=450GPa and v_2=0.19 deal with balls (silicon carbides).

$$F = \left\{(2^{2.5}/3)\left[\frac{(1-{v_1}^2)}{E_1} + \frac{(1-{v_2}^2)}{E_2}\right]^{-1} {\delta^*}^{-1.5}[\sum \rho]^{-0.5}\right\} {\delta_p}^{1.5} \tag{3.41}$$

In equation (3.41) δ_p stands for the deformation at the contact, F is the normal load transmitted between the contacting surfaces and δ^* is the already defined dimensionless contact deformation. By comparing equation (3.41) with the expression of contact force for linear radial stiffness theory of rolling bearing reported in (3.42), then the generic formula of load-deformation contact for a single point contact for hybrid ball bearings is obtained by dividing it for $(\delta_p)^{3/2}$, thus leading to equation (3.43).

$$F = K_p \, {\delta_p}^{1.5} \tag{3.42}$$

$$K_p = \left\{\left(\frac{2^{2.5}}{3}\right)\left[\frac{(1-{v_1}^2)}{E_1} + \frac{(1-{v_2}^2)}{E_2}\right]^{-1} [\sum \rho]^{-0.5}(\delta^*)^{-1.5}\right\} \tag{3.43}$$

If one applies equation (3.43) to the inner and outer ball-raceway contacts, the same expressions previously reported for K_{pi} and K_{po} are obtained, apart from the value of the constant A_0 which in case of hybrid bearings is different from the one adopted in [16]. This can be shown by grouping the constant part of (3.43). If one substitutes (3.44), then rearranging (3.43) gives the generic expression of K_p for ball bearings, as shown in (3.45). Then, this equation can be particularized both for the inner and for the outer ring contact leading to expressions formally identical to equations (3.17) and (3.18).

$$A_0 = \left(\frac{2^{2.5}}{3}\right)\left[\frac{(1-{v_1}^2)}{E_1} + \frac{(1-{v_2}^2)}{E_2}\right]^{-1} \tag{3.44}$$

$$K_p = A_0 \, [\sum \rho]^{-0.5}(\delta^*)^{-1.5} \tag{3.45}$$

Indeed, by substituting steel average mechanical properties (v_1=v_2=0.31 and E_1=E_2=206GPa) into (2.37) leads to A_0≈2.15*10^5MPa, which gives exactly expressions (3.17) and (3.18) to assess K_{pi} and K_{po} for steel bearings.

In the following, hybrid bearings radial stiffness versus its centre deflection is presented in the same way as for steel ones. In particular, in Figure 3.9 radial stiffness is plotted only for the minimum and medium allowable bearing internal pre-load. Such trend proves even in this case the effect of bearing radial pre-load in influencing bearing stiffness even for hybrid bearings, as stated in [18].

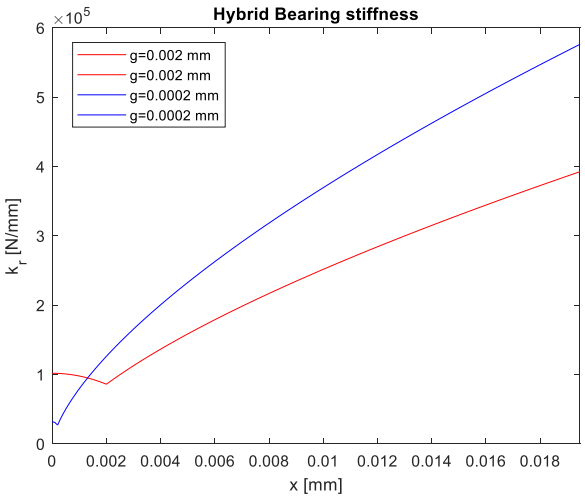

Figure 3.9 – Hybrid ball bearing radial stiffness for different radial pre-loadings

Indeed, the obtained trends are analogous to the ones computed for the equivalent steel bearing, but the average stiffness is bigger, as expected. As a matter of fact, in Figure 3.8 and Figure 3.9, two curves are plotted for the same radial pre-loads, and the ones referred to the hybrid bearing (Figure 3.9) are shifted towards bigger stiffness with respect to the ones referred to the equivalent steel bearing (Figure 3.8). Indeed, for $x=0$, it is easy to assess that an hybrid bearing is stiffer than a geometrically equivalent steel one, and then such difference is kept for each value of bearing center deflection, being equal the trend for hybrid and metallic bearings (that is, only the constant A_0 is different for the two cases, as already stated).

Finally, the medium value is assumed for hybrid bearing radial pre-loading to perform numerical modal analysis . With such stiffness law, ball bearing elements are modelled in Ansys® environment.

3.4 Comparison of experimental and numerical results

In this section, the obtained experimental results will be shortly presented and compared with the ones coming from rotor-bearings systems theoretical models in which the non-linear stiffness bearing model is adopted. The first results deal with RK since they are the most simply interpretable, both numerically and experimentally, as they come from analytic rotor system model combined with metallic ball bearings non-linear stiffness model. Once ball bearing stiffness non-linear model has been validated on the RK, it will be applied to FE models of industrial rotating machinery, namely a micro-gas turbine and a bladeless turboexpander (air Tesla turbine) mounted on hybrid ball bearings, as they represent two practical cases of respectively stubby and slender rotors, mounted on different kind of ball bearings (dimensions, materials, and mounted contact angle in case of spindle bearings).

3.4.1 One DOF analytical model applied to RK

The rotor system model of the RK4 test rig is firstly studied according to classical one DOF Jeffcott model by assessing ball bearing stiffness by means of the analytical model detailly described above.

In the first part of the script implemented in Matlab® environment, bearing and shaft geometry are described by means of the minimum number of required parameters. Refer to previous section for bearing input data required, whereas for the shaft only its length and diameter together with constituting material is sufficient in the case of the RK. Indeed, this is the reason why it has been chosen as the first test bench to validate the employed bearing stiffness model, since it has a simple geometry constituted by a unique material, differently from industrial rotating machinery that will be presented at the end of this chapter. Moreover, it is possible to quantify rotor residual mechanical unbalance, whereas in industrial rotating machinery an assumption on the degree of balance is necessary to assess somehow the rotating force acting on the supports together with shaft static load. In the second part of the script ball bearing stiffness on which the RK is mounted is assessed according to the non-linear model, whereas shaft bending stiffness is assessed by means of elastic beam formula supported by two hinges, according to equation (3.46), as well-known from linear elasticity theory.

$$k_F = \frac{48EI_z}{L^3} \qquad (3.46)$$

Where E is Young modulus of the material constituting the shaft (assumed to be 210GPa as the shaft is made up of stainless steel), I_z stands for shaft section area quadratic surface moment and L for shaft length (bearing center to center distance, equal to 150 mm). According to Jeffcott rotor model the shaft is assumed to be massless, and all its mass is reduced in the flywheel; such assumption is coherent with the adopted experimental model since the fly-wheel mass placed at shaft midpoint is heavier (weight 0.8 kg) than real shaft distributed mass. Finally, the resulting system flexural stiffness k_{eq} is obtained by assuming the two ball bearings as two non-linear springs working in parallel, whereas the shaft is modeled as a (linear) spring of constant stiffness in series with the bearings, according to equation (3.47).

$$\mathrm{k}_{eq} = \frac{2k_B * k_F}{2k_B + k_F} \qquad (3.47)$$

Where k_F stands for shaft stiffness and k_B represents bearing stiffness. In the experimental activity conducted on the RK, the mechanical unbalance has been firstly reduced as much as possible, by means of balancing masses mounted on the holes in the fly-wheel mass (refer to Figure 3.10); after the rotor has been balanced in this way, it is possible to set static unbalance to an adjustable value. In the present context, the aim is to impose a rotating force acting on the bearings; to this goal, the unbalance mass phase is not so important as in rotor balancing process, and then the desired static unbalance is obtained by adding a further mass of 0.2 g. in this way the mechanical unbalance is set to 1 g*mm. indeed, RK diameter is 5 mm, and then it is possible to assess the rotating force acting on

the supports. This is needed to make a balance between bearing non-linear restoring force and rotor centrifugal force due to mechanical unbalance plus its total weight which gives back bearing center radial displacement, which is necessary to compute bearing stiffness according to the presented model. Such procedure will be explained more in detail for the practical industrial study case examined hereinafter.

Figure 3.10 – Fly-wheel mass with holes for balancing masses

System first flexural critical speed is then obtained according to the classical formula reported in equation (3.2). RK4 shaft is mounted on ball bearings of the following characteristics (essential input data required for the code):

- Bearing external diameter D=35 mm
- Bearing internal diameter d=10 mm
- Bearing thickness s=11 mm
- Number of balls z=6

The experimental results are briefly reported in terms of both accelerometer and proximity probes 1X order RMS value and a critical speed is detected by both the sensor at around 8912 rpm (refer to Figure 3.11). The theoretical prediction is close to the obtained experimental result in this first case; indeed, a numerical critical speed of 8107 rpm is found which underestimates the experimental value by roughly 800 rpm thus leading to about 10% relative error in critical speed assessment.

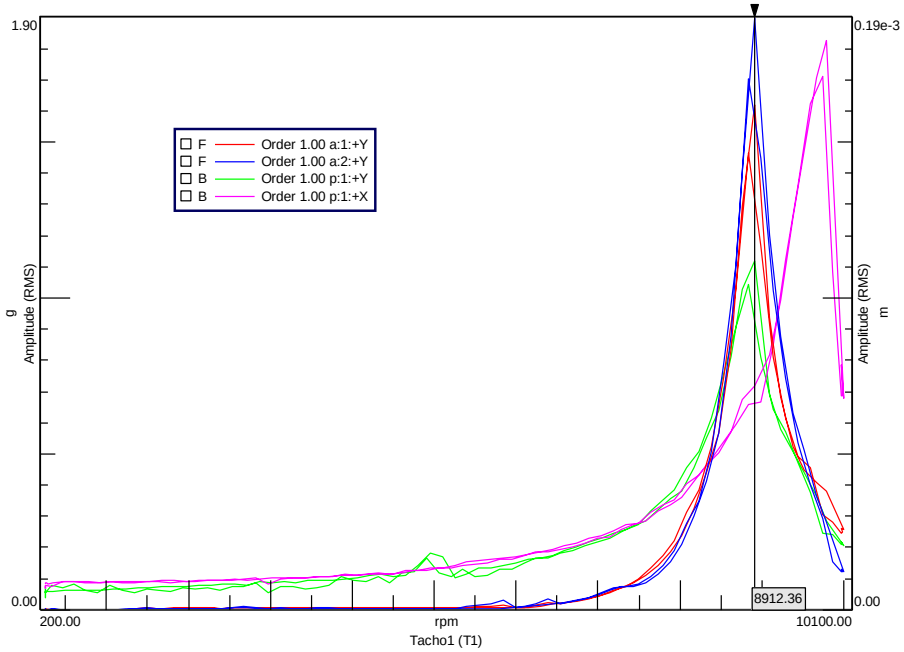

Figure 3.11 – 1Xrev RMS value of accelerometer and proximity sensors mounted on the RK

In the next section the results obtained from the four DOFs model are presented for completeness.

3.4.2 Four DOFs analytical model applied to RK

In this section system critical speed is assessed by means of the 4 DOFs Jeffcott rotor model. The reference experimental results are the same and the procedure remains unchanged apart from formulae complexity. Rotor geometry is the same, but this time inertia moments of the flywheel are kept in account, thus making the model more realistic. Also the employed ball bearing is the same but its stiffness becomes bidirectional, even if it is assumed to be equal in the two orthogonal axes. This hypothesis of isotropic supports leads to a bearings stiffness matrix with null terms out of the main diagonal, as it will be clear from its formula. Moreover, shaft rotational axis is assumed to be coincident with one of flywheel inertia main axes (*z* axis) in system undeformed configuration. In the first part of the script implemented in Matlab® environment, system geometry is described, and with respect to 1DOF model flywheel inertia moments are computed according to the following equations (3.48).

$$I_z = \frac{1}{2} m({r_1}^2 + r_2^2)$$

$$I_x = I_y = \frac{1}{12} m(3 * ({r_1}^2 + r_2^2) + h^2) \qquad (3.48)$$

Where m stands for flywheel mass (0.8 kg), r_1 and r_2 are respectively flywheel internal (5 mm) and external radii (37.5 mm), and h is flywheel thickness (10 mm). The cylindric shaft is assumed to be massless and its surface quadratic moment is computed according to the following equation (3.49)

$$J_z = \frac{1}{64}\pi D^4 \tag{3.49}$$

Where D is shaft diameter (also equal to internal flywheel and bearing internal diameters). The general expression of bearing stiffness matrix is obtained as follows, but in this context, we assume $k_1=k_2=k_B$. In analogous way to the 1 DOF case, this is the contribution to system overall stiffness due to only bearings flexibility, whereas shaft stiffness matrix represents solely the rotor flexibility. Indeed, in the hypothesis of linear elastic theory the effects can be superimposed, as previously done for the 1 DOF model. Moreover, bearing non-linear stiffness law can be linearized around an equilibrium position, and in this case the scalar value of k_B is assumed to be the same of 1 DOF case.

$$K_B = \begin{bmatrix} k_1 + k_2 & -k_2 c + k_1 c \\ -k_2 c + k_1 c & k_1 c^2 + k_2 c^2 \end{bmatrix} \tag{3.50}$$

Where k_1 and k_2 are bearing stiffness respectively in directions x and y and c is the distance between bearing and system center of mass (that is, half of shaft length). Therefore K_B becomes as follows:

$$K_B = \begin{bmatrix} 2k_B & 0 \\ 0 & k_B L^2/2 \end{bmatrix} \tag{3.51}$$

Once bearing stiffness matrix K_B has been computed, then shaft stiffness matrix K_S can be assessed according to equation (3.52), which holds for an elastic beam supported by two rigid hinges.

$$K_S = \frac{EJ_z L}{c(\mathrm{L} - c)} \begin{bmatrix} 12\dfrac{L^2 - 3cL - 3c^2}{c(\mathrm{L} - c)} & -6\dfrac{L - 2c}{c(\mathrm{L} - c)} \\ -6\dfrac{L - 2c}{c(\mathrm{L} - c)} & 4 \end{bmatrix} \tag{3.52}$$

Finally, in order to assess the resulting system stiffness matrix K_{eq}, the same procedure is followed, that is, the two ball bearings are regarded as two springs working in parallel, while the shaft is thought as a further spring in series with the bearings. In this case, such equivalent stiffness matrix is obtained by multiplying element per element of each matrix at the numerator, as reported in equation (3.53) according to Matlab syntax.

$$K_{eq} = \frac{K_c .* K_a}{K_c + K_a} \tag{3.53}$$

Once system equivalent stiffness matrix has been computed, its critical speed can be assessed by means of the following formula, reported in equation (3.54).

$$W_{cr} = \sqrt{\frac{K_{11}(J_p - J_t) - mK_{22} \pm \sqrt{\left[K_{11}(J_p - J_t) + mK_{22}\right]^2 - 4m(J_p - J_t)K_{12}^2}}{2m(J_p - J_t)}} \quad (3.54)$$

Where m stands for system total mass, K_{ij} represent the elements of K_{eq} whereas J_p and J_t respectively represent flywheel polar inertia moment (previously referred to as I_z) and transversal one (previously referred to as I_x, equal to I_y due to symmetry). The obtained results in terms of predicted critical speed are close to the 1 DOF case, with a significant complication in terms of coding.

3.4.3 FE model applied to air Tesla turbine

In technical literature there are still few papers dealing with Tesla turbine rotordynamics. The research activity performed in [12] deals with the validation of a dynamic simulation by means of experimental results about the vibrational rotordynamic response of a Tesla turbine tested in simplified working configurations.

This section is structured as follows: firstly, the rotordynamic experimental results coming from a 3kW air Tesla turbine installed at a suitable test rig operating in generation mode are briefly presented. Afterwards, the numerical model of air Tesla turbine rotor-bearings system based on beam elements is explained in detail. Finally, the obtained results coming from such reduced FE model, in terms of numerical modal analysis, are compared with system experimentally detected critical speeds.

The investigated air Tesla turbine is characterized by the geometric characteristics reported in Table 3.1. Its rotor is made up by several flat, smooth disks with a central opening for exhaust flow. A constant gap between neighboring disks is ensured by employing suitable spacers. The whole shaft is supported by hybrid ball bearings placed at the ends of the generator, while the turbine is mounted cantilever architecture [12].

Table 3.1 – Tesla turbine geometric characteristics

Air Tesla turbine	
Outer diameter of disk, mm	120
Inner diameter of disks, mm	60
Number of nozzles	1, 2 and 4
Gap between disks, mm	0.1
Disk thickness, mm	0.1
Number of disks	120
Nozzle angle, degree	2.2
Type of nozzle	Convergent

A suitable test rig had been already employed to characterize Tesla expander rotordynamic performance, and it is reported in Figure 3.12. Such experimental test bench is made up by both an expander and a high-speed generator within a single casing, an adequate turbine casing support, an air feeding system and mass flow controllers together with a power dissipation system.

A high-speed generator is employed to apply load on the turbine by keeping a constant angular speed. The mechanical power extracted by the turbine is converted in heat by means of thermal load resistor. Turbine air supply is obtained by means of suitable connection lines which are derived from the three mass flow controllers. Such mass flow controllers are employed to supply the wished air quantity into the turbine acting by remote. Stator and rotor design allow to modify some parameters to assess their effect on turbine performance. Moreover, it is possible to tune the number of disks, the interposed gap between them and nozzle geometry without modifying the other turbine elements. Finally, the whole casing is supported by means of four springs which are connected to a main supporting frame. Such configuration makes possible an easy access to all air feeding lines through eight ports and allows to significantly decouple turbine operating vibrations from the ones of its support frame.

The employed measurement system relies on several sensors to detect machine characteristic curves. In this context, focus is stressed mainly on rotordynamic measures, so that only the probes which are not related to the machine performance experimental characterization are described hereinafter. In particular, accelerometers and a tachometer (i.e. phase sensor) are the only essential sensors to conduct an experimental rotordynamic analysis; in this case, a triaxial accelerometer (with a nominal sensitivity of 10 mV/g) is placed on machine casing close to bearing housing, while a photoelectric phase sensor (with a response time of 200 μs for full output) is located facing machine rotor to detect its angular speed. The following Figure 3.12 reports in detail probes placement in the investigated test rig. In such simplified tested configuration, the machine is mounted on hybrid bearings, that is, rolling bearings whose raceways are made of steel while the balls are made in ceramic materials (in this specific experimental study case Tesla turbine is furnished with silicon carbides hybrid bearings).

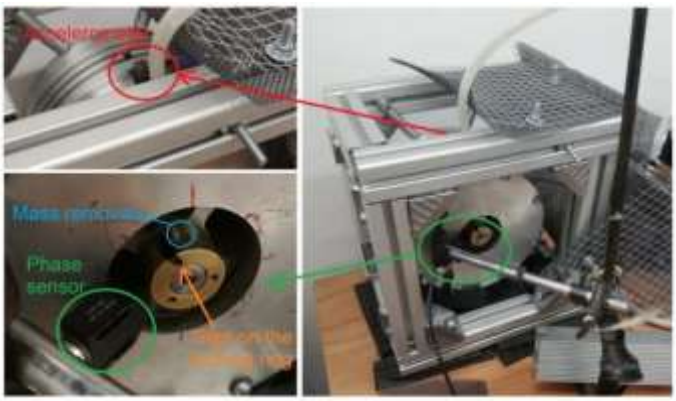

Figure 3.12 – Accelerometer and phase sensors placement

The employed acquisition system is based on Siemens Scadas to allow high frequency sample rate. In Figure 3.13 the trends of the two first engine orders detected by the accelerometer are reported in terms of their root mean square (RMS) values. The two considered order trends exhibit an amplitude peak ascribable to a rotor-bearings system resonance at about 545Hz; indeed, order 1Xrev amplitude trend shows a significant energy increase when the turbine speed approximates 32700rpm, whereas order 2Xrev increases its energy at around 32990/2=16495rpm. This confirms that a rotor-bearings system critical speed is identified, since both the considered orders can significantly amplify system vibrational response in correspondence with one of its flexural natural pulsation frequencies. Indeed, order 2 is characterized by lower energy with respect to order 1, and this agrees with rotating machinery theory which states that "secondary critical speeds", that is, the ones excited by order 2 are less dangerous than primary ones (that is, system critical speeds excited by order 1), which are commonly referred to as "critical speeds". However, in this context order 2 trend is reported only with the aim to prove that a system critical speed is actually excited: the amplitude peak due to 2X is not relevant in overall system vibrational response. Finally, in the graph the critical speed is not shown since the machine was stopped before reaching it in order to avoid mechanical damages

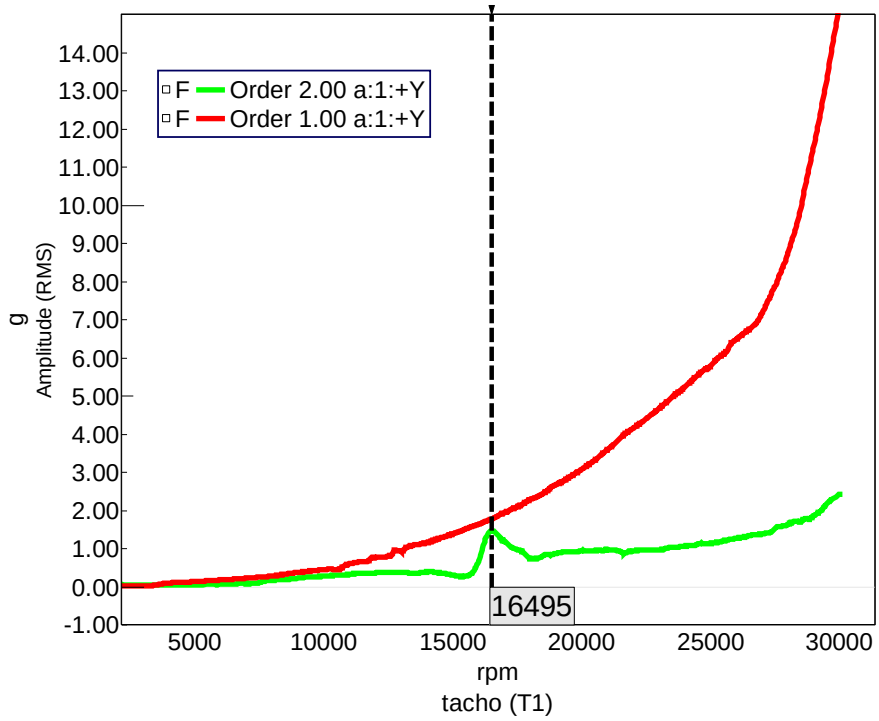

Figure 3.13 – Accelerometer 1X and 2X engine orders analysis

The devised FE model based on beam elements is presented in detail hereinafter. The tested rotor-bearings system is modelled in Ansys® environment by exploiting several type of lumped parameter elements, in order to ensure low computational costs and ease of application. On the other hand, if

one wishes to properly consider the effects of both distributed inertia and stiffness of the actual system, some preliminary assumptions must be clearly stated; indeed, the weight of such simplifying hypothesis will unavoidably lead to some discrepancies with experimental data, but this is known a priori. Tesla turbines are complex fluid machines made up of a large stack of thin disks [12], whose structural dynamic behaviour cannot be simply studied as an equivalent lumped inertia and neither as a simple disk, with the others behaving in the same way, as proposed in [17]. Nonetheless, it is possible to investigate in a simplified way Tesla turbine rotordynamic behaviour in some regions of its whole operating range; indeed, it is somehow reasonable that when disks vibration modes are characterized by natural frequencies far from the whole rotor-bearings system ones (since Tesla turbine disks are very thin while the motor shaft is stubby), one can separate disks vibration modes effects with respect to rotor modal shapes; indeed, in this context, rotor assembly is modelled as an equivalent beam with lumped inertias representing the disks. However, only in the low frequency region rotor and disks modal shapes can be thought as decoupled, while at higher ones (i.e. above rotor assembly first critical speed) disks stack dynamics becomes intrinsically coupled with rotor assembly one. In this context, attention is stressed in correctly predicting rotor-bearings system critical speed as a whole, thus it is allowable to neglect disks modal shapes and focus on assembly natural frequencies substituting Tesla turbine thin disks with equivalent lumped inertias.

In the following, a list of the main components of the investigated air Tesla turbine together with the equivalent lumped inertia and stiffness elements proposed to model the actual system is given in detail. Before of doing such a modelling of the bladeless turboexpander, all the element types employed in the FE analysis in Ansys® environment are presented and their characteristics are emphasized. The FE model of the whole rotor is made up with beam elements, equivalent lumped inertias and masses and finally even with hybrid ball bearings stiffness assessed in section 2; in numerical modal analysis within Ansys®, stiffness is required as a constant parameter; to overcome this issue, an equilibrium position for bearing centre is found between shaft external loads and bearing non-linear restoring force according to equation (3.55). External load is assumed to be equally distributed in the two bearings. Further assumptions are necessary to suppose rotor eccentricity *e*, as it is not an easily measurable quantity. Basing on workshop data, Tesla turbine has a degree of balance G equal to 0.1. By means of ISO 1940-1 [19] one can obtain *e*, for each angular speed below system first critical speed, as it relies on the hypothesis of rigid body (valid only far from rotor flexural critical speeds). In the present context, an average *e* is assumed below the expected system first critical speed (based on previous FE simulations) for nominal Tesla turbine angular speed. By doing so, the cubic equation (3.55) is solved in terms of *x*, and the only real positive solution is selected as physically meaningful.

$$\frac{m\omega^2 e+mg}{2} = kx => \frac{m(\omega^2 e+g)}{2} = (ax - bx^2)x \tag{3.55}$$

Subsequently, according to the obtained current bearing centre deflection, radial stiffness is assessed according to either equation (3.33) or (3.34). Such obtained value is then set in Ansys® to perform rotor-bearings system numerical modal analysis.

The employed elements in Ansys® to model the investigated physical system are mainly BEAM188, MASS21, COMBIN14, TARGE170 and COMBI240. As already mentioned, BEAM188 elements, which rely on analytical shape functions, are the fundamental structural entities in place of solid elements previously employed in other Tesla turbine structural models [17]. They are based on Timoshenko beam theory, that is, shear-deformations effects are not neglected, and represent the most recent element developed in Ansys® to model three-dimensional beams. In this context they are used to model turbine shaft together with its other main rotating structural elements. Then, MASS21 elements are employed as they stand for lumped mass elements, in order to model the equivalent inertia moments of the disk stack and of other assembly components. COMBIN14 are spring-damper elements with no mass, that is, without any inertial properties, which are employed to place lumped stiffness effects (in this context only spring capability is enabled, while damping one is disabled) in order to model equivalent stiffness of assembly components regarded as lumped parameters elements (e.g. disk stack flexural properties). COMBIN214 are two-dimensional spring-damper bearing elements, which are similar to COMBIN14 ones, but they are more suitable to deal with bearings, and hence they are used to model hybrid bearings. Finally, TARGE170 elements are used to model contacts (due to friction between rotating and frame-fixed parts) , and in particular frictional ones, for example to couple shaft surface within the bearing (even if in this case this contact is set as bonded, that is, frictionless, but this element is anyway necessary to close the model and make it run).

Regarding the mesh, in numerical modal analysis, it is well-known that the minimum element dimensions must be set in such a way that the maximum frequency of interest can be detectable []; in this context, mesh refinement is then chosen in order to be able to capture at least up to the expected first system critical speed.

In the following, a brief explanation of how beam-based model is devised and in particular a justification of the division between different beam elements, due to geometrical or constituting materials discontinuities is discussed. In Figure 3.13 a sketch of beam subdivision is shown for clarity.

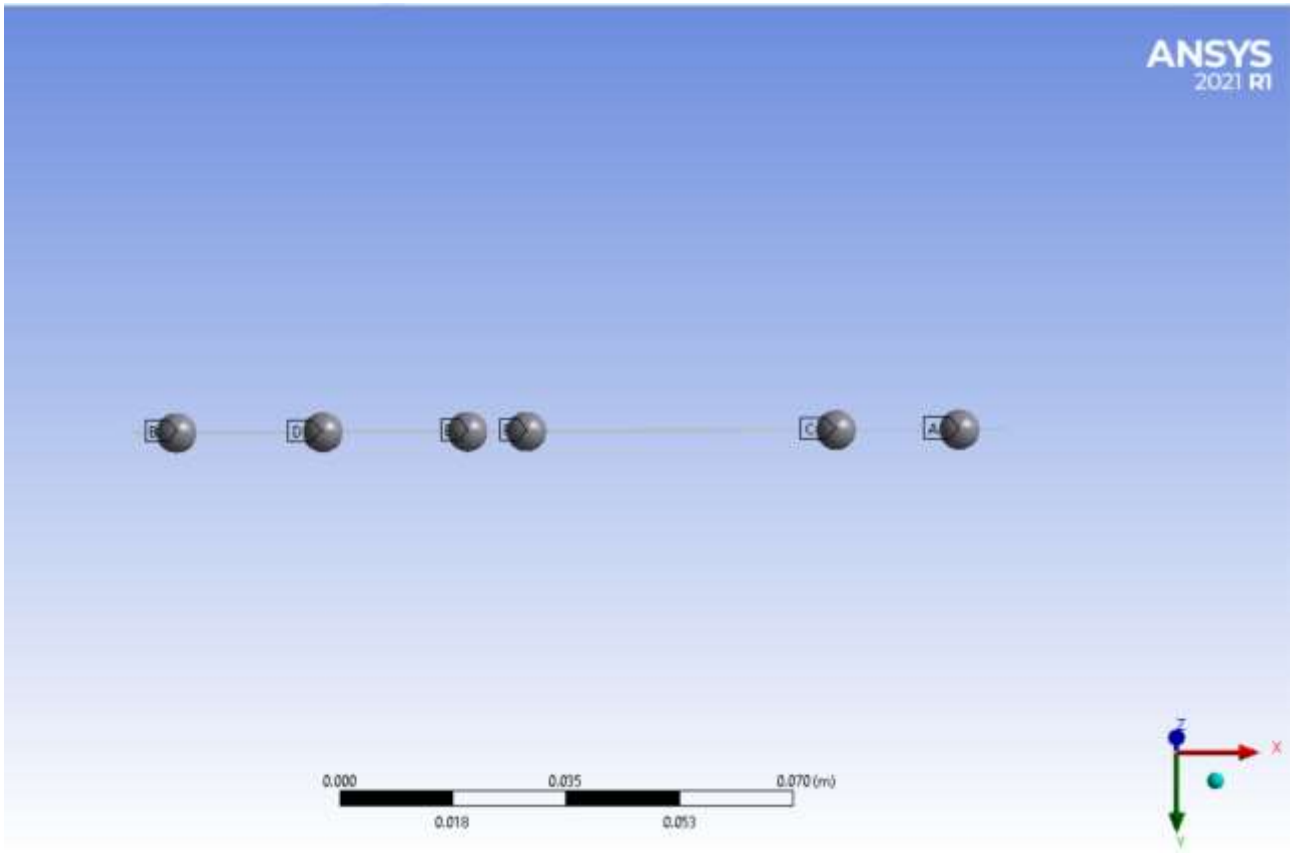

Figure 3.13 – Beams subdivision of simplified Tesla turbine structural model

Firstly, equivalent inertial properties for the two ferrules (depicted as A and B in Figure 3.13), for the disks stack (denoted by C in Figure 3.13), for the short bushing (denoted by D in Figure 3.13), for the electrical generator rotor (data sheet of mechanical properties by the constructor, denoted by E in Figure 3.13) and for the long bushing (denoted by F in Figure 3.13) are set basing on real components dimensions as well as on mechanical properties of their constituting materials. Subsequently, the shaft line is divided into segments which correspond to beam elements whose cross section inertial properties uniform, according to real system properties. Starting from the left side in Figure 3.13, the first beam starts from turbine discharge side and covers the length of the first ferrule. The second beam goes from the first ferrule barycentre and ends with the disks stack centre of mass. The third beam starts with the end of the disks stack and ends with the beginning of the flush. The remaining part of the shaft has a same diameter but needs to be divided into different beams because of constraints (bearings and bushings). Indeed, its structural model is made up by different beams: the first one starts from the flush and arrives to the first bearing on the turbine side. The second one goes from this bearing to the long bushing centre of mass. The third one starts from the long bushing barycentre and ends with the generator rotor centre of gravity. The fourth arrives to the short bushing centre of mass. The fifth goes from the short bushing barycentre until the second bearing. Finally, the

sixth part arrives to the second ferrule, while the last one covers the entire length of the second ferrule (on the left of B in Figure 3.13).

In the following, the obtained numerical results are presented in terms of Campbell diagram in order to assess numerically predicted critical speeds. In Figure 3.14 such diagram is reported for the simulated rotor-bearings system. Campbell diagram presents in the abscissa system actual rotational speed whereas on the ordinates system natural frequencies are reported. When the so modelled rotor assembly is excited by an operating forcing (that is, when the system is rotating) it is excited by synchronous frequency due to mechanical residual unbalance which could match some of system natural flexural frequencies. In this case, torsional and axial natural frequencies are at higher levels.

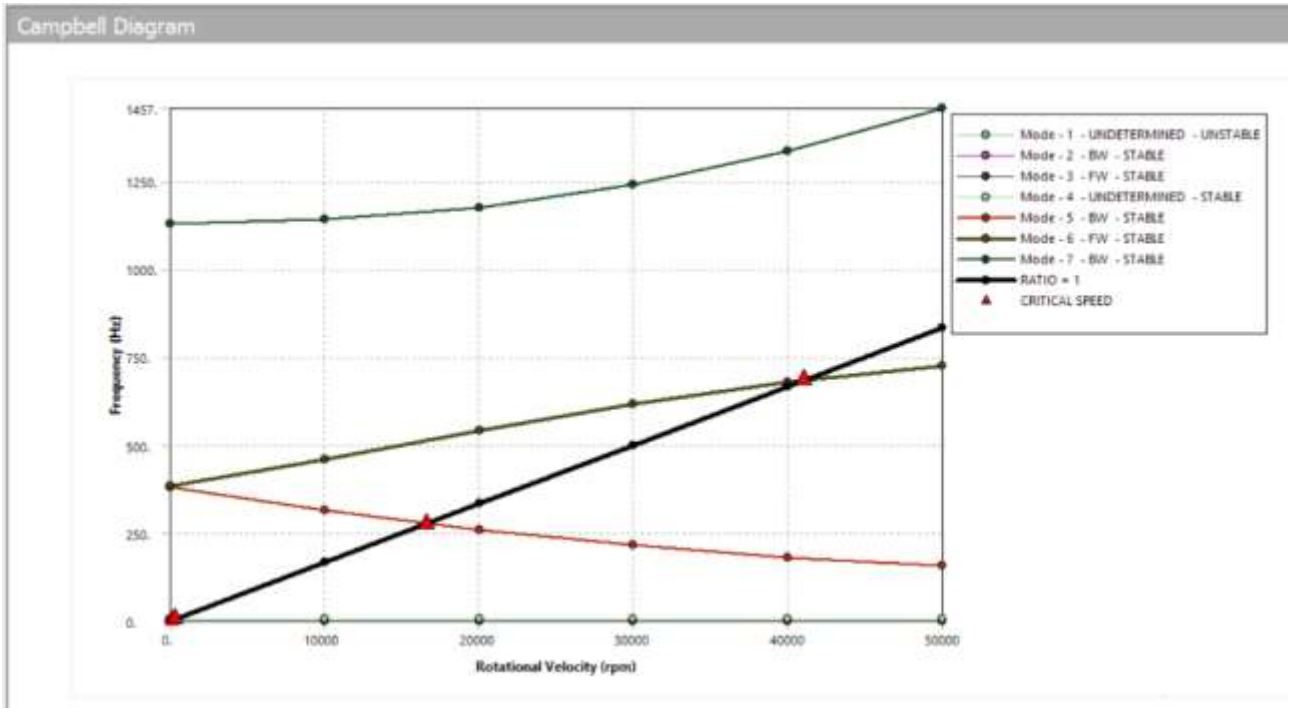

Figure 3.14 – Campbell diagram of the modelled Tesla turbine

From such plot a pair made up by backward whirling mode together with a forward whirling one which are excited by synchronous frequency (i.e. 1X engine order). Nonetheless, only the forward mode can be excited because it is in phase with the operating force, and hence this intersection represents the only excitable system critical speed. Both of such critical speeds are associated to an out of plane modal shape, that is, these vibration modes are due to Coriolis acceleration effect. The modal shape related to such identified vibration mode natural frequency (that is, critical speed divided by twice PI Greek) is reported in Fig. 3.15.

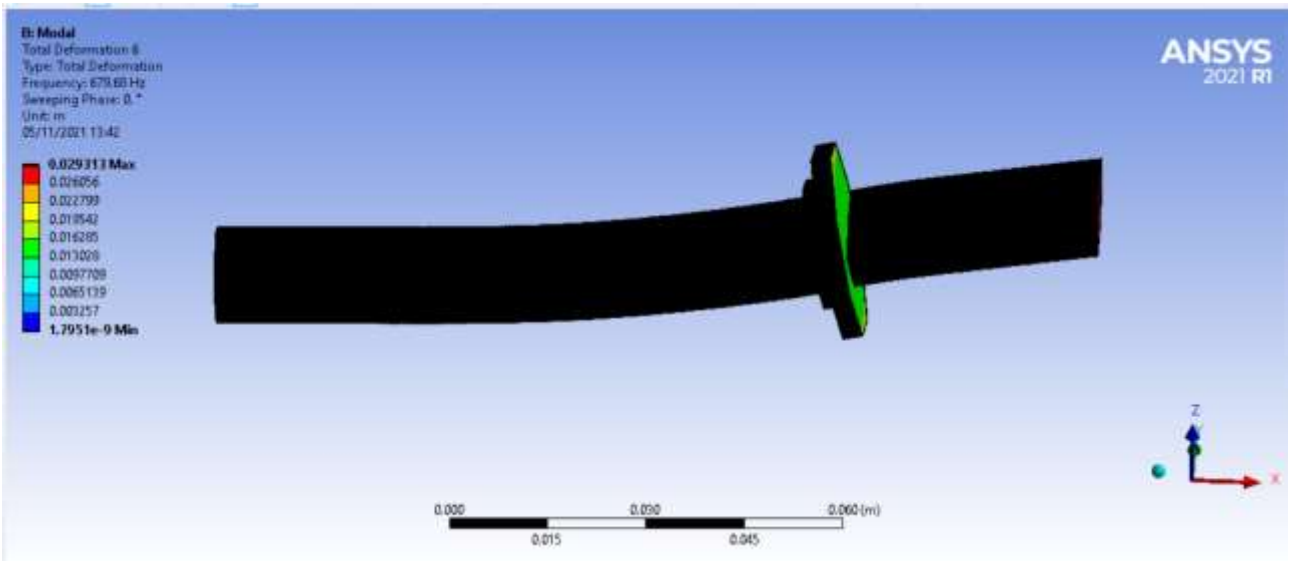

Figure 3.15 – Modal shape associated to system first vibration mode

Numerical modal shape associated with the equivalent rotor-bearings system first critical speed is characterized by only one node, and this is coherent with the first bending vibration mode, whose associated modal shape typically presents two antinodes, as for analytical solutions of unifilar study cases. The correlation between simulations and experimental results obtained with hybrid bearings is overall good, even if numerical results are not perfectly in agreement with experimental ones; this minimal mismatch in critical speeds prediction can be ascribable both to the beam-based FE model employed, which causes a stiffer behavior of the rotor with respect to solid elements, and to a partial uncertainty in bearing stiffness determination, which is mainly due to bearing radial pre-loading assessment.

3.4.4 FE model applied to microturbine

In this section bearing non-linear stiffness model is applied to an industrial microturbine mounted on metallic ball bearings in order to perform system numerical modal analysis. In this case, shaft geometry and materials are more complex than in the previous ones, therefore system structural modeling is not trivial, and several rotor models are devised with an increasing level of complexity in order to faithfully reproduce its experimental behavior. Moreover, the procedure is similar but as for the Tesla turbine, since an aprioristic assumption on residual mechanical unbalance must be done, because the degree of balancing given by the manufacturer is not always reliable and varies with machine usage time. Such microturbine is manufactured by the company “Advanced MicroTurbines S.r.l.”, a spin-off from the Italian Institute of Technology (IIT) and it is fed by compressed air ; indeed, it is employed for energy harvesting in those applications where pressure energy is available but it is typically dispersed in the environment, like in security valves where the energy is commonly wasted. Due to confidentiality issues, in the present section turbine exact dimensions and quantitative

drawings are not presented in detail, but anyway qualitative sketches are presented to illustrate its geometry. The microturbine system is made up by a fluid dynamic part, which converts fluid pressure energy in rotational motion, and by an electric one, which converts the extracted mechanical power into electric one. The fluid dynamic part is mainly made up by an aluminum rotor furnished with blades and stator channels which address the flow in the rotor. A picture of this part is reported in Figure 3.16, which gives an idea of microturbine dimensions with respect to a common coin.

Figure 3.16 – Detail of microturbine fluid dynamic part

The electric part is made up by a cylindrical permanent magnet, generator stator coils and external regulation electronics. Indeed, the peculiarity of such microturbine is that it carries out in only one component the typical duty of two different components, that is, turbine and generator ones, thus leading to a more compact design. Microturbine rotor is supported by two conventional ball bearings of small dimensions which are manufactured ad hoc for this application; indeed, they are customized in such a way that the rotor can reach and go beyond angular speed up to 100000 rpm. Their dimensions are not reported due to confidentiality but the procedure to assess their stiffness is identical to the Tesla turbine case. They are mounted in a purely radial configuration as in the RK. The system made up by mechanical stator and rotor and by electric stator is shown in Figure 3.17, where it is contained within an aluminum compact cover clearly visible in the picture.

Firstly, experimental results in terms of system first flexural critical speed are briefly presented and afterwards the employed models are shortly described in order to compare their predictions with experimental outcomes.

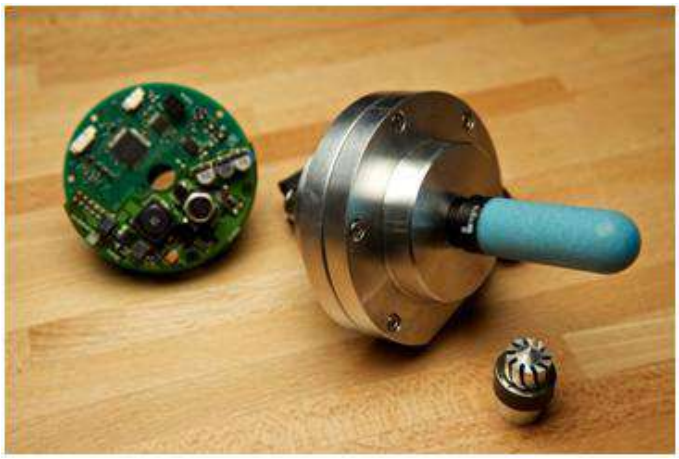

Figure 3.17 – Electronic board and aluminium cover of the microturbine

An experimental modal analysis of the microturbine had been previously performed by means of the impact technique in order to identify vibration modes of both the rotor and the frame. By relying on the hypothesis on system linearity, the reciprocity principle can be assumed and therefore "rowing hammer" technique is applied, that is, system response is detected by means of accelerometers located at structure points of interest while the instrumented hammer is exploited to obtain an impulsive excitation in each point of the experimental mesh. Such preliminary experimental activity had been carried out by means of a "Bruel & Kjaer" mono-axial accelerometer and a PCB modal micro-hammer furnished with load cell to at its end to detect the applied force and then to compute structural experimental FRFs. Data acquisition and processing system employed is the portable LMS Roadrunner Mobile which is suited for measurements on the field. Moreover, in order to better detect the onset of experimental critical speeds in run-up and coast-down tests, two PCB triaxial accelerometers are employed to acquire system response in three orthogonal directions at the same time. The employed digital processing and measurements elaboration software is LMS Test Lab, as in all the presented experimental campaigns. The triaxial accelerometers are placed at microturbine discharge zone and at the fluid inlet area, as observable in Figure 3.18, and the ramps are acquired while the machine is simulating a typical working condition. In this way, a more realistic behavior with respect to the experimental modal analysis previously conducted with the shaft stopped is detected that will be compared with numerical FE simulations.

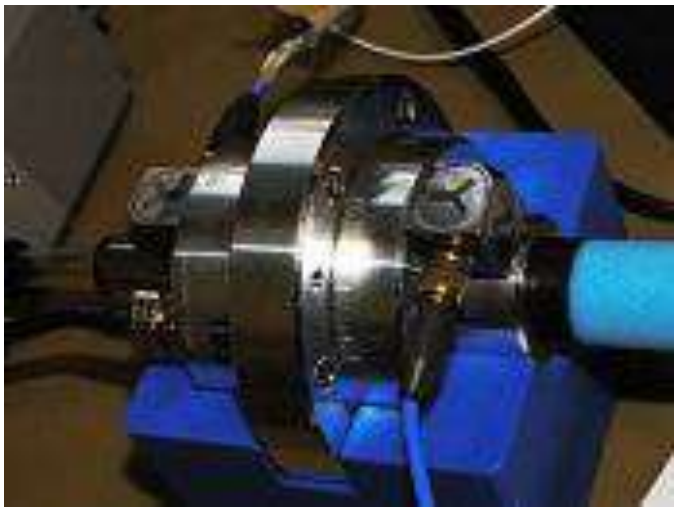

Figure 3.18– Instrumented microturbine for run-up test acquisitions

Only the experimental results related to the acquired microturbine ramps are presented since they represent the most interesting and directly interpretable ones. In particular, the trends of the first engine order (1X) detected by the two employed triaxial accelerometers are reported in Figure 3.19 in terms of their amplitude. From the reported graph it is clearly identifiable a rotor-bearings system mechanical resonance at around 64000 rpm, which is excited by the synchronous frequency (1X) that induces vibrations characterized by significant amplitude which are detected by both the sensors in all the directions. It is interesting to observe that accelerations amplitude detected by the accelerometer located at the turbine discharge are bigger in the components along X and Y axes with respect to the vibration amplitude along Z axis.

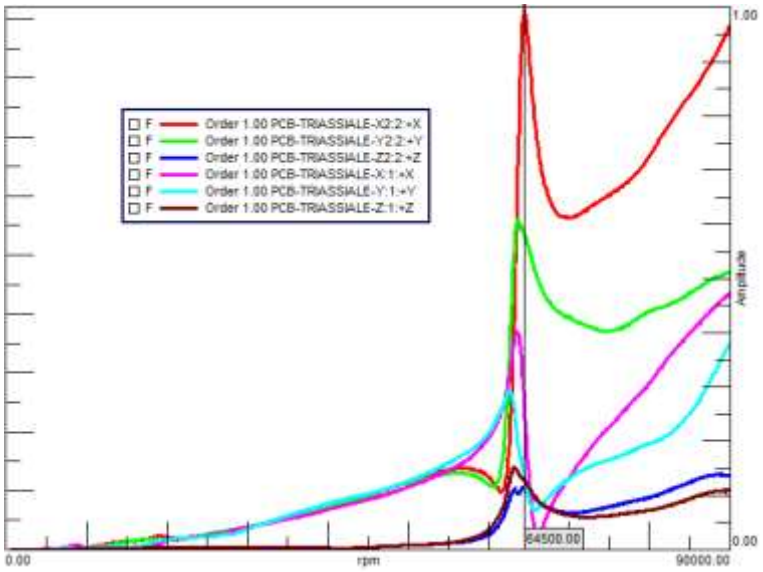

Figure 3.19 – Triaxial accelerometers 1X engine order analysis

In the following Figure 3.20 the trends relevant to the second engine order (2X) detected by the triaxial accelerometers are shown, from where it can be noted that an amplified vibrational behaviour

is still found at angular speeds around 64000 and 85000 rpm. Moreover, the onset of a small amplitude peak at about 32000 rpm furtherly confirms the hypothesis of a rotor-bearings system mechanical resonance close to 1070 Hz (that is, about 64000 rpm); indeed, such resonance in this case is excited by twice the synchronous rotational frequency (2X) and therefore it is expected to occur at half of its natural pulsation frequency (1070/2=535 Hz).

Finally, the other amplitude peaks which are found at angular speeds close to 65000 and 85000 rpm are probably ascribable to system non linearities which transmit a vibrational contribution due to 1Xrev energy to the 2Xrev thus generating a peak at 65000 rpm, whereas the contribution at 8500 rpm is probably attributable to the excitation due higher engine orders, between whom 3Xrev.

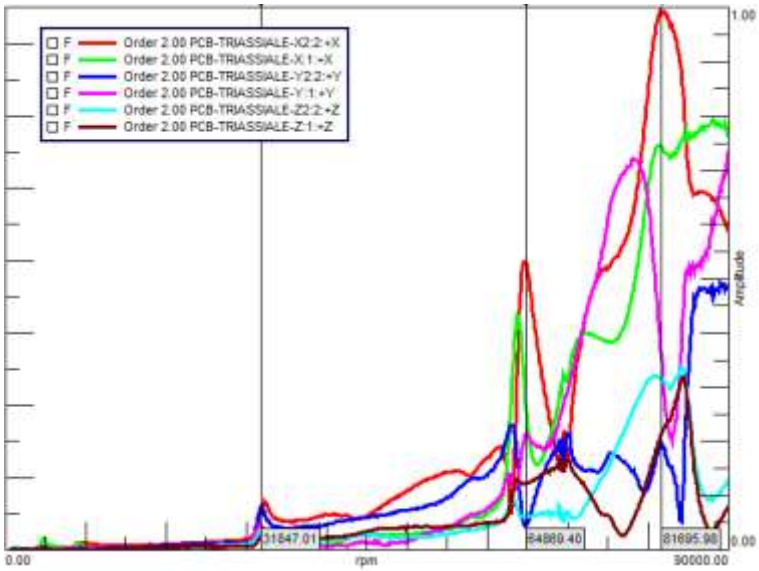

Fig. 3.15 – Triaxial accelerometers 2X engine order analysis

The rotor assembly to be simulated is reported in Figure 3.21 in a 3D CAD representation. With respect to the real assembly some assumptions are made to simplify numerical model geometry in order to perform numerical modal analysis on an equivalent symmetrical revolution solid, as recommended by Ansys® guide. Indeed, it is not suggested to numerically assess system critical speeds by means of Campbell diagram for not axisymmetric rotating elements in the case of a fixed reference system is employed (indispensable when the structural simulation comprises also microturbine frame).

Figure 3.21 – 3D CAD of real rotor assembly to be simulated

It must be remarked how shaft complexity yields to not reliable results obtained by 1DOF and 4 DOFs analytical models, therefore these are not reported for brevity whereas only numerical results are compared with experimental ones. However, the simplified shaft geometry made up by three contiguous layers of different materials and dimensions was modeled as three bending stiffness in parallel which acts in series with the radial stiffness of the two bearings. An equivalent rotor-bearings system was obtained and then its flexural natural pulsation frequencies were obtained but the agreement with experimental result was poor.

In order to gradually increase model complexity a beam-based FE structural model was implemented by means of APDL interface within Ansys® environment. Such simplified numerical model relies on the already introduced BEAM188, MASS21 and COMBIN14 elements; BEAM188 elements are employed to model the three different cylindrical parts which made up the rotor assembly: the one of smallest diameter represents the two areas of placement of the bearings, the biggest one represents shaft central part which has as external radius the root of rotor blades and the one with intermediate diameter represents the two shoulders which divide the above-mentioned parts. A comparison between the 3D original CAD and the devised beam-based FE model is given in Figure 3.22.

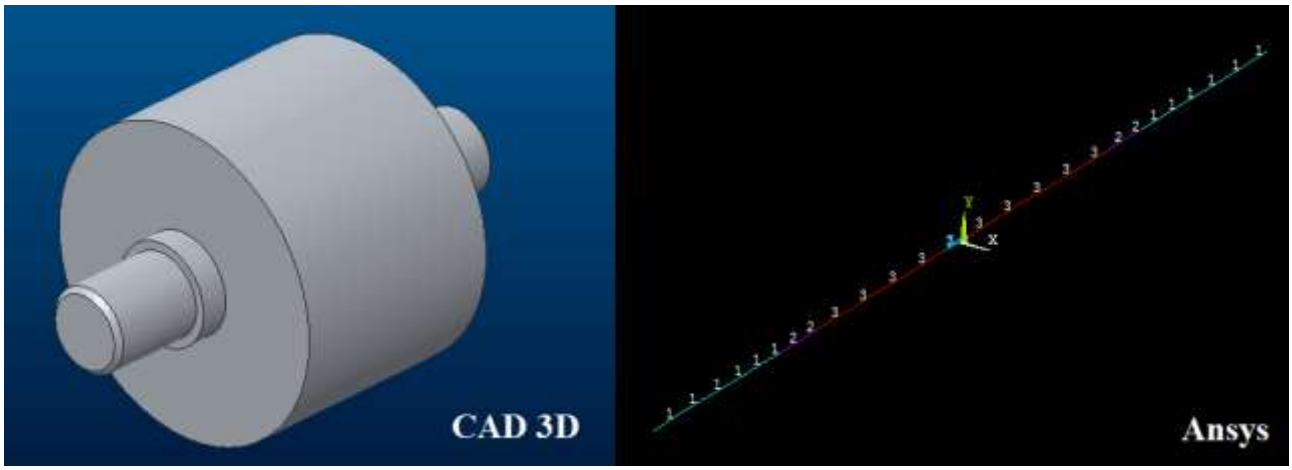

Figure 3.22 – Comparison between CAD geometry and beam-based FE model

MASS21 elements are exploited to represent the contribution to overall system mass and inertia due to rotor blades made up by aluminum and to the permanent magnet. The input data to be applied in the centerline of the beam elements model have been obtained from the original 3D CAD by excluding the central zone already simulated and by assigning to the two components their respective densities. Anyway, bearing stiffness law is taken into account together with shaft FE model, in such a way that both rotor and bearings stiffness contributions to overall system flexibility are properly assessed. To this aim, COMBIN14 elements are initialized with the stiffness values obtained according to equation (3.xyz), under the assumption of G=0.1, whereas damping coefficients are null.

The employed values for radial stiffness are in the order of magnitude of ten million of N/m, whereas axial stiffness can be neglected since the interest is stressed to lateral vibration modes in *x-y* plane. The spring elements (COMBIN14) which represent bearing stiffness are fixed to the frame by constraining all their DOFs. Moreover, in order to avoid physically meaningfulness natural frequencies to occur in numerical modal analysis results, all the model DOFs referred to the displacement along *z* direction and to rotation around *z* axis are constrained. At this point the beam-based FE model with all the updated constraints ready for the analysis appears as in Figure 3.23.

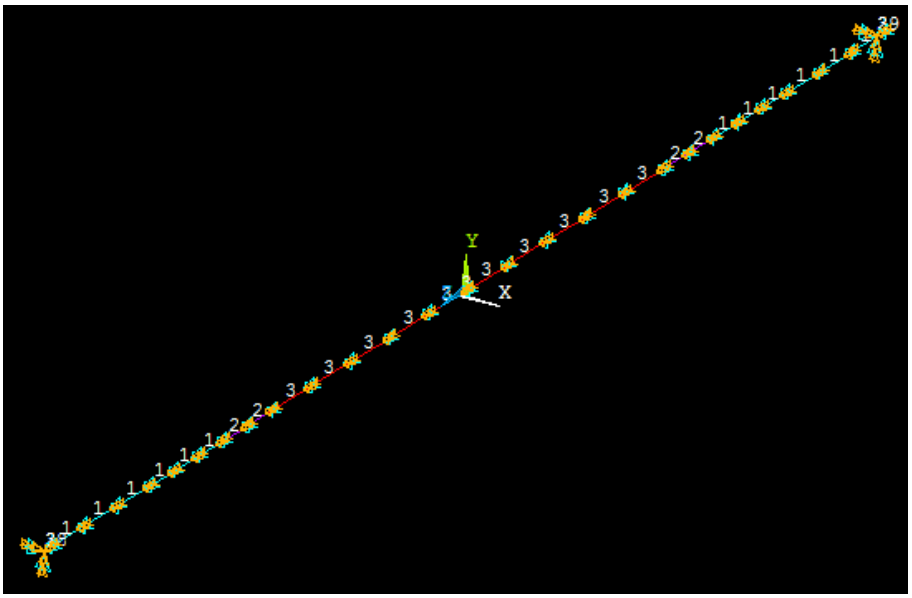

Figure 3.23 – Beam-based FE model with updated constraints

The obtained Campbell diagram for such simplified FE model is reported in Figure 3.24 and it shows that no natural flexural frequencies are reached within machine whole operating range thus not giving rise to significant critical speeds at least excited by 1X and 2X engine orders.

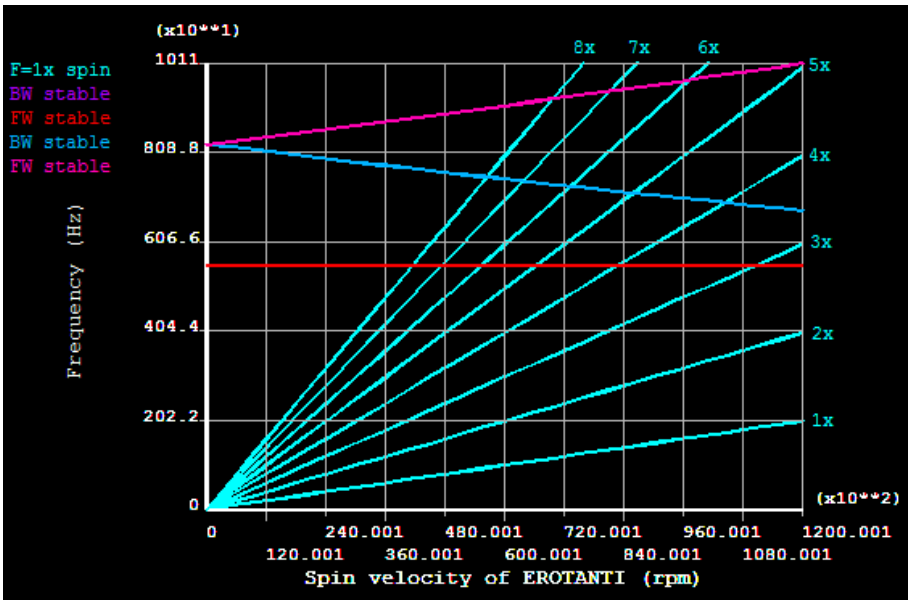

Figure 3.24 – Campbell diagram relevant to simplified FE model modal analysis

Finally, a three-dimensional FE model based on real rotor geometry is devised which relies on solid elements for spatial discretization, in order to look for a better agreement with experimental results. In such microturbine modeling its blades have been substituted by a concentric layer comprised between the internal part made in aluminum and the external one made up by the magnet in such a way that such cylinder equivalent density corresponds to the blades one. The correct density has been set by making total shaft mass and inertia moments to be as close as possible to the ones of actual geometry. In order to tune such structural model, Workbench interface has been exploited within Ansys® environment. Indeed, it allows a more direct and simpler interaction when dealing with complex geometries with respect to APDL, that is more suitable for simplified structural models. In any case, the procedure is conceptually analogous, it is only different the way of implementing it. The main advantage of such approach is its intuitiveness, but it presents the drawback of a lack in the control and in a loss of deep comprehension of each instruction which is typical of APDL interface. First, model constraints are imposed in such a way that only the rotational degree of freedom is left free. The rotor is then fixed to the ground by means of springs, whose stiffness is representative of actual ball bearings supporting the shaft. In this case, in order to perform a reliable numerical modal analysis, spring axial stiffness is set bigger than real one since the interest is mainly on system flexural critical speeds. To this aim, radial stiffness is imposed in x and y direction according to the non-linear stiffness model. The so constrained model is shown in Figure 3.25. In order to allow the solution, all the parts which made up the assembly are assigned to material properties found in Ansys® libraries, and then between the concentric cylinders a contact condition is needed. To simply overcome this issue, the connection between two contact surfaces is assured by assuming a stiffer surface with respect to another and this is made by default by the software in order to obtain a solution. Two

contact surfaces are generated in this case, namely a target one on the internal surface of the cylindrical magnet (regarded as stiffer or in any case discretized with a coarser mesh) and a contact one on the external surface of the layer equivalent to rotor blades (regarded as less stiff or in any case discretized by means of a refined mesh). After all model contacts have been properly set, it is essential to delete all the geometrical surface entities imported by the CAD, in order to allow a volumetric discretization of the model. Indeed, 3D model mesh is obtained by means of solid elements and therefore no surface entities must still be present, otherwise the structural elements, which are always at higher level of hierarchy with respect to geometrical ones, could not be defined properly elsewhere in the model. After this has been ensured, a mapped mesh has been generated where it was possible, in such a way that the minimum element dimensions could allow to detect the maximum frequency of interest, according to Nyquist principle applied in spatial domain, in order to avoid aliasing. Indeed, differently from static analysis, here the mesh refinement is not related to the accuracy of the obtained results in terms of primary (i.e. forces and displacements computed at the nodes) and secondary results (stress and strain computed for each model node), but to the maximum detectable frequency (or equivalently, angular speed). In this case the interest is mainly on the first system flexural critical speed and then this constraint is easily satisfied without requiring too high computational times by imposing "Minimum Edge Length" equal to 0.007 mm. It is fundamental to assess the obtained mesh quality before entering the solution routine, and this can be made by means of automatic mesh quality checks, in terms of elements aspect ratio. Once mesh quality has been checked, the final settings for modal analysis, must be defined, the most important of which are the number of vibration modes to be found and the number of points (i.e. angular speeds) to be computed for Campbell diagram visualization. Other "Analysis Settings" which are imposed are the presence of "Coriolis effect", to consider gyroscopic effects, and the presence of damping, needed in case of harmonic analysis. Moreover, the rotational axis must be defined before proceeding to the solution. Even the solver can be chosen, but in this case the default settings are not changed.

In this context the number of vibration modes is limited to 6, and therefore angular speeds to be computed are 6 with maximum value equal to 10krad/s (roughly 100krpm), while the *Z* axis is set as rotational one, according to model constraints. Finally, even the total deformations are required in "solution" routine in order to visualize the modal shapes associated to system natural pulsation frequencies reported in Campbell diagram which are excited by the first engine order (1X) thus giving rise to system (primary) critical speeds.

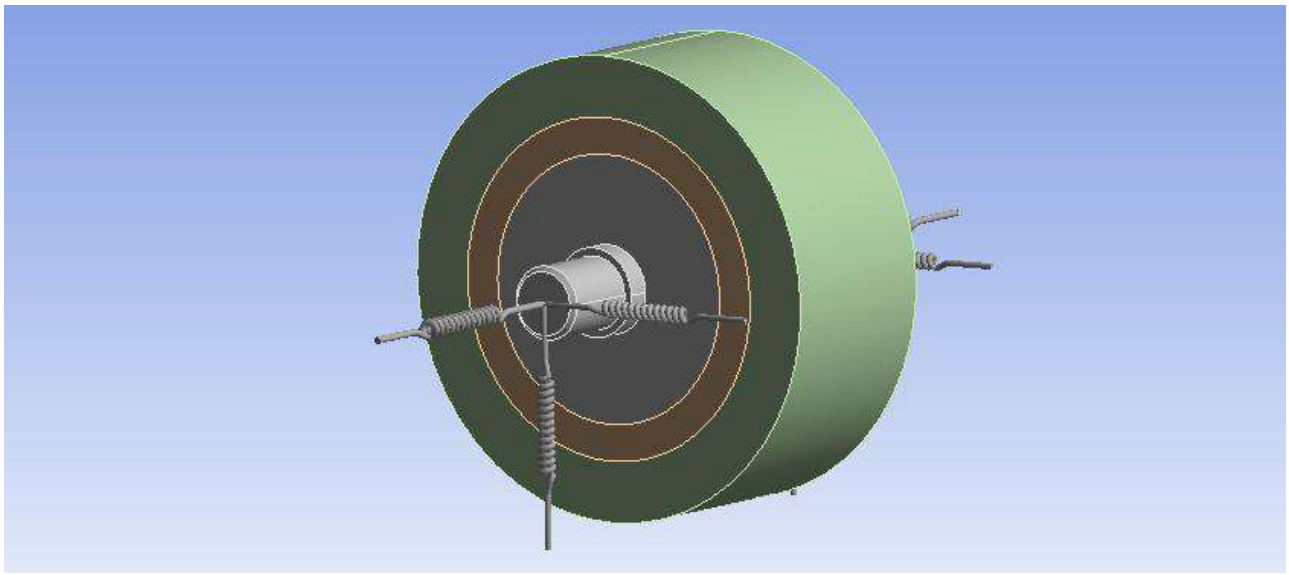

Figure 3.25 – 3D FE model with constraints and simplified rotor blades geometry

The so computed Campbell diagram is reported in the following Figure 3.26, where it can be observed that no mechanical resonances are excited by synchronous frequency the operating range 0-100krpm.

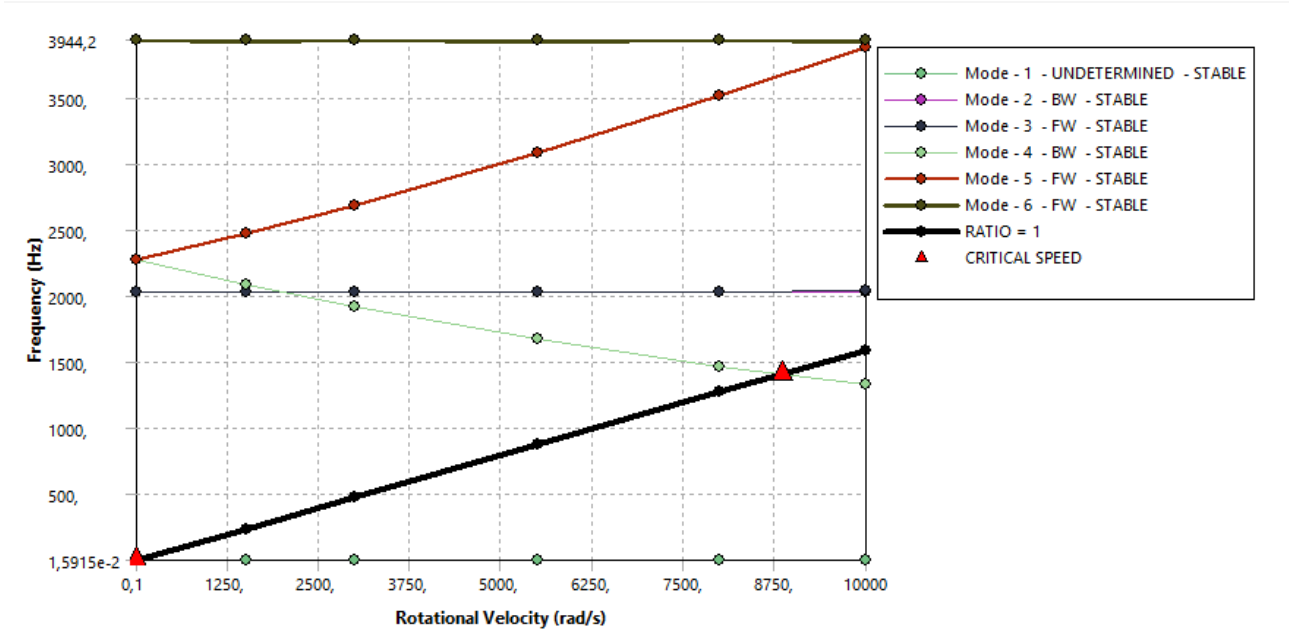

Figure 3.26 – Campbell diagram relevant to 3D FE model modal analysis

As it can be seen from the obtained Campbell diagram, the imposed shaft rotation has induced a rigid motion at zero frequency, which is identified by the software as the first vibration mode, even if physically not meaningful. The second and third vibration modes are related to system first flexural natural frequency with a locked frequency equal to 2036Hz. The fourth and fifth vibration modes are related to system second flexural natural frequencies which are subjected to gyroscopic effects. The

sixth vibration mode is related to system axial natural frequency which is not of interest and whose value is not significant since the axial motion has been constrained by means of a very stiff equivalent spring, in order to not interfere with flexural vibration modes which are the only ones of interest here. The only critical speed to be excited by engine order 1 is found at about 8841 rad/s and it is due to system fourth vibration mode, which is a flexural BW mode. Therefore, this is only a theoretical critical speed, since it is in phase opposition with respect to synchronous rotation and hence it cannot excite the structure.

All the modal shape relevant to the previously identified vibration modes are reported in Figure 3.27. As it could be expected the flexural modes involve a deformation of both the supports (bearings) and the shaft. In this case, being rotor bending stiffness comparable to bearings one, not purely flexural modal shapes are found, but a mixture of different deformative behaviors due to system complexity.

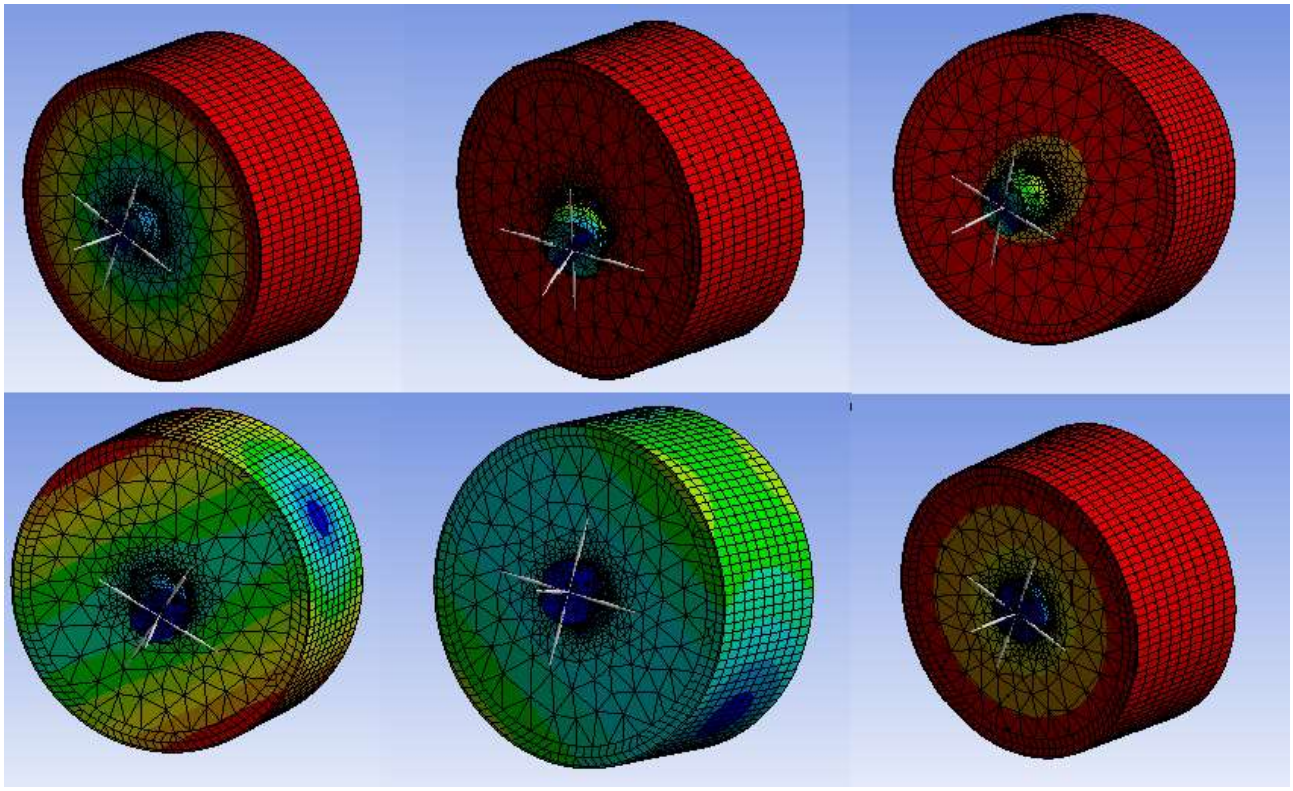

Figure 3.27– First six modal shapes of rotor-bearings system

References Chapter 3

[1] Stefani, F.A., Niccolini Marmont Du Haut Champ, C.A., Silvestri, P. (2020). "Experimental and numerical investigation about small clearance journal bearings under static load condition", Advances in Tribology, art. no. 8844879 (Open Access).

[2] G. Lundberg and A. Palmgren, "Dynamic capacity of rolling bearings," Acta Polytechnica Mechanical Engineering Series, vol. 1, no. 3, 1947.

[3] Jones, A. B., "A general theory for elastically constrained ball and radial roller bearings under arbitrary load and speed conditions", Trans. ASME, J. Basic Eng., vol. 82, series D, no. 2, pp. 309–320, 1960.

[4] J. V. Poplawski, J. H. Rumbarger, S. M. Peters, R. Flower, and H. Galaitis, "Advanced analysis package for high-speed multi-bearing shaft systems: COBRA-AHS," Final report, NASA Contract NAS3-00018, 2002.

[5] D. P. Fleming and J. V. Poplawski, "Transient vibration prediction for rotors on ball bearings using load-dependent nonlinear bearing stiffness," International Journal of Rotating Machinery, vol. 10, no. 6, pp. 489–494, 2004.

[6] J. W. Lund, Rotor-Bearing Dynamics Design Technology; Part V: Computer Program Manual for Rotor Response and Stability. AFAPL-TR-65-45, 1965.

[7] R. G. Kirk, "Nonlinear transient analysis of multimass flexible rotors", Ph.D. Dissertation, University of Virginia, Charlottesville, Va, USA, 1972.

[8] D. P. Fleming and J. V. Poplawski, "Unbalance Response Prediction for Rotors on Ball Bearings Using Speed- and Load-Dependent Nonlinear Bearing Stiffness", International Journal of Rotating Machinery, vol. 1, pp 53–59, 2005.

[9] Beatty, R.F. and Rowan, B.F., 1982, "Determination of Ball Bearing Dynamic Stiffness". Proceedings of a Workshop, Rotordynamic Instability Problems in High Performance Turbomachinery. NASA Conference Publication 2250, pp 98-104.

[10] Butner, M. F., Murphy, B. T., and Akian, R. A., (1991), "The influence of mounting compliance and operating conditions on the radial stiffness of ball bearings: Analytic and test results". Paper presented at the Proceedings of the ASME Design Engineering Technical Conference, Part F168436-2 155-162. doi:10.1115/DETC1991-0241

[11] Tiwari, R., Rotor Systems: Analysis and Identification, CRC Press, Boca Raton, 2017.

[12] Renuke, A., Traverso, A., Reggio, F., Silvestri, P., and Pascenti, M., (2020), "Experimental investigation on a 3 KW air tesla expander with high-speed generator", Proceedings of the ASME Turbo Expo, 5.

[13] Harris, T.A., 2001, Rolling Bearing Analysis, Wiley, New York.

[14] Timoshenko, S. and Goodier, J., 1951, Theory of Elasticity, 2nd edition, McGraw-Hills, New York.
[15] Ragulskis, K. M., Jurkauskas, A. Yu., Atstupenas, V. V., Vitkute, A. Yu., and Kulvec, A. P., (1974), Vibration of Bearings. Vilnyus: Mintis Publishers.
[16] Uday, P., Prabu, J., Solairaju, M., Shravankumar, C., Jegadeesan, K., and Rao, T.V.V.L.N., (2020), "Estimation of critical speeds of a rotor supported on ball bearings", IOP Conference Series: Materials Science and Engineering, 912 (2), art. no. 022033.
[17] Silvestri, P., Traverso, A., Reggio, F., Efstathiadis, T., (2019)," Theoretical and experimental investigation on rotor dynamic behavior of bladeless turbine for innovative cycles", Proceedings of the ASME Turbo Expo, 3.
[18] Tiwari, M., Gupta, K., Prakash, O., (2000), "Effect of radial internal clearance of a ball bearing on the dynamics of a balanced horizontal rotor", Journal of Sound and Vibration, 238 (5), pp. 723-756.
[19] ISO 1940-1

4 Hydrodynamic bearings unstable behavior and fluid-structure interactions

In some rotating machinery for specific industrial applications the driving as well as resistance torques or the inertias reduced to the rotation axis may be nonstationary, thus affecting system dynamics. Under such operating conditions, in some peculiar cases torsional response and rotational motion irregularity may influence system lateral vibrations.

The present work shows how such coupling phenomena may become significant in particular conditions, where the occurrence of fluid-structure interactions causes a reduction in stability threshold of hydrodynamic journal bearings and torsional energy yields a hysteresis behavior in system synchronous lateral response. A hypothesis based on Hopf bifurcation theory (HBT) is formulated in order to justify how and under which operating conditions such coupling phenomenon can develop. In order to validate such hypothesis, an experimental campaign is performed on a real-size shaft line including a TG rotor for heavy-duty power plants mounted on hydrodynamic bearings. The detected rotor-bearings system lateral operating response is found to become more complex in presence of a pulsating driving torque inducing significant angular speed oscillation as well as a dynamic perturbation, which causes strong coupling from torsional to lateral vibrations. Such coupling entity has been experimentally found to be dependent from excitation frequency with respect to revolution one. Particularly, localized hysteresis and jump-up phenomena are detected in trends of fundamental order contents measured during run-up and run-down tests when such torsional response is present. Consequently, a hydrodynamic bearing numerical model is built that can solve thin film dynamics equations in unsteady conditions in order to quantify journal lateral vibrations amplitude in presence of both an angular speed oscillation and a dynamic perturbation, characterized by well-defined amplitude and characteristic frequency.

The proposed approach, validated by means of both suitable measurements and numerical simulations, can justify the existence of such coupling phenomena. The detected anomalous response characterized by localized hysteresis is ascribable to journals unstable behavior onset within hydrodynamic bearings due to operating angular speed irregularity related to an induced torsional vibration.

4.1 Introduction

The individual behavior of rotordynamic components may strongly affect the performance of a generic whole mechanical system (e.g. rotor-bearings systems), thus making its dynamical operational response more complex and less predictable with respect to its expected behavior in terms

of theoretical and numerical classical models (e.g. contributions of aerodynamic bearings in system rotordynamics [1,2]).

The interpretation of stability threshold change phenomena that may arise within the mechanical system and the way in which they can affect the dynamical response of rotating machinery still represents a topic of great interest.

4.1.1 Nature of the issue

Hydrodynamic journal bearings play a significant role in determining stability threshold of real-size rotors when they are forced to work far from their on-design conditions [3]. Indeed, in particular industrial application cases some irregular external or internal loads, capable of influencing the rotational speed and not properly taken into account in journal bearing preliminary design, may modify the dynamic stability threshold of such hydrodynamic supports. For instance, an unsteady component in the driving torque or variable reduced inertia that causes a significant torsional response may modify journal bearings vibrational behavior and might even lead to a coupling between shaft line torsional and lateral vibrations. In such cases, the detected system response may become anomalous with experimental evidence of hysteresis and jump-up between run-up and run-down curves. The subsequent investigation becomes very complex, as it is not trivial to identify and isolate the causes of such unexpected behavior. Such instability phenomena are deeply investigated in the present work by employing and testing a real-scale rotor-bearings system. Indeed, their practical implication may become very influential. In example, when vibration amplitudes overall values must be optimized, the above-mentioned behavior makes very challenging to improve system dynamics.

When investigating dynamical behavior of complex mechanical system involving several degrees of freedom, under given external conditions, operational response can be also ascribable to coupling phenomena. Their entity may vary in a significant way, causing more or less marked cross-coupled behavior. In some cases, such operating response might be related even to hysteresis phenomena, which cannot be simulated by means of classic linear models. A typical example is represented by particular rotating machinery applications, whose response is not easily interpretable by means of standard aprioristic knowledge, as shaft torsional and lateral dynamics are not completely independent. In the most recurring case, as reported in [4-5], rotor torsional response is influenced by lateral vibrations. Indeed, technical literature concerning this topic can be summarized in two main classes; the first category of manuscripts includes works investigating the influence of lateral vibrations on torsional response. Particularly, some papers ([6-7]) present examples where such coupling is somehow ascribable to the presence of gearboxes or complex devices like multi-disk mechanical systems. Furthermore, in case of weakly damped rotor systems, a related instability onset may influence the machine functioning [8]. Other cases where lateral vibrations affect the torsional

response are studied in [9-11], where the cause is identified in the mechanical unbalance, which makes up the main external force acting on the system. In [10] such experimental evidence is also confirmed by resorting to FE models. A first example of different coupling mechanism direction is studied in [12], where an energy transfer from torsional to lateral vibration occurs, which is due to the presence of an interposed gearbox. The works presented in [13-14] discuss coupling phenomena involving rotating machinery due to rubbing between rotor and frame in presence of cracked shaft and rotor anisotropy, respectively. If strong non-linearities are present, the onset of a hysteresis loop due to coupled lateral and torsional response leads to a different behavior between run-up and run-down curves [15]. The coupled torsional-lateral dynamics has also been studied both analytically and experimentally in [16], where the case of a motor pump assembly is considered.

The work presented in [17] shows how torsional vibrations can interact with lateral ones in a mechanical system by means of both discontinuous friction and intrinsic cross-coupled behavior of torsional and lateral dynamics. The authors investigated both numerically and experimentally, by means of a custom designed prototype, the interaction between lateral vibrations caused by mass unbalance and torsional ones; such interaction may be due or to system intrinsic coupling between its lateral and torsional structural dynamics or it may happen by means of discontinuous friction torque. Furthermore, they proved both with experimental tests and numerical results that a bigger mechanical unbalance can lead to a stabilization of torsional response, thus making disappear the friction-induced limit cycle. The authors of [18] have performed a numerical investigation about vibrational response in a gear-rotor-bearings system, where the influence of gear eccentricity fluctuations is considered; indeed, the effects of an interposed gearbox in a shaft line are taken into account by varying mesh stiffness to assess dynamic system response since they are expected to relevant in causing a marked coupled torsional-lateral behavior.

The effects of geometrical non-linearities are discussed in [19] due to rotor's long overhangs, which exhibits a hysteresis cycle between run-up and run-down curves. In such particular case, the authors have observed that the described response is mainly attributable to the influence of overhang on operating mode shapes. In [20] numerical simulations have been performed to improve the identification of instability threshold speed in two different hydrodynamic journal bearings test bench arrangements. In the former, rotor-bearings system instability makes its onset at the characteristic oil-whip frequency, while in the latter unstable conditions arise before that the same threshold speed is reached. Indeed, oil-whip phenomenon is the only fluid-induced instability commonly taken into account in the design phase; nonetheless, experimental evidence in real application cases have demonstrated that stability thresholds may be found at lower angular speeds with respect to design

calculations, thus requiring a deeper comprehension of instability mechanisms affecting hydrodynamic journal bearings.

Reference [21] investigates both analytically and numerically coupling phenomena due to hydrodynamic journal bearings and gyroscopic effect in rotor-bearing systems. It presents relevant case studies involving both plain (cylindrical) and tilting-pad bearings. Indeed, although hydrodynamic journal bearings introduce high damping in the rotor-bearing system, they also involve cross coupling of rotor translational motions, which is one of the main sources of oil-induced instability. Hence, shaft speed should not surpass the threshold at which oil-induced instability arises. The inherent nonlinearity of hydrodynamic journal bearings turns out to be significant for relative eccentricities larger than 60%. Indeed, in such working conditions most existing linear models cannot reliably predict the journal trajectory. Such strong nonlinearities involving cross coupling behavior are the main sources of the complex dynamic phenomena encountered in rotor-bearing systems.

The second class of manuscripts includes works which rely on case studies where the external torque may induce lateral vibrations in shaft lines, and therefore where torsional vibrations might affect rotor-bearings system lateral dynamics. For instance, some works from literature evidence how an external perturbation whose amplitude is greater than a threshold value can modify fluid film bearings stability threshold. For instance, the authors of [22-23] have performed a comparison between numerical and experimental results aimed to predict the stability threshold of rotor-bearing systems. They have observed in the experimental facility consisting in a rotor supported by hydrodynamic bearings a hysteresis cycle, which has been accurately simulated by a numerical method based on HBT. Other authors ([24]) have studied hydrodynamic bearings by means of numerical analysis in order to assess the effect of damping on an actual industrial rotor-bearings system (i.e. steam turbine). In [25] the effect of rotor flexibility is added to the same numerical model proposed in [22-23] in order to assess how it affects rotordynamic system stability. Again, in [26] such numerical approach is applied to the particular case of floating ring bearings. The obtained results suggest that in equivalent operating conditions, they should lead to a wider rotordynamic stability field in comparison with rotors mounted on classical journal bearings. Finally, reference [27] presents an insight of the relative radial clearance influence on journal bearing stability. It shows that increasing the clearance enlarges the rotordynamic system stability threshold, all other conditions being equal.

4.1.2 Aim of the work

The goal of the study is to understand if a coupling mechanism from torsional to lateral vibrations can develop in a single shaft real-scale industrial facility and which phenomena can cause such behavior within some of its mechanical components. To this aim, a pulsating torque profile is applied to the system to induce a torsional response in order to understand how and under which operating

conditions it can induce lateral vibrations by means of modifications of hydrodynamic journal bearings response. To this goal, a shaft line driven by an induction motor piloted by an inverter is considered in order to assess the behavior of real-size rotors supported by hydrodynamic journal bearings. By acting on motor control it is possible to excite shaft line first torsional vibration mode whose natural frequency is almost invariant for all the operating conditions examined when the induction motor is turned on. By analyzing system response in run-up and run-down tests, where shaft line angular speed was varying in a well-defined angular speed range, a not deterministic trend in synchronous lateral response, typical of non-linear systems, is experimentally observed. The presented investigation must be developed from scratch, since in literature there are not many proofs of energy transfer from torsional to lateral vibrations, unless with the presence of an interposed gearbox [12].

Moreover, a numerical validation of the presented theory is performed by means of a suitable FE code in order to assess if the experimentally observed angular speed perturbation can actually affect shaft line response by exciting oil-film instability phenomena within the supporting journal bearings. At first, a lubrication model is devised in order to investigate non-linear stability of both circular and four-lobe hydrodynamic bearings. From a theoretical point of view, two equivalent mechanisms are likely to occur which can cause sub-synchronous instability inception within hydrodynamic bearings. The former is an angular speed fluctuation referred to as kinematic perturbation, while the latter is an external rotating force, i.e., a dynamic perturbation. Firstly, a kinematic perturbation is applied to a generic circular hydrodynamic bearing to check potential stability threshold changes by varying its dynamic characteristics within the whole sub-synchronous frequency range. Afterwards, the same numerical procedure is performed considering solely the effect of a sub-synchronous dynamic perturbation.

After this has been proven, the four-lobe bearing supporting the actual test bench is loaded by the perturbations computed according to the shaft line dynamic model and the angular speed fluctuations measured close to the most critical bearing in analysis. According to the results of the study, the above-described coupling mechanisms explain the localized hysteresis cycles observed between run-up and run-down tests in synchronous lateral vibration component. Actually, the detected hysteresis phenomena and the related bearings instability are caused by both the kinematic and dynamic perturbations of journal motion.

They interact that the kinematic perturbation triggers the dynamic one, which causes significant effects on journal lateral displacements. Their effect is amplified when the torque ripple main frequency is half of the shaft line rotating speed (0.5Xrev). Thus, the lubrication analysis of the most critical bearing within the shaft line justifies the detected system anomalous response.

4.2 Test rig description

The tested shaft line and the measurement system are presented and described in detail hereinafter. The main data required by the experimental study are provided by means of a suitable measurement system.

4.2.1 Shaft line geometrical and physical description

The investigated shaft layout is made up by a direct line (with no interposed gearboxes), where the shaft line is driven by an induction motor. It is piloted by an inverter which allows by means of adequate settings to introduce low frequency components in the exerted mechanical torque, so that it is fitted to excite system first torsional vibration mode. Consequently, it can create working conditions characterized by pulsating angular speed. Such electric motor, placed at the left end of the shaft line, is characterized by a moment of inertia J_m=130 kgm^2 while the driven shaft at the opposite end has a much higher inertia, i.e. a moment of inertia J_d equal to 28500 kgm^2 and a mass of 80·10^{3}kg. Shaft line total length is equal to 30 m, whereas the driven shaft has a length of 20 m. The shaft line is mounted on several fluid film supports (i.e. hydrodynamic journal bearings). As further connection, a double universal joint lets a degree of freedom to the driven shaft in lateral direction with respect to the electric engine, so that the system is not hyperstatic (Figure 4.1). This component turns out to be the most significant in terms of shaft line flexibility (i.e. the least stiff in comparison with the remaining parts). A turning gear, located between the induction motor and the double universal joint, has never been employed during the present activity. It acts as a joint that ensures the direct line connection between the electric motor and the driven shaft. During every experimental activity carried out in the present work all the shaft line elements are always kept mechanically connected, including the induction motor.

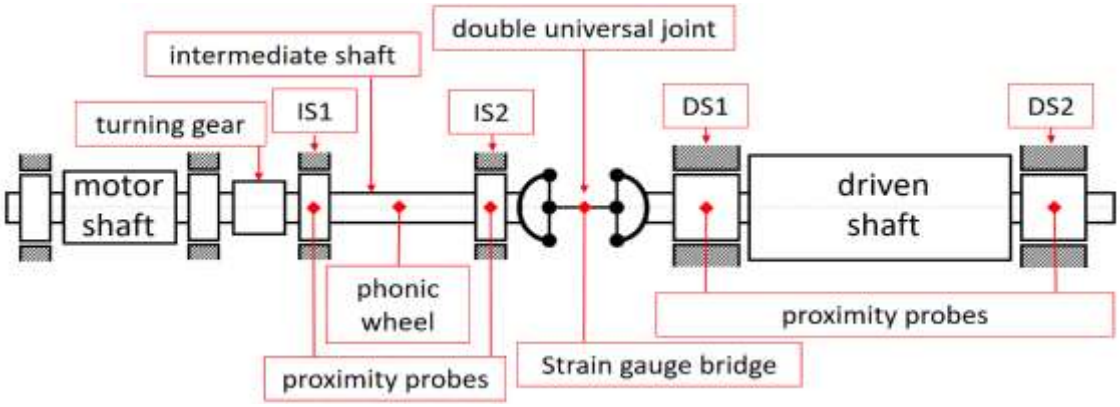

Figure 4.1 – Layout of the investigated shaft line including nomenclature of most significant hydrodynamic supports: IS1, left bearing of intermediate shaft; IS2, right bearing of intermediate shaft; DS1, left bearing of driven shaft; DS2, right bearing of driven shaft

The shaft line has been assembled with very high alignment tolerances in order to minimize the onset of disequilibrium moments that could lead to coupling phenomena between torsional and lateral behaviour. The bearings supporting the driven shaft (DS1, DS2) are lemon-bore (elliptical) hydrodynamic journal bearings, whereas the ones of the intermediate shaft (IS1, IS2) are four-lobe supports.

4.2.2 Measurement system

A suitable measurement system capable of detecting both torsional and lateral shaft line relevant operational responses has been tuned in order to capture the possible onset of coupling phenomena during all the conducted tests. In particular, phonic wheels and strain gauges are employed to properly acquire torsional response signals while proximity probes are chosen to adequately measure system lateral response at significant locations (e.g. journals lateral behaviour within hydrodynamic bearings).

Eddy current proximity sensors are employed to detect displacements of shaft line sections in two directions normal to rotor axis (x and y). Such probes are adopted in order to measure journal locations of both the bearing pairs supporting the driven shaft (downstream of the double universal joint) and the intermediate one (between the engine and the double universal joint).

One phonic wheel characterized by 141PPR (pulses per revolution) built with a zebra tape together with an optical sensor is employed in a suitable shaft line section in order to perform measurements of instantaneous angular speed.

A strain gauge bridge measures shaft circumferential deformation in an intermediate section between motor and driven shaft in correspondence with the shaft connecting the two single universal joints. The collected signals coming from the phonic wheel and the strain gauge bridge allow to obtain information respectively relative to shaft line rotational rigid motion and to its torsional strain. Such measurements, together with the identification of the first torsional vibration mode (see section 3.1) lead to a complete identification of the whole torsional response throughout the entire shaft line. Moreover, strain gauge bridge signal can be regarded as also representative of the drive shaft applied torque in correspondence with its measurement section. Indeed, the measured torsional deformation multiplied by the torsional stiffness provides the value of the torque that actuates the driven shaft in the measurement section. Nevertheless, the identification of operational torque is not mandatory in the present investigation since the proposed theory justifying the onset of hydrodynamic bearings instabilities is based on a system response parameter and in particular on journal instantaneous angular speed.

4.3 Identification of shaft line vibration modes

At first, an experimental identification of the most significant vibration modes (i.e. the ones more likely to affect the system operational response to a large extent) is performed. Later, operational responses are identified, in order to complete system identification to better predict its dynamic behaviour.

4.3.1 Torsional vibration modes

Torsional strain response detected by means of strain gauge bridge exhibits only a main spectral content in the investigated range, and this, together with shaft line layout dynamic characteristics, suggests that only the first torsional mode is significant in system operational response. Consequently, combining this information with a survey of shaft line actual distribution of inertia and stiffness, it is reasonable to assume as first approximation scheme of the system an equivalent mechanical model of "double torsion pendulum". It is a lumped parameter model that is equivalent to the rotor system from the torsional point of view. The relevant parameters of such model are the two moment of inertia J_m and J_d, whose values are reported in section 4.2.1, and the unknown torsional stiffness connecting the two inertias (K_C). It is therefore useful to estimate structural coupling torsional stiffness (K_C) once system torsional natural frequency has been experimentally determined in order to correctly identify such elementary structural model. Accordingly, the shape of the first fundamental vibration mode, which is exclusively structural, is characterized by an opposing motion of the two inertias. If the electromagnetic interaction generated by the induction motor is removed by the system, the natural frequency due to exclusively structural system properties can be experimentally identified. To this goal, two different experimental procedures have been carried out, i.e. an impact test [28] and an operational test. Both of them suggest an overall value of the first torsional natural frequency roughly equal to 11Hz. The impact test has been performed on the shaft line at zero speed in free-free conditions by acting on the rotational degree of freedom [29]. A detail of the correspondent modal shape is shown in Figure 4.2a for the driven shaft. The so identified torsional mode presents also a modal shape with opposite phase; coherently with shaft line inertia distribution the extracted modal amplitudes are found to be higher on the motor shaft with respect to the driven one. Since according to the double torsion pendulum in the first mode the motor inertia Jm oscillates with the maximum amplitude, the impact force has been applied to the motor side in order to excite the structural torsional vibration mode. Differently, the operational test consists in an instantaneous shutdown of the motor during a run-up test. It has allowed us to detect a spectral content of system response (Figure 4.2b). Due to the shutdown the sudden active torque variation from a run-up average value to zero introduces broadband energy into the system. In order to maximize such energy, the maximum run-up angular acceleration (300rpm/min) has been set before the switch-off of the electric motor. Consequently, the

relevant torsional response of the system includes a significant contribution of the structural torsional vibration mode. Since the effect of the magnetic field on the overall shaft line torsional stiffness does not vanish instantaneously after the power supply stop, only the last cycles of the free vibration caused by the shutdown excitation are taken into account in order to exclusively isolate the effect of the structural stiffness component. The direct analysis of such operational response in time-domain (Figure 4.2b) has allowed us to identify the average value of the natural frequency relevant to the purely structural torsional vibration mode. According to Figure 4.2b, such frequency can be located next to 11 Hz. The encountered discrepancies may be related to the two different operating conditions, in terms of angular speed, at which shaft line structural identification has been performed. Indeed, at two different angular speeds shaft line components may exhibit different dynamic behaviour. Moreover, the observed cyclic trend related to motor shutdown transient exhibits a strongly non-harmonic response, which may be related to backlashes and significant non-linear contributions within such transient.

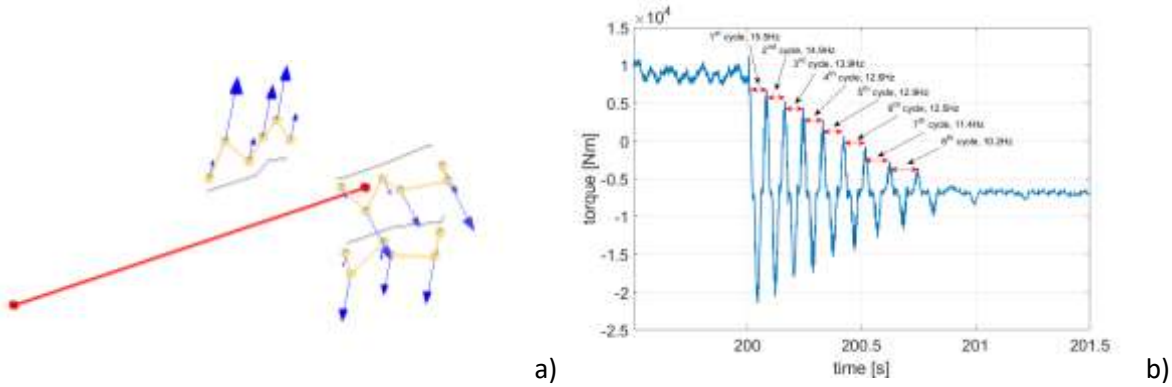

Figure 4.2 – Detail of modal shape in the last sections of the driven shaft extracted from impact test (a), operating torsional response during motor shutdown transient starting from 1300rpm (b)

Differently, when the rotor is driven by the electric motor, the main spectral content of the system operational response does not coincide with the characteristic frequency of the torsional structural vibration mode identified previously. In example, Figure 4.3 shows a time-frequency analysis in terms of auto-power spectrum performed by means of short-time Fourier transform (STFT) of the torsional vibration measured during a rotor transition from free motion to driven operation or, equivalently, from a run-down to a run-up operating condition. Correspondingly, the electric motor, initially switched off, subsequently supplies power to the rotor system. When the induction motor is applying the driving torque to the shaft line, the output amplitude in the system operational response is significant for two spectral contents. They are associated with frequencies near to 5.3 Hz (as well as to its double multiple order 10.6 Hz) and 16.7 Hz. Accordingly, the lumped parameter model can simulate such magnetic effect occurring during engine operations (e.g. when the shaft line is driven by the induction motor) by means of a supplementary spring element (K_M) of suitable stiffness acting

on the motor inertia J_M together with the structural one (K_C). A dynamic scheme of the considered mechanical system is reported in Figure 4.4. Furthermore, in the presented case, both structural (d_C) and magnetic damping (d_M) do not significantly affect the estimate of supplementary mode natural frequency and thus can be neglected in such elementary model. Mechanical coupling damping (d_C) can be neglected due to shaft line structural properties, since it is made up by low internal damping materials. Magnetic damping (d_M) is not relevant for system identification in terms of its natural frequencies, as reported in [30]. Actually, electromagnetic effects are known to cause interaction between shaft lines and induction motors [30-31]. Indeed, the shaft line dynamics is characterized by a further torsional vibration mode due to the electromagnetic stiffness acting between the rotor and stator [30].

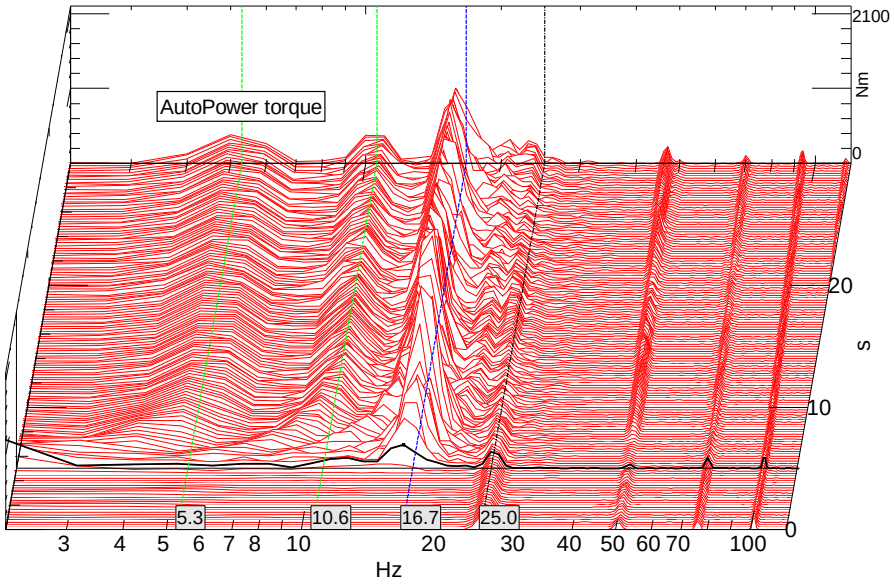

Figure 4.3 – Waterfall plot (STFT) of torsional operating vibration during a transient starting from free run-down (with induction motor switched off) to run-up with motor supplying power

Therefore, during engine operation, the previously identified torsional mode (with opposing motion between the two inertias and natural frequency close to 11Hz) is modified by the electromagnetic additional stiffness, so that its natural frequency becomes higher due to the stiffness increment related to the electromagnetic interaction. Indeed, as reported in literature systems with not enough stiff mechanical couplings can be extremely sensitive to the electromagnetic effect [30], due to the considerable interaction between the additional torsional mode and the purely structural one. In this specific case, the electromagnetic stiffness causes an upward shift in torsional natural frequency of about 30%. Indeed, for the purely structural double torsion pendulum, assuming a torsional natural frequency of 11Hz, it is possible to obtain, by highlighting k in (3.1), a torsional stiffness kC around $6.1 \cdot 10^5$ Nm/rad. Moreover, by analyzing operational electric parameters magnetic stiffness and

additional damping can be estimated, in agreement with [30]. Such supplementary magnetic stiffness k_M is found to be around $2 \cdot 10^5$ Nm/rad, while magnetic damping d_M is in the order of 26 Nms/rad. Therefore, structural and magnetic stiffness are comparable, and this justifies not negligible coupling between structural and magnetic phenomena, as experimentally observed.

$$f_n = \frac{1}{2\pi}\sqrt{\frac{k(J_m + J_d)}{J_m J_d}} \tag{4.1}$$

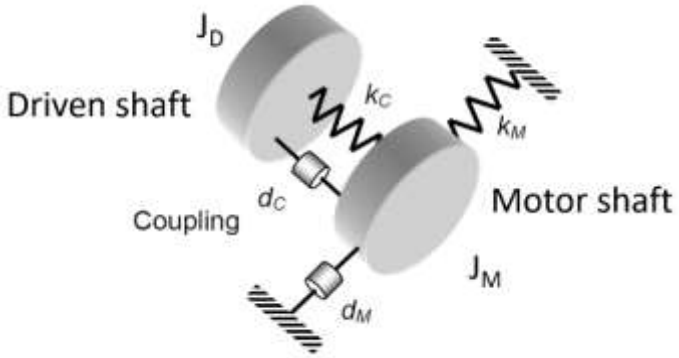

Figure 4.4 – Lumped parameter model including magnetic effects [30]

A preliminary identification of the system is usually helpful in the study of its dynamic behavior. Indeed, such procedure allows to interpret its operational response by detecting the most significant spectral contents in the assumption of linear behavior. Furthermore, the preliminary identification is capable of detecting the kind of excitations that cause a particular response. In the case at the hand, system torsional response is mainly related to the two vibration modes previously identified that are excited by the electromagnetic force. This type of interaction is determined by the way the induction motor is controlled. In addition, determining the response characteristics (and, particularly, the degree of irregularity) of a rotor-bearing system permits to assess aspects related to the stability of the hydrodynamic supports.

A time-frequency analysis is performed on torsional strain response during a free run-down where the induction motor acts as a simple mechanical inertia (i.e. it is switched off). In such operating conditions there is no significant spectral content, thus indicating the absence of a remarkable dynamic torsional response. On the contrary, in the same operating conditions, the lateral response highlights significant spectral contents ascribable to residual mechanical unbalance which excites flexural operational deflection shapes. Therefore, since lateral vibrations are present, the absence of relevant torsional response suggests how in the examined operating conditions lateral vibration

cannot induce significant torsional response in the shaft line, thus proving as no coupling phenomena from lateral to torsional dynamics is present.

4.3.2 Lateral vibration modes

In the operational field of interest, the analyzed mechanical system is characterized by two lateral critical speeds. Particularly, the first one is associated to a lateral vibration mode very close to the already identified torsional one and this, as deepened in the following, contributes to making torsional-lateral coupling phenomena more complex within the shaft line. The above-mentioned two lateral critical speeds are well identifiable at 930 and 1728 rpm from the STFT results plotted in Figure 4.5, which reports the lateral response of DS2 bearing detected in run-up test. Such cascade plot allows us to highlight spectral contents related to the operational response of lateral vibrations. In Figure 4.5 synchronous response represents the main component from an energetic point of view; nevertheless, there are other spectral contents whose energy contributions are less relevant which suggest system complexity, between whom 1X higher multiples (e.g. 2Xrev). There are also spectral contents with significant energy in the sub-synchronous range, which are not directly related to synchronous response and which exhibit lower energy level with respect to 1Xrev. Such contributions will be deeply investigated in the following.

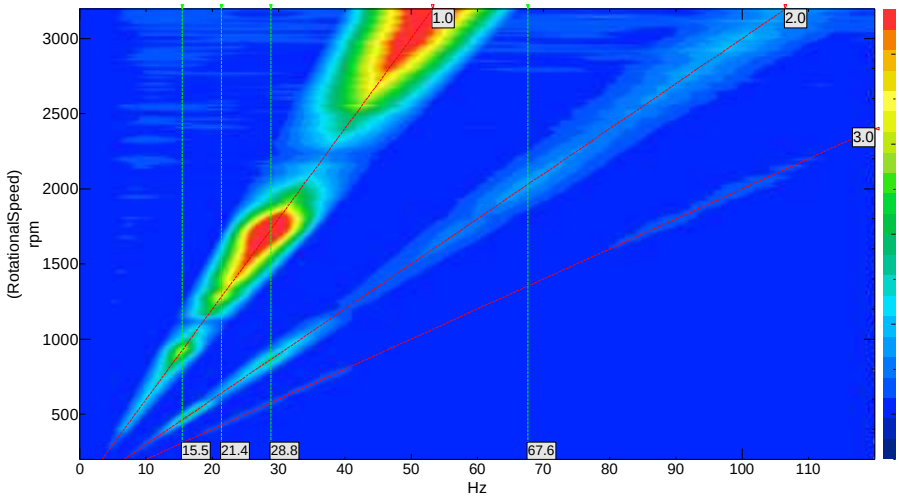

Figure 4.5 – Cascade plot relevant to time-frequency analysis (STFT) of lateral vibrations in DS2 bearing during run-up test

Moreover, side bands can be observed at the highest angular speed range indicating a modulation of 1X engine order: this furtherly confirm the onset of a sub-synchronous phenomenon interacting with synchronous response.

4.4 Analysis of operating responses

Run-up and run-down tests are conducted in the whole operational field of angular speed with constant average acceleration or deceleration intensities, by driving the shaft line with a dynamic torque sufficient to significantly excite system torsional response.

4.4.1. Torsional operating response

Figure 4.6 shows the torque transmitted through shaft line measurement section applied to the driven shaft obtained by means of strain gauge bridge signal, representative of shaft line torsional strain response during a run-up test followed by a subsequent run-down test, both with induction motor enabled. The detected time-history exhibits a strongly unsteady nature of the measured response which is due to the interaction between induction motor drive torque and shaft line dynamic properties. Moreover, the experimental angular speed trace is reported in green on the same plot in order to better identify run-up and run-down tests current operating condition.

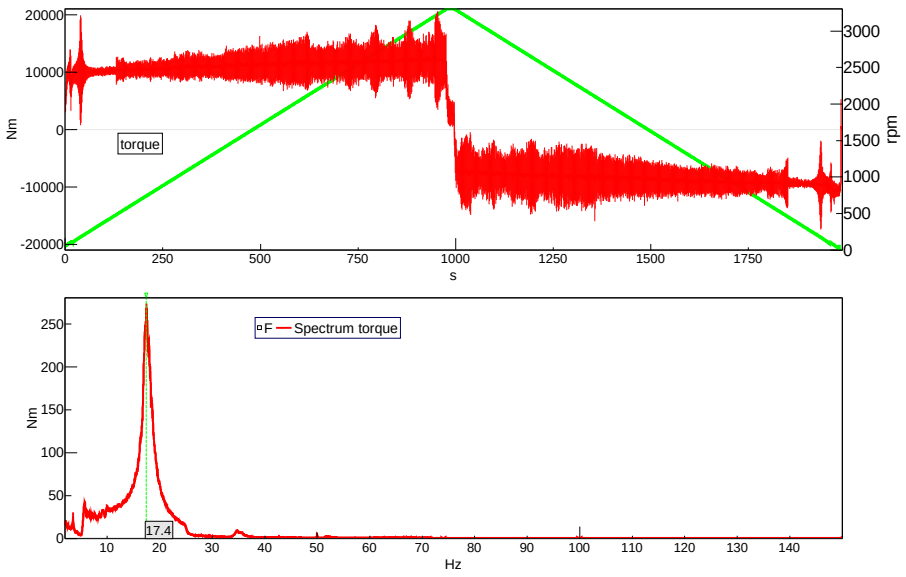

Figure 4.6 – Operating torsional strain during run-up and run-down tests (top – time history, bottom – frequency spectrum)

The spectrum response is characterized by two significant frequency contents related to the two previously identified torsional modes (with natural frequencies equal to 5Hz and 17Hz) that mainly characterize shaft line operational response. The detected behavior allows us to assess that the participation of the highest frequency torsional mode is dominant in the operational vibration. Indeed, from the analysis of spectral contents of operating torsional deformation, it can be noted how the torsional "rigid" vibration mode of the whole shaft line constrained by the equivalent stiffness due to the electromagnetic field gives a negligible contribution in system operational response.

In the following Figure 4.7 a time extract of the previously introduced transmitted torque is reported; moreover, on the same plot it is reported an extract of instantaneous angular speed trace acquired during a run-up test detected by means of the phonic wheel in correspondence with the intermediate shaft. From such experimental trace, angular speed fluctuations can be detected and quantified on the shaft line end characterized by lower inertia (i.e. motor shaft side). Indeed, rotational speed oscillations in the order of 20 rpm (peak to peak) are well evident from the diagram presented below. An evident main periodicity is detectable by the reported time-history which corresponds to system first torsional mode. However, the observed trend shows some spikes thus making it different from purely harmonic behavior due to drive torque ripples and system non-linear torsional response. Its corresponding time-frequency analysis performed on the whole run-up test exhibits a spectral content at fixed frequency persisting in all the run-up test which is characterized by higher amplitude.

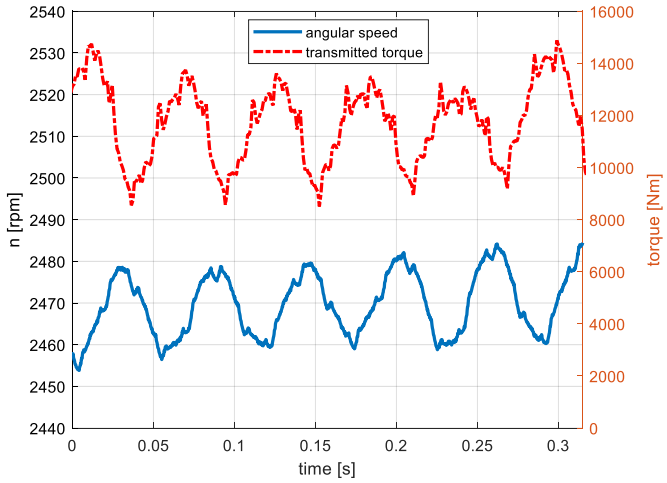

Figure 4.7 – Angular speed trace on the motor shaft and transmitted torque one measured during a run-up test extract

Journals kinematic condition within shaft line hydrodynamic bearings is consequent to the operational torsional deformation previously discussed. The already mentioned lumped parameters modelling allows to assume the shaft line as a two degrees of freedom mechanical system on which making simplified quantitative considerations. Consequently, the ratio of angular speeds as inversely proportional to the inertia moments (J), due to the angular moment conservation principle, angular speed on the motor shaft is scaled with respect to the one of driven shaft of a factor about 219. This allows to assume that the driven shaft side is characterized by a negligible angular speed oscillation.

4.4.2 Lateral operating response

Figure 4.8 reports Bode diagram of amplitude and phase of the fundamental component (synchronous response) of journal vibrations. It evidences the presence of localized hysteresis phenomena that make

their onset in the second part of the run-up test, beyond system first torsional critical speed. Differences between amplitude and phase are found between run-up and run-down tests in a well-defined rotational speed range and moreover these phenomena are more marked in case of low residual mechanical unbalance in the driven shaft.

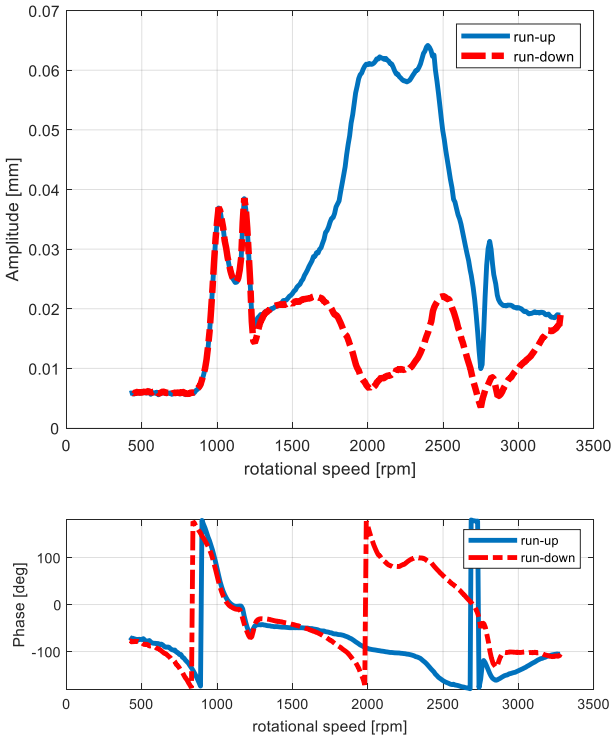

Figure 4.8 – Operational lateral response in run-up and run-down tests at DS2 bearing: Bode diagram of synchronous component

Such an operational system response cannot either be simulated by means of classical linear models, therefore it is necessary to employ more advanced theories which involve fluid-structure interactions (coupling phenomena between hydrodynamic journal bearings and shaft line rotordynamic behavior), as reported in section 4.5.

4.4.3 Possible causes of hysteresis

The difference between run-up and run-down test curves in Figure 4.8 (hysteresis) is an indicator of a typically non-linear behavior. Technical literature reports many cases of shaft-lines with no interposed gearbox where a similar behavior is described, but none of these is comparable to the presented case study. For instance, in [19] a rotor system is considered where hysteresis appears in the synchronous lateral response due to significant shaft line overhang. Indeed, it can cause large dynamic deformations.

In a rotor-bearing system non-linearity sources can be generally reconducted to shaft line misalignments [32], tribological problems (friction in boundary, mixed or hydrodynamic lubrication

regime), material non-linearities (inhomogeneous stiffness distributions causing mechanical unbalance and coupling). In the present case hysteresis is due to different causes. While material non-linearities are not responsible, since all of the components are correctly designed and the elastic limit is never reached, misalignments and hydrodynamic bearings can be influential. Indeed, a potential hydrodynamic journal bearings unstable behavior can cause local hysteresis, as reported in literature [20-21] and, in turn, misalignments can influence bearing behavior.

4.4.4 Interpretation of system operating responses

In the present section, shaft line lateral response is analyzed in a large frequency and rotation speed range, in order to capture all relevant spectral contents.

Figure 4.9, the cascade plot of DS1 bearing lateral vibrations, shows a sub-synchronous spectral content characterized by significant amplitude at a frequency of about 15 Hz above a rotational speed of roughly 2200 rpm, higher than the onset speed of localized hysteresis phenomena shown in Figure 4.8. Indeed, the rotational frequency corresponding to 2200 rpm roughly doubles the torsional critical speed and half-frequency perturbations are highly influent on bearing stability, as proved in the next paragraphs. At speed higher than 2200 rpm, the response frequency of the detected spectral content remains locked. Consequently, since the first critical flexural resonance is also close 15 Hz, the sub-synchronous phenomenon can be interpreted as oil-whip. Usually, below the whip frequency oil-whirl is visible on a 0,5X engine order. Differently, in the analyzed case whip appears abruptly. Therefore, the perturbation that allows the whip phenomenon to develop is different from a whirl instability. Accordingly, the bearings are correctly designed, so that they are sufficiently loaded to avoid oil whirl instability.

Even in forced run-down test the energy trend of the detected sub-synchronous spectral content is analogous to the one described for run-up test.

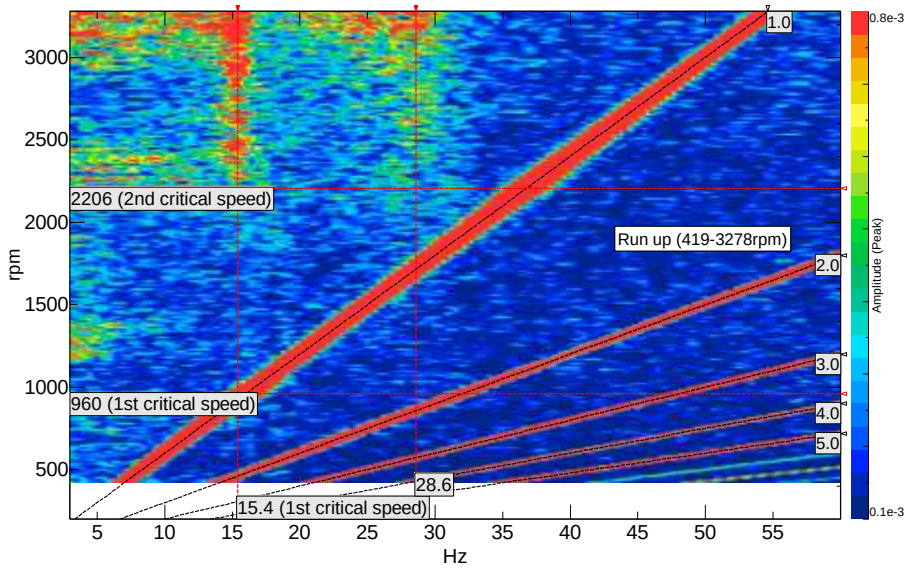

Figure 4.9 – Cascade plot relevant to time-frequency analysis (STFT) of forced run-up test of lateral vibrations in DS1 bearing

Torsional strain cascade plot reported in Figure 4.10 highlights a spectral content that exhibit an energy increase at system first resonant frequency (17 Hz) during run-up test for rotational speeds higher than 2000 rpm. Such energy rise is due to a further contribution in torsional system response that can be easily identified in the above-mentioned oil-whip phenomenon. Indeed, as for the lateral vibrations (cascade plot in Figure 4.11), even torsional response energy increases above the rotational speed of 2200 rpm due to oil-whip phenomenon at expense of the energy dissipated by the induction motor in driving torque oscillations. Moreover, some sub-synchronous spectral contents characterized by very low energy can be identified in the colormap which can be ascribable to ripples in driving torque profile.

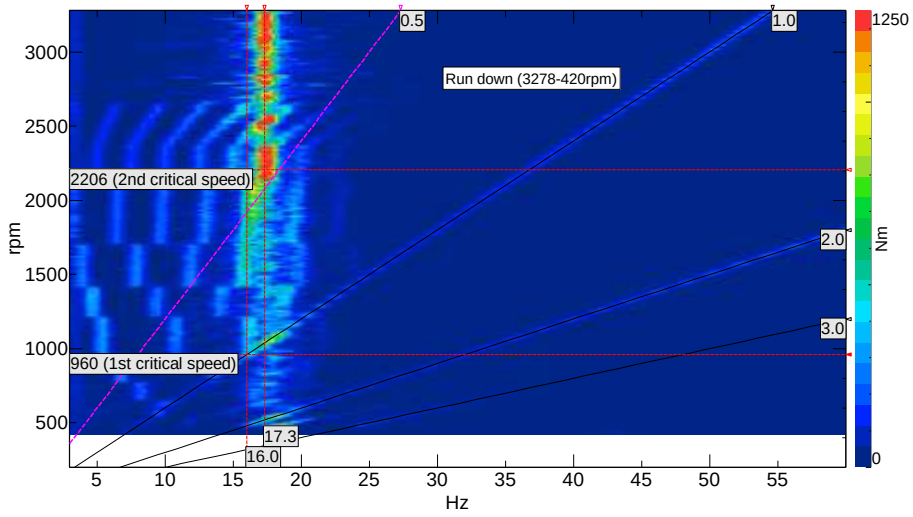

Figure 4.10 – Cascade plot relevant to time-frequency analysis (STFT) of forced run-down test on torsional strain of driven (nodal section) shaft

Figure 4.11 presents a comparison between time-frequency analysis (SFTF) performed on forced and free run-down evaluated on DS1 bearing lateral response. Figure 4.11b shows how the sub-synchronous spectral content with locked frequency persists even in the free run-down, so that hysteresis may also occur in such operating condition. Comparing the same figure and its counterpart in forced run-down (Figure 4.11a) yields that the energy associated with whip is lower in free run-down. Indeed, in such condition the induction motor does not excite the torsional natural frequency at 17Hz. Anyway, the residual sub-synchronous energy is still visible in Figure 4.11b. The comparison between run-up (Figure 4.9) and forced run-down (Figure 4.11a) would suggest a fast decay of the whip lateral vibration, so that the residual energy in free run-down (Figure 4.11b) seems to be excessive. Nevertheless, in such free run-down each portion of the time-frequency map is obtained after a run-up to the maximum velocity of the successive lower portion and therefore oil-whip decay appears to be slower, while in the forced run-down this decay seems faster since it is obtained after a single run-up. Moreover, in the case of forced run-down test, it is present a broadband response between 0 and 10Hz at around 2000rpm, detectable also in run-up (see Figure 4.9), that is probably related to a state change in bearing stability which occurs in correspondence with the onset of oil-whip conditions. In a nutshell, these results confirm that the oil-whip phenomenon can yield the hysteresis observed in Figure 4.8.

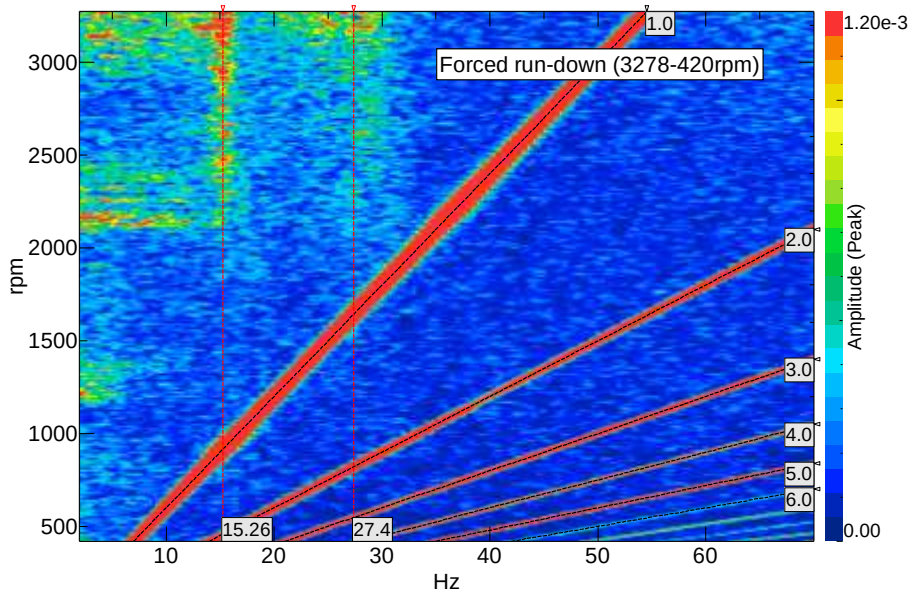

a)

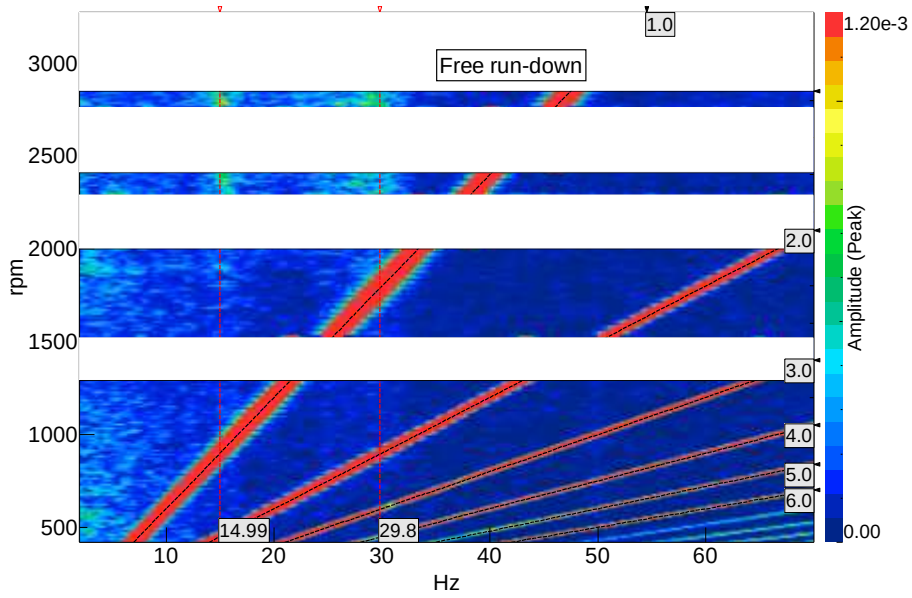

b)

Figure 4.11 – Cascade plot relevant to time-frequency analysis (STFT) performed on DS1 bearing lateral vibration: forced run-down (a), free run-down (b)

4.5. Bearing instability

4.5.1 Instability according HBT

Hysteresis can affect rotor-bearing systems where oil-whip occurs, since such phenomenon can develop differently in run-up and run-down phases. Accordingly, it can be characterized by distinct values of run-up threshold speed (RUTS) and run-down threshold speed (RDTS) [22, 23]. Such difference between run-up and run-down threshold speed or energy yields the hysteresis phenomenon

occurring in the presented experimental activity. Indeed, three different decays of the whip energy are detected in run-up, forced run-down and free coast-down, as discussed in section 4.4.4.

Hopf bifurcation theory (HBT) applied to rotors supported by radial hydrodynamic bearings [22, 23], allows to distinguish two different types of instabilities referred to as subcritical and supercritical bifurcation. If the conditions of supercritical bifurcation exist, when the rotor reaches a critical speed (considered as the threshold speed for the instability arise), the journal gradually begins to lose its stability and the amplitude of its precession motion (oil-whirl) increases continuously and progressively (ramp-up). On the contrary, in subcritical bifurcation conditions, the crossing of the critical speed (always defined as above) involves a sudden and total loss of journal stability similar to a whip (oil-whip), whose precession amplitude suddenly assumes high values, i.e. the amplitude of the oil-whip jumps up to such a large orbit that the journal tends to asymptotically approach the clearance circle (jump-up). The existence of such two important phenomena is supported by specific experimental investigation [23]. The hysteresis phenomenon can only exist in cases of subcritical bifurcation since it formally admits unstable periodic solutions from a rigorous mathematical point of view. In such case, a subcritical bifurcation profile can be determined within the hysteresis cycle. According to such profile, the stability of the rotor-bearing system between the rotational speeds (RDTS and RUTS) that delimit the cycle is determined by the magnitude of a perturbation affecting the system. Particularly, if the amplitude of the perturbation is comprised within the subcritical bifurcation profile, the journal remains stable, otherwise the perturbation is able to activate oil-whip and a jump-up occurs in the orbit of the journal.

The jump-up occurrence can be identified in Figure 4.9 and Figure 4.11 just above 2000rpm, where the already mentioned broadband response may also be found. A sub-synchronous spectral content at fixed frequency characterized by remarkable energy is found after such broadband excitation, at higher angular speeds, thus confirming oil-whip onset even from experimental data.

4.5.2 Perturbation mechanisms

The last missing element in a consistent explanation of the phenomena experimentally highlighted in the shaft line during run up/down tests is the nature of the perturbation cited in the previous paragraph. In the present case whip phenomenon appears without previous occurrence of oil-whirl (section 4.4.4). Therefore, the ramp-up cannot make up the required perturbation as in the case of lightly loaded bearings. For sufficiently loaded bearings, the perturbation may be a synchronous whirl due to the unbalance [23] and this rule holds generally. Nevertheless, in our case, since unbalance can be minimized, the instability and thus the perturbation are clearly related to the torque effect and its amplification at the natural frequency. Hence, the perturbation should be linked to a dynamic or a kinematic effect of the shaft line torsion. Both effects are capable to couple torsional and lateral

vibrations of the shaft line, where bending occurs at expense of the torsional energy introduced by the electric motor.

4.5.3 Dynamic perturbation

The dynamic effect is due to a rotating load caused by the driving torque and a precession motion of the two parts of the shaft. As explained in detail in section 4.5.5, such precession must occur at the torsional critical speed ω_t. Therefore, the rotating load can be calculated by means of the following expression

$$F_r = \frac{\Delta F_r}{2}\cos\left(\omega_t t + \varphi_r\right) \tag{4.2}$$

where ΔF_r is the intensity of the rotating load acting on the bearings and φ_r its phase. Since in the case of the analyzed shaft line the torsional critical frequency is roughly half the shaft rotation speed ($\omega_t \approx \omega/2$) at the onset of oil-whip (rotation speed about 2040 rpm), the load F_r can yield effective perturbation of the bearing and affect its stability. Indeed, as well known by designers of hydrodynamic bearings for reciprocating engines and widely reported in the relevant literature, e.g. [33], such dangerous working condition, usually referred to as "half-speed load vector" effect, causes the load capacity due to wedge effect to vanish, so that only the squeeze effect can temporarily avoid the occurrence of zero oil film thickness. Therefore, the half-speed load vector condition is acceptable in connecting rod bearing design only for limited periods of time, i.e., for short fractions of the load-cycle. Anyway, the bearings of the test rig in analysis are not permanently loaded by a full half-speed load, otherwise their operation would be impossible. Indeed, they are primarily loaded by the weight of the shaft, which is the main load considered in their design phase, and by secondary dynamic loads (or perturbations) due to various causes, which include magnetic effects, shaft unbalance and, exactly, the rotating load due to the engine torque ripple expressed by Eq. (4.2). Hence, the studied bearings are only partially loaded by a half-speed force. Since the oil film cannot steadily react to this load component, for sufficient entities of the torque ripple it can lead to large perturbations of the journal position exceeding the subcritical bifurcation profile and causing bearing instability (oil-whip) as discussed in section 4.5.1.

All of the bearings of the shaft line can be affected by the described dynamic perturbation.

4.5.4 Kinematic perturbation

The kinematic effect is the variation of the shaft rotating speed due to the external torque, which is reported in Fig. 7. Since in the forced response of the rotor-bearing system such variation occurs at a prevailing frequency, i.e. the critical torsional frequency ω_t, the following expression is assumed for the journal speed or, equivalently, twice the entrainment speed of the bearings:

$$U = \omega R + \frac{\Delta U}{2}\cos(\omega_t t + \varphi_U) = \omega R + \frac{\Delta\omega}{2} R\cos(\omega_t t + \varphi_U) \tag{4.3}$$

where ΔU is the (peak-to-peak) amplitude of the oil entrainment velocity variation, $\Delta\omega$ the corresponding angular speed rotation and φ_U a possible phase.

In agreement with the Reynolds equation, a variation of the shaft rotation speed at a given frequency yields a corresponding hydrodynamic reaction rotating at the same frequency. Consequently, since such reaction rotates at the speed ω_t, which is half the rotation speed ω at the onset of oil-whip for the test rig, it can also behave as a half-speed load vector. Since, the study of the effect of half-speed kinematic perturbation has not been retrieved in literature, it is numerically studied in the following. Since negligible angular speed oscillation involves the driven shaft (section 4.4.1), the kinematic perturbation involves only the bearings supporting motor shaft side, e.g. the IS2 bearing (Figure 4.1).

4.5.5 Dynamic model of the system

A simple dynamic model of the rotor-bearing system can be devised, which incorporates the effects of both kinematic and dynamic perturbations. While the driven shaft simply rotates around a fixed axis, the bearings of the motor shaft are subjected to kinematic perturbation. Section 4.7.2 proves by means of numerical lubrication analysis that a kinematic perturbation is capable of inducing a whirling precession occurring at the same frequency of the perturbation. Consequently, for the kinematic perturbation in Eq. (4.3), the precession frequency of the motor axis around the fixed driven axis is ω_t. Since the kinematic perturbation is small for the test rig in study, the relevant effects are equally small despite the amplification at the oil-whip onset speed. Nevertheless, the small whirl motion, sufficient to begin the precession between the two axes, is soon amplified by the system dynamics according to the model explained below. Therefore, it assumes that the discussed precession motion is already developed and, in addition, that angular misalignments between axes of shaft and bearings are neglected. The corresponding dynamic rigid-body model is reported in Figure 4.12, where e_s is the misalignment between the parallel axes, i.e. Shaft 1 and 2. The blue double Cardan joint allows their synchronous rotation θ with angular acceleration α. In turn, due to dynamic equilibrium the relative rotation θ_s of such two axes must occur with relative angular acceleration α_s such that the dynamic perturbation load applied to bearings is:

$$F_s = F_1 = -F_2 = m_d e_s \alpha_s \tag{4.4}$$

The perturbation load F_s is a radial load acting on the joint, which results in bending stress, lateral vibrations of the shaft and corresponding rotating load F_r for the bearings. Such load rotates at the relative rotation speed ω_s of the two shafts, whose variation can be found from the equation of dynamics for the whole shaft line as follows:

$$\alpha_s = \frac{M_m - (J_m + J_d)\alpha}{m_d\ e_s^{\,2}} \tag{4.5}$$

In the forced response of the system, the value of ω_s depends on the excited mode. Particularly, when the external torque of the electric motor excites the torsional mode, the perturbation load rotates at the torsional natural pulsation frequency. In such condition, the engine torque is determined near the torsional speed by the corresponding modal contribution solely

$$M_m = \frac{\Delta M_m}{2}\cos(\omega_t t) \tag{4.6}$$

where ΔM_m is the (peak to peak) amplitude of the engine torque ripple. Let $\Delta\omega$ be the (peak to peak) amplitude of rotational speed according to Eq. (4.3), where φ_U is assumed to vanish in resonance conditions. By substituting for the time derivatives finite differences with time increment equal to the period T of the critical torsional vibration (T = 1/ (2π ω_t)) and by taking advantage of Eqs. (4.3) and (4.6), Equation (4.5) becomes

$$\alpha_s \cong \frac{\Delta\omega_s}{T} = \frac{1}{2}\frac{\Delta M_m - (J_m + J_d)\,\Delta\omega/T}{m_d\ e_s^{\,2}}\cos(\omega_t t) \tag{4.7}$$

A more detailed model considers the rotor torsional flexibility (lumped in the joint) and allows different rotational speeds ω_m and ω_d for the motor and the driven shafts, respectively. If the conservation of angular momentum of the double torsion pendulum is also considered, Equation (4.7) is turned into the following expression

$$\alpha_s \cong \frac{1}{2}\frac{\Delta M_m - 2\,J_m\,\Delta\omega_m/T}{m_d\ e_s^{\,2}}\cos(\omega_t t) \tag{4.8}$$

Substituting Eq. (4.8) in Eq. (4.4) yields the rotating load acting on the motor shaft end

$$F_s = \frac{1}{2}\frac{\Delta M_m - 2\,J_m\,\Delta\omega_m/T}{e_s}\cos(\omega_t t) \tag{4.9}$$

Since the torque must be constant along the shaft axis, if a bearing is located at a distance d from the motor shaft end, the dynamic perturbation F_r defined according to Eq. (4.2) acting on the same bearing can be found from Eq. (4.9)

$$F_r = \frac{F_s e_s}{d} = \frac{1}{2}\frac{2\,J_m\Delta\omega_m\omega_t/\pi - \Delta M_m}{d}\cos(\omega_t t + \pi) \tag{4.10}$$

or, equivalently, its intensity and phase defined by Eq. (4.2) are respectively

$$\Delta F_r = \frac{2J_m\Delta\omega_m\,\omega_t/\pi - \Delta M_m}{d} \tag{4.11}$$

$$\varphi_r = \pi \tag{4.12}$$

Equations (4.10) and (4.11) evidence that the rotating load does not depend on the parallel misalignment es allowed by the joint, so that in first analysis (assumptions of simplified dynamic model and angular misalignments neglected) modifications on this component are ineffective in

reducing or suppressing the hysteresis phenomenon. In addition, the influence of secondary moments on the double Cardan joint is negligible. The rotating load amplitude at a shaft rotation speed of 2040 rpm (double the critical torsional speed) assessed by substituting the parameters of Table 4.1 in Eq, (4.11) is equal to 4554 N and is reported among the bearing calculation data in Table 4.2.

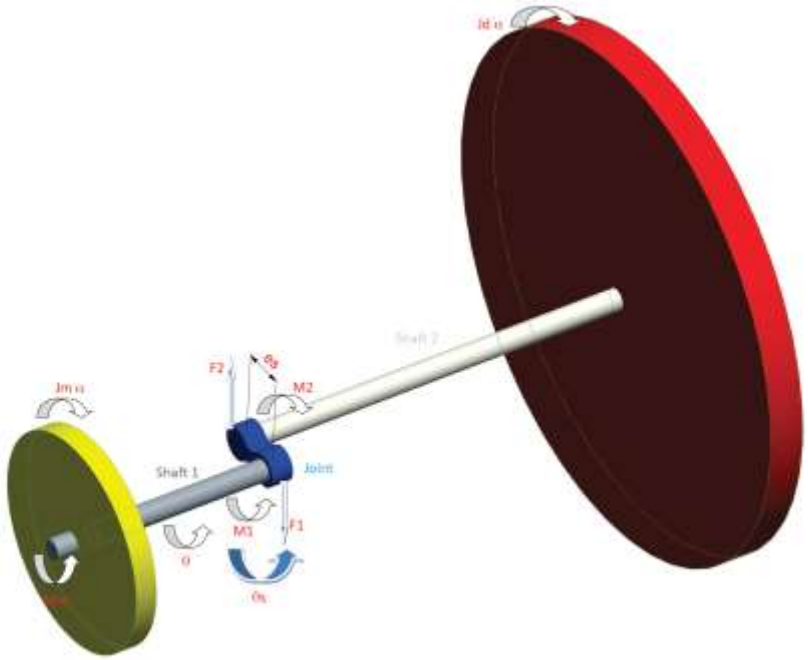

Figure 4.12 – Dynamic perturbation model of the shaft line

Parameter description	**Symbol**	**Value [unit]**
Moment of inertia of motor (or motor shaft)	J_m	130 [kg m^2]
Moment of inertia of turbine rotor (or driven shaft)	J_d	28500 [kg m^2]
Measured motor torque ripple amplitude (peak to peak) at a rotation speed of 2040 rpm	ΔM_m	6980 [N m]
Measured motor shaft angular speed oscillation amplitude (peak to peak) at a rotation speed of 2040 rpm	$\Delta\omega_m$	2.094 [rad/s] (20 [rpm])
Measured critical (natural) torsional frequency	ω_t	106.81 [rad/s] (17 [Hz])
Shaft overhang (distance between IS2 bearing and motor shaft end)	d	500 [mm]

Table 4.1 – Parameters of rotor-bearing system dynamic model

4.6 Experimental analysis of bearings

In view of the above considerations about bearing stability (section 4.5.1), the journal lateral vibrations of the IS2 bearing, which is submitted to both dynamic and kinematic perturbations, are measured. Figure 4.13 reports the cascade plot obtained by means of a time-frequency analysis (STFT) of the relevant signal recorded during a run-up test. It shows a sub-synchronous spectral

content with frequency locked at 17 Hz, which amplitude rise from a speed of roughly 2000 rpm on suggests the onset of oil-whip instability. Moreover, such sub-synchronous spectral content modulates the synchronous response (1X), as it can be detected by the visible sidebands, which energy is perceivable. Such modulation effects are highlighted by means of black dotted cursors located at ±17Hz with respect to the synchronous component (1X). Furthermore, 1X order together with its integer multiples are evidenced by means of black dashed line cursors for completeness. Finally, a blue dashed horizontal line together with 0.5X order cursor are reported to emphasize that where instability makes its onset, even modulated components increase their energy, thus confirming that the detected phenomenon is representative of a physical signal. Figure 4.14 is the cascade plot relevant to the STFT of lateral vibration signal recorded during the run-down test. Analogous considerations as for the corresponding run-up test can be made, with the difference that the sub-synchronous energy content persists below 2000 rpm. This can be noticed even by observing energy levels of sidebands, that is of components modulated by 1X order, which is higher even at lower angular speeds with respect to run-up test. Finally, sub-synchronous spectral contents with almost not remarkable energy levels attributable to induction motor torque ripples can be detected both in run-up and run-down tests. In short, the results presented in both the current section and section 4.4.4 provide experimental evidence that oil-whip and hysteresis occur. Particularly, the instability threshold speeds RUTS during run-up are roughly 2000 and 2200 rpm for IS2 and DS1 bearings, respectively. The corresponding values during run-down are about 1200 and 2200 rpm for the same bearings. Therefore, the hysteresis phenomenon (RDTS < RUTS) is limited to the IS2 bearing directly driven by the electric motor.

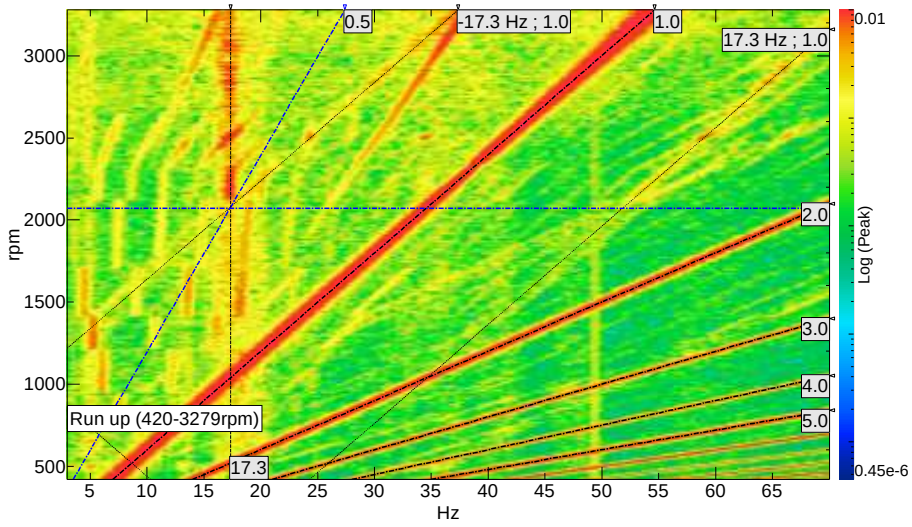

Figure 4.13 – Cascade plot relevant to time-frequency analysis (STFT) of lateral vibration of the journal within IS2bearing in run-up test

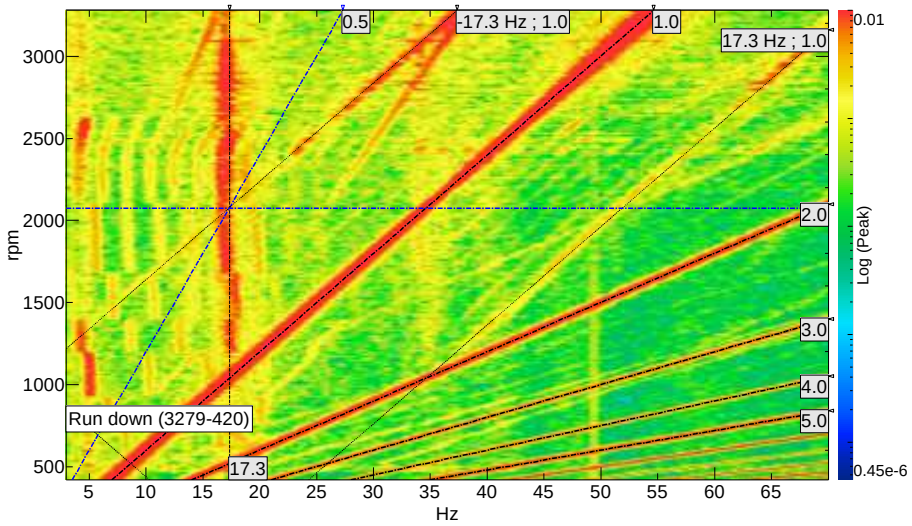

Figure 4.14 – Cascade plot relevant to time-frequency analysis (STFT) of lateral vibration signal of the journal within IS2bearing in run-down test

4.7 Numerical analysis of bearings

The dynamic and kinematic perturbations defined in sections 4.5.3 and 4.5.4, respectively, are turned into corresponding perturbations of the journal position by the lubricant film of the hydrodynamic bearings. Therefore, lubrication analysis is required in order to assess if a perturbation can affect journal stability, i.e. if the resulting journal displacement is comparable with the subcritical bifurcation profile. In order to simplify such assessment, the stability is analyzed with reference to the perturbation conditions solely at the onset of instability (2040 rpm). In other words, if the perturbation load yields large modifications of the journal displacement or causes small film thickness by itself, we assume that it can also cause the oil-whip. Such assumption allows us to check if the unstable behavior detected by the experimental study is confirmed by the non-linear dynamic analysis of the lubrication problem.

4.7.1 Lubrication analysis method

In order to evaluate the effect of the perturbations, the Reynolds equation is coupled with the dynamic equation of motion of the journal, considered as a material point. Thermal effects are ignored, so that the lubricant model is iso-viscous. All the classical Reynolds hypotheses, including the assumption of laminar flow, are considered valid. The adopted solution method of the Reynolds equation incorporates JFO boundary conditions to ensure a full dynamic simulation of cavitation or the conventional Swift-Stieber (Reynolds) conditions for quasi-static cavitation. Particularly, results reported in sections 4.7.2, 4.7.3 for the general case of a cylindrical bearing are obtained by means of the quasi-static cavitation model, while oil film history is considered in the final results of the test rig bearing in section 4.7.4. Details of the mathematical model as well as its Finite Element (FE) implementation are provided in [34], with the difference that in the present work the dynamic

equations [35] are used instead of the equilibrium equations to simulate the motion of the journal. To this goal, its acceleration is computed by means of standard finite differences, i.e. second order backward difference of journal center displacements. The boundaries of the journal mobility region are calculated according to the method explained in [36], which becomes essential in the case of the four-lobe bearing that support the studied shaft-line.

4.7.2 Effect of kinematic perturbation

As far as we know, the influence of kinematic perturbations on bearing stability has not still been studied. Therefore, a non-linear stability analysis of a benchmark circular bearing (for the sake of simplicity) is briefly presented in order to show the numerical evidence of such phenomenon. To this aim, Equation (4.3) is added to the mathematical model explained in section 4.7.1 in order to simulate the entrainment speed variation with time.

The independent dimensionless parameters of the analysis are the Sommerfeld number (S), the bearing aspect ratio (L / D), the mass of the shaft (M), the ratio between perturbation frequency and synchronous speed (ω_t / ω) and the relative perturbation (peak-to-peak) amplitude ($\Delta U/(\omega R)$).

Sommerfeld number is defined according to the following expression (usual in lubrication analysis)

$$S = \frac{\mu \pi \omega}{30\, p_m} \left(\frac{R}{c} \right)^2 \tag{4.13}$$

where μ is the (constant) viscosity of the lubricant, c the bearing radial clearance and p_m the static load (shaft weight W) per unit of projected bearing area ($p_m = W/(LD)$).

The shaft mass m is nondimensionalized as follows

$$M = m \frac{c\omega^2}{W} \tag{4.14}$$

All the simulations are carried out for the same bearing geometry and the relevant constant aspect ratio L/D is equal to 0.3.

Initially, the kinematic perturbation is excluded, and an unstable operating condition (oil-whirl) is simulated at a high Sommerfeld number (S = 1.3 104) for M = 110.5. In such condition the bearing is sufficiently unloaded to develop oil-whirl with the assigned shaft mass, as shown in Figure 4.15. Particularly, a spiral orbit (Figure 4.15a)) starts from an arbitrary initial journal location, until a stable periodic solution with frequency $\omega/2$ associated with supercritical bifurcation [23] (Fig. 4.15b)) is reached.

Oil-whirl instability can be suppressed by properly increasing the bearing load W for the same shaft mass m, e. g. for corresponding non-dimensional parameters S = 661 and M = 5.5, respectively. Indeed, Figure 4.16 shows that in such condition (with no kinematic perturbation) the journal center path reaches the static equilibrium position near the bearing center regardless of the initial location,

which is chosen at high eccentricity (0.9) in the presented plot. The simulation in the same working conditions (S = 661 and M = 5.5) is repeated adding a kinematic perturbation of considerable amplitude $\Delta U/(\omega R)$ = 0.5 and perturbation frequency ratio ω_t / ω = 0.4 near the "half-speed load vector" condition. As shown by Figure 4.17, a stable periodic solution is found, and oil-whirl reappears. Therefore, a kinematic perturbation of proper amplitude and frequency can modify the bearing stability threshold. Finally, a perturbation frequency ratio ω_t / ω = 0.5) that meets the "half-speed load vector" condition is chosen keeping unchanged the remaining simulation parameters (S = 661, M = 5.5, $\Delta U/(\omega R)$ = 0.5). Figure 4.18 shows a large amplification of the whirling amplitude. Hence, a half-speed kinematic perturbation is very effective in changing the stability threshold.

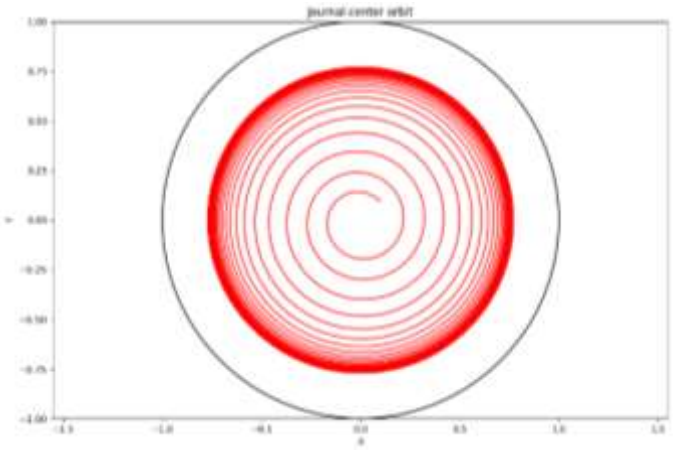

a)

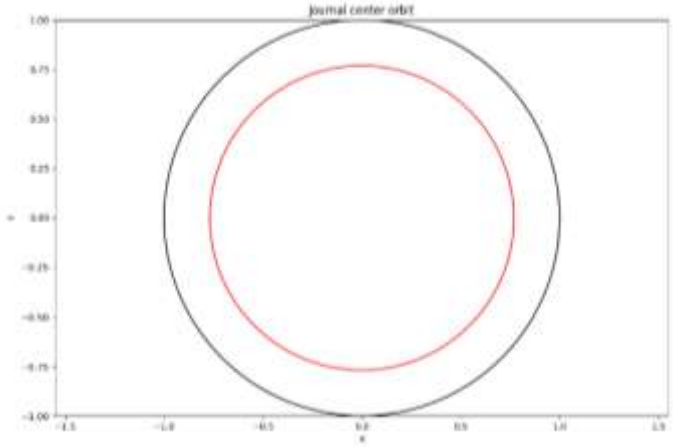

b)

Figure 4.15 – Journal center path in a circular bearing (L/D=0.3) for S = 1.3 104 and M =110.5 (without kinematic perturbation, with oil-whirl onset): a) transient motion, b) stable periodic solution

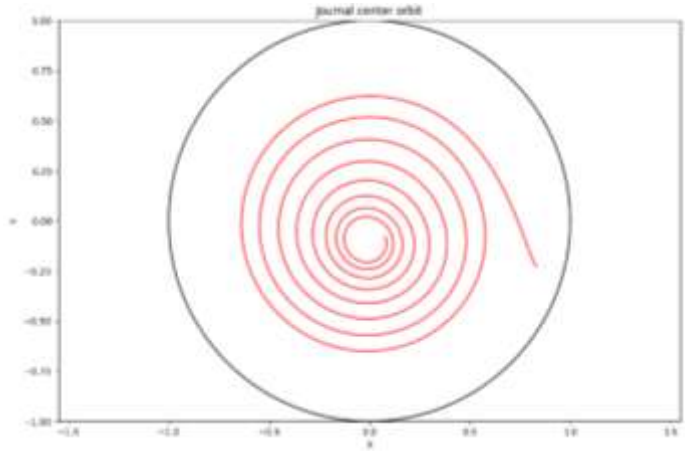

Figure 4.16 – Journal center path during transient motion toward equilibrium position in a circular bearing (L/D=0.3) for S = 661 and M =5.5 (without kinematic perturbation)

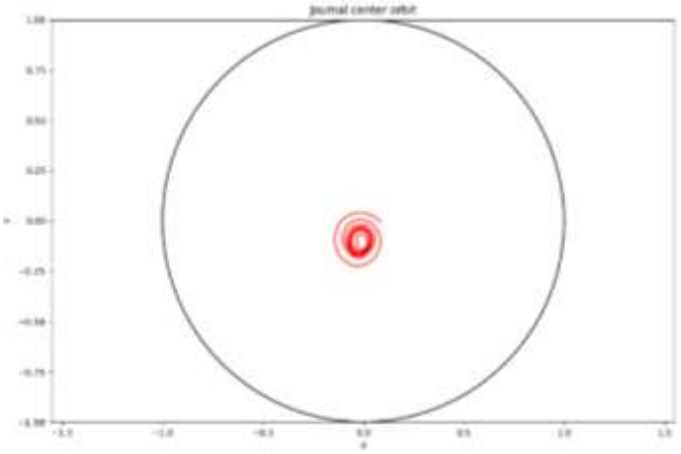

a)

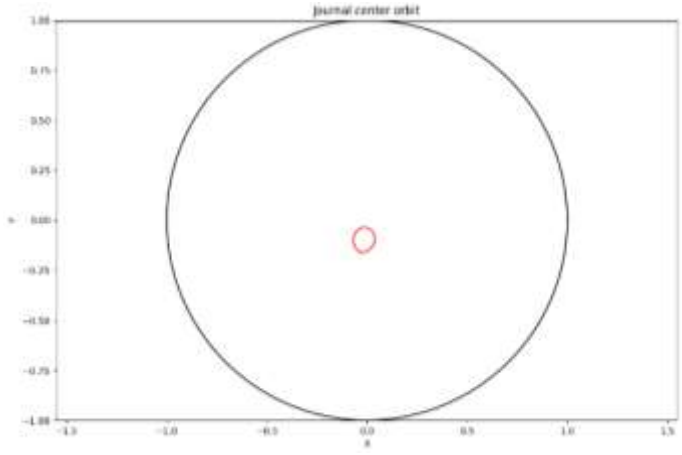

b)

Fig. 17 – Journal center path in a circular bearing (L/D=0.3) for S = 661 and M =5.5 under kinematic perturbation with ω_t/ω = 0.4, $\Delta U/(\omega R)$ = 0.5: a) transient motion, b) stable periodic solution

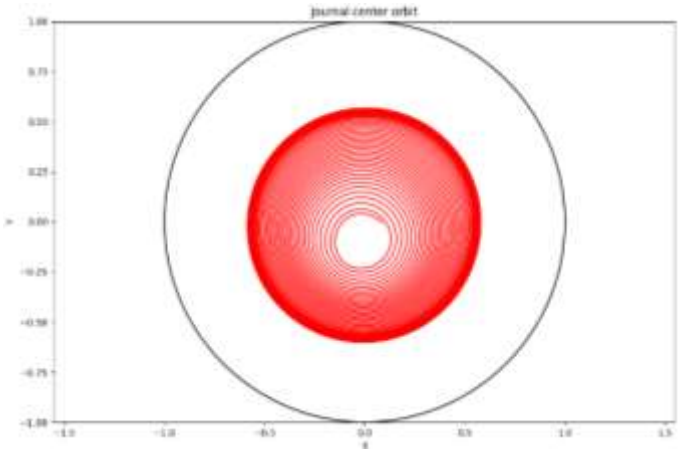

a)

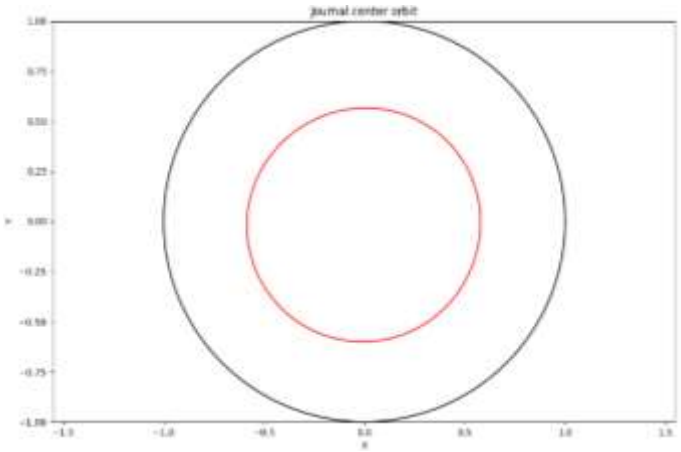

b)

Figure 4.18 – Journal center path in a circular bearing (L/D=0.3) for S = 661 and M =5.5 under kinematic perturbation with ω_t/ω = 0.5, $\Delta U/(\omega R)$ = 0.5: a) transient motion, b) stable periodic solution

The oil-whirl phenomenon induced by a perturbation numerically evidenced in the last two simulations (Figs 4.17-4.18) is very different from the classic "half-frequency oil-whirl" [37] in that the whirling precession occurs at the same frequency of the perturbation as for the forced vibration of a linear system. Therefore, such phenomenon will be referred to as "forced oil-whirl" in the following.

A campaign of simulations on the chosen circular bearing (L/D = 0.3) is performed for the same working conditions (S = 661 and M =5.5) and perturbation amplitude ($\Delta U/(\omega R)$ = 0.5) but different values of the frequency relevant to the harmonic perturbation speed in order to assess the forced response of the bearing and its sensitivity with respect to the perturbation frequency. The whirling amplitude A_{max} is measured by the major diameter of the nearly elliptical orbit shapes. The main result of the simulation campaign is illustrated by Figure 4.19, which plots the dimensionless whirl-amplitude A_{max}/c against the perturbation frequency ratio ω_t/ω.

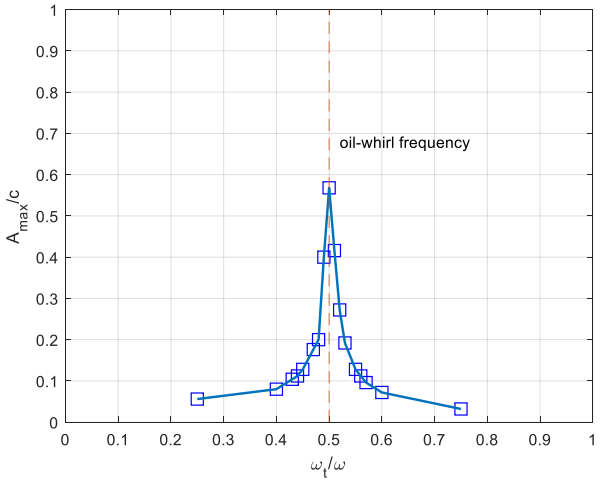

Figure 4.19 - Frequency response to harmonic kinematic perturbation ΔU/(ωR) =0.5) of a stable circular bearing (L/D=0.3, S=661, M=5.5)

As clearly suggested by Figure 4.19, the maximum amplification of the forced oil-whirl phenomenon is at the "half-speed load vector" condition corresponding to a perturbation frequency ω_t/ω=0.5, while the periodic orbit amplitude coherently decays when progressively moving away from such critical frequency.

In a further simulation campaign, "half-speed load vector" conditions are maintained, i.e. the half-speed perturbation frequency is kept constant (ω_t/ω=0.5), while the angular speed perturbation amplitude $\Delta U/(\omega R)$ is varied from 0 to 0.5. Figure 4.20 depicts the corresponding results by plotting the output amplitude Amax/c as a function of the input one $\Delta U/(\omega R)$. It shows how the trend is roughly linear below a threshold amplitude $\Delta U/(\omega R)$ = 1/4. Indeed, the bearing behaves like a spring-mass linear system for small perturbations [37, 38]. However, angular speed fluctuations larger than $\Delta U/(\omega R)$ =1/6 (peak to peak amplitude) are not likely to happen in real machines, thus suggesting that in practice the amplitude response is always linear with the perturbation amplitude, while it is strongly non-linear with the perturbation frequency in a narrow frequency range around the oil-whirl characteristic frequency ("half-speed load vector" conditions).

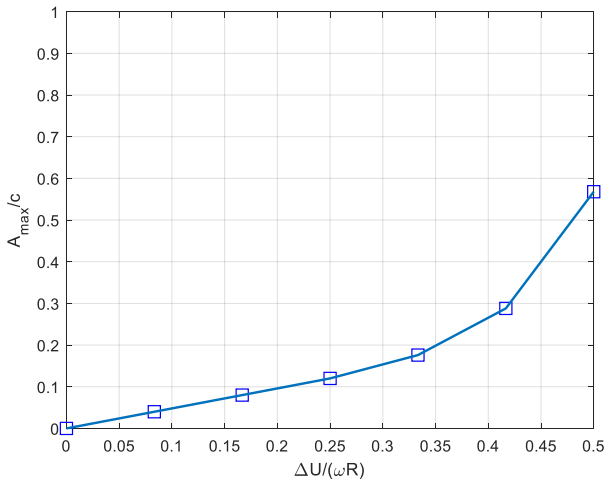

Figure 4.20 – Response to half-speed harmonic kinematic perturbation (ω_t/ω = 0.5) of a stable circular bearing (L/D=0.3, S = 661, M =5.5)

In the analyzed test rig, the measured oscillation (peak-to-peak) of the driven shaft speed is in the order of 20 rpm (see section 4.4.1) corresponding to a dimensionless kinematic perturbation amplitude in the order of 0.02. In addition, the four-lobe bearings are more stable than circular ones. Therefore, the influence of the kinematic amplification in the studied case is expected to be small also at the frequency of maximum amplification (ω_t/ω=0.5).

4.7.3 Effect of dynamic perturbation

In the present section the effect of a sub-synchronous dynamic perturbation is generally evaluated for a circular hydrodynamic journal bearing (with constant aspect ratio *L/D* = 0.3) as done in section 4.7.2 for the kinematic perturbation.

To this aim, further numerical simulations have been performed in order to assess if a sub-synchronous rotating force can actually affect shaft line operational lateral response, by replacing the angular speed perturbation with the dynamic one according to Eq. (4.2). Indeed, in technical literature it is well-known that half frequency loads cannot be supported by the wedge effect [33], but their influence on bearing stability is still unknown. Moreover, literature about half-speed load vectors refers to the whole bearing load rotating at half shaft revolution frequency (0.5X), while in this context the purpose is to investigate the effect of a rotating dynamic perturbation, which is a fraction of the nominal load applied to the hydrodynamic bearing. As done for kinematic perturbation, modifications of whirl stability threshold and the existence of half-frequency amplification under dynamic perturbation are both investigated. To this goal, a response analysis with respect to the perturbation input parameters, i.e. frequency and amplitude of the rotating force, is carried out in the nearly stable operating conditions determined in section 4.7.2, i.e. for *S* = 661 and *M* =5.5. Then the dynamic

perturbation is applied by varying its characteristic frequency, while the amplitude is kept constant at a value two order of magnitudes lower than the static load (i.e. F_r/W=0.01).

Figure 4.21 plots the resulting trend of the dimensionless whirl-amplitude A_{max}/c against the perturbation frequency ratio ω_t/ω, clearly showing how for frequency ratios far from 0.5 the journal displacements are not significantly affected, while in the frequency range centered at ω_t/ω =0.5 an amplified response is obtained due to torsional-whirl occurrence. This expected finding is consistent with the literature dealing with half-speed load vectors and applies such concept to hydrodynamic bearing stability analysis. In the case of the present study, it makes up a preliminary step in the lubrication analysis of the studied machine.

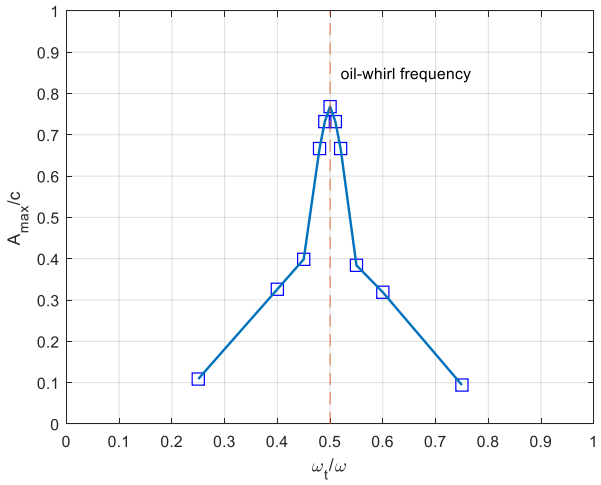

Figure 4.21 - Frequency response to harmonic dynamic perturbation (F_s/W=0.01) of a stable circular bearing (L/D=0.3, S = 661, M =5.5)

4.7.4 Bearing lubrication analysis

The lubrication analysis under dynamic loading conditions is finally applied to one of the bearings of the test rig in study. Particularly, the analyzed support is the four-lobe journal bearing referred to as IS2 in the test rig layout (Figure 4.1). As shown in Figure 4.22a, it operates in load-between-pad (LBP) configuration and oil is supplied by means of axial grooves, which span the θ_g angle and the whole bearing length L in circumferential and axial direction, respectively. The bearing is always statically loaded by the weight W, while different types of dynamic perturbations are applied in three loading conditions: in case A only the kinematic perturbation $\Delta\omega$ is applied according to Eq. (4.3) with phase φ_U = 0; case B only considers the dynamic perturbation F_r assessed by means of Eq. (4.10); in case C both the kinematic and dynamic perturbations defined in the previous load cases are included. Intensity of static and dynamic loads and rotational speed variation amplitude at the onset of oil-whip, i.e. at a shaft speed of 2040 rpm (double of the torsional critical frequency), are reported

in Table 4.2 together with all the bearing data required by the analysis. The resulting dynamic load diagram (for cases B and C) in Figure 4.22b plots the external load components in polar coordinates (θ_s, F_r) for different rotation angles θ of the shaft. The simulations consider the different perturbations required to cause the oil-whip, as the model focuses on the lubricant film solely. The structural behavior of the shaft line should be considered in the model in order to study the subsequent development of the oil-whip phenomenon at higher speed.

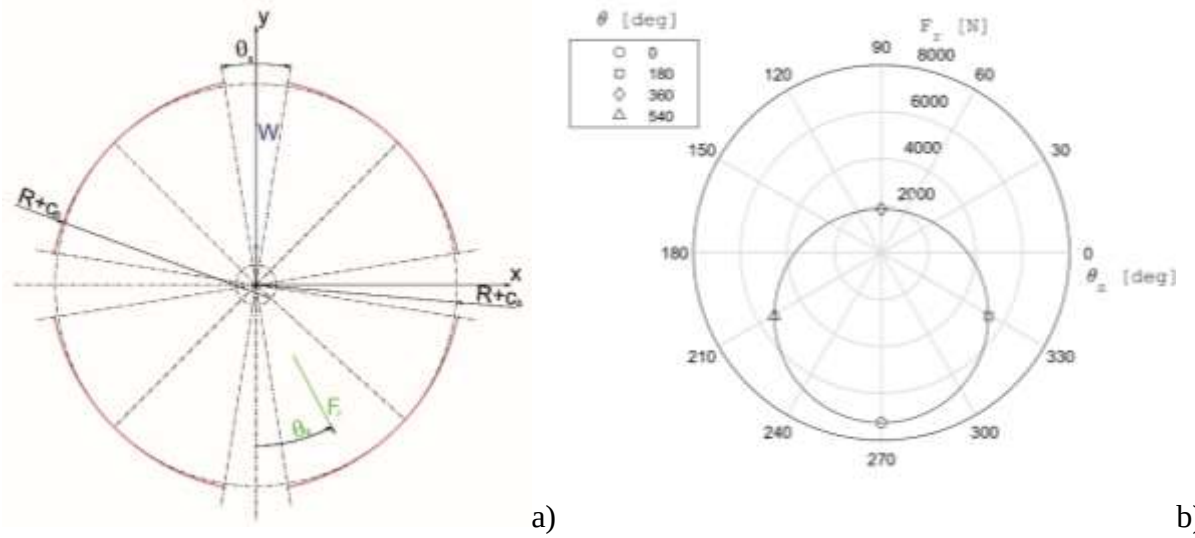

a) b)

Figure 4.22 – Four-lobe journal bearing IS2: a) scheme; b) polar load diagram at the onset of oil-whip (2040 rpm)

Parameter description	**Symbol**	**Value [unit]**
Bearing diameter	D	160 [mm]
Bearing length	L	65 [mm]
Nominal assembled radial clearance	c_b	0.170 [mm]
Pad preload	m	0.8844
Supply hole axial groove circumferential span	θ_g	18 [deg]
Oil viscosity	μ_0	0.0274 [Pa s]
Rotation speed	ω	2040 [rpm]
Rotor weight supported by the bearing	W	2702 [N]
Rotating load amplitude	ΔF_r	4554 [N]
Speed variation amplitude	$\Delta\omega$	20 [rpm]
Rotating load and speed variation frequency	ω_t	17 [Hz]

Table 4.2 – Geometrical parameters of the IS2 bearing and operating conditions at the onset of oil-whip (2040 rpm)

Numerical computations show that all the three cases admit a periodic solution, which main features (frequency and amplitude) are reported in Table 4.3. The listed amplitude components are expressed in the reference frame axes x and y defined in Figure 4.22a and are nondimensional values referred to bearing assembled clearance c_b so that, when such components are near 2 units, journal and bearing surfaces are very close to each other.

Load case	Frequency [Hz]	Relative x amplitude	Relative y amplitude
A (kinematic perturbation)	17.0	$7.58\ 10^{-4}$	$3.69\ 10^{-3}$
B (dynamic perturbation)	8.5	2.085369	1.953794
C (both perturbations)	17.0	2.084324	1.953956

Table 4.3 – Periodicity parameters of the journal orbits computed for the IS2 bearing at the onset of oil-whip (2040 rpm) in the three load cases A, B, C

As expected in case A, the journal precession occurs at the same frequency of the applied perturbation. In agreement with the finding reported in section 4.5.4, such type of response is typical of the kinematic mode of perturbation. Since the speed variation amplitude is not very significant, the relative amplitude of the orbit computed in case A is equally small despite the half frequency amplification, as predicted in section 4.5.4.

Therefore, in the next simulation including the dynamic load, i.e. case B, the kinematic perturbation is disregarded, as its effect on the journal orbit seems to be secondary. For load case B, Figure 4.23 shows the calculated journal orbit (red curve) inside the mobility region boundary (black curve). In such plot the horizontal and vertical coordinates X and Y, respectively, are non-dimensional versions of the spatial coordinates x and y shown in Figure 4.22a, where $X=x/c_p$, $Y=y/c_p$ and $c_p= c_b /(1-m)$ (pad clearance). Since the two curves are very close and the relative amplitude components are near 2 units (Table 4.3), the resulting working conditions of bearing IS2 are already critical at 2040 rpm and the perturbation can activate oil-whip. Unexpectedly, the journal response at the dynamic perturbation occurs at a frequency half the rotating load speed. In other words, as reported in Table 4.3, the period of the orbit is 0.118 s corresponding to a frequency of 8.5 Hz, which is half the rotating load frequency ω_t (17 Hz, the critical torsional speed) or, equivalently, a quarter of shaft rotation speed ω. This behavior is consistent with the hydrodynamic lubrication principles. Indeed, when the static load prevails over the dynamic component, the resulting whirling precession is synchronous, i.e. its frequency is the same as the rotating load one. Differently, if the dynamic load is exerted by a half speed load vector and its intensity overcomes the static load as in the present simulation (Figure 4.22b), the precession speed occurs at half the rotating load frequency (a quarter of the shaft rotation speed) so that mass conservation in the lubricant film is ensured. Such phenomenon can be explained by means of an analogy with the classical oil-whirl, which can be also considered as a mean to ensure mass conservation when the wedge effect is lacking. In order to understand such analogy, only the rotating load must be considered (reasonable when it is prevailing). In a reference system fixed to the half-speed load vector, which rotates at angular speed $\omega_t = \omega/2$, the wedge effect vanishes since the rotational speeds of journal and bearing are $\omega/2$ and $-\omega/2$, respectively, so that the resulting oil entrainment velocity is zero according to Couette linear distribution. Analogously, in classical whirl no wedge forms as the journal is located at the bearing center due to the negligible load entity.

Therefore, the two conditions are kinematically equivalent. In the classical whirl case, mass conservation is restored if a journal precession occurs at half the journal rotation speed. The same occurs in the reference frame fixed to the half-speed load vector, where the corresponding precession must have a frequency $\omega/4$, as the journal speed relevant to the frame is $\omega/2$. In any case, although such result is reasonable by the lubrication analysis point of view, it is not consistent with the dynamic model used for the assessment of the dynamic load, which assumes a precession of the journal at a rotation speed equal to ω_t. In a nutshell, when case B loading conditions are simulated, the lubrication model becomes incompatible with the overall dynamic simulation, as it does not consider the kinematic perturbation that allows to compute the rotating load in agreement with section 4.5.5. Accordingly, the kinematic perturbation is essential to trigger the precession, so it is included in the last (reasonable) load case C. In this way, lubrication analysis with consistent loading yields the same journal displacements obtained in case B (Figure 4.23) but they are predicted in a different period. Indeed, Table 4.3 reports numerically identical amplitude components in load cases B and C, while only the frequency response of case C is consistent with the assumed precession at frequency ω_t. Finally, the orbit computed for the consistent case C is compatible with the instability evidenced by the experimental results.

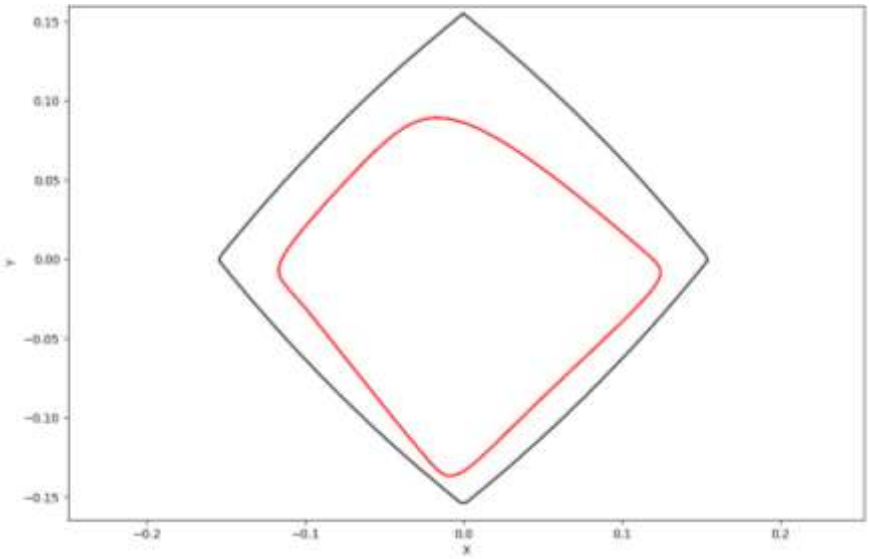

Figure 4.23 – Journal orbit of the IS2 bearing at the onset of oil-whip (2040 rpm) computed for load cases B and C

Bibliography chapter 4

[1] Liu, W., Bättig, P., Wagner, P.H., Schiffmann, J. (2020) "Nonlinear study on a rigid rotor supported by herringbone grooved gas bearings: Theory and validation" Mechanical Systems and Signal Processing, 146, art. no. 106983,

[2] Guenat, E., Schiffmann, J. (2020) "Dynamic force coefficients identification on air-lubricated herringbone grooved journal bearing", Mechanical Systems and Signal Processing, 136, art. no. 106498

[3] Niccolini Marmont Du Haut Champ, C.A., Stefani, F., Silvestri, P. (2020), "Experimental and numerical investigation about small clearance journal bearings under static load conditions", Advances in Tribology, 2020, art. no. 8844879.

[4] Childs D (1993), Turbomachinery rotordynamics: phenomena, modeling, and analysis. Wiley-Interscience publication, Wiley, New York

[5] Al-Bedoor B (2001) Modeling the coupled torsional and lateral vibrations of unbalanced rotors. Comput Methods Appl Mech Eng 190(45):5999–6008

[6] Kita M, Hataya T, Tokimasa J (2007) Study of a rotordynamic analysis method that considers torsional and lateral coupled vibrations in compressor trains with a gearbox. In: Proceedings of the thirty-sixth turbomachinery symposium, vol. 299, pp 1–2

[7] Chiu Y-J, Chen D-Z (2011) The coupled vibration in a rotating multi-disk rotor system. Int J Mech Sci 53(1):1–10

[8] Gosiewski Z (2008) Analysis of coupling mechanism in lateral/torsional rotor vibrations. J Theor Appl Mech 46(4):829–844

[9] Sukkar R, Yigit A (2008) Analysis of fully coupled torsional and lateral vibrations of unbalanced rotors subjected to axial loads. Kuwait J Sci Eng 35:143–170

[10] Mohiuddin M, Khulief Y (1999) Coupled bending torsional vibration of rotors using finite element. J Sound Vib 223(2):297–316CrossRefzbMATH Google Scholar

[11] Yuan Z, Chu F, Lin Y (2007) External and internal coupling effects of rotor's bending and torsional vibrations under unbalances. J Sound Vib 299(1):339–347 Google Scholar

[12] Rao J, Shiau T, Chang J (1998) Theoretical analysis of lateral response due to torsional excitation of geared rotors. Mech Mach Theor 33(6):761–783 Google Scholar

[13] Patel TH, Darpe AK (2009) Coupled bending-torsional vibration analysis of rotor with rub and crack. J Sound Vib 326(3–5):740–752 CrossRefGoogle Scholar

[14] Muszyńska A., Goldman P., Bently D.E., 1992, Torsional/lateral vibration cross-coupled responses due to shaft anisotropy: a new tool in shaft crack detection, Conference of Institution of Mechanical Engineers, Bath, Great Britain

[15] Giancarlo Genta, Vibration of Structures and Machines, ISBN 978-1-4612-1450-2, Springer Ed., 1999
[16] Ittapana Perera, PhD thesis “Theoretical and Experimental Study of Coupled Torsional – Lateral Vibrations in Rotor Dynamics”, Department of Mechanical Engineering, Calgary, Alberta
[17] N. Mihajlovi´c N. van de Wouw·P. C. J. N. Rosielle H. Nijmeijer, Interaction between torsional and lateral vibrations in flexible rotor systems with discontinuous friction, Nonlinear Dyn (2007) 50:679–699
[18] Xiang Ling, Gao Nan, Coupled torsion–bending dynamic analysis of gear-rotor-bearing system with eccentricity fluctuation, Applied Mathematical Modelling Volume 50, October 2017, Pages 569-584
[19] Max M. L’Vov, Edgar J. Gunter, “Application of rotor dynamic analysis for evaluation of synchronous speed instability and amplitude hysteresis at 2nd mode for a generator rotor in a high-speed balancing facility”, ISCORMA-3, Cleveland, Ohio, 19-23 September 2005
[20] Ricardo Ugliara Mendes and Katia Lucchesi Cavalca, “On the Instability Threshold of Journal Bearing Supported Rotors”, International Journal of Rotating Machinery, 2014.
[21] Jean-Claude Luneno, Coupled Vibrations in Horizontal and Vertical Rotor-Bearings Systems, master’s degree thesis, Luleå University of Technology SE-97187 Luleå, Sweden
[22] J. K. Wang, M. M. Khonsari, “On the Hysteresis Phenomenon Associated With Instability of Rotor-Bearing Systems”
[23] J. K. Wang, M. M. Khonsari, “Thermohydrodynamic Instability in Fluid-Film Bearings”
[24] Ying Cui, Yongliang Wang and Jingjun Zhong, “Numerical Analysis on the Nonlinear Hysteresis Phenomenon Associated with Instability of a Steam Turbine Rotor-Bearing System”
[25] M Chouchane, R Sghir, “Stability and bifurcation analysis of a flexible rotor-bearing system by numerical continuation”
[26] A Amamou, M Chouchane, “Non-linear stability analysis of floating ring bearings using Hopf bifurcation theory”
[27] J. K. Wang, M. M. Khonsari, “Bifurcation Analysis of a Flexible Rotor Supported by Two Fluid-Film Journal Bearings”
[28] D.J. Ewins, “Modal Testing: Theory and Practice”, Research Studies Press, United Kingdom, 1984
[29] Niccolini Marmont Du Haut Champ, C.A., Silvestri, P., “Experimental and numerical vibro-acoustic investigation on a trimmed car door to analyze slamming event”, Applied Acoustics, 166, art. no. 107380 (2020)

[30] Hauptmann, Eckert, and Howes, “The Influence on Torsional Vibration Analysis of Electromagnetic Effects Across an Induction Motor Air Gap,” Gas Machinery Conference, 2013”
[31] Feese Troy, Kokot Aleksander, “Electromagnetic effects on the torsional natural frequencies of an induction motor driven reciprocating compressor with a soft coupling”
[32] Niccolini Marmont Du Haut Champ, C.A., Stefani, F., Silvestri, P. (2019), “Development of a new test rig for the analysis of hydrodynamic bearings for rotors of microGT”, E3S Web of Conferences, 113, art. no. 03002
[33] Paper 4: Bearings for Reciprocating Machinery: A Review of the Present State of Theoretical, Experimental and Service Knowledge, Campbell, Love, Martin
[34] Stefani, F., “FEM Applied to Hydrodynamic Bearing Design”, in “New Tribological Ways”, edito da Taher Ghrib, InTech, Open Access Publisher, Rijeka, Croatia, 2011, pp.451-476.
[35] Brindley, J., M. D. Savage, and C. M. Taylor. "The Nonlinear Dynamics of Journal Bearings." Philosophical Transactions: Physical Sciences and Engineering 332, no. 1624 (1990): 107-19. Accessed February 23, 2021. http://www.jstor.org/stable/76823.
[36] Stefani F., “Computer-Aided Design of Pocket Elliptical Journal Bearings, Part 1: Theory”, Journal of Advanced Mechanical Design, Systems, and Manufacturing, Vol.7, No.4, 2013, pp. 576-593.
[37] “Hydrodynamic fluid film bearings and their effect on the stability of rotating machinery”, RTO-EN-AVT-143, NATO-OTAN, STO Educational Notes
[38] “Hydrodynamic Lubrication: Bearings and Thrust Bearings”, Edited by Jean Frêne, Daniel Nicolas, Bernard Degueurce, Daniel Berthe, Maurice Godet. Volume 33, Pages 1-470 (1990)

5 Rolling bearings behavior in presence of turbomachinery flow instability

In this chapter the results of signal processing techniques related to surge and rotating stall are presented, and the same energy system is considered for the experimental investigations and related collected data analysis; in the first part analyses are performed with the same interposed volume, whereas in the second one even the influence of different plenum is assessed by changing its value.

5.1 Signal analysis performed with the same plant configuration

The present section shows signal processing techniques applied to experimental data obtained from a T100 microturbine connected with different volume sizes. This experimental activity was conducted by means of the test rig developed at the University of Genoa for hybrid systems emulation. However, these results can be extended to all advanced cycles in which a microturbine is connected with additional external components which lead to an increase of the plant volume size. Since in this case a 100 kW microturbine was used, the volume was located between the heat recovery unit outlet and the combustor inlet like in the typical cases related to small size plants. A modular vessel was used to perform and to compare the tests with different volume sizes.

The main results reported in this section are related to rotating stall and surge operations. This analysis was carried out to extend the knowledge about these risk conditions; indeed, the systems equipped with large volume size connected to the machine present critical issues related to surge and stall prevention, especially during transient operations towards low mass flow rate working conditions.

Investigations conducted on acoustic and vibrational measurements can provide interesting diagnostic and predictive solutions by means of suitable instability quantifiers which are extracted from microphone and accelerometer data signals. Hence different possible tools for rotating stall and incipient surge identification were developed through the use of different signal processing techniques, such as Wavelet analysis and Higher Order Spectral Analysis (HOSA) methods. Indeed, these advanced techniques are necessary to maximize all the information conveyed by acquired signals, particularly in those environments in which measured physical quantities are hidden by strong noise, including both broadband background one (i.e., typical random noise) but also uninteresting components associated to the signal of interest. For instance, in complex coupled physical systems like the one it is meant to be studied, which do not satisfy the hypothesis of linear and Gaussian processes inside them, it is reasonable to exploit these kinds of tools, instead of the classical Fast Fourier Transform (FFT) technique by itself, which is mainly adapt for linear systems periodic analysis.

The proposed techniques led to the definition of a quantitative indicator, that is, the sum of all auto-bispectrum components modulus in the sub-synchronous range, which was proven to be reliable in predicting unstable operation. This can be used as an input for diagnostic systems for early surge detection. Furthermore, the presented methods will allow the definition of some new features complementary with the ones obtainable from conventional techniques, in order to improve control systems reliability and to avoid false positives.

5.1.1 Test rig description

The TPG experimental facility is composed by a modified microturbine (T100 machine: 100 kW electrical power at 70 krpm design angular velocity, 30% design efficiency is reached by means of a recuperated cycle) and external vessels located between the recuperator outlet and the combustor inlet [1][2]. Although they were invented in order to imitate hybrid energy systems furnished with a Solid Oxide Fuel Cell (SOFC), these vessels can reproduce power plants with considerable volume dimension moved by a gas turbine [1].

In the present context, these vessels were operated simply like supplementary volume elements, and not to imitate SOFC hybrid systems. Furthermore, vibro-acoustic analysis results reported in this paper were performed for innovative cycles based on gas turbines technology, making them a current tool for diagnostic purposes in advanced energy systems.

Figure 5.1 illustrates the facility layout: the system is equipped with two main control valves, VM and VO, to govern the coupling with vessels, a check valve located downstream of the compressor outlet and a bleed on/off emergency valve to eject a portion of the air flow. Three air/water heat exchangers located at the compressor inlet pipes (EX) are also employed to control its inlet temperature.

Performance indexes are collected and acquired by the control software developed in LabVIEW environment. It gives the capability of managing the physical system from the control room and it can store data measurements with low sampling frequency.

The earliest gas turbine control system guarantees its safe functioning: it controls the fuel flow in order to keep the TOT level steady at 918.15 K and manages the machine start-up and shutdown processes.

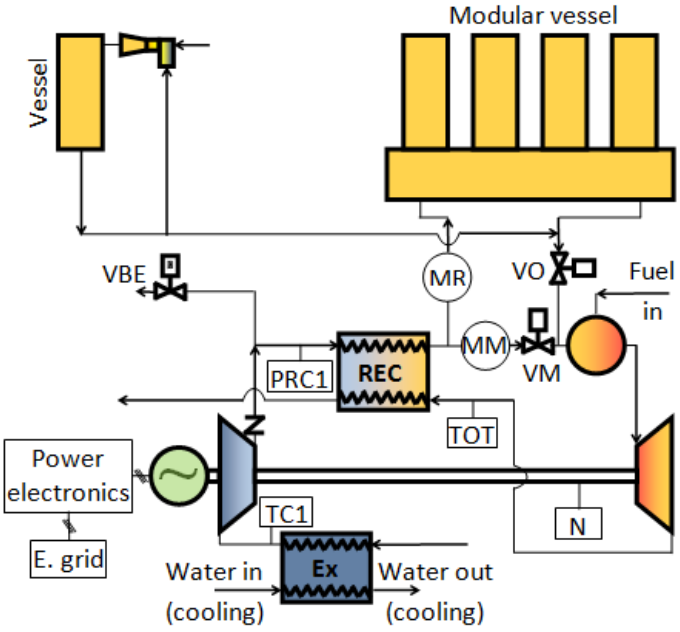

Figure 5.1: test rig layout

Siemens Scadas mobile acquisition system was employed to acquire and save vibro-acoustic data measures during a transient operation from a stable condition to an unstable (i.e., surge) one. The acquisition system is able to acquire at the same time up to 16 distinct signals with a sampling frequency (Fs) up to 204.8 kHz. A tachometer signal was obtained from the frequency of the electric generator current: then, this signal is synchronous and comparable with all the others coming from the sensors. One tri-axial accelerometer and a mono-axial one (axial direction) were respectively located on the electric generator case near to the rotor ball rolling bearing and at the compressor inlet. The employed probes are provided with high frequency response which permits dynamic investigations up to frequency levels of 10 kHz. In order to observe and investigate the blade pass frequency, two micro accelerometers characterized by resonance frequency greater than 55 kHz (radial direction) and 80 kHz (axial direction) were also employed. Lastly, a pre polarized Gras microphone provided with frequency response in a range between 2 and 50 kHz was located at the compressor inlet in order to investigate its local acoustical emission [5][6][7].

Multi sample rates were adopted, by defining a different sampling frequency for each acquired dynamic signal; this was made basing on the measurement position and sensor employed: 102.4 kHz for microphone and micro accelerometer and 16.384 kHz for accelerometers placed close to bearings. In some cases, a down sampling algorithm was applied on acquired signals to obtain suitable block size in post-processing phase for each signal processing technique adopted.

In the present section, focus has been posed on software signal processing operations in order to improve the capability of predicting compressor surge margin: then, experimental data considered are referred only to one physical configuration (i.e., the one with the intermediate volume).

5.1.2 Measurement system

Measurements were performed during some test days in which the T100, coupled with one of the three added volume configurations (0.3 m^3, 2.3 m^3, 4.1 m^3), worked in grid connected mode with the variable speed control system that maintained the Turbine Outlet Temperature (TOT) constant at a target level (equal to 918.15 K).

The turbine was started-up to a production of 40 kW electrical power (angular velocity around 62 krpm). This starting load was selected on the basis of some goals: meaningful off-design condition (mGT systems are required to be very flexible in terms of part-load functioning) together with a great initial margin from surge, and prevention of too low load functioning, in which the plant control system would decrease TOT set-point; ultimately, it had to be an achievable starting point with respect to the available plant apparatuses (e.g., the VBE size).

After a stationary working point is reached, surge event was produced gradually by closing the VO valve (in 2.3 m^3 and 4.1 m^3 cases) or the VM one (0.3 m^3 case), located in the air path between recuperator outlet and combustor inlet (by enlarging pressure drops). These valves were closed by consecutive steps of 10% (5% near to the surge line) until surge phenomenon occurred, typically in a range between 20-30% of valve fractional opening. Vibro-acoustic measurements began before every valve motion started, until the plant moved to a new stable working point. Therefore, consecutive data sets comprising signals from all sensors were acquired and saved. A sampling frequency of 8196 Hz was selected in order to be capable of detecting all meaningful frequency contents within the signals; while emulating transient operation towards unstable working point, rotational speed remained in the range between 62000 and 65000 rpm (1033-1083 Hz) [8]. This had influence on the choice, since sample frequency must be much higher than the double of the rotational frequency [9] to allow the analysis of all sub-synchronous content (essential to find surge precursors). Upper levels of sampling frequency (up to 200 kHz) were adopted for one micro accelerometer to allow investigating frequency values around the blade pass frequency (about 13 kHz). Indeed, compressor impeller is characterized by 13 blades, and by 13 additional splitter ones; the turbine is only equipped with 13 main blades.

When the system arrived at an unstable condition, only few surge cycles were acquired since the control system instantly turned-off the compressor to reduce damage dangers.

5.1.3 Type of test investigated

Some different kinds of transient behavior of the compressor are considered in order to show operating responses on its stable and unstable operating conditions in order to extract more information as possible from them.

The transient analyzed is obtained closing gradually the two valves previously described in the outlet compressor circuit and system response signals of different nature (acoustic and structural) have been acquired (mono axial accelerometer response mounted on the rolling bearings, microphone at the compressor inlet section, high frequency response micro-accelerometer on the compressor housing). In this case the aim is to look for the condition of intermittent phenomena which occurs between deep and mild surge cycles when the machine becomes unstable.

This is made in order to investigate system response just before the first deep surge cycle happens and to look for contents in signals that make us able to discover the onset of rotating stall phenomenon. Differently from the works performed in [1][3][4], where attention was paid only on the last stable operating points just before surge, in this case the investigation was focused on experimental vibro-acoustic responses collected on the compressor when it undergoes succession of deep and mild surge cycles; then, they were compared with nominal working conditions, far from instability zone (i.e. surge line of the compressor).

The transient chosen to represent the unstable behavior is characterized by entrance in surge with two cycles, and subsequent shutdown of combustion chamber; consequently, rotational speed goes down before the machine recovers a condition closer to its stable region (probably it founds itself in mild surge conditions in this phase). This could be ascribable to mass flow rate oscillations which can make critical the machine working condition. After about 2 s, another deep surge condition is encountered again, and the compressor undergoes another surge cycle. All this information can be seen from the accelerometer time-history reported in Figure 5.2. Starting from this time-signal, we obtained one significant time segment to focus on short time-windows: the first one starts from the approach of surge and contains a sequence alternating deep and mild surge. Then we will investigate its frequency contents to identify a likely rotating stall condition before each surge cycle begins. Indeed, observing accelerometer time-history trend, one can confirm that the acceleration peaks are abnormal and thus can generate damage also to the bearings and reducing residual life of the plant.

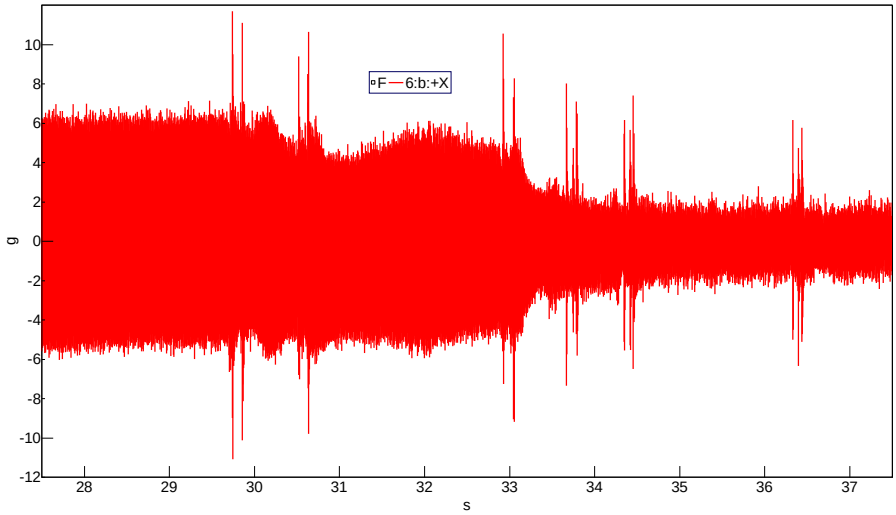

Figure 5.2: accelerometer time-history during surge transient

In Figure 5.3 the detail of the central part of the transient is reported as it is the starting point for the investigation. It is compared with tachometer signal reported in Figure 5.4, in order to show the trend of measured angular speed when the machine operates in undesired conditions: cursors in Figs. 5.3 and 5.4 define the main instants corresponding to the deep surge conditions encountered in the temporal sequence.

From angular velocity trace one can see that just after each deep surge sequence (starting respectively from time instants 29.75 s and 30.52 s) the mGT system accelerates: this can be explained by the blocking of mass flow rate aspirated from the compressor while the turbine is still giving power to the energetic system. Indeed, the power absorbed from the compressor decreases instantaneously leading to a torque unbalance on the shaft and thus to a positive angular acceleration. After the first surge cycle occurs, the fuel alimentation in the combustion chamber is switched off by the control system and thus angular speed and power of the mGT decrease.

This happens because the mGT is equipped with a monitoring system based on an industrial accelerometer signal; when a critical vibration level is reached, a forced shutdown is activated to protect the plant [2]. This is also confirmed by the fact that the fuel mass flow rate stabilizes to zero till the transient ends, soon after the mGT undergoes the first deep surge. Then, the second surge cycle condition happens because of the change of turbine operating condition together with the decrease of angular velocity which reduces the stability margin of the compressor.

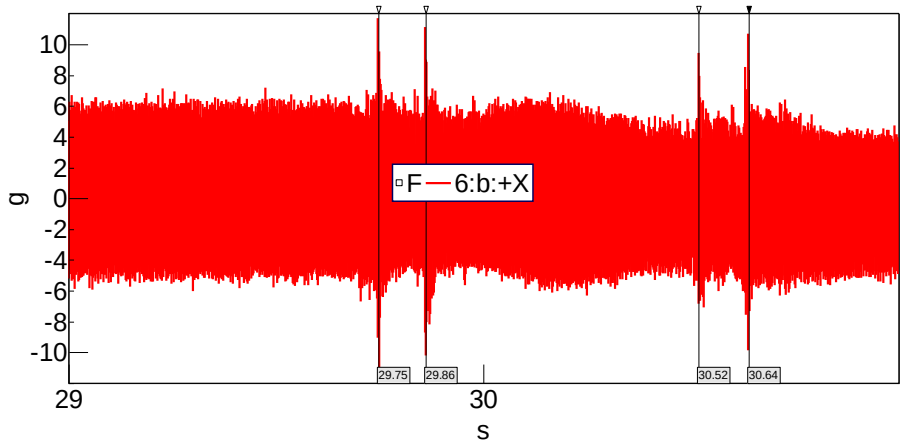

Figure 5.3: detail of previous time-history from the first surge cycle and future instability

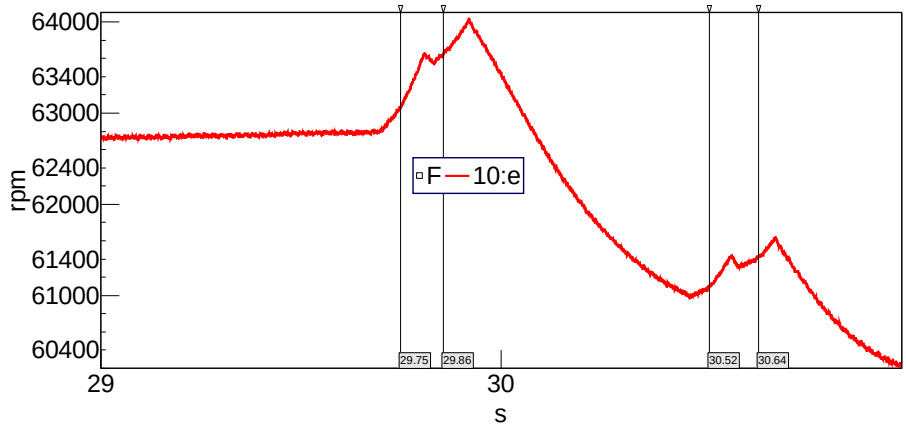

Figure 5.4: rotational speed trace corresponding to the previous surge transient extract

5.1.4 Signal processing techniques on operational responses

Short Time Fourier Transform (STFT) was compared with Wavelet Transform [10][11] and complemented by HOSA techniques [12][13][14] applied to the accelerometer signal reported in Figure 5.2. These two methodologies are very common in other fields of research (e.g., vibrational diagnostics). HOSA techniques are used to better highlight deterministic contents of acquired physical signals, and thus to minimize measurement noise, both random and frequency localized one, since they rely on statistics of higher order [12][15]. Wavelet Analysis may be useful to detect in advance incipient surge conditions since from a theoretical point of view it can provide better resolution in time or frequency, depending on the settings adopted, and thus it can recognize some coherent patterns related to rotating stall inception [16]. Indeed, Wavelet Transform is characterized by variable time-frequency resolution (differently from STFT), which can be adapted on the whole frequency range. In the following, wavelet analysis results are reported by means of time-frequency maps which allow to detect how the signal energy contents vary according to a chromatic scale. In the following a time-frequency analysis about the vibrational response of the mGT during the different chosen transients is conducted. First of all, it is reported a comparison between STFT and

Wavelet Transform performed on a system response far from instability zone. The investigation is limited to the sub-synchronous range and this highlights that the response attributable to acoustic modes, not so evident and characterized by low energy contents in low frequency, is well identified by Wavelets but not clearly by STFT. Indeed, in order to be able to observe an entire transient together with its hidden discontinuous temporal trends, one loses information about the accurate identification of the characterizing frequencies of the occurring phenomena. In Figure 5.5 STFT and Wavelet are performed over a temporal segment acquired from accelerometer placed in correspondence with mGT bearings, oriented in axial direction; very far from unstable conditions; from Wavelet map it can be noted that there is no significant sub-synchronous content, as expected for this nominal operating condition. Indeed, signal energy content, under the rotational frequency (about 1 kHz), is low, as can be deducted considering the color bar range. Different time and frequency resolutions can be observed, revealing better identification of low frequency contents by Wavelets. For example, in the range 5-100 Hz Wavelet analysis allows to identify frequency contents for well-defined frequency levels, maybe related to an acoustic modal response, not excited in a marked way in the stable state. At higher frequency, both STFT and Wavelets show that in system response sub-synchronous contents are characterized by low energy levels. Then, the same kind of investigation is conducted on the surge transient (Figure 5.6). Frequency domain techniques are applied on the accelerometer signal in order to highlight significant signal contents related to unstable phenomena.

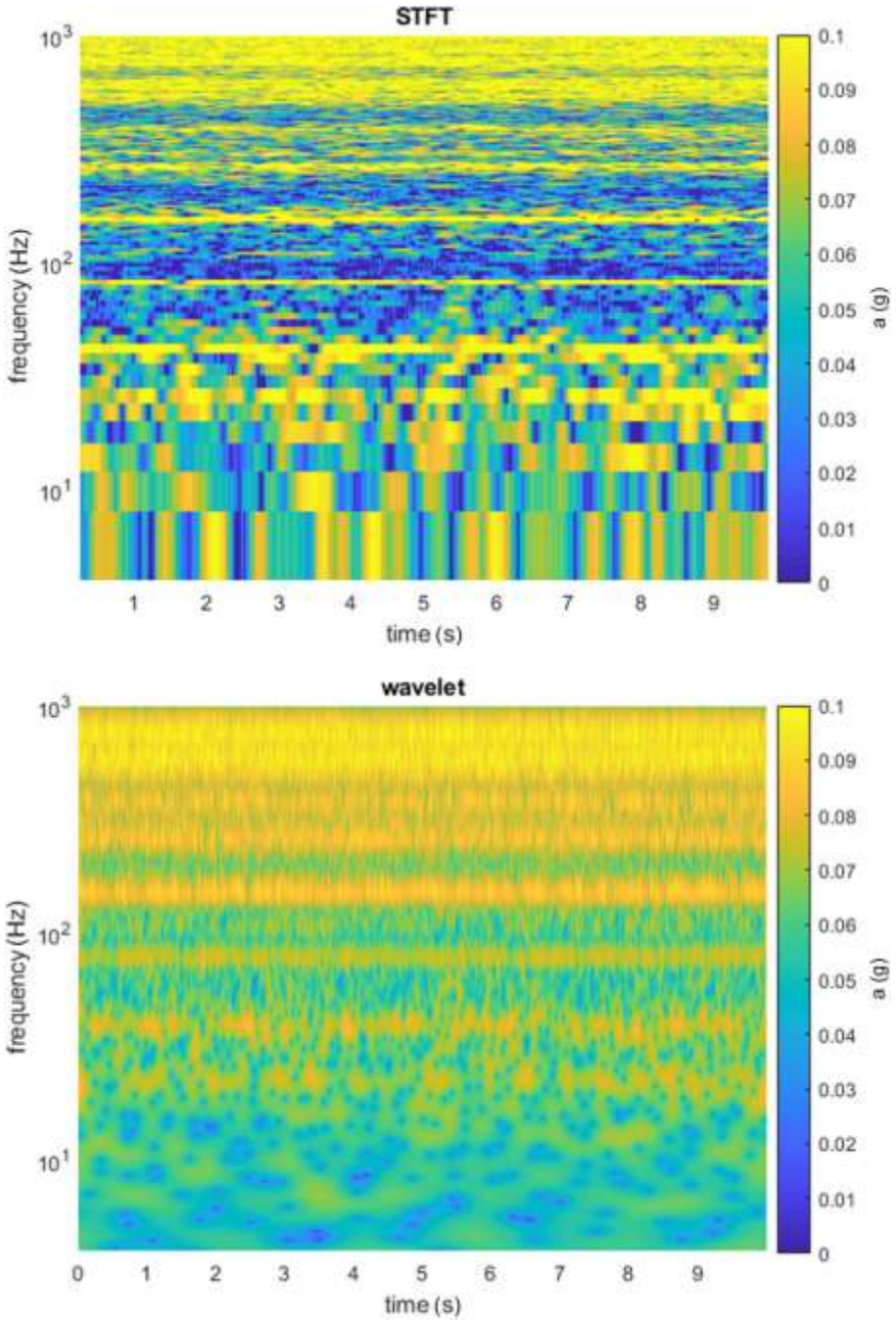

Figure 5.5: color map of STFT (up) and Wavelet (down) analyses in stable operating conditions

STFT shows limitations on frequency resolution for the lowest frequency levels, while it allows the correct identification of the energy contents at the higher frequency values, such as the synchronous revolution frequency (1X). In terms of temporal resolution, in this specific case, STFT analysis was set with not fine values in order to do not degrade its frequency resolution. Indeed, these two signal properties are in conflict between them (in particular, improving one implies degrading the other). In detail, these two main parameters were set in order to be able to detect low frequency acoustic modes. Nonetheless, from figure 5 it can be noted that, under 10 Hz, it is almost impossible to distinguish energy contents frequency. Wavelet Transform has better frequency resolution at low frequencies,

since it has a logarithmic law such as human hearing [17]. Both STFT and Wavelet analyses show the alternation of deep and mild surge cycles (three deep surge sequences respectively begin at time instants 2, 5 and 9 s): also here the investigation is limited to the sub-synchronous frequency range; again, the revolution frequency is next to 1.1 kHz, and the one attributable to rotating stall is next to 0.35 – 0.55X (normalized frequency values expressed as fractions of the synchronous revolution frequency), as expected for this kind of vaneless diffuser radial compressor.

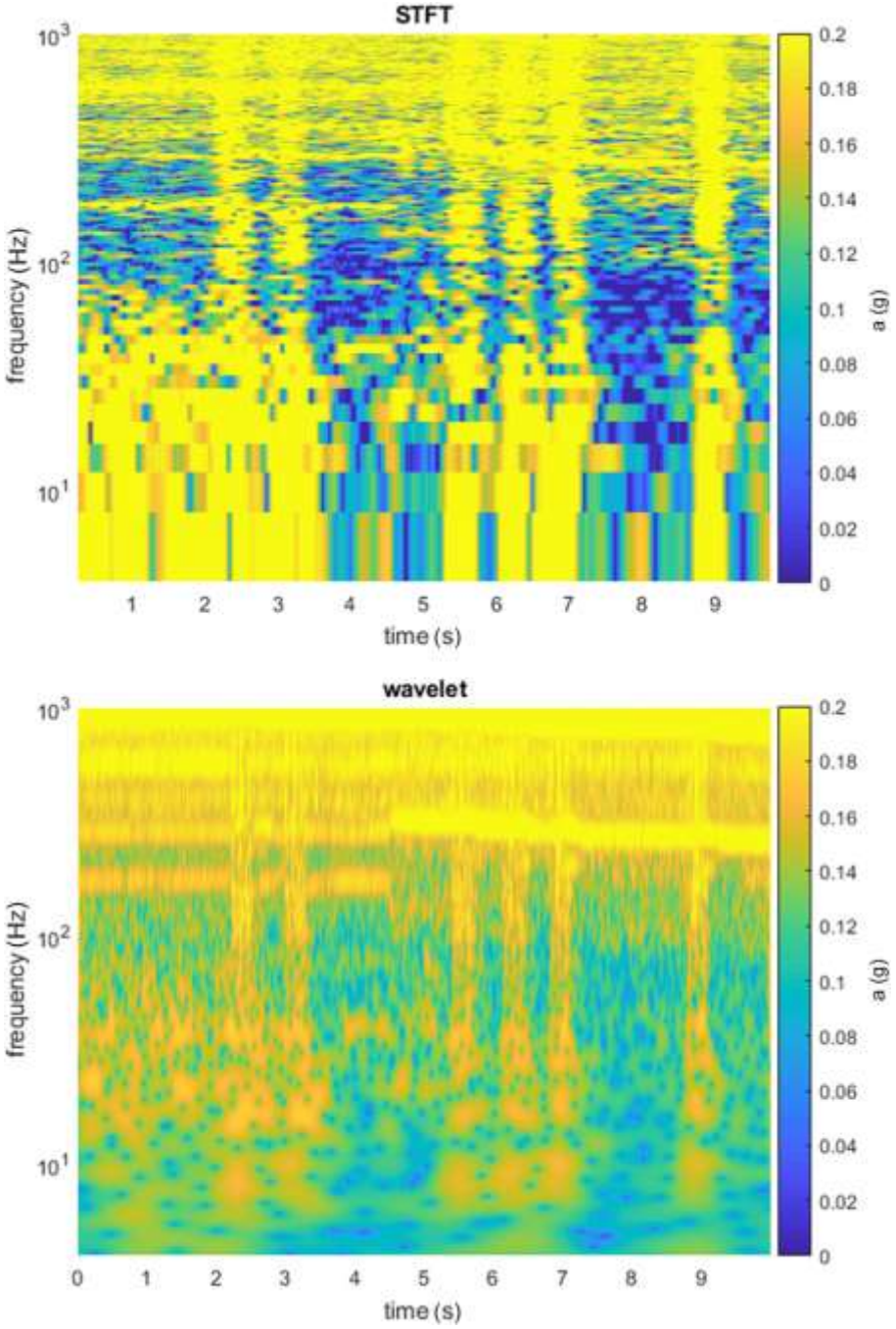

Figure 5.6: color map of STFT (up) and Wavelet (down) analyses in unstable operating conditions

In the following Wavelets are employed to classify system dynamic responses contents in different segments of the considered transient. Indeed, a detailed analysis of this one showing rotating stall evolution is reported in Figure 5.7 on a shorter time window. From Wavelet colormap results, both the frequency contents of 1X (synchronous revolution frequency) and a sub-synchronous one, attributable to rotating stall, at less than 0.5 s from the first deep surge cycle, are well detectable in incipient surge conditions. In the time interval 0-0.4 s this frequency content is enough persistent, while in the last instants just before the first deep surge cycle Wavelet analysis reveals an intermittent nature of this phenomenon (see color intensity of sub-synchronous frequency contents close to 400 Hz, ranging in a discontinuous way in the last 0.1 s before deep surge). It must be underlined that this accelerometer vibrational response content is practically absent in the transient between the two deep surge cycles; the approach to the second surge cycle does not seem to be preceded by rotating stall onset (see figure 7 Wavelet map, in the time interval 0.4-0.5 s). This seems to agree with experimental evidence reported in literature [1] in which it is stated that stall inception is not a necessary condition when the machine is approaching surge condition starting from an operating point far from its stable zone., while it is normally encountered approaching from a nominal condition. The same Wavelet colormap results convey information on the low frequency contents and how the modal response increments its energy approaching instability range. In detail, one can see as these contents, in the case considered in Figure 5.5, are characterized by the same frequency level both in incipient and in deep surge conditions. The most interesting information we get from Wavelet results is that rotating stall phenomenon disappears just after the first deep surge cycle occurs, as proved by the fact that a frequency content at 500 Hz firstly appears intermittently and then vanishes.

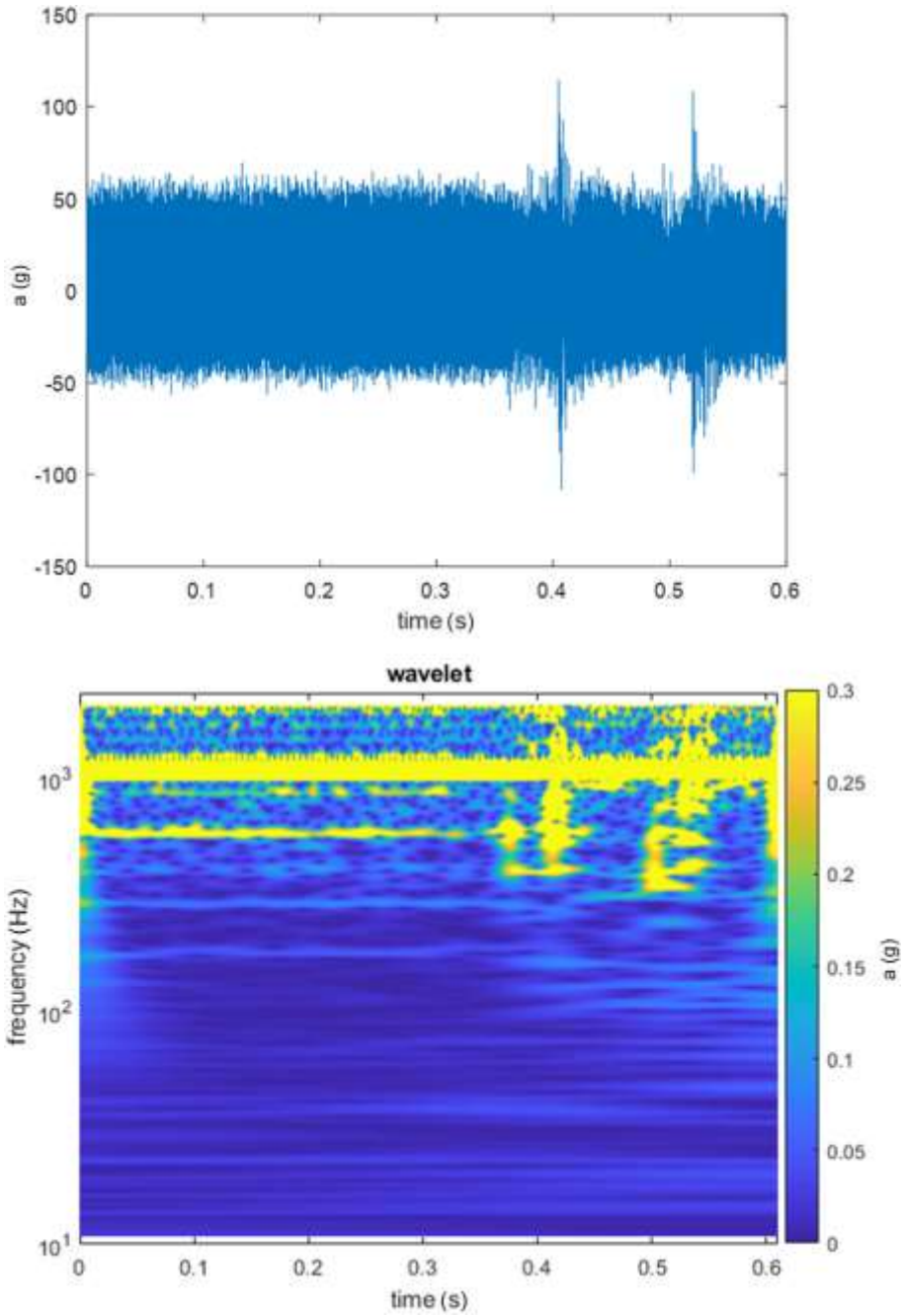

Figure 5.7: detail of the first deep surge cycle accelerometer time-history in [m/s2] (up) and its Wavelet Transform (down)

In the next figures, also high frequency range is investigated in order to find frequency contents related to phenomena developing within the system.

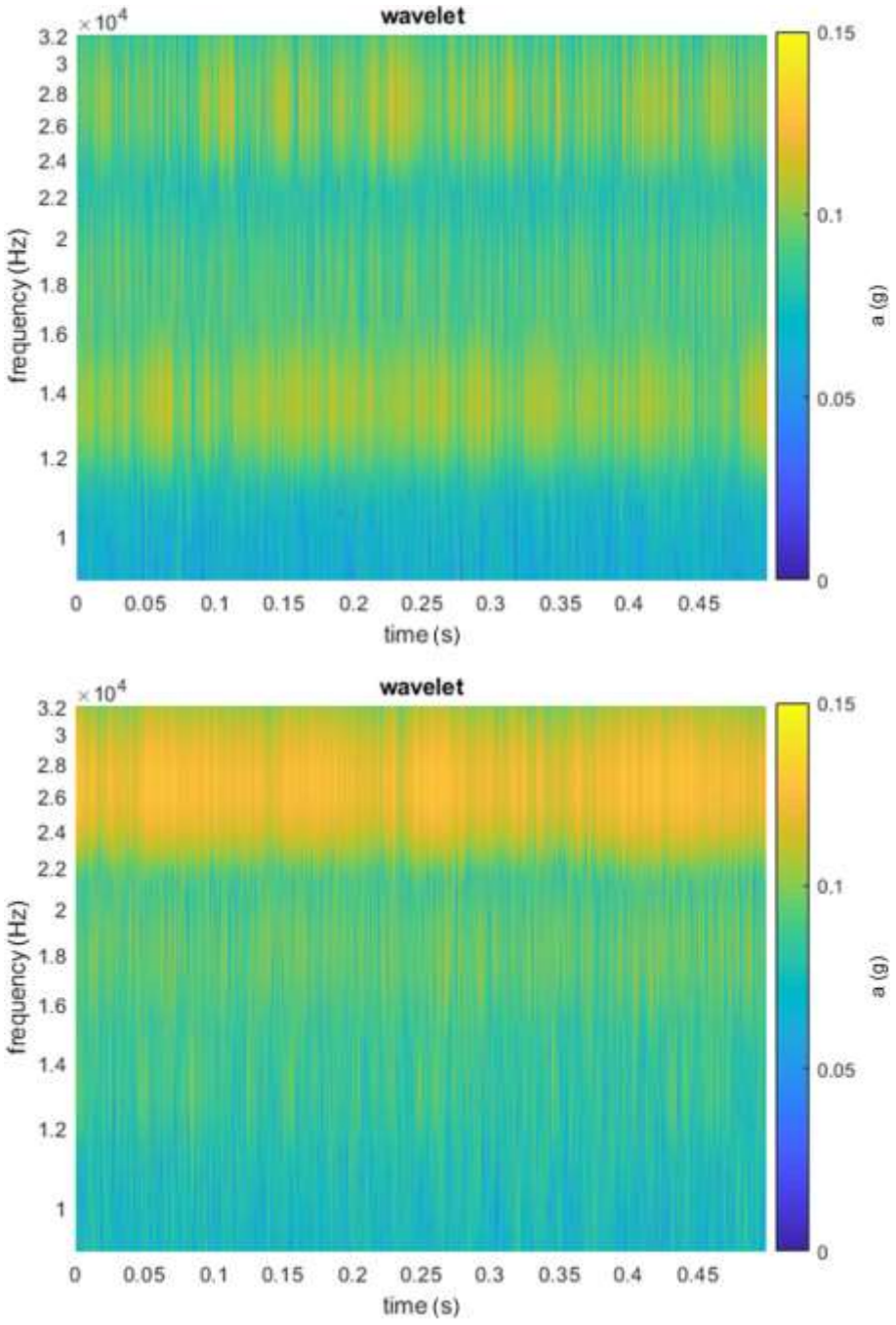

Figure 5.8: Wavelet Transform in stable (up) and unstable (down) operating conditions of the compressor from the accelerometer on its housing

All the color bars reported together with the presented results maps have the same maximum and minimum limits, in order to compare the two different system states. Output signals from high frequency response accelerometer mounted on compressor housing, whose time window is of 0.5 s, were considered for the subsequent analysis. In the unstable case, by means of Wavelet Transform, we can observe that Blade Pass Frequency (BPF) loses its energy with respect to the stable one; its value is next to 13 kHz since the compressor is equipped with 13 blades (plus 13 splitter ones, see

Figure 5.9). On the contrary, the energy of the second order (26X) increases its value while the first one decreases. This might be justified by the fact that a developed rotating stall interacts with impeller blades from its entering section, where splitter blades are not present and thus only 13X forcing order is present; hence, 13X is the component mainly weakened by the stall, whereas 26X one persists, since in inner impeller sections splitter blades are not affected by this interaction and so their contribution is not affected by 13X reduction. Furthermore, in the unstable case it is to be remarked the presence of an energy contribution between BPF and its second order, which is more relevant with respect to the stable condition. To summarize, the onset of instability phenomena of the fluid flow within the machine, such as rotating stall, may interact with typical blade passage frequency content, because of an alteration of the nominal machine behavior is occurring (i.e. abnormal blade load distribution). A physical explanation of this behavior might be that close to instability line, all the inter blade canals in compressor impeller are stalled from its inlet section, resulting in a less strong contribution of the conventional blades with respect to the splitter ones as usually happens in stable operation.

Figure 5.9: compressor impeller: detail of main and splitter blades (additional masses on some blades are present for dynamic structural mistuning purpose in impact test)

BPF results to be less evident in unstable operation, whereas other components in high frequency enlarge their energy in this configuration. In the following we mean to exploit higher-order-spectra method to show possible coupling between fluid flow phenomena and their interaction with system structural behavior, since this leads to a nonlinear response of the whole system [15]. Furthermore, also transmissibility of acoustic emissions can be studied by means of these techniques, deepening the strong coupling present not only between fluid and structure but also between the structure itself and the surrounding environment. This is made by processing signals acquired from both

accelerometers and microphones, for a fixed plant configuration with an intermediate added volume. The main advantage in using HOS approach is the chance of removing steady and unsteady Gaussian noise from the signals of interest investigated [15]. In literature applications of this methods are not so present, whose potentialities can be then exploited to set up diagnostics systems based on reliable indicators. The first techniques adopted begin with second order approaches and move to higher order ones; then, respectively in time and frequency domains auto and cross-correlations functions and their spectra are evaluated. Starting from auto-correlation functions (order 2 statistics), microphone acoustic signals acquired near the compressor inlet section have been post-processed. These autocorrelations are first computed for both the unstable and stable operating condition of the centrifugal compressor and then their Fast Fourier Transform (FFT) are evaluated in order to find out significant energy contents at different frequency levels. By comparing auto-correlation functions of microphone signals reported in Figure 5.10, a higher amplitude is encountered, particularly for time-shift equal to zero (which corresponds to second order statistical moment, i.e., variance), in the unstable condition with respect to the stable one.

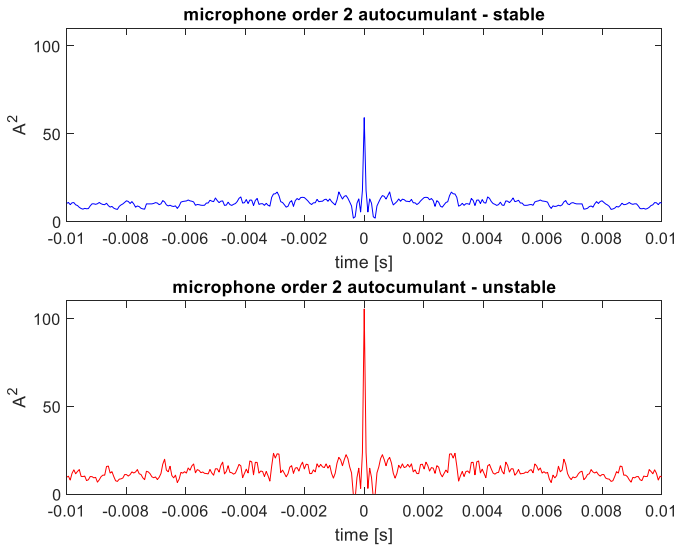

Figure 5.10: microphone autocorrelation function in stable (up) and unstable operating condition (down)

Significant amplitude peaks corresponding to precise time-shift close to 2.5 ms are associated with perturbations propagation phenomena, such as reflections present in the measurement point in which the microphone was placed (case of the mGT with its reflecting walls). These peaks result to be higher in unstable conditions and some of them can be identified with a characteristic period of about 3 ms together with others at multiple values of the previous time-shifts, attributable to further reflection phenomena. From the FFT of the previous described autocorrelation function (Figure 5.11), attention has been posed on sub-synchronous frequency range of acquired signals, delimited by revolution

frequency (close to1.1 kHz and slightly higher for the unstable condition) which is clearly visible in both the spectra. In the unstable case, low frequency contents attributable to an acoustical system modal response seem to be more significant, which becomes more and more relevant going far from the stable zone. Only in unstable condition, a sub-synchronous component characterized by an energy peak around 300 Hz is clearly present (marked by data tip); it could be related to the onset of a rotating stall pattern in the compressor. Furthermore, in the frequency range 0.5X-1X an energy increment in the acoustic response measured by the microphone can be noticed.

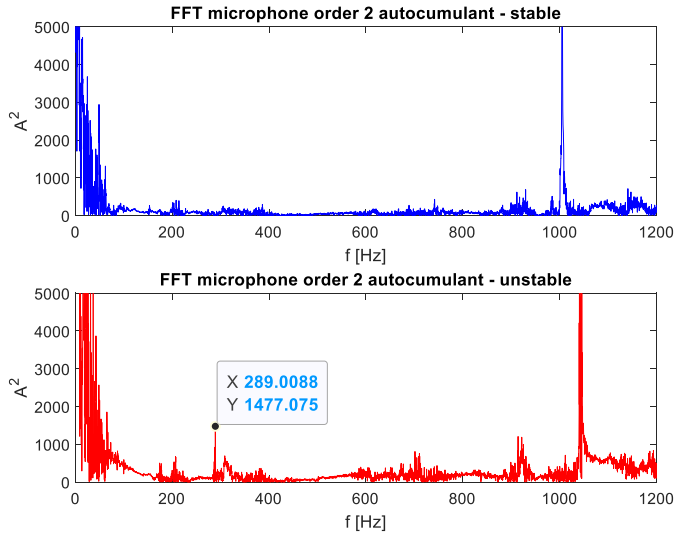

Figure 5.11: FFT of microphone autocorrelation functions in stable (up) and unstable (down) operating conditions

The same procedure is then carried out for high frequency response accelerometer signal: in Figure 5.12 its autocorrelation function is shown for both stable and unstable compressor behavior. With respect to the acoustics, time-shifts become significant already for values in the order of milliseconds since perturbations velocity is sensibly higher in solid means than in fluid ones. Comparing the autocorrelation function for the accelerometer in a time-shift range of ± 1.5 ms, in the stable condition the resulting trend is more regular with the presence of less pronounced peaks.; on the contrary, in the unstable one more peak is found: they indicate a higher energy level correlated to propagation and reflection phenomena within the system. In Figure 5.13 the autocorrelation function of the microphone over a more extended range, with respect to the first plot (Figure 5.12), is reported and a low frequency periodic content is well detectable; indeed, the trends show an amplitude modulation phenomenon characterized by maxima corresponding to periodicity present in microphone signals; a sequence of maxima separated by a time-shift of 0.01 s is present in both cases, indicating system response frequency contents close to 100 Hz.

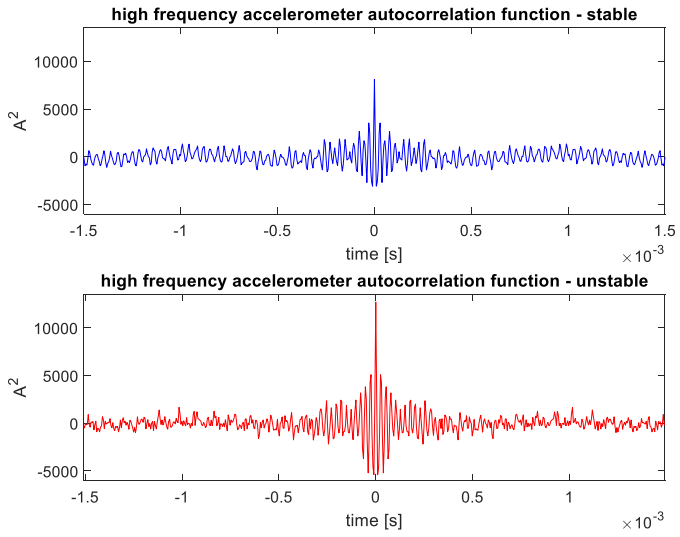

Figure 5.12: high frequency accelerometer autocorrelation functions in stable (up) and unstable (down) operating conditions

In the condition next to instability, two other maxima are detectable at time shifts ±0.14 s, corresponding to a period associated with a cyclic phenomenon (whose frequency is then lower than 10 Hz); this could be attributable to a forced response due to incipient surge that excites system acoustic resonances. The acoustic response coming from the microphone seems to detect this phenomenon and the autocorrelation function changes its trend (moving from stable to unstable condition) underling the presence of energy contents at low frequency by exhibiting oscillations.

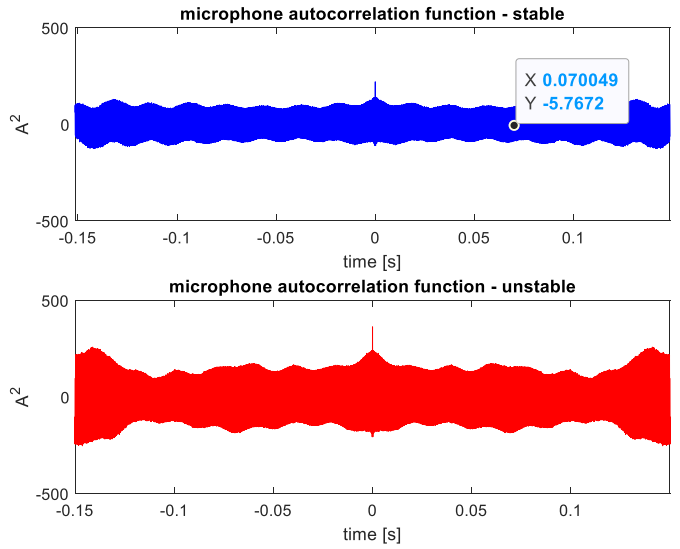

Figure 5.13: microphone autocorrelation function with higher time-shift range

In Figure 5.14 FFT of auto-correlation functions of the accelerometer are reported, underling that some frequency contents change passing from a stable condition to an unstable one next to incipient surge. In particular, BPF and its order two (two times the blade pass frequency) reduce their energy contents in unstable operation (peaks at 13 and 26 kHz) and at the same time other frequency contents increase their energy; they could be related to the presence of a phenomenon related to incipient surge (rotating stall) which interacts with blade passage. In both cases, in the two spectra there are cyclic contents related to the impeller rotation frequency (see peak at1.1 kHz) and to its 4X multiple related to the properties of the electric generator with two polar couples. Moving from stable to unstable status, while order 4X seems to be invariant, order 1X energy level seems to increase, due to an additional unbalance caused by distorted fluid distribution within the compressor impeller.

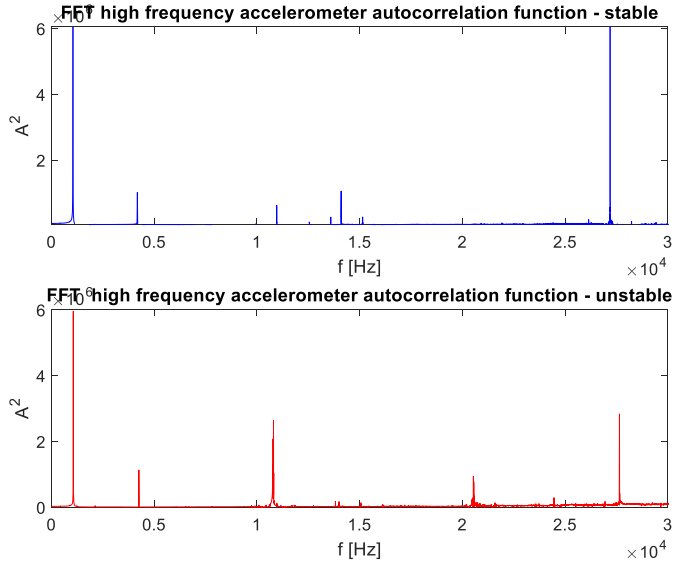

Figure 5.14: FFT of high frequency sampled accelerometer autocorrelation functions in stable (up) and unstable (down) operating conditions

In the following part, cross-correlation functions between accelerometer and microphone signals are performed, in order to minimize measurement noise and to underline the common contents; indeed, they could reveal vibro-acoustic system response identifying also low S/N ratio contributes which are covered by noise. In Figure 5.15 such cross-correlation function is reported: in the unstable case it can be seen that harmonic contents related to rotation frequency are predominant, since they are detected by both the types of sensors. The FFT of the previous showed cross-correlation function reported in Figure 5.16 shows a significant increment of low frequency contents in the unstable condition; it can be attributable to an increasing modal vibro-acoustic response moving towards unstable status. Even the peak at 300 Hz can be remarked and it is ascribable to a contribution of rotating stall, detectable both from the structural and from the acoustic probes.

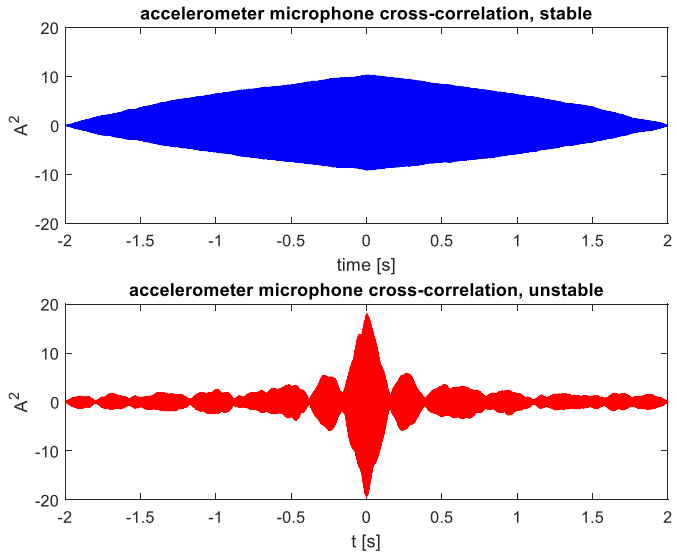

Figure 5.15: accelerometer microphone cross-correlation functions

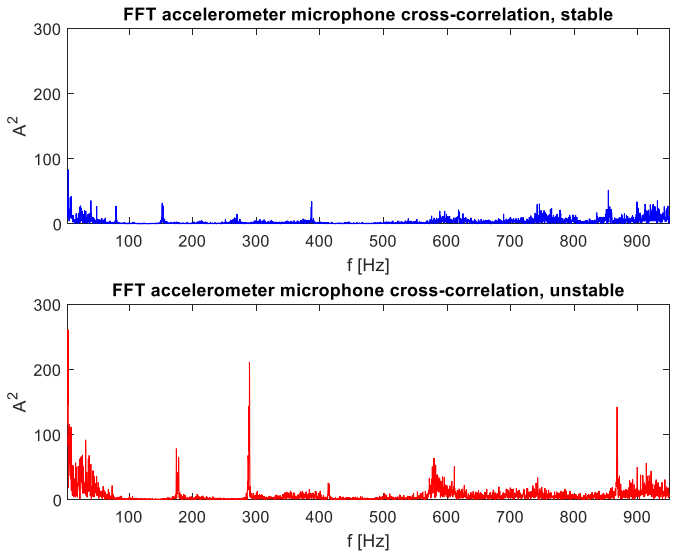

Figure 5.16: FFT of accelerometer microphone cross-correlation functions in sub-synchronous frequency range

The analysis of the cross-correlation function has been extended up to the higher frequencies, close to the BPF range, as shown in Figure 5.17. In the stable condition, peaks in correspondence of the 1X and 13X (BPF) are well marked (see markers at 1047 Hz and 13594 Hz). Furthermore, it presents, a multiple of order 2 with significant energy content. Close to incipient surge, BPF seems to lose energy, while its order 2X results to be less detectable in the cross-spectrum. This could be attributable to the incipient unstable condition which makes the system responses less stationary and so with frequency contents less marked and more variable, resulting in less deterministic characterizing frequencies of the phenomena.

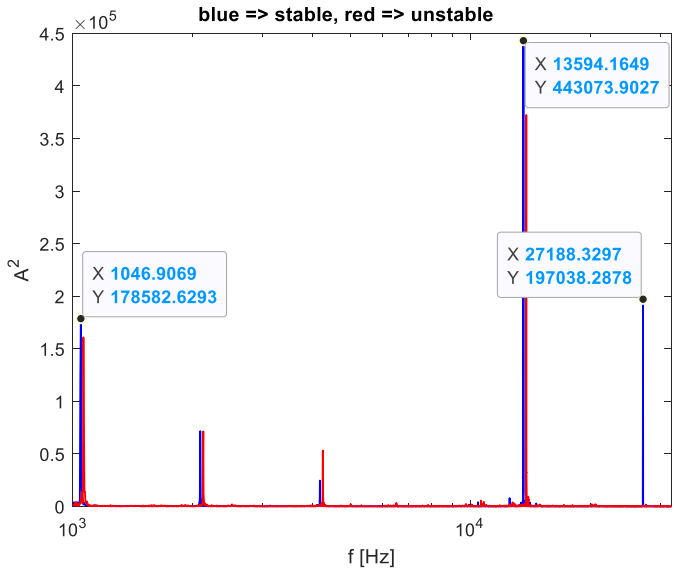

Figure 5.17: FFT comparison between accelerometer microphone cross-correlation functions in high frequency range

In the last part, bispectrum analysis was performed on microphone and accelerometer signals in order to extract more hidden information from them, and above all, to remove all background noise. Auto-bispectrum was calculated by means of both the direct approach (based on FFT) and the indirect one [19]. Indeed, this function allows to investigate the interactions between spectral contents in the acquired system responses [15], and this can be displayed adopting a color map with two independent (normalized) frequencies on the axes. Modulation phenomena are well distinguishable as the bispectrum function increases its amplitude in correspondence of their characteristic frequencies. In Figure 5.18, for the microphone signal, auto-bispectrum estimated via the indirect method is shown both for stable and unstable operating conditions. In the unstable one, the onset of a phenomenon with sub-synchronous frequency (next to f1= 0.05*Fs ≅ 400 Hz) and low frequency contents are more evident with respect to the stable conditions. Furthermore, this typical frequency related to rotating stall does not change varying f2 (y axis); this underlines how such phenomenon is coupled with a broadband frequency range in the system responses, showing the presence of a modulation behavior in system dynamic responses. In the following Figure 5.19 auto-bispectrum estimated via the direct method is reported for high frequency accelerometer signal. It is to be noticed that this auto-bispectrum, computed for higher frequency values with respect to the first one showed above, can reveal BPF interaction with sub-synchronous phenomena and with rotation frequency and its higher orders (2X).

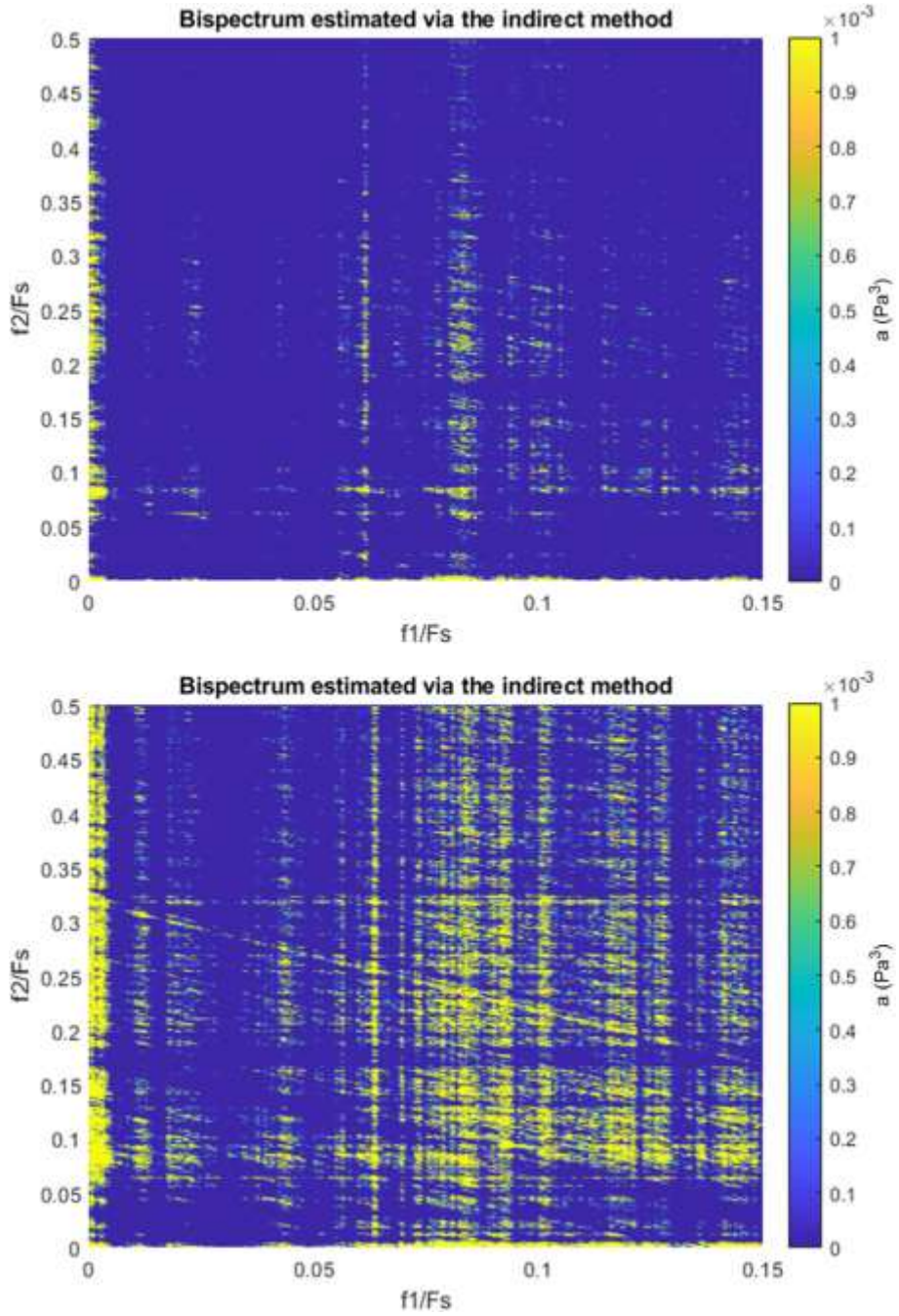

Figure 5.18: microphone auto-bispectrum in stable (up) and unstable (down) operating condition (F_s = 8192 Hz)

In the unstable case, both the 13X and 26X (corresponding on the abscissa axis to f1/Fs respectively equal to 0.2 and 0.4) seem to be related to a sub-synchronous content that could be ascribable to rotating stall (corresponding to f2/Fs ≅ 0.005). Furthermore, in the stable case, frequency contents with well distinguishable values are detectable (13X and 26X, respectively BPF and its order 2), whereas in incipient instability conditions, high frequency structural response presents an energy distribution spread on a wider frequency range with respect to the limitations imposed by 13X and 26X. This auto-bispectrum seems to reveal a correlation between BPF (13X, corresponding to f1/Fs

≅ 0.2) and its order two (26X, corresponding to f1/Fs ≅ 0.4) and the synchronous component (1X, corresponding to f1/Fs ≅ 0.02) both in stable and unstable case.

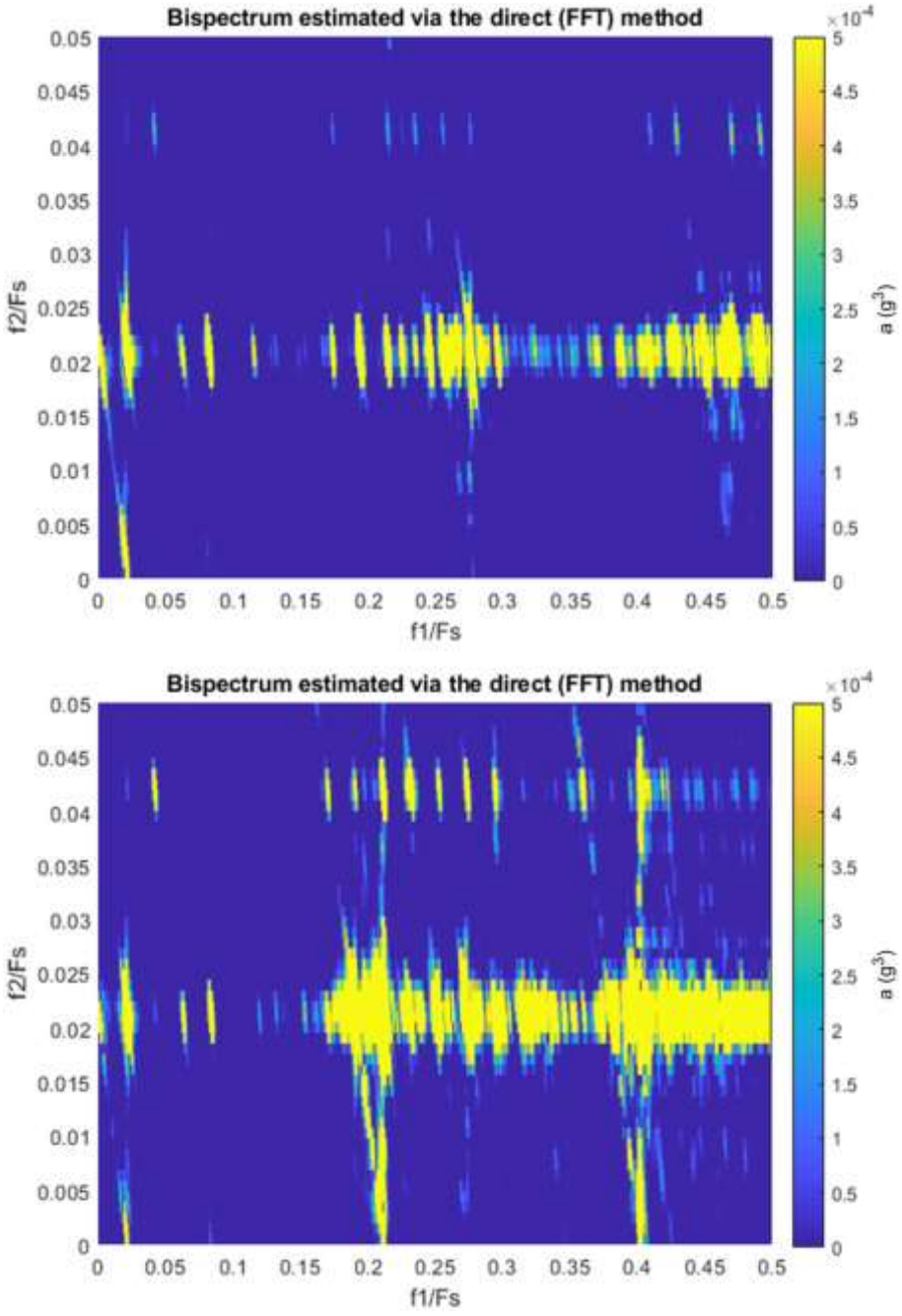

Figure 5.19: high frequency sampled accelerometer auto-bispectrum in stable (up) and unstable (down) operating condition (F_s = 65536 Hz)

Then, it has been made an addressed sum of all auto-bispectrum components modulus in the sub-synchronous range, since it is regarded as the most significant field for a possible diagnostic indicator. This has been chosen because phenomena that grow up close to instability create energy contents in system responses within this frequency range. This indicator looks like it is enough robust and thus it can be regarded as a reliable predictive tool with respect to low mass flow rate instability

phenomena in centrifugal compressors. These indicators are reported in Figure 5.20 for experimental data respectively for stable and unstable status, coming from structural and acoustic signal responses.

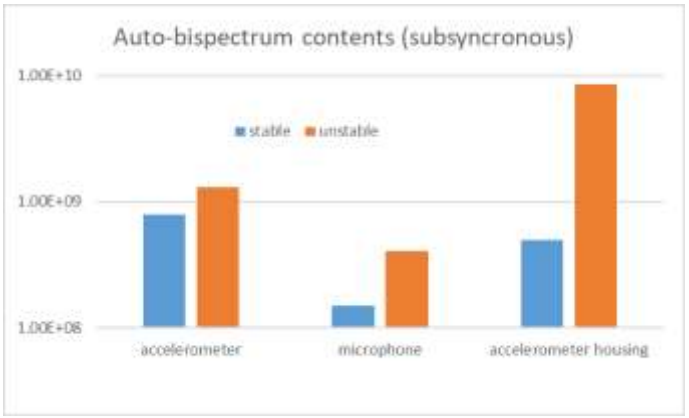

Figure 5.20: sum of all auto-bispectrum components modulus in the sub-synchronous range

5.2 Signal analysis performed with different plant configurations

Compressor response investigation in nearly unstable operating conditions, like rotating stall and incipient surge, is a challenging topic nowadays in the turbomachinery research field. Indeed, turbines connected with large-size volumes are affected by critical issues related to surge prevention, particularly during transient operations. Advanced signal-processing techniques conducted on vibrational responses provide an insight into possible diagnostic and predictive solutions which can be derived from accelerometer measurements. Indeed, vibrational investigation is largely employed in rotating-machine diagnostics together with time-frequency analysis such as smoothed pseudo-Wigner Ville (SPWVD) time-frequency distribution (TFD) considered in this section. It is characterized by excellent time and frequency resolutions and thus it is effectively employed in numerous applications in the condition monitoring of machinery. The aim and the innovation of this work regards SPWVD utilization to study turbomachinery behavior in detail in order to identify incipient surge conditions in the centrifugal compressor starting from operational vibrational responses measured at significant plant locations. The so developed investigation allows us to assess the reliability of this innovative technique with respect to conventional ones in this field of research, highlighting at the same time its qualities and drawbacks in detecting fluid machinery unstable behavior. To this aim, an experimental campaign has been conducted on a T100 microturbine connected with several volume sizes and this has allowed to assess diagnostic technique reliability in plant configurations with different dynamic properties. The obtained results show that SPWVD is able to successfully identify system evolution towards an unstable condition, by recognizing different levels and features of the particular kind of instability that is going to take place within the plant.

Instability phenomena regarding rolling bearings have also been identified and their interaction with surge onset has been investigated for diagnostic purposes.

The innovative aspects of this work regard the application of this technique that has not been yet fully exploited in the turbomachinery research field, in order to identify unstable phenomena like incipient surge detection. Indeed, thanks to its good resolution properties, it is a powerful tool in detecting anomalous operational responses, and thus it can also be employed in fluid machinery diagnostics in order to highlight hidden contributions that take place while, in the case of early surge detection, the compressor is moving towards its unstable operating region. It may be regarded as a progress with respect to well-established methods (e.g., overall sub-synchronous RMS value) since it can allow a reliable identification of the most significant coupled phenomena, ranging from the lowest to the highest frequencies, which typically arise moving towards turbomachinery off-design operating conditions. In the next section details of the technique considered are presented, while the results obtained from a mGT specific experimental investigation are shown and discussed in the following sections. Finally, SPWVD is compared for one significant operating condition with short-time Fourier transform (STFT) and Wavelet Transform (WT), which have been already employed in [20] for diagnostic purposes on the same mGT plant, in order to assess its reliability and to evaluate its merits and drawbacks with respect to other widely employed TFDs.

5.2.1 Overview on the adopted time-frequency signal processing technique

A diagnosis methodology is hereafter proposed, where WVD is performed in order to early detect incipient surge and rotating stall. WVD, together with other time–frequency distributions like WT and STFT, can describe temporal evolution of spectra or poly-spectra (moment spectra). A TFD is a transform which maps a one-dimensional signal into a two-dimensional time-frequency map, that describes how the spectral contents conveyed by experimental data vary with time. Therefore, TFDs are the natural tools for the analysis, synthesis, interpretation, and digital signal processing of nonstationary signals. Among the more employed TFDs there are the STFT [21], the Gabor representation [22], and the WT [23][24]. Linearity is a desirable property of algorithms used in investigating linear systems; on the other hand, quadratic time-frequency distributions have also been proposed, studied, and interpreted as time-varying power spectra, in order to investigate non-linear systems [25][26]. The so-called Cohen class of shift-invariant distributions comprises particular cases such as the Spectrogram, Rihaczek, Page, Wigner-Ville distribution (WVD) and Choi-Williams distributions [25][26]. The WVD became very widespread since it is characterized by several useful properties and was employed in the investigation of phase modulated signals, that are usual in radar and sonar [27]. Moreover, each member of Cohen's class can be interpreted as a two-dimensional linearly filtered version of the WVD [26]. A third order WVD was presented in [28]; then it was

generalized, and its properties were investigated in [29][30][31][32][33]. Higher-order WVDs describe the evolution in time of the higher-order moment spectra of the signal, in the same way that higher-order moment spectra evaluated on Fourier transform (FT) describe time-evolution of spectral contents evaluated by a linear transformation [21]. A theoretical basis of the Wigner–Ville distribution, is given in the following, in order to highlight its peculiar features with respect to other TFDs.

The Wigner distribution (WD) was presented in 1932 by Wigner in the context of quantum mechanics; its effectiveness to problems in communication theory was found by Ville in 1948; consequently, it is also called the Wigner-Ville distribution (WVD). A sequence of works by Classen and Mecklenbraüker [34] considered the effectiveness of the WVD for time-frequency analysis of continuous and discrete-time signals and was dedicated to applications in digital signal processing; sampling issues when working with discrete-time signals are also examined in [35]. Tutorial overviews over the WVD and its relationships with other time-frequency distributions (TFDs) can be found in [25][26][27][28][29]. In order to distinguish the second order WVD from the higher-order WVD it is common to refer to the conventional WVD as the Wigner spectrum (WS). Differently from the STFT, that is always resolution constrained either in time or in frequency (determined by the window function, which imposes resolution limits either in time or in frequency), and undergoes smearing and side lobe leakage, the WS provides excellent resolution in both the frequency and time domains. The Wigner cross spectrum (WCS) of two signals, x(t), y(t), can be defined in time or frequency domains, according to (5.1) or (5.2), respectively:

$$W_{xy}(t,\omega) = \int x\left(t+\frac{\tau}{2}\right) y^*\left(t-\frac{\tau}{2}\right) e^{-j\omega\tau} d\tau \tag{5.1}$$

$$W_{xy}(\omega,\xi) = \frac{1}{2\pi}\int X\left(\omega+\frac{\xi}{2}\right)\, Y^*\left(\omega-\frac{\xi}{2}\right) e^{j\xi t} d\xi \tag{5.2}$$

In which X(ω) and x(t) constitute an FT pair. The auto WS can be obtained by choosing x(t) = y(t) and it is a bilinear function of the signal x(t). The ambiguity function, that is widely used in radar, is defined as the two-dimensional FT of the WS, and can be expressed according to (5.3):

$$AF(\theta,\tau) = \int x^*\left(t-\frac{\tau}{2}\right) x\left(t+\frac{\tau}{2}\right) e^{j2\pi\omega\theta t} \tag{5.3}$$

Cohen's general class of TFD is defined as expressed in (5.4):

$$W_C(t,f) = \iint \Phi(\theta,\tau)\, AF(\theta,\tau) e^{-j2\pi t\theta} e^{-i\omega t - j2\pi f\tau} d\tau d\theta \tag{5.4}$$

In which the kernel $\Phi(\theta, \tau)$ specifies the kind of distribution which is desired to obtain. Let us define $x(n)$ as $x(n)$: = y(n) + $z(n)$; then it follows that:

$$W_{xx}(f,n) = W_{yy}(f,n) + W_{zz}(f,n) + W_{y,z}(f,n) + W_{z,y}(f,n) \tag{5.5}$$

Since the WVD is a quadratic transform, the WVD of the sum of two signals is not equal to the sum of the individual WVD, but it is affected by the presence of cross-terms. Due to the presence of cross-terms it is difficult to interpret the WVD. The influence of cross-terms can be limited by adopting appropriate filtering, in the ambiguity function domain, that is, by a suitable choice of the smoothing kernel $\Phi(\theta, \tau)$. In order to mitigate the effects of the cross-terms, Choi and Williams [36] suggested to employ the following kernel:

$$\Phi(\theta,\tau) = exp(-\theta^2\tau^2/\sigma^2) \tag{5.6}$$

In which the parameter σ regulates the amount of reduction of cross-terms (their amplitude is proportional to σ). On the other hand, increased suppression of cross-terms always leads to smearing or loss of resolution of the auto terms (the ones related to the actual signal) in the time-frequency domain.

In practice, signals are discretized in time, and then FTs are computed on a sampled frequency grid, too. The discretization in time and frequency of the continuous-time WVD leads to the non-aliasing condition that the original signal must be sampled at twice the Nyquist rate [35]. The discrete-time algorithm is also presented in the following [25][26]. The instantaneous cross-correlation can be defined as follows:

$$r_{xy}(m,n) = x^*(n-m)y(n+m) \tag{5.7}$$

in which n corresponds to the discretized time and m to the lag. The WCS, similarly to the continuous-time case, is then defined by:

$$W_{xy}(f,n) = \sum_m r_{xy}(m,n)\exp(-j\pi f m) \tag{5.8}$$

The auto WS can be obtained by choosing $x(n) = y(n)$. The original time-signal must be sampled at twice the Nyquist rate or faster, in order to prevent aliasing. In practice, even the frequency variable f is discretized, $f = k/K$, in which K regulates the frequency resolution. The WCS defined in (5.8) can also be implemented via two FFT algorithms, following the approach presented in [37]. Both approaches require the same computational and storage complexity. This algorithm in (5.8) is implemented in many routines, as it is the simplest way to compute WVD. The ambiguity function, AF, is computed as:

$$AF(m,\theta) = \sum_n r_{xy}(m,n)\exp\left(j2\pi n\theta\right) \tag{5.9}$$

The AF is then multiplied by the Choi-Williams filter, as below reported:

$$w(m,\theta) = \exp\left(-\left(\frac{m\theta}{\sigma}\right)^2\right) \tag{5.10}$$

A two-dimensional FT (θ to n and m to f) returns the filtered WVD, also known as SPWVD. Cross-terms can normally be mitigated following this approach, but always with a concomitant loss of frequency resolution. In practice, θ represents a discretized frequency grid.

5.2.2 Investigated operational mGT transients

Experimental investigation consisted in some tests where the mGT was connected with one of the three added volume arrangements. The T100 operated in grid connected mode while the variable speed control system was keeping the Turbine Outlet Temperature (TOT) fixed at a target value (set at 918.15K). The T100 was started-up to a production of 40 kW net electrical power (angular speed around 62 krpm). This beginning power was chosen according to several aims: significant off-design functioning (mGT plants are expected to be quite flexible in terms of part-load operating), sufficient initial surge margin, and at the same time prevention of too low load operation, in which plant control system would reduce TOT set-point; finally, it had to be a feasible beginning condition basing on the available plant devices (e.g., the VBE size). When a stationary operating condition was reached, surge occurrence was generated by progressively closing the VO valve (in 2.3 m^3 and 4.1 m^3 cases) or the VM one (0.3 m^3 case), that is in the air path between recuperator outlet and combustor inlet (by augmenting pressure losses). These valves were closed by successive steps of 10% (5% when close to the surge region) until surge event raised, usually in a span between 20-30% of valve fractional opening. Table 5.1 provides an overview of the test rig working conditions both for the initial and for

the last stable operating points actually considered in the measurements, for the three plant configurations investigated [1].

Table 5.1 – Initial condition (i.c.) and last stable point (l.s.p.) plant parameters

Volume	$V_1 = 0.3m^3$		$V_2 = 2.3m^3$		$V_3 = 4.1m^3$	
Operating point	i.c.	l.s.p.	i.c.	l.s.p.	i.c.	l.s.p.
N [krpm]	61.6	63.6	62.9	64.4	62.8	63.9
Net power [kW]	40.0	39.1	40.0	35.2	40.0	35.0
M [kg/s]	0.59	0.53	0.59	0.53	0.59	0.51
TOT [K]	918.15	918.15	918.15	918.15	918.15	918.15
Kp [-]	1.11	1.00	1.18	1.00	1.19	1.00
PRC1 [bar]	3.27	3.66	3.42	3.73	3.40	3.60

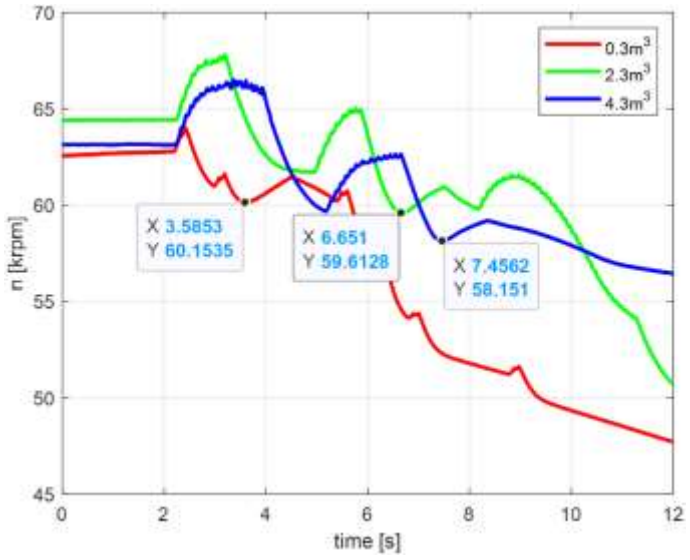

Figure 5.21 – Rotational speed traces corresponding to different volumes surge transients

From Figure 5.21 it can be noticed how qualitative angular speed trends are similar for the three different volumes investigated. In all considered cases the trend is influenced by surge cycles, and a pseudo-periodicity is characterized by lower frequencies by passing from the smallest interposed volume to the biggest one (see the markers corresponding to the end of two consecutive pseudo-cycles for each single speed trace indicating different fundamental pseudo-period). From the previous traces it is evident how the system response is not periodic even when deep surge conditions are encountered, and the necessity of employing TFD to identify spectral contents temporal evolution in response signals.

5.2.3 SPWVD application to mGT vibrational operational responses

In the following a time-frequency analysis based on SPWVD technique on mGT vibrational responses collected in different compressor operating conditions is performed. At first, SPWVD investigation is reported to detect vibration signature in stable conditions. This has allowed to identify spectral contents pattern from which a baseline has been defined that is typical of system normal working state and whose change may be regarded as representative of the onset of an anomalous condition.

After this, the proposed technique is applied in a systematic way to investigate its diagnostic capabilities. To this aim, operational vibrational responses during surge transients are analyzed by means of SPWVD for the three plant configurations adopted, corresponding to three different interposed volumes, according to the scheme reported in Table 5.2, which specifies frequency ranges investigated for each volume and observation time for each time-frequency analysis.

Frequency range analysis	Stable Stationary	Stable run up	Surge transient (whole)	Surge transient (extract)
Low frequency (<200Hz)	V_1	V_1	V_1, V_2, V_3	-
Sub-synchronous	V_1	V_1	V_1	-
High Frequency	V_1	-	-	V_1

Table 5.2 – summary of conducted time-frequency analyses

This is made with the aim of comparing different plant responses to look for possible surge precursors whose features (i.e., frequency characteristic and energy levels) may vary with the examined volume configuration. In the following, obtained results as well as motivation and significance for each considered specific plant configuration are reported.

The first signal analyzed with SPWVD technique is a vibrational response system acquired in a stable working condition (mGT vibrational reference signature) for 10 s, very far from surge line. In Figure 5.22, it is shown a SPWVD performed on data collected by the accelerometer placed in axial direction, close to mGT bearings. The investigation is limited to the whole sub-synchronous range.

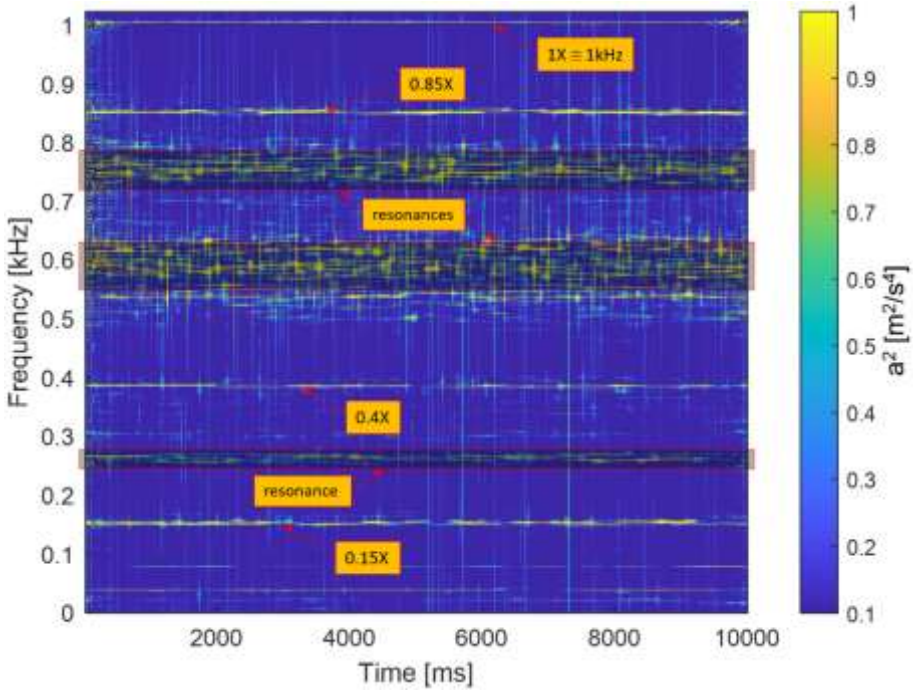

Figure 5.22 – SPWVD stable case, Volume 1 (0.3 m^3)

Indeed, the effect of mGT bearings on system response is strongly decoupled from volume configuration as it does not involve fluid-dynamic phenomena and it mainly depends only on shaft line rotordynamic behavior.

In stable conditions, some spectral contents can be clearly identified: the first one is related to the rotational frequency, which will be referred to as 1X from here on, which is next to 1 kHz, according to expected nominal rotational speed that is around 60 krpm. Then, spectral contents at 0.28 kHz, 0.6 kHz and 0.75 kHz are also well detectable and they might be related to resonance contributions in vibrational response. They are characterized not only by one frequency value, but they are spread in a narrow frequency band. For this reason, these response contents might be excited from broadband fluid-dynamic forcing and cannot by self-excited by a mechanical rotation of specific components.

This will be also deepened in the following by means of a run-up analysis. Then, sub-synchronous spectral contents with characteristic frequencies next to 0.15 kHz (and its second order 0.3k Hz) and 0.4 kHz are well distinguishable and their energy persists at almost the same level for all the observation time (10s). Nonetheless, in some specific time instants, a slight reduction of their energy levels can be observed, thus highlighting a not deterministic nature. These spectral contents may be attributed to an instability taking place in rolling bearings due to an unstable cage-whirl related to thermo-elastic instability contact phenomena in rolling elements that can significantly affect system response [44][45][46]. Indeed, under low loading conditions, as in mGT nominal working conditions, it may happen that the rolling element cannot drive the cage to move continuously and hence it is easier to identify spectral contents related to these unstable phenomena in system response. Indeed, the investigated system is equipped with two high speed ball rolling bearings with interposed lubricant fluid film between their housing and the external ring, which can be subjected to these phenomena. Figure 5.23 shows mGT rotor that is mounted with a cantilever configuration with two high-speed rolling bearings at the two opposite ends of electric generator rotor.

Figure 5.23 – mGT rotor (from left to right: turbine impeller, compressor impeller and electric generator rotor)

Moreover, spectral contents related to bearings can be useful for surge diagnostic purposes since their energy trend is dependent on fluid-dynamic forces acting on the rotor and hence they are sensible to surge onset, as shown in the following part. Finally, a possible modulating effect is identifiable at 0.85 kHz, involving 1X and the previous 0.15 kHz spectral content related to rolling bearings phenomena; indeed, this frequency value is obtainable as the difference between the carrier frequency (1X ≅ 1 kHz) and the modulating one (0.15 kHz).

In certain time instants spectral contents at 0.15 kHz and 0.4 kHz related to bearing instability are accompanied by others very close, which can be identified precisely in frequency thanks to the high frequency resolution typical of SPWVD. The presence of these spectral contents can be justified with the features of rolling bearing instability, whose characteristic frequencies are not strictly locked, but they can move in a narrow band frequency. This may happen because these are non-linear phenomena that might cause responses with more complex strongly time-variant spectral contents.

Furthermore, mGT rotational speed run up analysis is performed by means of SPWVD in order to better identify operational signatures; the investigated run up has been carried out by maintaining the outlet throttle valve in a sufficiently open position to never achieve unstable operating states. In the analysis reported in Figure 5.24, a specific run-up extract has been chosen where mGT rotational speed was increased from 30 krpm to 40 krpm, as deducible observing the main spectral content related to 1X, ranging from 0.5 kHz to 0.67 kHz. SPWVD analysis results allow to recognize the main critical velocities which excite structural natural frequencies. Indeed, from time-frequency map reported in Figure 5.24 (left) it is evident a natural frequency at 0.6 kHz that is excited by 1X forcing contribution at 36 krpm in a marked way. Moreover, this spectral content is not absent in the remaining part of the run-up, but it is weakly excited in almost all the observation time window, indicating the presence of a possible broadband forcing, that is always present for the whole investigated run-up. This content is the same that had previously been detected in steady state nominal conditions, that is well identifiable by means of SPWVD even if in some instants its energy level is very low. Another sub-synchronous spectral content at 0.28 kHz is present in the first part of the investigated extract for a localized time interval, indicating the presence of an exciting forcing whose frequency is dependent from rotational speed.

In the following Figure 5.24 (right), a detail of the previous map is shown in a lower frequency range, up to 0.4 kHz; in order to better visualize sub-synchronous contents in this map color-axis scale has been reduced, since otherwise these spectral contents with low energy would not be well identifiable, with particular reference to their energy level fluctuations.

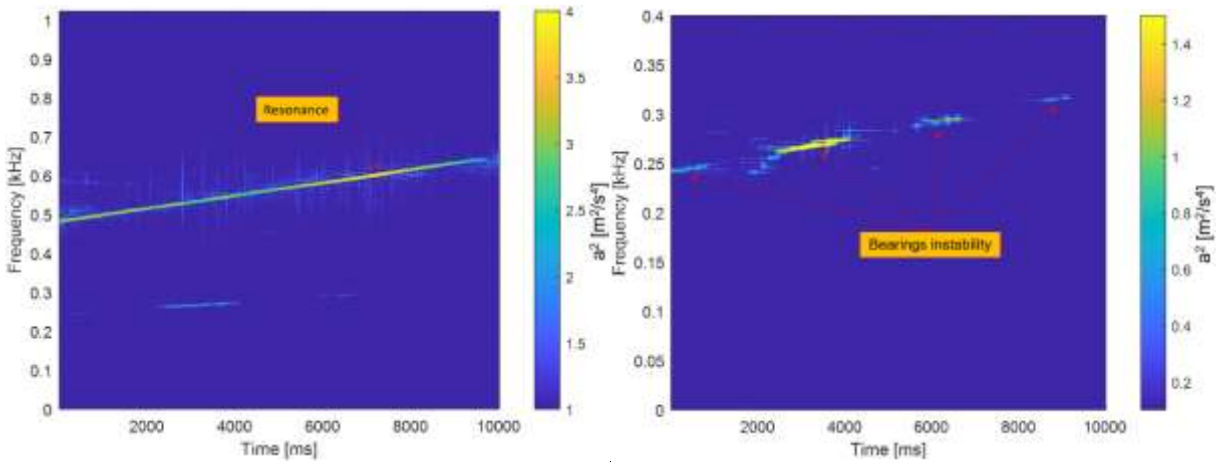

Figure 5.24 – SPWVD on run-up extract 30-40 krpm - left: whole sub-synchronous range; right: detail in frequency range 0-0.4 kHz

In Figure 5.24 (right) it can be recognized a sub-synchronous contribution whose frequency characteristic is dependent from rotational speed and whose energy level is variable, indicating the presence of an intermittent phenomenon. These two features make suppose that this content may be related to rolling bearings instability. Indeed, at nominal rotational speed this spectral content reaches the frequency of 0.4 kHz and it seems to be the same contribution previously identified in Figure 5.22 and already attributed to rolling bearings instability.

In Figure 5.25 a run-up analysis is conducted on a wider rotational speed range (30-50 krpm) and the whole sub-synchronous range is represented: all the previous identified spectral contents are well detectable. At the lower frequencies, energy levels of detected spectral contents are largely lower than 1X energy and then it is necessary to change maps color-axis scales in order to be able to recognize their energy trend. Due to adopted color axis limits, 1X energy variation is not well detectable, as it has been already discussed in Fig 5.24 (left). Moreover, from Figure 5.25 it can be identified, in the run-up second half, a sub-synchronous contribution at 0.2 kHz with not negligible energy level. This is a spectral content whose frequency characteristic is invariant with rotational speed; this indicates the possible onset of structural resonances that may be excited by some fluid dynamic forcing which is someway coupled with the structural vibration modes.

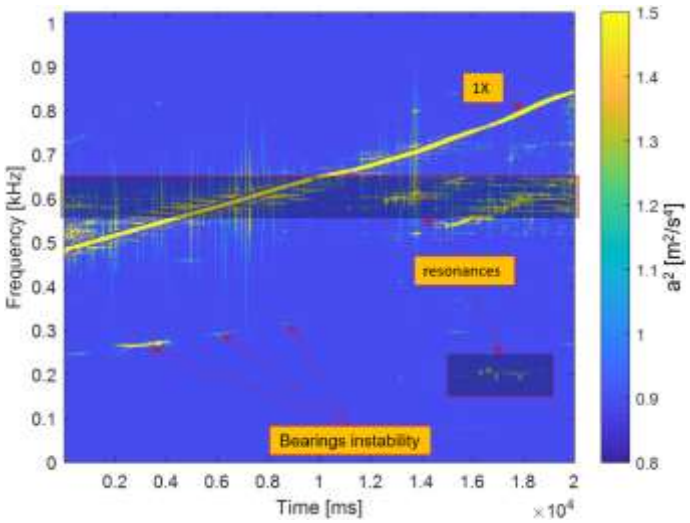

Figure 5.25 – SPWVD on run-up 30-50 krpm

The first selected surge event regards the smallest interposed volume. Figure 5.26 reports system vibrational response for the incipient-deep surge transient. After an incipient surge condition (0-2 s), a sequence of deep surge events happen in the remaining observation time window (2-10 s). vibration overall reduction at the end of the time extract is due to rotational speed decrease.

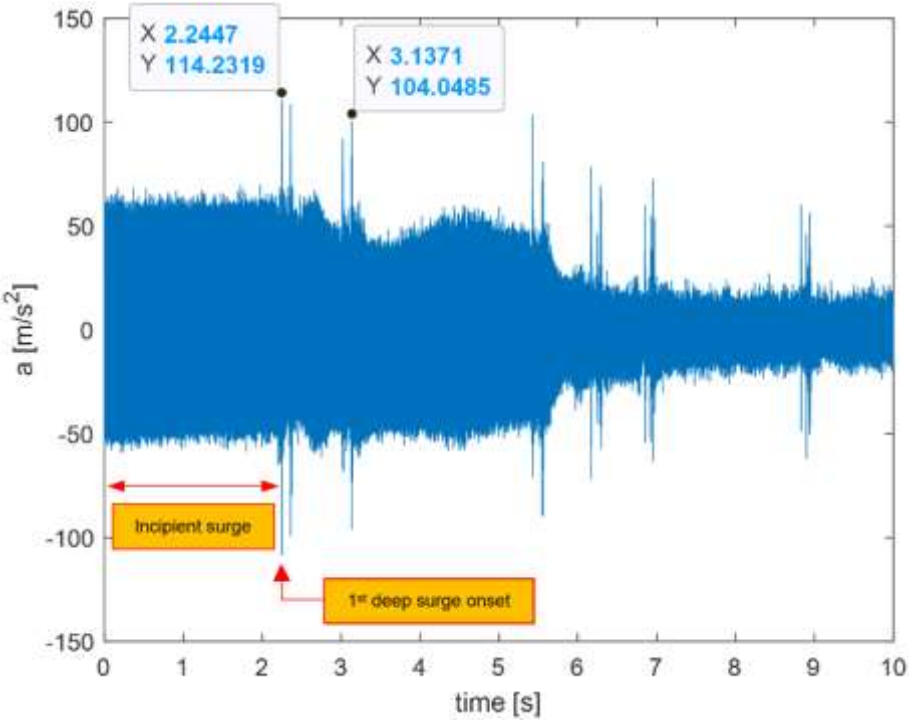

Figure 5.26 – Accelerometer signal in 10s surge transient with minimum volume (0.3m^3) – Time interval between incipient and deep surge: 0-2s

The blue markers evidence acceleration peaks due to the presence of anomalous forces, associated to surge, that are characterized by shock nature. Furthermore, additional labels indicate the onset of the first deep surge cycle starting from incipient surge conditions. After the first deep surge cycle is

encountered, the same sequence is experienced in the following time instants of the analyzed surge transients. The present section is structured as follows :firstly, SPWVD investigation is presented for the minimum volume in all the sub-synchronous frequency range during its whole surge transient. Afterwards, the same approach is presented for the three considered plant volume configurations but limited to the lowest frequency range. Moreover, a comparison with STFT and WT is performed to deepen merits and drawbacks of each signal processing technique. Finally, a SWOT analysis is presented by including also cyclostationary technique [38][39]. Finally, SPWVD is performed only for the minimum volume configuration in the high frequency range, by analyzing a shorter time extract; indeed, due to the higher computational effort required while processing such a big amount of experimental data, since no down-sampling strategy [20] has been adopted in this case, observation time has been reduced accordingly to focus only on the most relevant temporal interval.

In Figure 5.27 SPWVD analysis of the surge transient vibrational response shown in Figure5.26 is performed in the range 0-1.024 kHz (including all sub-synchronous contents together with synchronous one), in order to investigate how spectral contents are affected by changing system operating condition. It is possible to clearly identify 1X spectral content (close to 1 kHz at the beginning of the transient), that just after the first deep surge cycle is characterized by a decreasing frequency trend, according to rotational speed decay reported in Figure 5.21 for the minimum interposed volume. A 0.6 kHz spectral content, previously identified in stable behavior as a possible system resonance, is markedly present for all the time interval investigated, and it increases its energy level in correspondence with the entrance in each deep surge cycle. Before the first deep surge cycle happens (time interval 0-2 s), this content is present due to broadband excitations related to an off-design flow incidence within the impeller that gives rise to anomalous blade loads distribution. This structural resonance [42] has higher energy level than in the stable case since it may be excited by fluid-dynamic operating loads related to compressor off-design conditions. Furthermore, soon after each deep surge cycle, its energy level suddenly increases due to shock excitation related to mass flow rate strong oscillations. Its structural resonance nature is confirmed by frequency characteristic that is independent from 1X, as it can be seen from the shutdown phase when rotational speed markedly decreases.

In the 0-0.4 kHz range, the presence of contents ascribable to instability bearings phenomena related to cage-whirl seems to be further confirmed even in these operating conditions. Indeed, spectral contents previously identified in the stable case (0.3 kHz and 0.4 kHz), during this transient exhibit intermittent trend in their energy levels, in particular between two consecutive series of deep surge cycles. External loads have a significant influence on cage stability, and it can be stated that in particular axial loads have a great influence on cage dynamic behavior in high-speed rolling bearings

[44][45][46][47]. These contributions related to bearings are characterized by weak energy before the first deep surge cycle happens, that is in incipient surge conditions. This may be justified by anomalous fluid-dynamic forcing which stabilize bearings by enhancing operating loads acting on the rotor. On the contrary, the previous contents increase their energy after the first deep surge cycle, indicating the onset of bearing instability phenomena. This happens because the first deep surge cycle gives broadband energy which is able to excite this phenomenon, jointly with the reduction of fluid-dynamic loads on the rotor that contributes in reducing bearing stability margin (unstable cage-whirl and thermo-elastic instability). Moreover, these spectral contents exhibit a frequency characteristic dependent from rotational frequency (1X), since their frequency level decreases in correspondence with velocity reduction related to combustor shutdown, confirming their self-excited by rotation nature. These spectral contents imputable to bearings, change their energy and persistence in vibrational response operational spectrum when approaching surge conditions, becoming thus a possible diagnostic precursor of this kind of compressor instability.

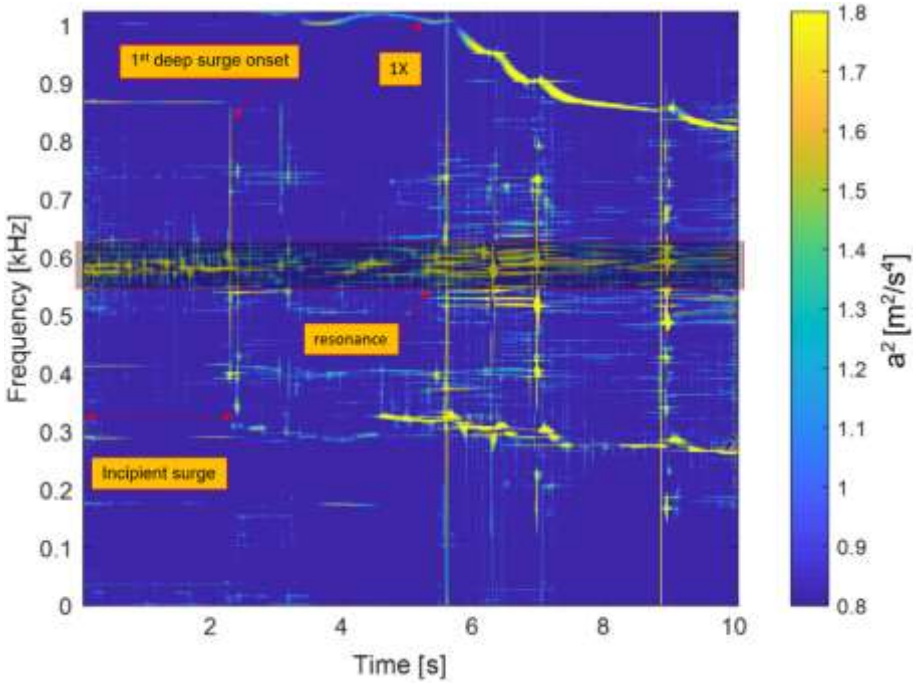

Figure 5.27 – SPWVD unstable case, minimum volume (0.3 m^3) – Time interval between incipient and deep surge: 0-2s

Other spectral contents with lower characteristic frequency (below 0.2 kHz) might be in the same way reconducted to mGT bearings instability phenomena. They could be due to a mechanical interaction between the two mGT bearings equipping the shaft line, that can generate modulating effects. Indeed, these contributions are always present with high energy levels in the stable case map (refer to Figure 5.22), while in the unstable case they are characterized by low energy levels for almost every time instants.

Even in this case, it seems that anomalous loads due to unstable working conditions influence bearings behavior by mitigating their unstable phenomena and consequently the interaction among them. At the highest frequency values in the sub-synchronous range, the spectral content at 0.85 kHz is still present with relevant energy only in the first instants, while after the first deep surge cycle it significantly reduces its energy level. Indeed, in the investigated surge transient, this spectral content exhibits a similar trend with respect to the low frequency sub-synchronous ones related to rolling bearings instability and this agrees with the hypothesis of a modulation phenomenon involving 1X order. The previously conducted analysis on plant minimum volume configuration has evidenced how the spectral contents in the lower frequency range (up to 0.2 kHz) also contain useful information for diagnostic purposes. Hence, in the following, SPWVD analysis is performed for the three different interposed volumes with a higher frequency resolution, to better identify significant spectral contents. With reference to previous analyses, a surge transient extract with a wider incipient surge conditions part is chosen by doubling observation time (20 s) in order to better focus on low frequency contents evolution. In Figure 5.28 results are reported for the previous plant configuration (minimum volume), in the final part of surge transient, including incipient and deep surge. Analyzed incipient surge starts at the beginning of the extract and ends at 12 s, where the first deep surge cycle is encountered.

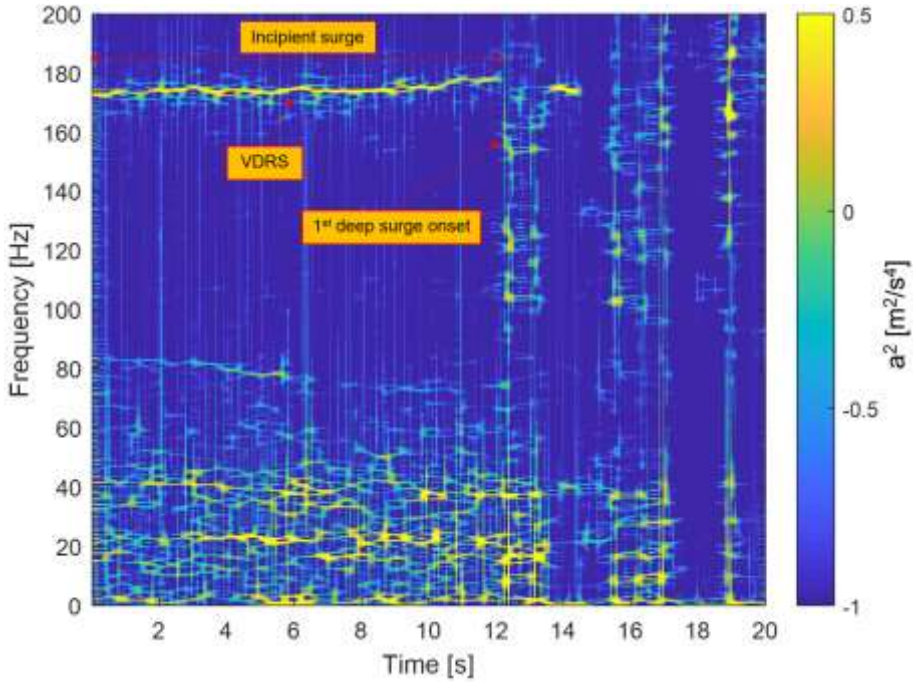

Figure 5.28 – SPWVD in 0-200 Hz frequency range, minimum volume (0.3 m^3) - Time interval between incipient and deep surge:0-12s

The analysis is performed up to 0.2 kHz since this frequency level may contain characteristic frequencies of surge precursors (e.g., rotating stall) for this kind of fluid machine. Indeed, mGT centrifugal compressor is equipped with a vaneless diffuser, and for this kind of radial

turbomachinery, rotating stall inception mechanism is peculiar; hence, its typical frequency is expected to be found at lower frequency levels with respect to vaned diffusors centrifugal compressor or axial ones. For a similar kind of compressor investigated in [48] vaneless diffuser rotating stall VDRS was found at a frequency level around 0.15 – 0.2X. From Figure 5.28 it can be observed that there is a spectral content at about 180 Hz at the initial instant whose frequency characteristic is variable in the considered surge transient extract. It can be attributed to VDRS, also because its frequency is influenced by impeller rotating frequency (1X). The most remarkable fact is that this spectral content is not present in stable conditions, while it is well detectable in the first 12 s before surge onset; indeed, in incipient surge conditions VDRS is characterized by high energy levels, while after the first deep surge cycle its energy goes rapidly to lower values. This happens because when surge conditions are reached, VDRS cannot exist at the same time, since surge is an instability phenomenon that modifies mass flow rates in the plant; consequently, in this condition the compressor is subjected to sudden mass flow rate fluctuations which does not allow VDRS persistence within the fluid machine [49]. Spectral contents at lower frequencies (40 Hz, 80 Hz) may be related to rolling bearings instability, since their trend is similar with what has been found in the higher frequency sub-synchronous range for the contents at 0.3 kHz and 0.4 kHz previously identified as related to rolling bearings (refer to Figure 5.27). Indeed, they are characterized by high energy levels in the stable case (refer to Figure 5.22), while in unstable conditions they generally reduce their energy content, in particular between one deep surge cycle and the following one. Even the trend exhibited by these contributions seems to suggest that incipient surge stabilizes bearings by increasing anomalous load acting on them that overcome regular operating one (e.g., residual imbalance). In the following, SPWVD analysis is performed for the intermediate and maximum volume configurations. In Figure 5.29, results are presented for the interposed medium volume plant configuration (2.3 m^3) during a surge transient in which the first deep surge cycle starts at around 6s. As in the previous case, in incipient surge conditions there is a spectral content in the sub-synchronous range that might be associated to VDRS. Its frequency value is the same of the one found for the minimum volume, and this agrees with VDRS hypothesis, since this phenomenon is substantially independent from system volume and plant fluid-dynamic characteristics. Indeed, when the first deep surge cycle occurs, its energy level strongly decreases, while it is well marked in incipient surge conditions. After the entrance in surge conditions, this contribution does not reach again relevant energy levels, thus confirming the hypothesis of VDRS within the compressor. Even in this plant configuration, at lower frequency levels there are spectral contents which are present in the stable case with a constant energy level, while in unstable conditions they are characterized by an intermittent energy; hence, they can be attributed to rolling instability phenomena, as it was found for the minimum volume configuration.

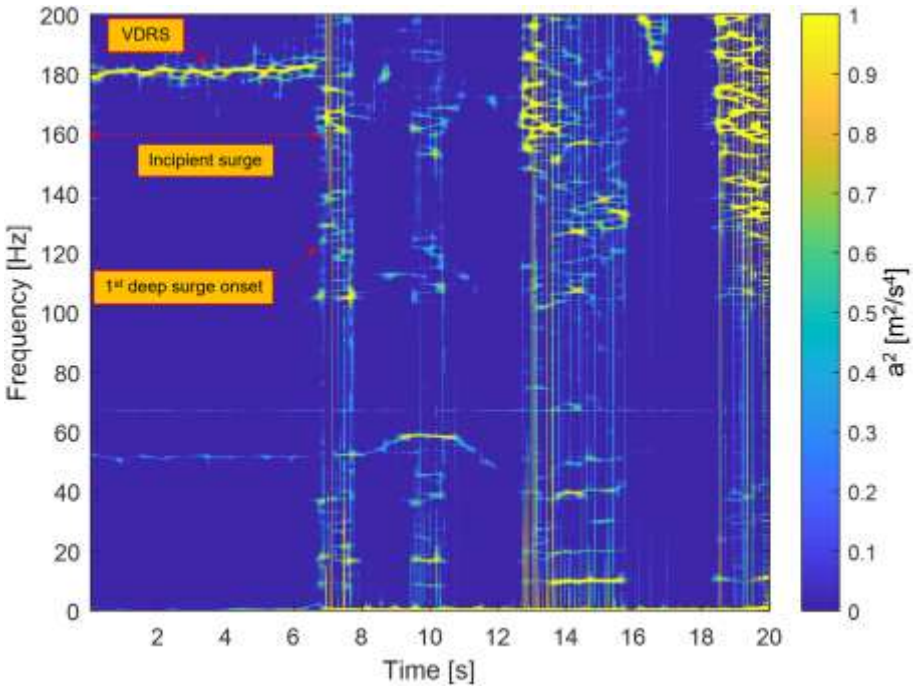

Figure 5.29 – SPWVD in 0-200 Hz frequency range, intermediate volume (2.3m^3) - Time interval between incipient and deep surge: 0-6s

In Figure 5.30 results are presented for the maximum interposed volume configuration (4.3 m^3), during a surge transient in which the first deep surge cycle begins at around 9.5 s. Even in this case, there is a spectral content that may be related to VDRS with the same peculiar characteristics found in the two previous cases (frequency around 180 Hz, energy level intermittent with time). In detail, its energy level suddenly decreases in correspondence with the entrance in the first deep surge cycle. Hence, this contribution is present only in incipient surge conditions in agreement with the hypothesis of a VDRS phenomenon. Furthermore, there is a spectral content at around 50 Hz which decreases its energy level in incipient surge conditions, before entering the first deep cycle. This contribution might be related to bearings instability, as observed for the other two plant configurations examined. A dispersion in frequency values (ranging from 40 Hz to 50 Hz) of spectral contents related to bearings instability can be justified by a sensitivity in load values acting on the supports, which are not exactly the same in the three considered transients due to slightly different operating conditions which unavoidably affect mGT. In all cases, very low frequency contents (under 30 Hz) are present and they may be related to acoustic modes; their identification seems to be critical since analyses are performed on accelerometer signals whose energy depends on structure dynamic characteristics, which acts like a high-pass frequency filter; consequently, it may significantly reduce low frequency energy contents making difficult the detection of these phenomena. VDRS spectral contents identification must take into account actual stall configuration taking place within the compressor which is not always easily predictable; indeed, VDRS apparent rotating frequency depends on its

pressure pattern and therefore it can vary due to a change in the stall configuration (e.g., number of lobes). In some cases, it can be identified only by means of a detailed analysis of system response (e.g., by means of dynamic pressure probes) and the lack of a priori information on the specific spectral contents to be observed may affect the capability of detecting surge inception.

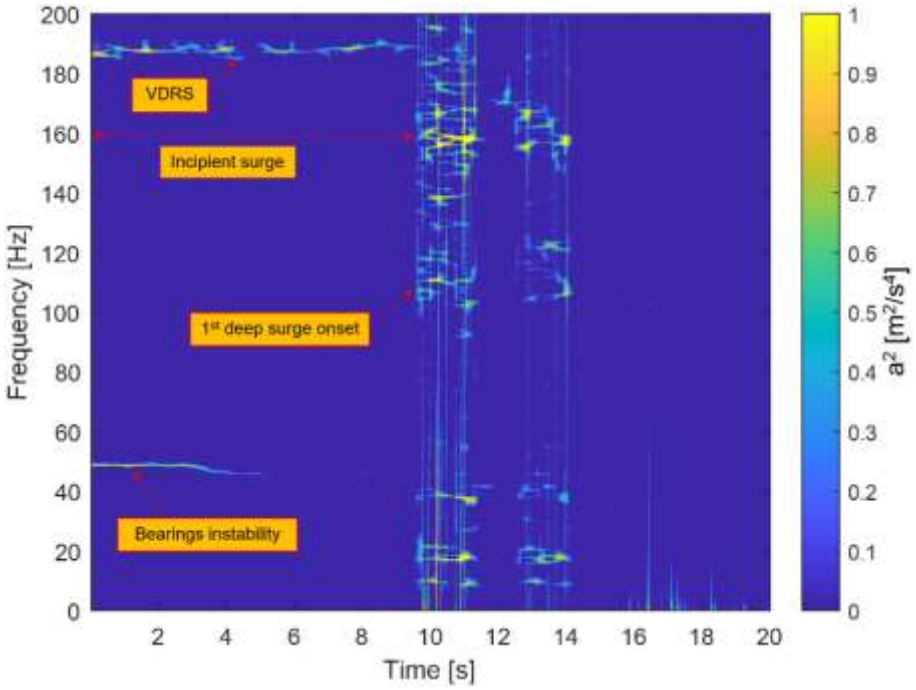

Figure 5.30 – SPWVD in 0-200 Hz frequency range, maximum volume (4.3 m³) - Time interval between incipient and deep surge: 0-9.5s

For the maximum interposed volume plant configuration, a comparison among TFDs is performed on the investigated surge transient, in order to underline advantages of SPWVD with respect to classical TFD like STFT and WT. However, it is important to remark that there are other methodologies that proved to be useful for surge precursors identification, like cyclostationary signal analysis, as proved in recent works reported in [38][39]. In Figure 5.31 surge transient is investigated by means of STFT and WT techniques and obtained results are reported hereinafter.

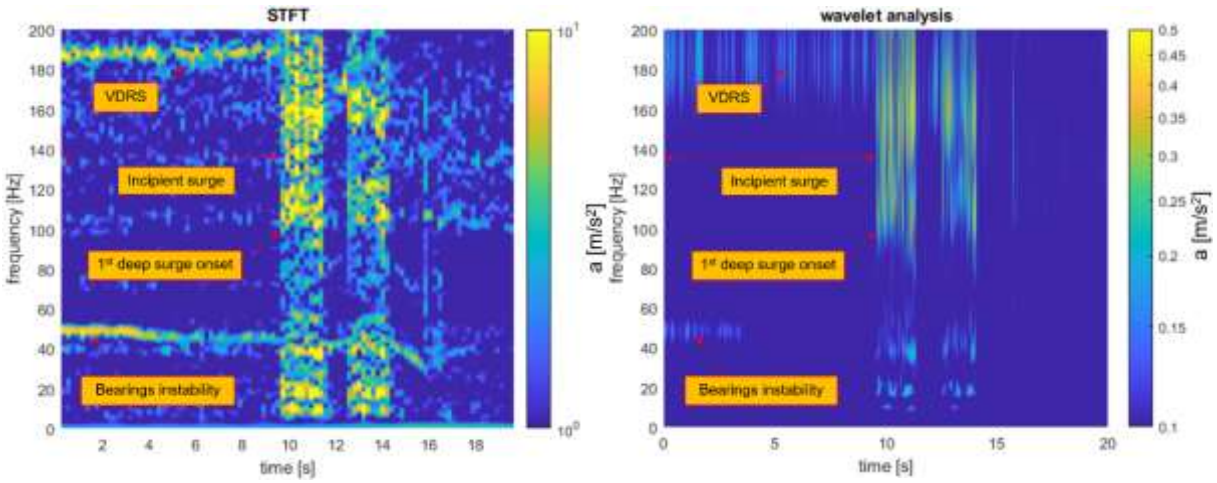

Figure 5.31 – Comparison on unstable case in 0-200 Hz frequency range, intermediate volume (2.3 m^3) - left: WT; right: STFT - Time interval between incipient and deep surge: 0-8s

By comparing STFT with SPWVD it is confirmed what is predicted from theory: STFT, which is either time resolution or frequency resolution limited, cannot detect rotating stall intermittency since it is not characterized by enough temporal resolution. Indeed, parameters are set in order to obtain the best compromise between time and frequency resolutions; in this case, the time window is chosen to keep a good frequency resolution, and then unavoidably STFT loses in terms of temporal frequency. Indeed, spectral contents identified by SPWVD are well detected also by STFT in terms of their amplitude trend, but it is more difficult to understand the exact time instants where they appear or disappear. WT results, on the contrary, exhibit a bad frequency resolution, in particular at low frequency levels, while they are characterized by excellent temporal resolution. SPWVD seems to be the best TFD, although it is necessary to mitigate cross-terms influence by means of adequate smoothing kernels (e.g. Choi-Williams kernel) and this unavoidably leads to resolution loss in the time-frequency domain. Despite this, it gives the best results in terms of frequency resolution and at the same time it maintains a good temporal resolution. Its main drawback is related to computational effort required to process experimental data with respect to classical techniques, together with the presence of slightly negative energy levels due to a not complete suppression of cross-terms, that is never met when adopting conventional techniques like STFT and WT. In order to further improve diagnostic capabilities, in some cases it is appropriate to identify also unstable properties of spectral contents in system response; to this goal, the adopted technique needs to present adequate jointly time and frequency resolution. Phenomena with a complex dynamic like VDRS can be well detected if these aspects are considered in the choice of the signal processing technique. Indeed, SPWVD seems to improve VDRS identification, since it gives an additional diagnostic contribution by capturing a not permanent energy temporal evolution together with its typical sub-synchronous frequency. Combining these two response properties allows to avoid false positives. Finally, a SWOT analysis

about the main signal processing techniques employed in this research field has been performed and its highlights are summarized in Table 5.3.

Table 5.3 – SWOT analysis of main signal processing techniques

	Strengths	Weaknesses	Opportunities	Threats
STFT	Simplicity of mathematical framework, most employed technique in industrial and academic world, classic implementation algorithm convergence velocity	Indetermination principle: both time and frequency resolution are bounded by time window that dictates a reciprocity relation between them	Real-time applications, easiness to implement and manage, widespread knowledge and therefore immediate interpretation of obtained time-frequency maps	False positives: not enough jointly time and frequency resolution can lead to wrong identification of detected spectral contents
Wavelet	Transient events characterization, multi-resolution analysis: frequency resolution can be set choosing different wavelet mother functions (i.e. by selecting a suitable mathematical basis)	Complexity of mathematical framework, computational effort required (depending on the implementation algorithm), and so higher computational times	Detailed investigation of fast transient phenomena, good interpretability of time-frequency distribution, tunable choice of frequency resolution by selecting mathematical basis functions	Computational effort depending on implementation algorithm, and so not always possible to perform real-time diagnostics with conventional memory properties
SPWVD	Jointly high time and frequency resolutions: from a theoretical point of view it can preserve its resolution properties in all frequency ranges	Computational effort required, and so even higher computational times, therefore no real-time applications (STFT could be more suitable for this purpose)	Investigating high frequency range with jointly high time and frequency resolutions in all the possible frequency ranges to be explored in signal analysis	High computational effort, therefore, no chance for real-time diagnostics with standard memory properties typical of common hardware
Cyclostationary	Best technique to detect both amplitude and frequency modulation phenomena (e.g. rotating stall) and all periodic phenomena related to synchronous response	It cannot detect spectral contents which are not modulation phenomena (e.g. spectral contents not related to 1X rev), hence not suitable to study non-synchronous response	Real-time application in turbomachinery and energy systems field, detection of all modulation spectral contents related to 1X and its relevant multiples	No chances of detecting spectral contents not related to 1X, not effective in high frequency range, no related time-frequency maps

Cyclostationary technique can effectively capture only modulated contents of synchronous components, while SPWVD allows to identify also the overall spectral contents pattern, including structural and acoustic resonances; due to this, in some applications SPWVD can provide a diagnostic feature set completer and more efficient for anomalous condition detection. With respect to STFT and wavelet time-frequency distributions, SPWVD can require higher computational times, but this also depends on the implementation algorithm employed. Thus, a further optimization of SPWVD implementation algorithm might reduce the required computational effort. However, with respect to STFT classical implementation algorithm, surely both wavelet and SPWVD always involve higher computational effort. To conclude the presented investigation, the same methodology is proposed to study how the blade pass frequency (BPF) is influenced by moving towards surge conditions. This analysis is presented only with reference to the minimum volume, since the influence of interposed

volume is negligible for the frequencies which are meant to be studied; indeed, for the frequency band of 10-30 kHz it is reasonable to expect that phenomena are mainly due only to the compressor, since their characteristic frequencies suggest that they do not involve big fluid masses. To this purpose, experimental data collected by a high frequency accelerometer are processed by means of SPWVD and the obtained results are presented by comparing maps concerning a stable working condition, far from surge line, with the ones related to an unstable one. In this experimental campaign, data were sampled at 204.8 kHz, and 20 ms time extracts have been defined for the analysis. This is made to obtain a significant but not excessive number of samples not to increase computational times and at the same time to allow to observe how spectral contents evolve with reference to each single shaft rotation. In Figure 5.32, SPWVD results coming from surge transient extract (right) are compared with the ones obtained from a same time-window extract in stable conditions (left).

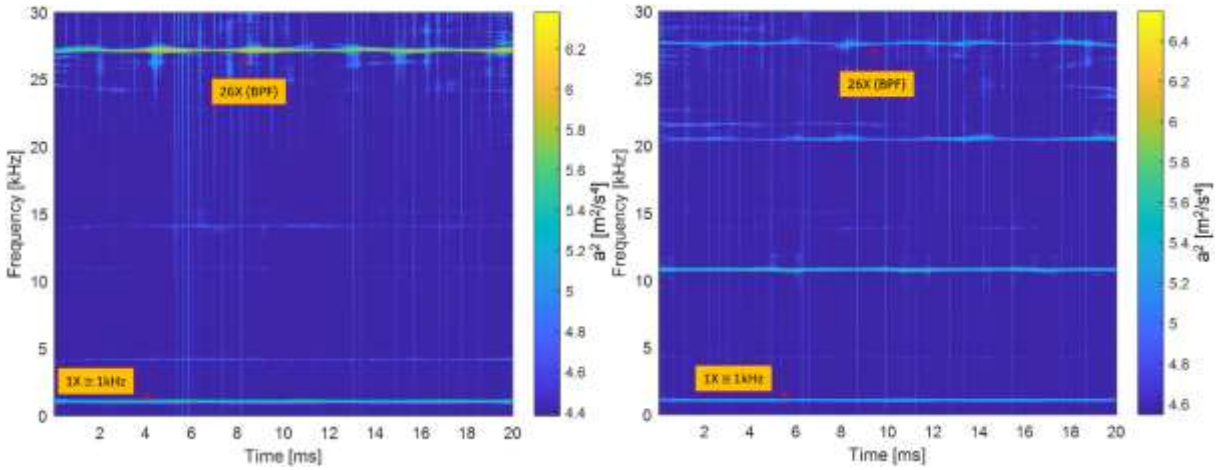

Figure 5.32 – SPWVD in 0-30 kHz frequency range, minimum volume (0.3 m^3) - left: stable case; right: unstable case

It can be noticed how in the stable case there is a spectral content whose energy is persistent with time at a frequency level around 26 kHz (which is 26X order, corresponding to the BPF taking into account both main and splitter blades). Its energy level is very high, and this may be explained by the blade passage phenomenon, that in stable conditions is influenced by the presence of both the main blades and the splitter ones (see in Figure 5.23 compressor impeller). On the contrary, in the condition close to instability, the blade passage phenomenon is not influenced only by the rotor blades, but also from phenomena related to fluid flow in the inter-blade channels. Indeed, phenomena associated to effluxes within the impeller are modified by compressor operating condition, by showing as more significant the cyclic nature of the more external blades, that is altered with respect to the nominal working point.

In the colormap related to the unstable case, it is evident how the spectral content at 26 kHz is characterized by a lower energy level with respect to stable conditions, while a spectral content with a characteristic frequency just less than the 13X order (BPF considering only the main blades) has a much higher energy level; moreover, other two spectral contents at high frequency, just higher than 20 kHz which are not present in the stable case, are well identifiable and their energy levels are similar to the 26X. These contents have lower frequencies with respect to the 26X, that is a typical content well identifiable in stable behavior, but at the same time they are always higher than the 10X. The onset of these contents in structural responses may be ascribable to a modification of fluid flow within the inter-blade channels of the impeller when approaching unstable behavior. Indeed, low mass flow rate conditions close to instability conditions cause anomalous incidence values at the impeller inlet thus modifying significantly spectral contents of the measured response in the high frequency range. In Figure 5.33 a more detailed analysis in a shorter time window is presented, in order to appreciate how spectral contents modify their energy levels in the last 5 ms of the surge transient. In the stable case (left), spectral contents characterizing compressor nominal behavior are confirmed to be the previous identified ones: 26X and 1X, that is related to rotor dynamic unbalance.

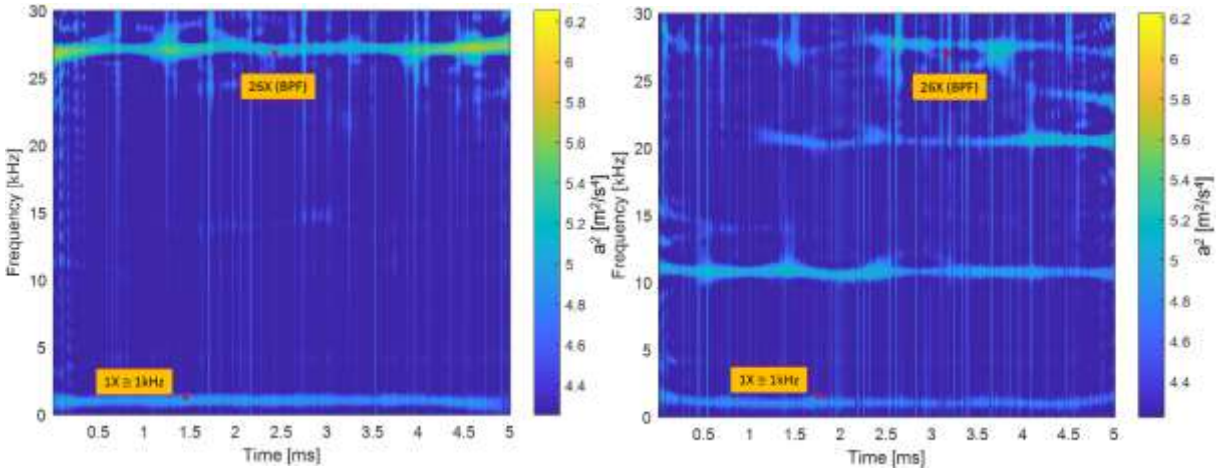

Figure 5.33 – SPWVD in 0-30 kHz frequency range, minimum volume (0.3 m^3), detail of 5ms - left: stable case; right: unstable case

In the unstable case (right), it can be noticed how, just before entering the first deep surge cycle, the spectral content corresponding to 26X, that is characterized by much lower energy level with respect to the stable case, is also intermittent with time; on the contrary, the spectral content just above 10 kHz is persistent with time and its energy level is almost invariant with respect to the 26X one. In the first 2.5 ms, the content at 10 kHz has a higher energy, while the one at 26 kHz is not well identifiable; as soon as the content related to the 26X order increases its energy and thus it appears on the colormap, the one at 10 kHz partially decreases its energy, according to the color-scale reported for each map. This confirms what has been stated before: there is an energy exchange between 26X order and 13X

one, that happens in a very limited time interval, since the compressor is working in a condition close to the stability limit, and thus in some instants also splitter blades contribution is relevant for the blade passage phenomenon. Finally, also a spectral content close to the 20X order, makes its onset after about 1 ms and its energy increases progressively when approaching the first deep surge cycle. The spectral content that is present at about 10 kHz in incipient surge conditions can be used as a diagnostic surge precursor, since in system stable response there is no relevant energy content at that frequency level. Indeed, in the unstable case, spectral content at order 26X decreases its energy level and the response energy is spread in a wider frequency range, between 9X and 20X. This specific energy content reduction can be another robust indicator of approaching surge and then it may be used jointly with the previous high frequency feature (10X trend). Basing on this evidence it is possible to define rules to be implemented in an expert system which is able to early detect incipient surge. Indeed, when high frequency dominant content (26X) loses part of its energy it means that non-deterministic phenomena arise with a not well-defined cyclic nature and hence response signals energy distribution changes its frequency pattern. This technique has allowed to better visualize spectral contents time evolution, even very fast and in short observation times, also in the case of with very high frequencies spectral contents. This is an advantage with respect to conventional techniques, making it potentially of interest for early diagnostics. Even if the proposed high frequency analysis is more challenging due to both difficulties in performing measurements and post-processing, it relies on phenomena characterizing the compressor itself; therefore, it can be generalized and somehow extended to other configurations in other cases (e.g., different vessels). Indeed, the spectral contents sensitive to surge approaching suitable to act as a diagnostic feature are a priori well predictable on the basis of impeller characteristics (e.g., BPF characteristic frequency in stable behavior) and thus the presented approach can be applied to other systems or application cases without requiring any kind of experimental characterization. On the contrary, the sub-synchronous analysis seems to be dependent from the plant configuration and thus it is less immediate to predict even a priori the spectral contents that can be exploited for diagnostic purposes [50].

Bibliography chapter 5

[1] Ferrari M.L., Silvestri P., Pascenti M., Reggio F., Massardo A.F., "Experimental Dynamic Analysis on a T100 Microturbine Connected with Different Volume Sizes", Journal of Engineering for Gas Turbines and Power, 140 (2018) 021701_1-12.

[2] Ferrari M.L., Pascenti M., Magistri L., Massardo A.F., "MGT/HTFC hybrid system emulator test rig: Experimental investigation on the anodic recirculation system.", Journal of Fuel Cell Science and Technology, 8 (2011) 021012_1-9.

[3] Reggio F., Ferrari, M.L., Silvestri P., Massardo A.F., "Vibrational analysis for surge precursor definition in gas turbines" 2019 Meccanica

[4] Ferrari M.L., Silvestri P., Reggio F., Massardo A.F. "Surge prevention for gas turbines connected with large volume size: Experimental demonstration with a microturbine" 2018 Applied Energy

[5] Lucifredi A., Noceti D., Ferraro A., Silvestri P., Ortenzio G., "Acoustic and vibrational characterization for noise reduction of a Piaggio P180 cockpit blower" (2011) 8th International Conference on Condition Monitoring and Machinery Failure Prevention Technologies 2011, CM 2011/MFPT 2011, 1, pp. 254-264.

[6] Craig R. R., Kurdila A. J., "Fundamentals of structural dynamics" John Wiley edition, New Jersey - USA, 2006

[7] Lucifredi A., Silvestri P. "An overview of fundamental requirements for a condition monitoring and fault diagnosis system for machinery and power plants" (2003) Proceedings of the Tenth International Congress on Sound and Vibration, pp. 4691-4698.

[8] Harris C.M., Piersol A. G., "Harris' Shock and vibration handbook", McGraw-Hill, New York, 2002, ISBN 0-07-137081-1

[9] Vance J. M. "Rotordynamics of Turbomachinery" Wiley-Interscience Hoboken, NJ, USA, ISBN: 978-0-471-80258-7, 1988

[10] Chui C.K., 1994, "An Introduction to Wavelets", Academic Press.

[11] Walnut D.F., 2002, “An introduction to wavelet analysis” Boston - Birkhäuser.

[12] Nikias CL, Petropulu A. Higher-order spectra analysis: a non linear signal processing framework. Englewood Cliffs, New Jersey: Prentice-Hall; 1993.

[13] Mendel J. M. Tutorial on higher order statistics (spectra) in signal processing and system theory: theoretical results and some applications. Proc. IEEE 1993;79:287–95.

[14] Guoji S, Mc Laughlin S, Yongcheng X, White P. Theoretical and experimental analysis of bispectrum of vibration signals for fault diagnosis of gears. Mech Syst Signal Process 2014; 43:76–89.

[15] Saidi Lotfi, Ben Ali Jaouher, Fnaiech, Farhat “Application of higher order spectral features and support vector machines for bearing faults classification” 10.1016/j.isatra.2014.08.007; JO - ISA Transactions

[16] Liao S., Chen J., “Time-frequency analysis of compressor rotating stall by means of wavelet transform” - ASME 1996 International Gas Turbine and Aeroengine Congress and Exhibition, June 10–13, 1996, Birmingham, UK

[17] Buresti G., Lombardi G., “Application of continuous wavelet transforms to the analysis of experimental turbulent velocity signals” - S. Banerjee, J.K. Eaton (Eds.), Turbulence and shear flow phenomena—1, Begell House Inc, New York (1999), pp. 767-772

[18] Greitzer E.M., “Surge and Rotating Stall in Axial Flow Compressors. Part I: Theoretical Compression System Model”, Journal of Engineering for Power, 98 (1976) 190-198.

[19] Nikias C.L., Raghuveer M.R., “Bispectrum estimation: A digital signal processing framework” - Proc. IEEE, Vol. 75, pp. 869-91, July 1987.

[20] Niccolini Marmont Du Haut Champ, C.A., Silvestri, P., Ferrari, M.L., Massardo, A.F., Signal Processing Techniques to Detect Centrifugal Compressors Instabilities in Large Volume Power Plants, ASME Journal of Engineering for Gas Turbines and Power, December 2020, Vol. 142 / 121002-1

[21] Allen, J.B., “Short-time spectral analysis, synthesis and modification by discrete Fourier transform,” IEEE Trans ASSP, Vol. 25, pp. 235-38, June 1977

[22] Gabor, D., “Theory of communication,” J.i.e. E., Vol. 93, pp. 429-59, 1946.

[23] Mallat, S., “A theory for multi-resolution signal representation: the wavelet transform,” IEEE Trans. PAMI, Vol. 11, pp. 674-93, July 1989.

[24] Rangoussi, M. and G.B. Giannakis, “FIR modeling using log-bispectra: Weighted least-squares algorithms and performance analysis,” IEEE Trans. Cir Sys, Vol. 38, pp. 281-96, 1991.

[25] Cohen, L., “Time-Frequency Distributions: A Review,” Proc. IEEE, pp.941-81, July 1989.

[26] Hlaswatch, F., and G.F. Boudreaux-Bartels, “Linear and Quadratic Time-Frequency Representations,” IEEE Signal Processing Magazine, pp. 21-67, Apr. 1992.

[27] Boudreaux-Bartels, G., Time-Frequency Signal Processing Algorithms: Analysis and Synthesis Using Wigner Distributions, Ph.D. dissertation, Rice University, 1984.

[28] Gerr, N.L., “Introducing a third-order Wigner distribution,” Proc. IEEE, pp. 290-92, Mar. 1988.

[29] Fonollosa, J.R. and C.L. Nikias, “Wigner Higher-Order Moment Spectra: Definitions, Properties, Computation and Applications to Transient Signal Detection”, IEEE Trans. SP, Jan. 1993.

[30] Fonollosa, J.R. and C.L. Nikias, “Analysis of finite-energy signals using higher-order moments- and spectra-based time-frequency distributions”, Signal Processing, Vol. 36, pp. 315-28, 1994.

[31] Swami, A., System Identification Using Cumulants, Ph.D. Dissertation, University of Southern California, pp. 107-8, 1988.

[32] Swami, A., “Higher-Order Wigner Distributions,” in Proc. SPIE-92, Session on Higher-Order and Time-Varying Spectral Analysis, Vol. $1770, 290-301, San Diego, CA, July 19-24, 1992

[33] Swami, A., “Third-order Wigner distributions,” Proc. ICASSP-91, pp.3081-84, Toronto, Canada, May 1991.

[34] Classen, T.A.C.M. and W.F.G. Mecklenbraüker, “The Wigner distribution —a tool for time-frequency signal analysis,” Phillips J. Res., Vol. 35, pp. 217-50, 276-300, 372-89, 1067-72, 1980.

[35] Classen, T.A.C.M. and W.F.G. Mecklenbraüker, “The aliasing problem in discrete-time Wigner distributions,” IEEE Trans ASSP, pp. 1067-72, Oct. 1983.

[36] Choi, H. and W.J. Williams, “Improved Time-Frequency Representation of Multicomponent Signals Using Exponential Kernels,” IEEE Trans. ASSP, pp. 862-71, June 1989.

[37] Perryin, F. and R. Frost, “A unified definition for the discrete-time, discrete-frequency, and discrete time/frequency Wigner distributions,” IEEE Trans. ASSP, Vol. 34, pp. 858-67, Aug. 1986.

[38] Antoni J (2009) Cyclostationarity by examples. Mech Syst Signal Process 23:987–1036

[39] Antoni J (2007) Cyclic spectral analysis in practice. Mech Syst Signal Process 21:597–630

[40] Harris C.M., Piersol A. G., “Harris’ Shock and vibration handbook”, McGraw-Hill, New York, 2002, ISBN 0-07-137081-1

[41] Vance J. M. “Rotordynamics of Turbomachinery” Wiley-Interscience Hoboken, NJ, USA, ISBN: 978-0-471-80258-7, 1988

[42] Reggio F., Ferrari, M.L., Silvestri P., Massardo A.F., “Vibrational analysis for surge precursor definition in gas turbines” 2019 Meccanica

[43] Ferrari M.L., Silvestri P., Reggio F., Massardo A.F. “Surge prevention for gas turbines connected with large volume size: Experimental demonstration with a microturbine” 2018 Applied Energy

[44] Ye Z., Wang L., Effect of external loads on cage stability of high-speedball bearings. Proc Inst Mech Eng Part J, J Eng Tribol 2015;229:1300–18.

[45] Linkai Niu, Hongrui Cao, Zhengjia He, Yamin Li, an investigation on the occurrence of stable cage whirl motions in ball bearings based on dynamic simulations, Tribology International, 2016, 103: 12-24.

[46] Han, C.-F., Chang, C.-S., Wu, C.-J., Chu, H.-Y., Horng, J.-H., Wei, C.-C., Lin, J.-F., Determinations of thermoelastic instability for ball-bearing-like specimens with spacers and in grease lubrications (2020) Tribology International, 151, art. no. 106415

[47] Gupta PK. Frictional instabilities in ball bearings. Tribol Trans 1988;31(2):258–68.

[48] Bianchini, A., Biliotti, D., Giachi, M., Belardini, E., Tapinassi, L., Ferrari, L., & Ferrara, G. (2014). Some Guidelines for the Experimental Characterization of Vaneless Diffuser Rotating Stall in Stages of Industrial Centrifugal Compressors. Volume 2D: Turbomachinery.

[49] Bianchini, A., Biliotti, D., Tommaso Rubino, D., Ferrari, L., & Ferrara, G. (2015). Experimental Analysis of the Pressure Field Inside a Vaneless Diffuser from Rotating Stall Inception to Surge. Journal of Turbomachinery, 137(11), 111007.

[50] Niccolini Marmont Du Haut Champ, C. A., Silvestri, P., Ferrari, M. L., and Massardo, A. F., “Incipient Surge Detection in Large Volume Energy Systems Based on Wigner-Ville Distribution Evaluated on Vibration Signals”, ASME. J. Eng. Gas Turbines Power, January 22, 2021

6 Conclusions

As it concerns hydrodynamic bearings static performance characterization, the comparison between numerical and experimental results underlines a consistent behaviour of simulation models even with very small clearances, whose reliability is enhanced by model complexity and accuracy. Furthermore, a good correlation between journal locations predicted by numerical computations and measured in modified RK has been found out. Therefore, a relative radial clearance of 8/1000 fulfils the thin film Reynolds hypothesis on which calculation models are based. Furthermore, since the employed FE codes had been already validated in the past, this also confirms that the modified test bench is reliable for further experimental investigations on this type of journal bearings, thus allowing us to study their dynamic behavior in future research activity. Indeed, TEHD analysis results prove that, while displacements due to hydrodynamic pressures are negligible, thermal deformations strongly affect journal position even under low external load (rotor weight is around 0.5 kg) and small temperature rise in the bearing. This is due to the high expansion coefficient of the bearing polycarbonate material and the high differential thermal dilatation between steel journal and polymeric bushing. After a series of experiments and related data processing, reasonable temperature boundary conditions have been determined based on the temperature control at the bearing supply and simulations performed by means of different models. Discrepancies found in journal center location predictions may also be ascribable to oil temperature variations with angular speed. Indeed, bearing supply oil temperature control has shown that such variations are not substantial so that they have not been simulated numerically. This can explain part of the obtained differences between experimental and numerical results. From the relevant results the most accurate simulation model for the bearing in analysis has been identified. It includes three-dimensional simulation of heat exchange phenomena. Indeed, at the rotational speeds investigated (250-3000 rpm), the thermal model is crucial in the assessment of bearing static characteristics. The reduction of relative radial clearance from original to modified RK values has improved the correlation between experiments and real-world applications as well as their agreement with numerical results from in-house developed FE codes implemented for lubrication analysis. This result is the starting point of future studies about dynamic behavior of journal bearings and, particularly, about fluid-structure interactions in this class of fluid film bearings. Nevertheless, industrial bearing casings are still different from our test rig ones in that they are usually manufactured in metallic materials. Therefore, thermo-mechanical behaviour in real-world bearings differs from our experimental models and numerical simulations, so that temperature and thermal displacements distribution within the bearing pair cannot be fairly compared. Obviously, in the present work we have assumed as main simulation parameter an average hot clearance and we have subsequently run the bearings in order to achieve that corresponding operating condition. Therefore, our numerical and

experimental assessments of journal center location are reasonable and consistent. In order to appropriately deal with industrial bearings considering thermo-mechanical effects, only the experimental device should be enhanced, simply by manufacturing a metallic bushing. On the contrary, our numerical model would not require any correction. We expect that employing a metal bush would simplify experimental procedure by both improving repeatability and ensuring quicker stationarity of experimental conditions, thus allowing to study even lower relative clearance ratios. We have not yet adopted this expedient as we are gradually updating an existing test rig. Indeed, in order to achieve the clearance adjustments required for the present investigation, only the journal has been modified accordingly. The high differential thermal dilatation between PC and steel makes it practically impossible to study clearance ratios lower than 3/1000 by assuming an average running temperature of 40°C. To summarize, a reduction in the clearance of the original RK has improved the correlation between experiments and real-world applications as well as the agreement with numerical results from codes implemented for lubrication analysis. In future research, the new test rig set up in this work will be employed for the dynamic analysis of rotor-bearings systems. Aerodynamic bearings for oil-free lubrication will be also investigated.

As it regards rotordynamics, an analytical model to assess ball bearings non-linear stiffness is proposed which relies on Hertz contact theory, which is first validated by mounting them on a RK4 commercial RK and then testing such simplified rotor-bearings system. Such bearing stiffness model is then extended to the study case of hybrid ball bearings since the investigated air Tesla turbine is mounted on such kind of supports. Indeed, the main goal is to predict critical speeds of a Tesla turbine rotor assembly, which is made up by a lot of thin disks held together in a stack by means of spacers to ensure a little gap between them; in order to adequately investigate such bladeless turboexpander from a structural point of view, a simplified FE model is devised within Ansys® environment, which is based only on beam elements, lumped masses as well as spring elements (i.e. lumped inertias and stiffnesses). Such reduced structural model is then provided with bearings stiffness computed in Matlab® environment by means of the already cited non-linear analytical model to perform system numerical modal analysis. In order to comply with modal analysis it is necessary to give as input a unique stiffness value, whereas the employed non-linear model gives stiffness as a function of bearing center deflection. A balance between external forces acting on the shaft (i.e. mechanical unbalance) and bearing non-linear restoring force is then imposed, by means of the hypothesis of rigid body (as assumed in ISO 1940-1) to found bearing center dynamic equilibrium position. Once it has been found, then current stiffness is assessed by means of bearing characteristic curve; if it is bigger than radial pre-load, then stiffness is evaluated by the increasing tract of its curve, otherwise it is assessed by the decreasing one. Indeed, the predicted non-linear stiffness law is a piecewise defined function,

whose trend is markedly affected by bearing radial pre-loading itself. Reasonable values of such parameter are assumed for the applicative study case of Tesla turbine, basing on literature findings, since it is almost impossible to rigorously assess such quantity. Anyway, a sensitivity analysis is given both for conventional steel bearings and for hybrid ones, and coherent trends are found among them; by passing from the maximum to the minimum allowable pre-load allowable values (one order of magnitude, according to literature findings), the curves are significantly different: all the values comprised between them can be regarded as acceptable in case of no information available about bearing radial pre-load. Afterwards, the so obtained critical speeds numerical predictions are compared with experimental data collected on a horizontal axis Tesla turbine, mounted on hybrid bearings in spindle configuration. In the experimental trends of engine orders 1 and 2 rms plotted versus machine angular speed, some amplitude peaks are present which can be ascribable to the first flexural critical speed onset. The so obtained experimental values are in good agreement with the corresponding numerical ones, which can be easily obtained from rotor-bearings system Campbell diagram by intersecting synchronous frequency (i.e. operating load due to residual mechanical unbalance) with system bending natural frequency curve. The so validated approach can be applied to other rotor-bearings systems in innovative energy plants as it is charcterized by lower computational times with respect to solid elements FE structural models and it is easily interpretable in terms of obtained results. In this context another rotor-bearings system made up by a gas microturbine is investigated by following the same procedure and the obtained results, coming from models with an increasing complexity level, are compared with experimental outcomes to test their reliability. The obtained results are not always in perfect agreement with experimental ones since such approach unavoidably leads to a loss of information, as it emerges in the test case of the microturbine mounted on metallic ball bearings; in case of preliminary structural analysis of innovative power plants based on rotating machinery mounted on ball bearings it could be a simple but reliable tool even for not specialists in structural dynamics. In future research activity, the aim is to improve the agreement with experimental data by finding empirical correlations to correctly assess bearing radial pre-loading and by tuning equivalent inertia and stiffness suited for modelling real system mechanical properties in a simplified way.

As it concerns fluid-structure interactions assessment in rotor systems, the conducted research activity deals with an experimental and numerical investigation about coupling phenomena from torsional to lateral vibrations of a complex shaft line with no interposed gearbox, mounted on hydrodynamic journal bearings and operated by an induction motor with high degree of torque irregularity. In such peculiar configuration, the observed system operational behavior exhibits an anomalous trend in terms of its synchronous lateral response, which cannot be caused by the classical non-linearity

sources described in literature (e.g. shaft line overhang mounting). Particularly, a localized hysteresis phenomenon is found between run-up and run-down tests. It is due to oil-whip within the journal bearings in agreement with current literature findings. The onset of such instability occurs at a speed double the torsional frequency, so that amplification of the torsional vibration yields high irregularity in rotation of a part of the shaft. The instability starts developing in a bearing where journal angular speed oscillation is significantly present. Such speed variation acts as a kinematic perturbation, which triggers a further perturbation of dynamic type. In specific operating conditions the combination of such two perturbations is turned into perturbation of the journal motion by the lubricant film. As described in literature, the stability margin is affected by large journal displacement perturbations, which in the test rig in study cause oil whip as well as hysteresis during run up/down tests. In this way, it can be explained how torsional vibrations can affect shaft line lateral response. Both experimental and numerical results support such explanation. The main experimental findings relevant to the studied test rig are the following:

- Oil-whip not preceded by oil-whirl can be detected in cascade plots of both lateral and torsional vibrations of journal bearings roughly at the same frequency.
- A perceivable degree of irregularity is measured in the rotation speed of the driven shaft, i.e. the part of the shaft directly driven by the electric motor, due to the large driving torque variations.
- Particularly, the threshold speeds RUTS and RDTS identified in cascade plots of the lateral vibrations can be different in the bearings of the driven shaft due to their rotation irregularity, so that the cause of the hysteresis detected in the machine is identified according to HBT.

By means of numerical simulations the conclusions in the following list can be drawn.

- A kinematic perturbation can modify the stability margin of a journal bearing; such phenomenon is identified as “torsional whirl”.
- The torsional whirl occurs at the same frequency of the excitation.
- The journal precession due to the dynamic perturbation can develop either at the same frequency of the excitation, when static load is higher than the rotating load or at half the excitation frequency, when the dynamic load component prevails.
- The maximum amplification of the journal precession whirling due to both kinematic and dynamic perturbation is found when excitation frequency is half the rotation speed.
- Although its isolated contribution to the journal vibration is very small, torsional whirl is required to trigger the dynamic perturbation in the dynamic model and must be also simulated in lubrication analysis to achieve consistent results.

Torsional oil-whirl is required to cause the oil-whip inception detected in experimental system responses and predicted by HBT. In the analyzed case, the presented experimental-numerical

approach can explain the significant localized hysteresis detected in synchronous lateral shaft line response. It proves the existence of coupling phenomena from torsional to lateral vibrations within single shaft real-size rotating machinery linked to unstable operating conditions within hydrodynamic bearings.

Finally, as it regards the investigation of rotating machinery behavior in case of fluid induced instability, wavelet analysis showed good prediction capabilities in detecting incipient surge conditions, with respect to conventional methods, such as STFT technique. Exploiting its features in terms of good frequency and time resolution allowed to recognize different contributions in system responses regarding different kinds of phenomena which take place close to surge line. Furthermore, this kind of analysis was able to confirm the intermittent nature of some of these phenomena in conditions very close to deep surge ones (e.g. rotating stall and acoustic modal response). Both HOSA and Wavelet methods allowed to identify low frequency phenomena related to the acoustic system response, together with sub-synchronous contents at medium frequency levels (0.25 – 0.45X), attributable to rotating stall. Moreover, BPF was studied in high frequency range in order to investigate its energy contents and understand how they change interacting with rotating stall inception when moving close to surge line. HOSA approaches were conducted on structural and acoustic signal responses in order to find some indicators for predictive diagnostics with regards to surge instability, reliable also for on-field measurements where background noise can cover diagnostic signal content. Indeed, this characteristic could provide an earlier detection of instability phenomena onset, with respect to conventional methods. In this work, an effort was made in order to characterize different stall and surge patterns depending on their bi-spectrum and wavelets maps. As a consequent step, the definition of an original feature based on pattern characteristics of previous maps, is proposed and it reveals to be reliable for all the tested conditions. However, further investigations are required to better validate the proposed diagnostic approach. The obtained results are encouraging, and thus future developments of these techniques might plan further experimental tests and the implementation of diagnostic systems based on new indicators from them extracted, in order to assess their robustness in different compressor circuit layout. All the presented methods showed limited computation times while ensuring at the same time good reliability with reference to conventional methods; therefore, they seem to be adequate also for the implementation both in real-time diagnostic systems and in control ones for surge prevention. Moreover, attention will be focused in the improvement of suitable features definition, on the basis of the frequency ranges characterized by more sensible energy contents linked to the onset of instability phenomena.

The peculiar aspect of the last presented investigation has been primarily to prove the capabilities of adopting SPWVD for incipient surge detection by relying only on vibrational response signals. To

this aim, appropriate surge transients have been selected and SPWVD has been performed on suitable time extracts to focus on how spectral contents evolve with time from a condition close to instability to a fully unstable one, that is, from incipient surge conditions to deep surge ones. The investigation has been conducted on a modular plant in which it is possible to modify compressor discharge volume in order to emulate mGT real plant configurations and so to investigate how SPWVD is effective in detecting system functioning variation by changing its volume configuration. This technique allowed a detailed system identification procedure by showing well-distinguishable spectral contents pattern depending on plant actual working state. It has been investigated how mGT high-speed rolling bearings operating status may change in terms of stability when approaching incipient surge conditions by modifying vibrational system response. mGT bearings seem to be affected by unstable cage-whirl, a sub-synchronous instability phenomenon (0.3-0.4X) related to contact phenomena in rolling elements; this may be associated with spectral contents which exhibit an energy level decrease passing from a stable condition to an unstable one. As reported in technical literature, this unstable cage-whirl phenomenon, can be mitigated by increasing external loads acting on the bearings; therefore, the additional forces associated with approaching surge may justify energy reduction in corresponding spectral contents. Moreover, it has been found that in incipient surge conditions spectral contents ascribable to structural resonances increase their energy levels. This is probably related to an anomalous flow pattern within the impeller that may generate broadband forcing that can excite some system natural frequencies. A deeper insight into 0-0.2 kHz range has been performed in order to assess very low frequency content energy variations in the last instants before the first deep surge cycle; two distinct and mutually independent diagnostic features have been found; one may be related to resonances (structural and/or acoustics), while the other may be associated with the stabilization mechanism of rolling bearings instability phenomena and their modulating effects. In 0-0.2 kHz frequency range, SPWVD has identified a spectral content (0.18X), well detectable some instants before reaching deep surge conditions that can be associated with a VDRS; its energy level is relevant in incipient surge conditions while it suddenly decreases as soon as entering surge. The results obtained show that its characteristic frequency is invariant with interposed volumes; this seems to confirm this hypothesis, as it is coherent with theory, since VDRS is a physical phenomenon that involves only the compressor and does not depend on the entire plant volumes. In this case, the results coming from SPWVD have been compared with the ones obtained from other TFDs, such as STFT and WT, in order to validate its robustness in identifying in detail spectral contents dynamic evolution. A further investigation has been performed on vibrational data coming from a high frequency accelerometer to study how BPF is influenced by passing from stable to unstable compressor operating conditions. Even if these results require further deepening about the fluid-dynamic behavior

within the compressor, they allow to identify noticeable phenomena related to a problem of incidence at impeller inlet. Indeed, it has been found that there are spectral contents which increase their energy levels in incipient surge conditions, while a dominant frequency in stable conditions (BPF considering both splitter and main blades) loses its energy, which is spread in a wider frequency band. This information coming from high frequency responses can be exploited for diagnostic purposes, together with the other features coming from specific content trends in the sub-synchronous range (unstable cage-whirl instability, resonances, VDRS) in order to develop a robust diagnostic system for surge detection. The implementation algorithm of SPWVD employed in this context is characterized by high computational times and hence it may require high performance workstations in order to develop both real-time diagnostic systems and control ones for surge prevention. However, a further optimization of SPWVD implementation algorithm might reduce the required computational effort.

In all the considered cases SPWVD allows to clearly distinguish different patterns with reference to the current operating condition, ranging from stable to incipient and deep surge conditions. The investigation has highlighted how rolling bearings are sensitive to a change in an operating condition of the mGT by modifying system operating vibrational response. In this specific case, observing how spectral contents related to bearing instability change their energy level with high resolution properties typical of SPWVD seems to be a more robust diagnostic tool with respect to other TFDs for early surge detection.